Tales of Instability and Decay: an Integrable Perspective



Aleksandra A. Ziółkowska
St John's College
University of Oxford

A thesis submitted for the degree of
Doctor of Philosophy

Trinity 2021

"Nothing in life is to be feared, it is only to be understood. Now is the time to understand more, so that we may fear less."

Maria Skłodowska-Curie

Acknowledgements

On my DPhil journey, I have received generous support from many individuals, but most significantly from the community of researchers in integrability. I credit them not only with fuelling my passion for research through the challenges of the doctoral degree, but also making together incredible memories during conferences. In this group, special thanks go to my fellow organisers of the Student Workshop on Integrability, Gilles Parez, Phillip Jaeger, and Andrew Urilyon, and all the other participants of "integrable" beers.

I extend my gratitude to my thesis supervisor, Fabian Essler, for enabling me to pursue research at the University of Oxford, dedicating countless hours to scientific discussions, and introducing me to the field of integrability I fell in love with.

I am thankful to have been inspired by many amazing women in physics I have met during research and outreach events. Most prominently, I am deeply indebted to my collaborator, Olalla Castro-Alvaredo, for her academic and personal mentorship, endless patience and compassion, and being a role model for academic excellence.

I am enormously grateful also to my collaborators, Cecilia de Fazio, for creating the kindest and most nourishing atmosphere in research, and Benjamin Doyon, for always swooping in with just the right insight.

Sincere thanks to my colleagues, Glenn Wagner and Sam Garret, for the comradeship and the continuing support during the highs and lows of the DPhil.

I am thankful to the St. John's College MCR community, for making my time in Oxford unforgettable, as well as the salsa and bachata dancing community, for all the hours together on the dance floor and opportunities to escape the Oxford "bubble".

Above all, I thank my family, for their unwavering faith in me.

Last but not least, the completion of this thesis was only possible thanks to the financial support from the Engineering and the Physical Sciences Research Council UK and the British tax payer.

Abstract

This thesis presents theoretical groundwork for the investigation of particular phenomena of instability and decay in out-of-equilibrium many body systems. By employing mathematical methods of integrability, we succeed in gaining new insights into problems not traditionally associated with an integrable realm.

The family of homogeneous sine-Gordon models provides a rare example of an integrable quantum field theory where both stable and unstable excitations are present in the spectrum. We studied the effect of unstable particles in different out-of-equilibrium settings and have shown that their presence is associated with specific signatures in many quantities of physical interest. Adopting the generalized hydrodynamic approach, we investigated the non-equilibrium dynamics following a quench and observed hallmarks of the creation and decay of unstable particles. Furthermore, we explored in considerable detail their quantitative and qualitative dependence on the parameters of the problem.

Decay processes due to environmental interactions are an experimentally relevant problem, yet the theory of open systems is substantially less developed than for their closed counterparts. We concentrate on Markovian open quantum systems described by a Lindblad time evolution equation and design a framework for analytic investigation of Lindblad dynamics via establishing a connection with integrability. We identify a number of Lindblad equations that can be mapped onto non-Hermitian interacting Yang-Baxter integrable models. The key ingredient of the proposed map is the structural similarity between the operators considered. We present examples of mappings between integrable Hamiltonians and Lindblad generators and underline several models of physical interest which can be investigated within this framework. By employing Bethe ansatz techniques, we study the dynamics of some of these models.

Contents

1 Introduction **1**

2 Integrable Perspective **3**

2.1 What Makes a Model Integrable? 5

2.2 Scattering Matrix 6

2.2.1 Yang-Baxter Relation 8

2.2.2 Symmetries 9

2.2.3 Analytic Structure of the Scattering Matrix in Quantum Field Theory 12

2.2.3.1 Asymptotic Particles 13

2.2.3.2 Unstable Particles 13

2.3 Quantum Inverse Scattering 15

2.4 Bethe Ansatz Techniques 17

2.4.1 Coordinate Bethe Ansatz 17

2.4.2 String Hypothesis 22

2.4.3 Thermodynamic Bethe Ansatz 24

2.4.3.1 Parity Violation 27

2.5 Equilibration in Integrable Systems 28

2.5.1 Quench Dynamics 29

2.5.2 Generalised Gibbs Ensemble 30

2.6 Generalised Hydrodynamics 31

3 Tales of Instability: Unstable Particles in an Integrable Quantum Field Theory **36**

3.1 Out-of-Equilibrium Physics in Quantum Field Theory 36

3.2 Homogeneous Sine-Gordon Models 38

3.2.1 General Features 38

3.2.2 $SU(3)_2$-Homogeneous Sine-Gordon Model 40

3.2.2.1 Thermodynamic Bethe Ansatz and Generalised Hydrodynamics . . . 42
3.3 Gaussian Quench Setup . . . 44
3.4 Free Fermions in a Gaussian Quench . . . 46
3.4.0.1 Decay . . . 47
3.5 Equilibrium Signatures of Unstable Particles . . . 49
3.6 Non-Equilibrium Phenomenology of Unstable Particles . . . 52
3.6.1 Time Evolution . . . 53
3.6.2 Bath Effects . . . 54
3.6.3 Comparison with Free Particle Evolution . . . 56
3.7 Subsidiary Peak: Persistence versus Decay . . . 60
3.7.1 Propagation . . . 60
3.7.2 Quantifying Decay . . . 64
3.7.2.1 Early Times: Gaussian Decay . . . 66
3.7.2.2 Intermediate Times: Exponential Decay . . . 68
3.8 Persistent Peak: Emergence of a Magnetic-Fluid . . . 71
3.8.1 Persistent Peak Position . . . 72
3.8.2 Persistent Peak Height and Volume . . . 77
3.9 Other Temperatures Profiles . . . 80
3.9.1 Inverted Gaussian Profile . . . 80
3.9.2 Double Gaussian Profile . . . 82
3.9.2.1 No Bath . . . 82
3.9.2.2 Finite Bath . . . 85
3.10 Discussion . . . 87

4 Tales of Decay: Integrability in Open Quantum Systems 89
4.1 Importance of Open Quantum Systems . . . 89
4.2 Markovian Open Quantum Systems . . . 90
4.3 Solutions to the Lindblad Equation . . . 95
4.3.1 Tight Binding Hamiltonian with a Dephasing Noise . . . 95
4.3.2 Other Known Results . . . 96
4.4 Superoperator Formalism . . . 98
4.4.1 Definitions . . . 98
4.4.2 Vectorisation . . . 101
4.4.2.1 Fermionic Jump Operators . . . 103
4.5 Superoperator Lindblad Structure . . . 104

4.5.1 Single-Site Jump Operators . . . 105
4.5.1.1 2-State Fermionic Example . . . 106
4.5.2 Single-Bond Jump Operators . . . 107
4.5.3 Single-Bond Hamiltonian . . . 108
4.5.4 Single-Bond Liouvillian . . . 109
4.6 Integrable Lindbladians . . . 109
4.6.1 Generalized Hubbard Models . . . 109
4.6.2 $SU(2)$ Hubbard Model . . . 112
4.6.2.1 Quench Dynamics . . . 112
4.6.3 USW Model . . . 119
4.6.3.1 Associated Lindblad Equation . . . 119
4.6.3.2 Correlation Functions . . . 120
4.6.4 Maassarani Models . . . 121
4.6.4.1 Associated Lindblad Equation . . . 122
4.6.4.2 3-State Maassarani Model . . . 123
4.6.4.3 4-State Maassarani Model . . . 124
4.6.4.4 Bethe Ansatz Solution . . . 125
4.6.4.5 String Solutions and the Liouvillian Gap . . . 127
4.6.5 $GL(N, M)$ Maassarani Models . . . 129
4.6.5.1 3-State $GL(1, 2)$ Model . . . 129
4.6.5.2 4-State $GL(2, 2)$ Model . . . 130
4.6.6 Other Integrable Two-Legged Ladder Models . . . 130
4.6.7 $GL(N^2)$ Magnets . . . 130
4.6.7.1 Associated Lindblad Equation . . . 131
4.6.7.2 Twisting the Boundary Conditions . . . 132
4.6.7.3 $GL(4)$ Spin Ladder . . . 133
4.6.7.4 $GL(4)$ Anisotropic Spin Ladder . . . 134
4.6.8 $GL(n_B^2 + n_F^2|2n_Bn_F)$ Magnets . . . 135
4.6.8.1 Associated Lindblad Equation . . . 135
4.6.9 Generalised Integrable Spin Ladder . . . 136
4.6.9.1 Associated Lindblad Equation . . . 136
4.7 Scaling Limits of the Lindbladian . . . 136
4.8 Operator Space Fragmentation in Lindblad Dynamics . . . 138
4.9 Spin-1/2 Dissipative Chains . . . 140
4.9.1 Asymmetric Simple Exclusion Process . . . 143
4.9.1.1 Additional Terms . . . 144

4.9.2 Symmetric Simple Exclusion Process with Balanced Particle Creation and Annihilation . . . 145
4.9.3 Correlated Hopping with Correlated Particle Creation and Annihilation . . . 146
4.9.4 XXZ Bethe Ansatz . . . 147
4.9.5 Higher Dimensional Generalisation . . . 147
4.9.6 XYZ Model in Operator Space Fragmentation . . . 149
4.10 Discussion . . . 150

5 Conclusion and Outlook **152**

A Numerical Generalised Hydrodynamics Investigation of the $SU(3)_2$-Homogeneous Sine-Gordon Model **154**
A.1 Generalities . . . 154
A.2 Precision and Consistency Checks . . . 155
A.3 Space and Rapidity Discretisations . . . 156

B Analytic Computation of $\mathfrak{q}_0(0,0)$ **160**

C Single-Bond Jump Operator **162**
C.1 2-State Fermionic Example . . . 162

D Some Unsuccessful Lindblad Maps **164**
D.1 Perk-Schultz Models . . . 164
D.2 Higher Conservation Laws . . . 164
D.3 Alcaraz-Bariev Model . . . 166
D.4 Spin-1/2 Ladder Models . . . 168
D.4.1 Dzyaloshinsky-Moriya Spin Chain . . . 169

Bibliography **171**

Glossary

ABA Algebraic Bethe Ansatz

ASEP Asymmetric Simple Exclusion Process

BA Bethe Ansatz

BAE Bethe Ansatz Equations

CBA Coordinate Bethe Ansatz

CFT Conformal Field Theory

DMRG Density Matrix Renormalization Group

GGE Generalised Gibbs Ensemble

GHD Generalised Hydrodynamics

HSG Homogenous Sine-Gordon

NABA Nested Algebraic Bethe Ansatz

NAT Non-Abelian Toda

QFT Quantum Field Theory

QISM Quantum Inverse Scattering Method

SSEP Symmetric Simple Exclusion Process

TBA Thermodynamic Bethe Ansatz

USW Umeno-Shiroishi-Wadati

List of Figures

2.1 Diagrammatic representation of the Yang-Baxter relation for particles with no internal degrees of freedom. Interaction of particles labelled i, j is described by a diagonal scattering matrix $S_{ij} \equiv S_{ij}(p_i, p_j)$. . . . 9

2.2 Analytic structure of the S-matrix in the square of the centre of mass plane s. Solid dots and lines represent the branch points and the branch cuts respectively. 12

2.3 S-matrix pole structure with the corresponding excitations. 15

2.4 Examples of the possible string solutions to the Hubbard model BAE. 24

2.5 A rescaled counting function Lc_a versus rapidity θ. A graphical solution for three different integers is shown, where only two of them, I_j and I_{j+1}, are allowed quantum numbers. The roots and holes are marked with filled and empty circles respectively. 26

2.6 An isolated quantum system partitioned into a finite subsystem A and its complement $\bar{A}$ [94]. The subsystem interacts with the remainder of the system. 28

2.7 Mesoscopic scale of a fluid-cell. Figure reproduced after [18]. 32

3.1 Two-body scattering kernel for the $SU(3)_2$-HSG model with $\sigma = 10$. . 41

3.2 Zamolodchikov's c-function versus the logarithm of the inverse temperature $\beta = 1/T$. Each curve corresponds to the $SU(3)_2$-HSG model with the resonance parameter set to (in order from left to right) $\sigma = 25, 20, 10, 0$. The figure has been taken from [177]. 42

3.3 Initial temperature profile for $2T_m = e^7$ and $2T_a = e^3$. 45

3.4 Free fermion particle density $\mathfrak{q}_0^{\mathrm{FF}}$ for a choice of parameters $\sigma = 10, \log 2T_m = 9, T_a = 0$ for a Gaussian temperature profile (3.22). After separating at $t = 0.8$, two identical peaks propagate in opposite directions at velocities ± 1. 48

3.5 $SU(3)_2$-HSG effective velocity cuts $v^{\text{eff},+}$ as a function of rapidity θ for a choice of parameters $\sigma = 10, \log 2T_m = 9, T_a = 0$. Each cut is taken at a different position x corresponding to a different local equilibrium temperature in the Gaussian temperature profile $T(x)$. The temperature is the highest at $x = 0$ (red), with $\log 2T = 9$, and decays to $\log 2T = 0$ at $x \approx 3$ (blue). 50
3.6 Local equilibrium ($t = 0$) effective velocity for the particle + in the HSG model initialised in a temperature profile (3.22) with a choice of parameters $\sigma = 10, \log 2T_m = 9, T_a = 0$. 51
3.7 Cross-section of the spectral density for the HSG model particle + (left) and for free fermions (right) at $x = 0$ as a function of rapidity in a Gaussian temperature profile at local equilibrium ($t = 0$). The resonance parameter for the HSG model is $\sigma = 10$ and the temperatures in both cases were chosen to be $\log 2T_m = 9, T_a = 0$. We see that, in comparison to free fermions, a secondary maximum emerges in the spectral density of the HSG model and the height of a primary maximum in the interaction region is increased. 52
3.8 Spectral density for the HSG model at local equilibrium ($t = 0$) in a Gaussian temperature profile (3.22) and a choice of parameters $\sigma = 10, \log 2T_m = 9, T_a = 0$. 52
3.9 Particle + dynamics for various time snapshots. The parameters are $\sigma = 10$, $T_a = 0$ (no bath) and $2T_m = e^7$. Row 1: Spectral density exhibits three characteristic local maxima, the least of which decays in time leading to the formation of a tail. Row 2: Spatial particle density exhibits both a tail and decay. Row 3: Effective velocities are dominated by the values ± 1 but also exhibit intermediate plateaus in rapidity space which are correlated with the decaying peak position in the spectral density. The dynamics of particle − follow from the relations (3.21). See also the video [187] for the time evolution of functions $\rho_p^+(x, t, \theta)$ and $v^{\text{eff},+}(x, t, \theta)$ in the presence of bath. 54

3.10 Time snapshots of the spectral densities $\rho_p^{\pm}(x,t,\theta)$ for $x \geq 0$ in the presence of a bath. The parameters are $\sigma = 10$, $2T_m = e^7$, $2T_a = e^3$. Recall that $\rho_p^+(x,t,\theta) = \rho_p^-(-x,t,-\theta)$. Whilst the interacting and free fermion peaks remain largely unchanged, the bath facilitates the formation of a persistent peak that travels at speed $+1$ "riding" on top of the bath. The two light-blue ridges are also due to the bath whose temperature is in the free fermion region of the theory. The ridges look "static" because they are uniformly distributed in space but actually propagate with opposite effective velocities ± 1. See also the video [188] for a spectral density comparison between the cases with and without a bath. 55

3.11 The partial spatial particle density $\mathfrak{q}_0^+(x,t,\theta<0)$ showing the decay in the absence of bath (inset) and persistence in the absence of bath (main figure) of the subsidiary peak. See also the video [188] for a spectral density comparison between the cases with and without a bath. 56

3.12 Particle density in the HSG model $\mathfrak{q}_0^+(x,t)$ (red) versus $\mathfrak{q}_0^+(x-t\tanh\theta,t)$ (blue). The top/bottom rows correspond to the absence/presence of a bath. The peak in the first column has been cut so as to show the remaining figures more clearly. The dotted curves represent the change in the height of the local maxima of the particle densities as function of time. Red and blue curves generally differ in the height of the local maxima as well as the presence (absence) of a tail. 58

3.13 Particle density in the HSG model (red) compared to the particle density that would result from free evolution of the same initial conditions (blue). The top/bottom rows correspond to the absence/presence of a bath. The peak in the first column has been cut so as to show the remaining figures more clearly. The dotted curves represent the change in the height of the local maxima of the spectral densities as function of time. 59

3.14 Time snapshots of the spectral density $\rho_p^+(x,t,\theta)$ for $x \geq 0$, $\sigma = 10$ and $\alpha_m = 7$, in the presence of a bath at temperature $\alpha_a = 3$ (row 1) and in the absence of bath (row 2). Both cases show qualitatively identical decay behaviour. In the case where a persistent peak on top of a bath ridge is present, it is superimposed onto the decaying feature. See also the video [188] for a comparison between the cases with and without a bath. 63

3.15 Effective velocities (left axis, blue) and spectral density cross-sections (right axis, red) of particle + in row 1 and − in row 2 at time $t = 10$ in the case without bath. For particle + we see the subsidiary (decaying) and free fermion peaks whereas for particle − we see the interacting peak. Columns shows these quantities sequentially for positions $x = 9, 9.2, 9.4, 9.6, 9.8$. The central emphasised column corresponds to $x = x^* = 9.4$, that is the position of the maximum of the subsidiary peak of particle +. The vertical dashed lines indicate the maximum of particle + subsidiary peak cut in row 1 and the maximum of particle − interacting peak cut in row 2. The horizontal dashed lines indicate the corresponding effective velocity of particle + and are annotated with the numerical values. 64

3.16 Effective velocities (left axis, red) and spectral density cross-sections (right axis, blue) of particle + in row 1 and − in row 2 at time $t = 10$ in the case with a bath at temperature $\log 2T_a = 3$. For particle + we see the subsidiary (persisting) and free fermion peaks whereas for particle − we see the (large) interacting peak and a very small bump corresponding to the bath (for particle + this is marked by the persisting peak sitting right on top). Columns show these quantities sequentially for positions $x = 9.6, 9.8, 10, 10.2, 10.4$. The emphasised central column corresponds to $x = x^* = 10$ the position of the maximum of subsidiary peak of particle +. The vertical dashed lines indicate the maximum of particle + subsidiary peak cut in row 1 and the maximum of particle − interacting peak cut in row 2. The horizontal dashed lines indicate the corresponding effective velocity of particle + and are annotated with the numerical values. 65

3.17 Time snapshots of the normalised particle density $\Delta\mathfrak{q}_0^+(x,t)$ for times from $t = 0$ (blue) to 10 (red). The function H_0^+ is plotted in black. The parameters are fixed to $\sigma = 12, \alpha_m = 7.5, \alpha_a = 3$. 66

3.18 Logarithm of the normalised particle density subsidiary peak maximum $\log H_0^+(t)$ for parameters $\sigma = 12, \alpha_m = 7.5$ as well as zero bath or bath exponents $\alpha_a = 2, 3, 4, 5$. Early time quadratic fit and intermediate time linear fit are also plotted in a black dashed line. 67

3.19 Logarithm of the particle density subsidiary peak maximum $\log H_0^+(t)$ for fixed $\kappa = 1.5$ in zero bath. Intermediate time linear fit follows a function $\log H_0^+(t) = -t/\tau + C + \log H_0^+(0)$, where $\tau \approx 1.68$ and $C \approx -0.05$. 69
3.20 Logarithm of the normalised particle density subsidiary peak maximum $\log H_0^+(t)/H_0^+(0)$ for a range of κ values in zero bath. 70
3.21 Logarithm of the subsidiary peak characteristic decay time τ versus the parameter κ. The linear fit follows a relation $\log \tau = a_\kappa \kappa + b_\kappa$ . . 71
3.22 Cuts in the spectral density $\rho_p^+(x = t, t, \theta)$ across the subsidiary peak in the $x = t$ plane for different time steps from $t = 0$ (blue) to 5 (red). The parameters are $\sigma = 12, \alpha_m = 7.5, \kappa = 1.5$ and zero bath (on the left) or $\alpha_a = 3$ (on the right). The subsidiary peak decays in the absence of the bath (left panel) and persists in a shape that "hugs" the bath profile plotted in black (right panel). 74
3.23 Left: Persistent peak of particle + position in the rapidity space $\theta^\star$ as a function of the interaction maximum $\theta_{max} = \theta_i^\star - \sigma$ with $\theta_i^\star$ indicating the position of the interacting peak maximum of particle $-$. Data is presented for two fixed parameters $\sigma = 12, 10$ and a fixed bath exponent $\alpha_a = 3$. Right: Persistent peak of particle + position $\theta^\star$ as a function of the bath maximum θ_b for a fixed parameter $\sigma = 12$ and a fixed maximum exponent $\alpha_m = 7.5$. 76
3.24 Column 1: Logarithm of the persistent peak height (top) and volume (bottom) as a function of the higher temperature exponent α_m for resonance parameters $\sigma = 12, 10$ and fixed bath temperature exponent $\alpha_a = 3$. Column 2: Logarithm of the persistent peak height (top) and volume (bottom) as a function of the bath temperature exponent α_a for resonance parameters $\sigma = 10$ and fixed bath temperature exponent $\alpha_a = 3$ as well as logarithm of the bath ridge height (top) for the same parameters. 78
3.25 Spectral density $\rho_p^+(x, t, \theta)$ (on the left) and the effective velocity $v_p^{\text{eff},+}(x, t, \theta)$ (on the right) local equilibrium ($t = 0$) cuts for several values of x in the inverted Gaussian profile (3.55). The parameters are $\sigma = 10, \alpha_a = 7, T_m = 0$. 81

3.26 Row 1: Spectral density of particle + for different time snapshots in the case of an inverted Gaussian profile (3.55). Row 2: Effective velocity of particle + with the particle flow plotted in white. The parameters are $\sigma = 10, \alpha_a = 7, T_m = 0$. 82
3.27 Local equilibrium ($t = 0$) spectral density of particle + (on the left) and the particle − (on the right) with the corresponding peak labelling. 83
3.28 Spectral density of particle + (row 1) and its effective velocity (row 2) snapshots from time $t = 0$ to 8 for a double Gaussian initial temperature profile (3.56). The parameters are $\alpha_m = 7$, $T_a = 0$, $\sigma = 10$ and $x_0 = 4$. At early times, left magnet drags some of the particles from the left interacting peak into the left subsidiary peak. 83
3.29 Spectral density of particle + (row 1) and its effective velocity (row 2) snapshot from time $t = 10$ to 40 for a double Gaussian initial temperature profile (3.56). The parameters are $\alpha_m = 7$, $T_a = 0$, $\sigma = 10$ and $x_0 = 4$. At late times, the decay of the left subsidiary peak lags behind the decay of the right subsidiary peak. 84
3.30 Spectral density cuts of particle + for $\theta = -3$ cutting across the subsidiary peaks. From time $t = 0$ to 10 we observe the decay of the right subsidiary peak and the transfer of the left subsidiary peak from the left tail to the right tail. 85
3.31 Spectral density close-ups of particle + (row 1) and particle − (row 2) for $\sigma = 10, \alpha_m = 7, \alpha_a = 3$ and $x_0 = 4$. $t = 0$: Two subsidiary peaks of particle + and two interacting peaks of particle − are identical. $t = 5$: The left subsidiary peak of particle + acquires additional particles from the right interacting peak of particle +. $t = 10$: The right subsidiary peak of particle + is persistent whereas the left one is still decaying. $t = 20$: The right persistent peak of particle + aligns in the coordinate space with a larger magnet, the right interacting peak of particle −. As a result, the right persistent peak of particle + is larger than the left one. 86
3.32 Spectral density and effective velocity cuts for particle + and $\theta = -3, t = 20$. Right-hand side is a close-up of the left-hand side figure. The right subsidiary peak, which aligns with a larger magnet, is both larger and has a higher effective velocity than the left subsidiary peak. The parameters chosen are $\alpha_m = 7$, $\alpha_a = 3$, $\sigma = 10$ and $x_0 = 4$. 86

4.1 Open system diagram [94]. 90
4.2 Ladder interactions accommodated by a Liouvillian with single-site and single-bond jump operators [94]. 105
4.3 Quench dynamics of $\mathrm{Re}\,[F_{k-l}(t)]$. Non-zero correlation appears only for odd separation values. No time-dependence is present. 115
4.4 Quench dynamics of $\mathrm{Re}\,[F_{k-l}(t)]$ with additional dissipation. Non-zero correlation appears only for odd separation values. Dephasing introduces an exponential suppression of the Green's function's magnitude. 115
4.5 Quench dynamics of $\mathrm{Re}\,[G_{k-l}(t)]$. Non-zero correlation appears only for odd separation values. Time-dependent quantum interference effects are present. 117
4.6 Quench dynamics of $\mathrm{Im}\,[G_{k-l}(t)]$. Non-zero correlation appears only for even separation values. Time-dependent quantum interference effects are present. 117
4.7 Quench dynamics of $\mathrm{Re}\,[G_{k-l}(t)]$ with additional dissipation. Non-zero correlation appears only for odd separation values. Time-dependent quantum interference effects are present, as well as an exponential suppression of the Green's function's magnitude due to dephasing. 118
4.8 Quench dynamics of $\mathrm{Im}\,[G_{k-l}(t)]$ with additional dissipation. Non-zero correlation appears only for even separation values. Time-dependent quantum interference effects are present, as well as an exponential suppression of the Green's function's magnitude due to dephasing. 118
4.9 Sketch of the string pattern for the Maassarani Bethe roots. Empty circles represent the case of real interaction strength whereas the solid circles correspond to the case considered in this chapter, with imaginary interaction strength. Figure reproduced after [227]. 128
4.10 A 1D lattice with periodic boundary conditions. Lattice sites are occupied by dynamic (blue) or static (orange) degrees of freedom. Linbladian projections onto each subspace (blue sites separated from others by defects) have an independent spectrum for Lindblad operators with only single-site and single-bond interactions. 139

A.1 Right: The rapidity discretisation interval as a function of rapidity for different numbers of points in a fixed rapidity interval $\theta \in [-17, 17]$. The markers indicate the values of N that are considered in Figure A.2. Left: Comparison of the rapidity discretisation interval in the middle and towards the edges of the interval with non-trivial dynamics for the choice of parameters considred in this thesis. $\Delta\theta_0$ and $\Delta\theta_{10}$ are defined to be the rapidity discretisation intervals for $\theta = 0$ and $\theta = 10$ respectively. 157

A.2 Particle density of particle + for different numbers of points in the fixed rapidity interval $\theta \in [-17, 17]$. The $N = 200$ panel shows regular oscillations. The oscillations persist for $N = 300$, disappear around $N = 500$ and are consistently absent for higher numbers of points, such as $N = 700$. Variations of space and time discretisation parameters have not produced any significant changes in the same functions. . . 158

List of Tables

3.1 Numerical results for the subsidiary peak of the spectral density of particle + in the absence ($T_a = 0$) and presence ($\alpha_a = 3$) of a bath. The other parameters are fixed to $\sigma = 10$ and $\alpha_m = 7$. x^*, θ^* and h^* are respectively the phase-space coordinates and the height of the local maximum of the subsidiary peak and $v^* \equiv v^{\text{eff},+}(x^*, t, \theta^*)$. The quantity x^*/t represents the observed propagation velocity of the subsidiary peak of particle + resulting from its interaction with the interacting peak of particle − which propagates at speed +1. The numerical uncertainty of phase-space coordinates is $\Delta x^* = 0.10$ and $\Delta\theta^* = 0.07$ to 0.08, with lower rapidity resolution for less negative values of θ^*. . . . 61

3.2 Linear fit parameters $\log H_0^+(t)/H_0^+(0) = -t/\tau + C$ to the normalised particle density subsidiary peak maximum for particle + and fixed $\kappa = 1.5$ in zero bath. R^2 is the R-squared goodness of fit parameter. . 69

3.3 Linear fit parameters $\log H_0^+(t)/H_0^+(0) = -t/\tau + C$ to the normalised particle density subsidiary peak maximum for particle + and a range of κ values in zero bath. R^2 is the R-squared goodness of fit parameter. 71

3.4 Linear fit parameters $\log \tau = a_\kappa \kappa + b_\kappa$ to the subsidiary peak characteristic decay time τ and a range of κ values in zero bath. R^2 is the R-squared goodness of fit parameter. 71

3.5 $\sigma = 12, \alpha_a = 3$ persistent peak data for a range of parameters α_m and κ. h_s is the height of the persistent peak in the spectral density and V_s is the volume of the subsidiary peak. We denote the rapidity position of the subsidiary peak maximum by $\theta^\star$, the bath ridge maximum by θ_b and the interaction maximum by θ_{max}. 73

3.6 $\sigma = 10, \alpha_a = 3$ persistent peak data for a range of parameters α_m and κ. h_s is the height of the persistent peak in the spectral density and V_s is the volume of the subsidiary peak. We denote the rapidity position of the subsidiary peak maximum by $\theta^\star$, the bath ridge maximum by θ_b and the interaction maximum by θ_{max}. 73

3.7 $\sigma = 12, \alpha_m = 7.5, \kappa = 1.5$ persistent peak data for a range of parameters α_a. h_s is the height of the persistent peak in the spectral density and V_s is the volume of the subsidiary peak. We denote the rapidity position of the subsidiary peak maximum by $\theta^\star$, the bath ridge maximum by θ_b and the interaction maximum by θ_{max}. 74

3.8 Parameter of the fit (3.48) for two values of the resonant parameter $\sigma = 12, 10$ and bath temperature exponent $\alpha_a = 3$. $\Delta a'_m, \Delta b'_m$ are the uncertainties of parameters a'_m, b'_m respectively. R^2 is the R-squared goodness of fit parameter. 77

3.9 Parameter of the fit (3.49) for resonance parameter $\sigma = 12$ and maximum temperature exponent $\alpha_m = 7.5$. $\Delta a'_a, \Delta b'_a, \Delta c'_a$ are the uncertainties of the parameters a'_a, b'_a, c'_a respectively. R^2 is the R-squared goodness of the fit. 77

3.10 Parameter of the fit (3.50) for the resonant parameter $\sigma = 12$ and maximum temperature exponent $\alpha_m = 7.5$. $\Delta a'_b$ is the uncertainty of parameter a'_b. R^2 is the R-squared goodness of fit parameter. 79

3.11 Parameters of the fit (3.54) with respect to α_m for two values of the resonance parameter $\sigma = 12, 10$ and bath temperature exponent $\alpha_a = 3$. $\Delta a''_m, \Delta b''_m$ are the uncertainties of parameters a''_m, b''_m respectively. R^2 is the R-squared goodness of the fit. 80

3.12 Parameters of the fit (3.54) with respect to α_a for resonance parameter $\sigma = 12$ and maximum temperature exponent $\alpha_m = 7.5$. $\Delta a''_a, \Delta b''_a, \Delta c''_a$ are the uncertainties of parameters a''_a, b''_a, c''_a respectively. R^2 is the R-squared goodness of the fit. 80

A.1 Numerical values of the total particle density Q_0 at several times. Here, the parameters are $\sigma = 10$, $\log(2T_m) = 7$ and $T_a = 0$ (no bath). To evaluate Q_0, we have computed $\mathfrak{q}_0^{\pm}$ and performed a cubic spline interpolation for the integration, implementing additional grid points whose spacing in x is $\Delta x = 1. \times 10^{-5}$. Q_0 is numerically conserved, up to a variation on the first decimal place, which can be attributed to the discretisation procedure. 156

A.2 Representative discretisation parameters and quadratures chosen for the numerical simulations discussed in section 3.6. From the left, the columns indicate (respectively for t, x, θ): the variable, the lowest resolution (i.e. the largest spacing between two grid points $\Delta_{\mathbf{max}}$), the number of grid points, the largest absolute value the variable takes, and the type of quadrature implemented. In the rectangular quadrature we have implemented equidistant grid points with fixed spacing $\Delta_{\mathbf{max}}$. 156

A.3 Numerical values of the rapidity discretisation intervals $\Delta\theta$, for a given number of rapidity points N in the range of rapidities $\theta \in [-17, 17]$. . 158

Chapter 1

Introduction

Progress in experimental capabilities in cold atom systems and solid state physics has given rise to a growing number of experiments involving out-of-equilibrium quantum many-body systems with increasingly long quantum coherence timescales [1–3]. These setups often present a significant challenge to analysis due to strong correlations. Despite some progress made with perturbative techniques, an exact description of such experiments is clearly needed. An abundance of mathematical techniques are available if the experiment can be described by an integrable theory.

Integrability techniques constitute a powerful mathematical machinery but are almost dogmatically associated with stable excitations and particle number conservation. However, integrability is richer than these constraints suggest. In fact, the presence of unstable particles in integrable models is possible and consistent with all physical requirements. Similarly, systems with decaying modes can be accommodated within the structure of integrability. Hence, in a sense, the typical integrability paradigm can be broken and it is this possibility we are exploring. In the following, I would like to summarise my research into instability and decay in integrable models and explain how the techniques of integrability can elucidate out-of-equilibrium phenomena in this unusual context.

The thesis is organised in five chapters. Following the introduction in Chapter 1, Chapter 2 presents the theoretical background necessary to apply the techniques of integrability in out-of-equilibrium setups. We introduce the concept of quantum integrability, underline the implications of integrability on the properties of physical systems, and review the key mathematical techniques used to study integrable models.

Chapter 3 applies these methods to study instability of bound states in an integrable Quantum Field Theory (QFT), the $SU(3)_2$-Homogenous Sine-Gordon (HSG) model. We study the formation and decay of unstable particles by analysing the release of hot matter into a low-temperature environment. The key phenomena observed are

the formation of tails and the decay of the emitted nonlinear waves in spectral and particles densities, in sharp contrast to the situation without unstable excitations. Moreover, a new phenomenon is uncovered by which a wave of a stable population of unstable particles may persist without decay for long times, and which links to new asymptotic states at finite-density. We expect these signatures of instability to have a large degree of universality. The chapter concludes that the out-of-equilibrium dynamics of many-body systems can be strongly affected not only by the asymptotic spectrum, but also by excitations with finite life-times.

In Chapter 4 the focus turns to the phenomenon of decay due to interactions with the environment. We concentrate on Markovian open quantum systems with Lindblad dynamics. By designing a vectorisation protocol, we identify the structure of the Lindblad generator and look for its equivalent in the realm of integrable models. Furthermore, it was found that many integrable Hamiltonians indeed can be mapped onto the vectorised Lindblad generators if they are rendered non-Hermitian through complex interaction parameters. In particular, a large family of generalised Hubbard models shows a clear structural similarity already at the level of its scattering matrix. For a subgroup of these models, we analysed their physical properties, such as time evolution of correlators, certain eigenstates and eigenvalues. We have also found other families of integrable models with Lindblad equivalents and present multiple examples of mappings between them. In this way, we pave the way for the analysis of open quantum systems with the methods of integrability.

Chapter 5 summarises the results and presents future research ideas this work has inspired.

This thesis is based on the following original publications.

Chapter 2

"Generalised Hydrodynamics of Particle Creation and Decay" O. A. Castro-Alvaredo, C. De Fazio, B. Doyon, A. A. Ziolkowska, *arXiv:2112.05462 (2021)*

"Tails of Instability and Decay: a Hydrodynamic Perspective" O. A. Castro-Alvaredo, C. De Fazio, B. Doyon, A. A. Ziolkowska, *arXiv:2103.03735 (2021)*

Chapter 3

"Yang-Baxter integrable Lindblad equations" A. A. Ziolkowska, F. H.L. Essler, *SciPost Phys. 8, 044 (2020)*

Chapter 2

Integrable Perspective

"I cannot help mentioning that working with the integrable models is a delightful pastime." -Ludvig Faddeev

Apart from being a delightful pastime, integrable models constitute a paradigmatic example of exactly solvable systems, which provide invaluable insights into many-body physics. Mathematically, they are described by coupled nonlinear equations to which we have a systematic approach of finding solutions. Thanks to a hidden enhancement of symmetries, which substantially constrain the dynamics, the solution to the integrable system's spectrum can be written in the form of algebraic relations whose complexity grows merely polynomially with the number of degrees of freedom. This is in stark contrast to the chaotic behaviour admitted by most nonlinear systems. The notion of integrability was first formulated for classical dynamical systems by Liouville. He ascertained that solutions to particular Hamiltonian systems can be solved by quadrature, meaning that they can be expressed in terms of integrals. However, only in the 1960s was a systematic way of solving classical integrable models devised. The first success of this approach, called the classical inverse scattering method, was in application to the Korteweg-de Vries equation of fluid mechanics [4]. It has been a vital tool in investigating classical dynamical systems ever since [5]. Quantum integrability can be traced to the seminal work of Bethe in 1931 [6], where, via the now-called Coordinate Bethe Ansatz (CBA), an analytic solution for the spectrum of the quantum Heisenberg model was presented. The initial statistical and quantum mechanical approaches to quantum integrability were eventually unified by the Leningrad Group in the Quantum Inverse Scattering Method (QISM) [7–9]. Subsequently, this led to the development of the Algebraic Bethe Ansatz (ABA) and allowed QFT and spin lattice systems to be encompassed into a single mathematical construction.

The underlying structure of quantum integrable models allows for exact analytic calculations of quantities otherwise accessible only numerically, with the equilibrium properties tractably computed with Density Matrix Renormalization Group (DMRG) algorithms [10–13], and more recently, the time evolution being attainable through its time-dependent extension going by the name of t-DMRG [14–17]. In the majority of cases, we are able to analytically obtain spectra and various thermodynamic quantities in integrable systems, and in some instances, much has also been learned about the correlators and the scattering amplitudes. Despite such progress, the structure of the eigenstates of interacting integrable systems is notoriously complicated. As a result, the understanding of non-equilibrium behaviour of integrable systems often remains out of reach. Recently, a new method was developed which remedies this problem. Generalised Hydrodynamics (GHD) [18, 19] is an approach based on the Thermodynamic Bethe Ansatz (TBA) and allows for efficient examination of the dynamics of conserved quantities at the mesoscopic scales, giving an unprecedented access to the dynamical properties of quantum many-body systems.

Integrable theories are mostly (1+1)- or 2-dimensional, where the former comprises 1D classical or quantum models evolving in time, and the latter 2D statistical mechanics problems. Even so, these low dimensional systems can teach us about a 4D world. In string theory, the 2D physics of a worldsheet can be related to a higher dimensional world, its target space. Moreover, there is evidence that the high energy scattering in 4D quantum chromodynamics is mainly a 2D phenomenon [20–22]. There are also significant similarities between non-linear sigma models in 2D and Yang-Mills theories in 4D, such as asymptotic freedom and mass through dimensional transmutation (i.e., the emergence of a mass scale through the renormalisation procedure) [23]. This strongly suggests that 2D physics can shed light on the corresponding 4D problems.

2D physics itself became ubiquitous in physics laboratories in recent years. In many condensed matter experiments, a $(1 + 1)$D problem arises naturally from the constraints of the material investigated. Rapid progress in nanofabrication and crystal growth technologies led to integrable physics being realised in solid state systems and the development of laser and vacuum technologies contributed to integrable interactions being engineered in cold atom and molecular experiments [24–28]. One spatial dimension results in amplification of the quantum effects, and also puts the interactions at the forefront of the dynamics [29]. For this reason, $(1 + 1)$D models form a perfect setup to study quantum collective phenomena such as non-linear optics [30], superconducting correlations [31], and spin-charge separation [32,33]. The predictions of integrability have led to the explanation of important experimental results, such as

equilibration properties of cold atom gases due to multiple conserved charges [24,34], and spectroscopic signatures of states arranged in Bethe strings [35]. Remarkably, having integrability as a starting point, one can study systems which depart from it and integrability breaking is a growing field of research [36–39]. These applications not only show integrability to be a vibrant area of investigation, but also underline the relevance of applying an integrable lens to novel problems in out-of-equilibrium many-body physics.

2.1 What Makes a Model Integrable?

The notion of integrability has become almost synonymous with exactly solvable models. Indeed, integrability is the basis of many mathematical methods which provide analytic results. Yet, at the same time, there do exist solvable models which are not integrable. A simple example is a dissipative mechanical system, such as a classical free-falling particle subject to air-resistance. The property of integrability itself should be refined beyond the simple solvability property.

A distinctive feature of integrable models is the presence of an extensive number of local conservation laws. For a classical dynamical system, we have conserved charges

$$\partial_t Q_i = 0 \ , \tag{2.1}$$

which belong to a real linear space of functions on the phase-space manifold. A classical system is then Liouville integrable when defined on a $2N$-dimensional phase-space it possesses N independent conserved charges which are mutually commuting [40]

$$\{Q_i, Q_j\} = 0 \ , \quad \text{for} \quad i \neq j \ . \tag{2.2}$$

Using the canonical coordinates p_i and q_i, the operation of commutation is described by a Poisson bracket

$$\{Q_i, Q_j\} = \sum_k \left(\frac{\partial Q_i}{\partial p_k} \frac{\partial Q_j}{\partial q_k} - \frac{\partial Q_i}{\partial q_k} \frac{\partial Q_j}{\partial p_k} \right) \ . \tag{2.3}$$

The name "integrability" then arises, because the differential equations of motion for these quantities can be explicitly integrated in terms of action-angle variables.

The situation becomes somewhat more complicated in the quantum realm. In both quantum mechanics and quantum field theory, the conserved charges are operators and belong to the space of endomorphisms on a Hilbert space. They can be

represented as integrals over a conserved charge density q_i,

$$Q_i = \int d\vec{x}\ q_i(\vec{x})\ , \tag{2.4}$$

which together with an associated conserved current density j_i fulfills a continuity equation

$$\partial_t q_i(\vec{x}) + \partial_x j_i(\vec{x}) = 0\ . \tag{2.5}$$

Analogous to the classical case, we require having a set of mutually commuting conserved quantities, only now using the quantum commutator

$$[Q_i, Q_j] = Q_i Q_j - Q_j Q_i = 0\ . \tag{2.6}$$

However, this is hardly a constraint for a quantum model. For any finite dimensional Hilbert space of a size $N \times N$ we can always find a set of N independent operators which are diagonal and hence all commute with each other. As a result, a naive translation of the Liouville integrability into the quantum context does not give a particularly useful definition. Quantising the problem means elevating the classical algebraic structure to a quantum group one [41–43] while retaining the constraints on the system dynamics. This procedure though leads to ambiguity and there is no universally accepted definition of quantum integrability, see [44] for an interesting discussion. The most widely used one imposes a condition of *locality* onto the conserved charges [40]. A local conserved quantity Q_i is an operator supported on the entire system with a uniformly local density operator q_i such that in the thermodynamic limit of infinitely large system size, q_i acts non-trivially only on a finite subsystem. To further specify the definition of quantum integrability, in this work, a quantum integrable model is such that its scattering matrix is a solution to the quantum Yang-Baxter equation, which will be elaborated on in the next section.

2.2 Scattering Matrix

The scattering matrix, usually referred to as the S-matrix, is an operator relating the initial and final states of a scattering event and allowing a description of the relevant interactions without referring to the Hamiltonian or Lagrangian formulation [45,46]. This section largely follows reference [47]. The details of the discussion regard particle conserving systems with a $U(1)$ symmetry, but the properties mentioned can be generalised to other cases, for instance to spin chain systems [48]. The S-matrix construction for point-like particles, the case of our present interest, relies on the

assumption that any interaction happens in a finite, small volume of space and far enough from it we can treat all particles as free. Then, we can define the so-called asymptotic states of n particles

$$|p_1, \dots, p_n\rangle_{in/out}^{a_1 \dots a_n} \ , \tag{2.7}$$

with the initial state annotated by *in* and describing the incoming particles at time $t = -\infty$ and the final state *out* describing the outgoing particles at time $t = +\infty$. Here, the ordering is such that the i^{th} particle from the left is described by an asymptotic momentum p_i and an internal quantum number a_i. The scattering matrix maps the asymptotic states of incoming particles onto the asymptotic states of the outgoing particles

$$|p_1, \dots, p_n\rangle_{in}^{a_1 \dots a_n} = \sum_{m=2}^{\infty} \sum_{p'_1 > \dots > p'_m} \sum_{b_1, \dots, b_m} S_{b_1 \dots b_m}^{a_1 \dots a_n}(p_1, \dots, p_n; p'_1, \dots, p'_m) \, |p'_1, \dots, p'_m\rangle_{out}^{b_1 \dots b_m} \ , \tag{2.8}$$

where $S_{b_1 \dots b_m}^{a_1 \dots a_n}(p_1, \dots, p_n; p'_1, \dots, p'_m)$ describes the scattering of n incoming particles with momenta p_i and internal degrees of freedom a_i resulting in m outgoing particles with momenta p'_i and internal degrees of freedom b_i. This linear map relies on an assumption that both sets of initial and final states form a complete basis. Essentially, the S-matrix is a time evolution operator from minus to plus infinity. If the model described admits a Hamiltonian description, the scattering operator can be represented in terms of the interacting Hamiltonian in the Dirac picture

$$S = \mathcal{T} \exp \left\{ -i \int_{-\infty}^{+\infty} dt H_I(t) \right\} \ , \tag{2.9}$$

where $\mathcal{T}$ denotes time-ordering.

The structure of integrability puts drastic constraints on possible S-matrices and equips them with certain common properties. Particularly in the case of QFTs, the existence of an infinite number of higher spin conserved charges has been shown to lead to model independent features of integrable, relativistic S-matrices [49–51]. The key ingredient is the dimensionality of potential integrable systems. In dimensions higher than two, any integrable relativistic field theory has been shown to admit only a free particle S-matrix [52]. In 2D though, non-trivial QFT solutions can be found. Indeed, almost all of the currently known integrable models, whether field theoretical or on the lattice, are 2D or admit dimensional reduction which renders them effectively 2D. One notable exception is the Zamolodchikov tetrahedron equations [53–56], which are 3D generalisations of the Yang-Baxter equation (see subsection 2.2.1).

In the following, we describe some key characteristics of an S-matrix describing an integrable system. Most importantly, any scattering event for an integrable model is elastic. This can be understood by considering the set of eigenvalues $\{q_i^{(a_k)}(p_k)\}$ of any conserved charge Q_i. Conserved charges form a mutually commuting set and can be simultaneously diagonalised. As they are local, their eigenvalues are additive

$$Q_i \left|p_1, \ldots, p_n\right\rangle^{a_1 \ldots a_n} = \sum_{k=1}^{n} q_i^{(a_k)}(p_k) \left|p_1, \ldots, p_n\right\rangle^{a_1 \ldots a_n} \ . \tag{2.10}$$

For a quantity to be conserved, we require the initial and final states to have the same eigenvalues

$$\forall_i \left(\sum_{k=1}^{n} q_i^{(a_k)}(p_k) = \sum_{k=1}^{m} q_i^{(b_k)}(p'_k) \right) \ . \tag{2.11}$$

As we have an extensive number of such constraints, the only way to fulfil them is to take $n = m$ and for the two sets to be equal $\{q_i^{(a_k)}(p_k)\} = \{q_i^{(b_k)}(p'_k)\}$. This means no particle production or annihilation during the scattering event and momenta being merely rearranged between the particles. For particles with internal degrees of freedom, these can also be only exchanged (but not changed) during collisions. Another significant consequence is the factorisability of the S-matrix. It states that every integrable S-matrix can be represented as a product of two-particle S-matrices

$$S_{a_1 \ldots a_n}^{b_1 \ldots b_n}(p_1, \ldots, p_n) = \prod_{i=1}^{n-1} \prod_{j=i+1}^{n} S_{a_i a_j}^{b_i b_j}(p_i, p_j) \ , \tag{2.12}$$

where only one set of momenta is necessary to determine the scattering matrix and the sets of internal quantum numbers are equal $\{a_i\} = \{b_i\}$, i.e. consist of the same elements. The proof of this property can be found in several publications [49, 51, 57].

2.2.1 Yang-Baxter Relation

Factorisability of the S-matrix has further crucial implications. Consider a scattering process involving three point-like particles. We know that only two of them interact at one time, but we do not know in what order. In fact, as long as such processes commute with the Hamiltonian and the S-matrix, they lead to physically equivalent situations. This can be formalised by the Yang-Baxter relations [58, 59], also referred to as the star-triangle relations [60], for the scattering matrix

$$\begin{aligned} \sum_{c_1, c_2, c_3} S_{a_1 a_2}^{c_1 c_2}(p_1, p_2) S_{c_1 a_3}^{b_1 c_3}(p_1, p_3) S_{c_2 c_3}^{b_2 b_3}(p_2, p_3) = \\ \sum_{c_1, c_2, c_3} S_{a_2 a_3}^{c_2 c_3}(p_2, p_3) S_{a_1 c_3}^{c_1 b_3}(p_1, p_3) S_{c_1 c_2}^{b_1 b_2}(p_1, p_2) \ . \end{aligned} \tag{2.13}$$

A diagrammatic representation of this relation is shown in Figure 2.1. The visual similarity to knot theory diagrams [61] bears mathematical consequences which give a further argument for integrable models to exist in 2D. In dimensions higher than two, the particle trajectories shown in Figure 2.1 can always be chosen not to cross by pulling the strands out of the plane. This gives a more intuitive understanding of the triviality of higher dimensional integrable QFTs.

In the case of lattice models, an object more commonly used to capture the physics of interactions is the R-matrix $R^{b_1 b_2}_{a_1 a_2}(u)$, which contains the ratios between the amplitudes of the scattering states

$$S^{b_1 b_2}_{a_1 a_2}(u) = \frac{1}{f(u)} R^{b_1 b_2}_{a_1 a_2}(u) \ . \tag{2.14}$$

Here, both $R^{b_1 b_2}_{a_1 a_2}(u)$ and $f(u)$ are meromorphic functions of the parameter u. The Yang-Baxter equation can alternatively be formulated in terms of these R-matrices

$$\begin{aligned} \sum_{c_1,c_2,c_3} R^{c_1 c_2}_{a_1 a_2}(u-v) R^{b_1 c_3}_{c_1 a_3}(u) R^{b_2 b_3}_{c_2 c_3}(v) = \\ \sum_{c_1,c_2,c_3} R^{c_2 c_3}_{a_2 a_3}(v) R^{c_1 b_3}_{a_1 c_3}(u) R^{b_1 b_2}_{c_1 c_2}(u-v) \ . \end{aligned} \tag{2.15}$$

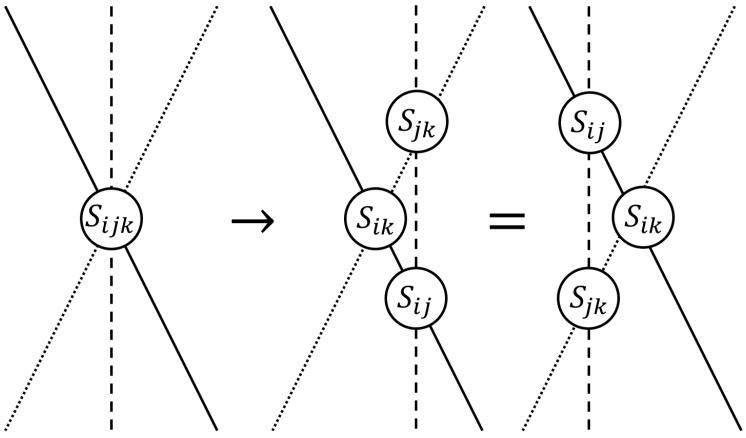


Figure 2.1: Diagrammatic representation of the Yang-Baxter relation for particles with no internal degrees of freedom. Interaction of particles labelled i, j is described by a diagonal scattering matrix $S_{ij} \equiv S_{ij}(p_i, p_j)$.

2.2.2 Symmetries

As a consequence of the property (2.12), computing the $2 \to 2$ scattering matrix is sufficient to determine all scattering processes in an integrable theory. To obtain it,

one needs to solve a set of analytic constraints arising from basic physical principles. The main model-independent properties of an integrable S-matrix are unitarity and analyticity. In case of the theory being relativitic, the S-matrix also has to be Lorentz invariant and satisfy the crossing symmetry. We will describe these and some commonly encountered additional symmetries in the following.

- Probability conservation is the basic requirement in physical processes in isolated systems and is ensured by imposing *unitarity* of the scattering processes

$$\sum_{c_1,c_2} S^{c_1 c_2}_{a_1 a_2}(p_1,p_2) S^{b_2 b_1}_{c_2 c_1}(p_2,p_1)^* = \delta^{b_1}_{a_1}\delta^{b_2}_{a_2} \ . \tag{2.16}$$

- Many theories feature *parity invariance* which implies that scattering is equivalent under the space inversion around the origin

$$S^{b_1 b_2}_{a_1 a_2}(p_1,p_2) = S^{b_2 b_1}_{a_2 a_1}(p_1,p_2) \ . \tag{2.17}$$

  Breaking of the parity invariance gives rise to a number of interesting phenomena and an example of such an integrable QFT will be considered later in this work.

- *Time-reversal invariance* applies when the Hamiltonian under consideration is Hermitian and time-independent

$$S^{b_1 b_2}_{a_1 a_2}(p_1,p_2) = S^{a_2 a_1}_{b_2 b_1}(-p_1,-p_2) \ . \tag{2.18}$$

- *Lorentz invariance* has several significant implications. In a massive relativistic theory, momenta and energies can be parametrised in terms of a rapidity variable θ,

$$p_i = m_i \sinh\theta_i \quad \text{and} \quad E_i = m_i \cosh\theta_i \ , \tag{2.19}$$

  where m_i is the mass of a particle considered. In these coordinates, it is convenient to work with the so-called Mandelstam variables [62], which are relativistic invariants

$$\begin{aligned} s &= (\hat{p}_1+\hat{p}_2)^2 = m_1^2+m_2^2+2m_1m_2\cosh\theta_{12} \ , \\ t &= (\hat{p}_1-\hat{p}_3)^2 = m_1^2+m_3^2-2m_1m_3\cosh\theta_{13} \ , \\ u &= (\hat{p}_1-\hat{p}_4)^2 = m_1^2+m_4^2-2m_1m_4\cosh\theta_{14} \ , \end{aligned} \tag{2.20}$$

  where $\theta_{ij} = \theta_i - \theta_j$, $\hat{p}_i = (E_i \ , \ p_i)$ is a relativistic two-momentum in a Minkowski space and the subscripts $\{1,2,3,4\}$ label the two incoming and two outgoing

particles. By choosing which pairs of momenta are incoming or outgoing, the Mandelstam invariants define different "channels" via which scattering takes place. Overall, Lorentz invariance purports the scattering matrix to depend only on the rapidity differences.

- Relativistic theories also require the imposition of a *crossing symmetry*. In a two particle elastic scattering process with incoming particles with rapidities $\theta_{1,2}$ and outgoing ones with $\theta_{3,4}$, we have $\theta_1 = \theta_4, \theta_2 = \theta_3$ and $S(\theta_1, \theta_2) = S(\theta_{12})$. Such a process can be formally written as

$$|\theta_1, \theta_2\rangle_{in}^{b_1 b_2} = \sum_{a_1, a_2} S_{a_1 a_2}^{b_1 b_2}(\theta_{12}) \, |\theta_1, \theta_2\rangle_{out}^{a_1 a_2} \ . \tag{2.21}$$

  Taking $\theta_{12} > 0$, we have $u = 0$ and $t(\theta_{12}) = s(i\pi - \theta_{12})$. Thus, s is the only independent variable, which we identify with the square of the centre of mass energy $\sqrt{s}$. Consequently, we arrive at a dynamical crossing symmetry, whose essence is the equivalence between the s and t channels

$$S_{a_1 a_2}^{b_1 b_2}(s) = S_{\bar{b_2} a_1}^{\bar{a_2} b_1}(t) \ , \tag{2.22}$$

  where barred indices indicate particles propagating backwards in time (antiparticles). An equivalent non-relativistic symmetry can also be derived by employing the Zamolodchikov-Fadeev algebra [46].

- It is also customary to impose on the S-matrix a *Hermitian analyticity* assumption

$$S_{a_1 a_2}^{b_1 b_2}(s^*) = S_{b_1 b_2}^{a_1 a_2}(s)^* \ , \tag{2.23}$$

  which, in the presence of parity symmetry is promoted to a stronger real analyticity requirement [63].

Imposing the relevant symmetries reduces the task of finding a general form of an integrable S-matrix to solving a set of analytical conditions for the solution of the Yang-Baxter equation. To determine the scattering of a particular model, information about the details of the particle spectrum is required. This can be obtained from the so-called bootstrap program [45, 64]. Among the most prominent methods based on it are the TBA [65] and the form factor approach [66, 67]. Crucially, the latter allows for the determination of the correlators of a theory, which have a correspondence to quantities measurable in experiments.

2.2.3 Analytic Structure of the Scattering Matrix in Quantum Field Theory

The Hermitian analyticity assumption (2.23) combined with a unitarity condition (2.16) can be re-expressed as

$$\sum_{c_1,c_2} S_{a_1 a_2}^{c_1 c_2}(s^+) S_{c_2 c_1}^{b_2 b_1}(s^-) = \delta_{a_1}^{b_1} \delta_{a_2}^{b_2} \ . \tag{2.24}$$

where $s^- = s - i\epsilon, s^+ = s + i\epsilon$ and ϵ is an infinitesimal parameter which ensures that s is slightly below or above the real axis. This is analogous to the Feynman $i\epsilon$ prescription in perturbation theory. Such a formulation manifestly implies a non-analytic transition between the regions where s^+, s^- are defined. In fact, there is a branch cut in the s-plane starting at $s = (m_i + m_j)^2$, the point which corresponds to the two-particle production threshold and results in a discontinuity in the imaginary part of the amplitude. By crossing symmetry, there is also a branch point at $s = (m_i - m_j)^2$ as well as two more at $s = \pm\infty$ seen explicitly in (2.20). The two branch cuts joining the threshold points with infinity along the real axis are the only two branch cuts for an integrable S-matrix because particle production thresholds for more than two particles are not permitted. Moreover, we can deduce that the branch cut is of a square-root type from the expression (2.24), with a "square" of the S-matrix equal to unity. The resulting analytic structure is depicted in Figure 2.2.

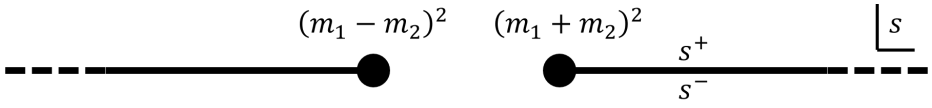


Figure 2.2: Analytic structure of the S-matrix in the square of the centre of mass plane s. Solid dots and lines represent the branch points and the branch cuts respectively.

We can translate this structure into rapidity space by inverting the relation (2.20)

$$\theta_{ij} = \operatorname{arccosh}\left(\frac{s - m_i^2 - m_j^2}{2m_i m_j}\right) \ . \tag{2.25}$$

The physical region producing on-shell scattering processes (the first Riemann sheet) maps onto a strip $0 \leq \operatorname{Im}\theta_{ij} \leq \pi$. The width of the physical strip can also be justified by considering the fact that a shift $\theta \to \theta + i\pi$ results in both energy and momentum in equation (2.19) being reversed, $p \to -p$ and $E \to -E$. Hence such a shift leads to transition from a particle to its corresponding antiparticle [68]. Each further Riemann sheet maps onto the subsequent strip of width π stretching along the real axis in the θ-plane. As a crucial consequence of this considerations, the S-matrix is a meromorphic

function of the rapidity, making the rapidity space an ideal basis for its analysis. We will continue with a particle interpretation of the analytic structure, specialising to diagonal S-matrices. These describe models with no back-scattering, where both the incoming and outgoing states are the same. Because the internal degrees of freedom are then not exchanged, only one set of indices is sufficient to describe the scattering process.

2.2.3.1 Asymptotic Particles

The physical strip in the rapidity space is defined for

$$0 \leq \operatorname{Im} \theta_{ij} \leq \pi \ , \tag{2.26}$$

yet the lack of particle decay in integrable theories constrains the physical poles to $\theta = iu$, where $u \in [0, \pi]$ is real. Such poles are below the two-particle production threshold energy and as a result the final state can have at most one particle. We therefore expect any simple poles in this region to correspond to bound states. In an integrable theory we necessarily require the bound states to be a part of the asymptotic spectrum, which puts a constraint on the rapidities of particles forming the bound state and requires the corresponding S-matrix to fulfil the bootstrap equations [64]. The mass of the bound state m_3 can be derived from the expression for the centre of mass energy (2.20) to be

$$m_3^2 = m_1^2 + m_2^2 + 2m_1 m_2 \cos u_{12}^3 \ , \tag{2.27}$$

where u_{12}^3 is the fusing angle between particles 1 and 2 required to form a bound state 3. As a matter of fact, each of the particles $\{1, 2, 3\}$ can be seen as a bound state of the other two by employing the crossing symmetry. The bootstrap equations for a diagonal S-matrix are then

$$S_{a_1 a_4}(\theta + i\pi - iu_{1\bar{3}}^2) S_{a_2 a_4}(\theta - i\pi + iu_{2\bar{3}}^1) = S_{a_3 a_4}(\theta) \tag{2.28}$$

and describe the fact that, for the theory to be integrable, the scattering of particles $1, 2$ with particle 4 has to be equivalent to the scattering of their bound state 3 with particle 4.

2.2.3.2 Unstable Particles

Poles in the remainder of the rapidity space can be mapped onto the unphysical strip defined as

$$-\pi \leq \operatorname{Im} \theta_{ij} \leq 0 \ . \tag{2.29}$$

Poles in the unphysical strip correspond to excitations which are not part of the asymptotic spectrum and necessarily have a finite life-time. Their cross-sections follow the Breit-Wigner distribution [69], which is indeed associated with particle decay. Thus, we identify these poles with unstable particles. The S-matrix is expected to have a resonance pole for a complex value of the centre of mass energy

$$s_R = \left(M_u - \frac{i}{2}\Gamma_u \right)^2 \tag{2.30}$$

and the scattering matrix in the vicinity of the resonance pole is given by the Breit-Wigner formula [69]

$$S_{a_1 a_2}(s) \approx 1 - \frac{2iM_u\Gamma_u}{s - s_R} \ . \tag{2.31}$$

It is a standard procedure to complexify the mass parameter in order to describe a decaying excitation. In the limit of $M_u \gg \Gamma_u$, M_u acquires a clear interpretation of the mass of the unstable particle and Γ_u of its decay width. The inverse of Γ_u indicates the lifetime of this excitation. The corresponding pole in the rapidity plane has a form

$$\theta_R = \sigma_{12}^{\bar{3}} - i\tilde{\sigma}_{12}^{\bar{3}} \tag{2.32}$$

with $\tilde{\sigma}_{12}^{\bar{3}} \in [0, \pi]$ and $\sigma_{12}^{\bar{3}} \in \mathbb{R}^{\geq 0}$. In terms of the coordinates of the rapidity pole, the unstable particle has a mass and width

$$2M_u^2 = \sqrt{A^2 + B^2} + A \qquad \text{and} \qquad \frac{\Gamma_u^2}{2} = \sqrt{A^2 + B^2} - A \ , \tag{2.33}$$

where

$$\begin{aligned} A &= m_1^2 + m_2^2 + 2m_1 m_2 \cosh\sigma_{12}^{\bar{3}} \cos\tilde{\sigma}_{12}^{\bar{3}} \ , \\ B &= 2m_1 m_2 \sinh\sigma_{12}^{\bar{3}} \sin\tilde{\sigma}_{12}^{\bar{3}} \ , \end{aligned} \tag{2.34}$$

in analogy to the fusing relation (2.27) for the stable bound states. A particular case of a resonance pole is when its real part goes to zero $\sigma_{12}^{\bar{3}} \to 0$. Then, the decay time becomes infinite, but the pole is still in the unphysical strip. The corresponding excitation is a virtual particle. Virtual particles have off-shell energies and hence are not energetically allowed to be among initial or final state excitations. As a result, they do not alter the asymptotic spectrum of the theory. The pole structure of the S-matrix described in this section is shown in Figure 2.3. While stable bound states are a common feature of most interacting integrable QFTs, unstable bound states are a rare occurrence. Their impact on the integrable dynamics requires further exploration and is an important part of this work.

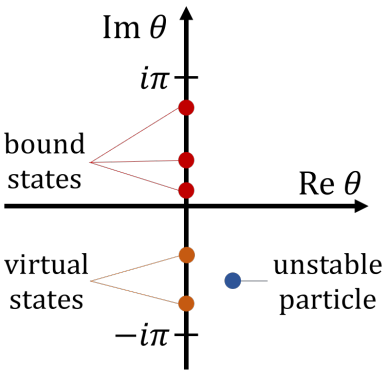


Figure 2.3: S-matrix pole structure with the corresponding excitations.

2.3 Quantum Inverse Scattering

The QISM was formalised by the Leningrad group in the 80's [7–9] and is a crucial approach to constructing the conserved charges of an integrable model. It emerged at the intersection of Bethe Ansatz (BA) techniques dating back to the work by Hans Bethe on the Heisenberg chain [6] and the classical inverse scattering method, originally used to study the soliton solutions to a classical Korteweg-de Vries equation [4]. QISM formed the basis of the later ABA and brought more attention to the underlying algebraic structures of integrability, in particular to the connection with quantum groups. It is also an important technique from a perspective of unifying the treatment of 2D models in classical statistical mechanics with quantum chain and quantum field theories in $(1+1)$D. QISM established the existence of a systematic connection between the quantum spin lattice models and classical vertex models. In fact, every solution of the Yang–Baxter equation is associated with a corresponding exactly solvable vertex model. This section is based on reference [70].

Vertex models are defined on a lattice and differ by the number of configurations of bond states each vertex can be attached to. Each such configuration has an associated Boltzmann weight which governs the probability of the particular configuration occurring. These weights depend on a spectral parameter λ and information about them is included in a so-called Lax operator $L_{jk}(\lambda)$, where now the indices indicate the physical space (vertex coordinates) the operator acts on rather than degrees of freedom. The Lax operator itself is a local vertex operator acting on a tensor product of two complex vector spaces $C \otimes C$ and essentially describes the trajectory of the vertex in the configuration space. In the context of an integrable chain, the Lax operator is usually defined to be acting on a physical site of a chain and an auxiliary space, which replaces one of the vertex degrees of freedom. In order to describe

an integrable model, the Lax operators for different physical space indices have to commute as well as fulfil the Yang-Baxter equation

$$R_{12}(\lambda,\mu)L_{a1}(\lambda)L_{a2}(\mu) = L_{a2}(\mu)L_{a1}(\lambda)R_{12}(\lambda,\mu) \ , \tag{2.35}$$

where a is the auxiliary space index and $R_{12}(\lambda,\mu)$ is an R-matrix of an integrable model, as defined in (2.14). To describe the projection between states in the configuration space of the entire chain, we need to construct a quantum monodromy matrix, which consists of a product of Lax operators acting on every site or vertex in a quantum or classical system respectively

$$\mathcal{T}_a(\lambda) = L_{a,L}(\lambda)\dots L_{a,2}(\lambda)L_{a,1}(\lambda) \ . \tag{2.36}$$

Alternatively, one can view the monodromy as introducing an "unphysical" particle into the system and scattering it through all the physical particles in the system in order to determine their scattering phases. The R-matrix is of utmost importance at this stage, because it determines the commutation relations of the quantum monodromy matrix, which in principle allow for the construction of all the eigenstates of the Hamiltonian operator. An integrable model is defined in a representation space of a quadratic algebra of the monodromy

$$R_{a_1,a_2}(\lambda,\mu)\left[\mathcal{T}_{a_1}(\lambda)\otimes\mathcal{T}_{a_2}(\mu)\right] = \left[\mathcal{T}_{a_2}(\mu)\otimes\mathcal{T}_{a_1}(\lambda)\right]R_{a_1,a_2}(\lambda,\mu) \ , \tag{2.37}$$

also referred to as RTT-relations. For a two-dimensional auxiliary space, we can define a fundamental transfer matrix which acts only on the physical space and serves as a generator of the conserved charges

$$T(\lambda) = \mathrm{Tr}_a\,\mathcal{T}_a(\lambda) \ . \tag{2.38}$$

As a consequence of the RTT-relations (2.37), the transfer matrices for different values of a spectral parameter commute

$$[T(\lambda),T(\mu)] = 0 \tag{2.39}$$

and share a common set of eigenvectors. Considering the entire family of transfer matrices allows us then to find the "easy" eigenvectors first and deduce that they also form an eigenbasis for transfer matrices with other spectral parameter values. The transfer matrix itself admits an expansion in terms of the conserved charges. Consequently, the quest of finding the conserved charges of an integrable model is equivalent to finding the eigenvalues $\{\Lambda_i\}$ of the transfer matrix. Taking a logarithmic

derivative with respect to the spectral parameter λ and evaluating it at a shift-point λ^*, we can generate strictly local conserved quantities

$$Q_n = \frac{\partial^n}{\partial \lambda^n} \ln T(\lambda)\Big|_{\lambda=\lambda^*} \ . \tag{2.40}$$

To obtain the full set of conserved charges, one needs to consider higher spin Lax operators $L^{(s)}_{a,j}(\lambda)$ associated with $(2s+1)$-dimensional auxiliary spaces. These allow for construction of higher spin transfer operators $T^{(s)}(\lambda)$ which also obey commutation relations

$$[T^{(s)}(\lambda), T^{(s')}(\mu)] = 0 \ . \tag{2.41}$$

Higher spin transfer matrices can be used to generate quasi-local conserved charges, albeit in a less straightforward manner [71].

2.4 Bethe Ansatz Techniques

A ubiquitous set of techniques applied in different areas of integrability are named after Hans Bethe who exploited the unique structure of integrable models to devise a method which yields exact, analytic results for their spectra. In his first paper on the topic [6], he investigated the quantum Heisenberg spin-1/2 model with what is now called the CBA. Since then, the BA techniques developed in various directions evolving into a truly imposing mathematical machinery. Among the most widely used are the TBA, the ABA and the Nested Algebraic Bethe Ansatz (NABA). The essence of BA approaches is the reduction of the exponentially difficult problem of finding all eigenvalues of an integrable Hamiltonian to solving a set algebraic equations, whose number increases only polynomially with the size of the system.

2.4.1 Coordinate Bethe Ansatz

The key objective of the BA approach is to arrive at algebraic expressions for the rapidities which define eigenfunctions of an integrable Hamiltonian. Let us illustrate this point with the following example. Consider a system of N particles on a ring of L sites described by an integrable theory with a $U(1)$ particle symmetry. The construction can also be generalised to theories which are not $U(1)$ invariant, such as the XYZ spin chain [8, 72], with aspects of the derivation modified. Here, in the asymptotic limit, the particles are well-separated and each particle is considered to be free. Consequently, we can describe each of them by a plane wave given in terms of

the asymptotic momenta of the particles. The BA wavefunction is a sum over these plane waves including every particle in the system

$$\Psi(\vec{x}) = \sum_{P \in S_N} \text{sign}(P) A(P) e^{i \sum_{j=1}^{N} x_j k_{P_j}} \ , \tag{2.42}$$

where the example given is for one species of fermions with no internal degrees of freedom. Here the positions x_i are ordered so that $x_1 < \cdots < x_N$ and k_{P_i} are the corresponding particle momenta. We need to consider all possible orderings of the momenta so we sum over $N!$ permutations P with corresponding amplitudes $A(P)$. $\text{sign}(P)$ accounts for the particle statistics and is equal to $+1$ and -1 for an even and odd permutation respectively. To find the exact form of the wavefunction, that is to fix the amplitudes $A(P)$, we have to impose boundary conditions as well as continuity at the sector boundaries where particles are exchanged.

For simplicity, we will specialise here to the particular case of the Hubbard model [73] which prominently features in further chapters. The Hubbard model is important in solid state physics as it provides a description of strongly interacting electrons in situations where the band theory predictions fail [74]. Most interestingly, the Hubbard model is presumed to describe the electronic properties of high-temperature cuprate superconductors [75–77]. If the underlying lattice is 1D, this model is integrable. Its eigenvalues were first computed by Lieb and Wu [78] and the exact wavefunction by Woynarovich [79]. The explicit calculation that follows is mostly inspired by reference [80]. Consider the Hubbard Hamiltonian on a 1D lattice of size L with periodic boundary conditions

$$H = -\sum_{j=1}^{L} \sum_{\sigma \in \{\uparrow,\downarrow\}} \left(c_{j,\sigma}^{\dagger} c_{j+1,\sigma} + c_{j+1,\sigma}^{\dagger} c_{j,\sigma} \right) + U \sum_{j=1}^{L} \left(n_{j,\uparrow} - 1 \right) \left(n_{j,\downarrow} - 1 \right) \ , \tag{2.43}$$

where $c_{j,\sigma}^{\dagger}, c_{j,\sigma}$ are the raising and lowering operators for canonical spin-1/2 fermions, $n_{j,\sigma} = c_{j,\sigma}^{\dagger} c_{j,\sigma}$ is a local density operator, subscript $\sigma \in \{\uparrow,\downarrow\}$ indicates the spin orientation up or down, and U is the Hubbard interaction strength. Physical particles that the Hubbard model describes are for instance electrons. During the scattering events, they can exchange not only momenta, but also internal degrees of freedom. This leads to a so-called nesting of Bethe Ansatz Equations (BAE). Nesting arises due to the hierarchical structure of the problem. In this case, the internal spin degrees of freedom decouple from the kinematics. By solving these two types of dynamics separately, we reduce the complexity of the calculations. The spin dynamics

of electrons governed by the Hubbard Hamiltonian are described by the inhomogenous Heisenberg model. The R-matrix for the spin-1/2 Heisenberg model is

$$R(\mu,\nu) = \begin{pmatrix} f(\mu,\nu) & 0 & 0 & 0 \\ 0 & g(\mu,\nu) & 1 & 0 \\ 0 & 1 & g(\mu,\nu) & 0 \\ 0 & 0 & 0 & f(\mu,\nu) \end{pmatrix} , \tag{2.44}$$

where

$$f(\mu,\nu) = 1 - iU/2(\mu-\nu) , \quad g(\mu,\nu) = -iU/2(\mu-\nu) . \tag{2.45}$$

To define the inhomogenous Heisenberg model, we first consider the relevant Lax operator

$$L_{a,j}(\mu) = \frac{1}{\mu + iU/2} \begin{pmatrix} \mu + iU/4(1+\sigma_j^z) & iU/2\sigma_j^- \\ iU/2\sigma_j^+ & \mu + iU/4(1-\sigma_j^z) \end{pmatrix}_a \tag{2.46}$$

which acts on a physical space labelled with j, such as the site of a chain, and an auxiliary space labelled with a. $\vec{\sigma}_j = (\sigma_j^x, \sigma_j^y, \sigma_j^z)$ are the canonical Pauli matrices acting on site j. The inhomogeneity in this model is incorporated at the level of the monodromy matrix defined in (2.36) by introducing a variation in the spectral parameter for the Lax operators acting on different sites of the chain

$$\mathcal{T}_a(\mu \mid \{\nu_j\}) = L_{a,L}(\mu-\nu_L)\dots L_{a,2}(\mu-\nu_2)L_{a,1}(\mu-\nu_1) . \tag{2.47}$$

BA for the inhomogenous Heisenberg model can be solved separately by ABA and imposes additional constraints on the roots of the Hubbard BAE. The details of this calculation can be found in [80].

The Hubbard Hamiltonian itself conserves the number of particles N as well as the number of spin down particles M. Hence, these are good quantum numbers and we can look for solutions in each (N, M) sector separately. Let us consider the two-particle case. Nesting of the BAE imposes an alteration on the form of the BA wavefunction [58]

$$\psi_{\sigma_1,\sigma_2}(x_1,x_2) = \sum_{P,Q\in S_2} \mathrm{sgn}(PQ) A_{\sigma_{Q_1}\sigma_{Q_2}}(k_{P_1},k_{P_2}) \exp\left(i\sum_{j=1}^{2} k_{P_j} x_{Q_j} \right) , \tag{2.48}$$

where P, Q are permutations of momenta and spin degrees of freedom respectively and the summation over the permutations of N particles belongs to the symmetric group S_N. The parity factor $\mathrm{sgn}PQ = \pm 1$ for even or odd permutations needs to be

included to account for the anticommutation relations of the canonical fermions. The Schrödinger equation for the proposed wavefunction takes the form

$$\begin{aligned} -\psi_{\sigma_1,\sigma_2}(x_1-1,x_2)-\psi_{\sigma_1,\sigma_2}(x_1+1,x_2)-\psi_{\sigma_1,\sigma_2}(x_1,x_2-1)-\psi_{\sigma_1,\sigma_2}(x_1,x_2+1) \\ +U\delta_{x_1,x_2}\psi_{\sigma_1,\sigma_2}(x_1,x_2)=(E+U-UL/4)\,\psi_{\sigma_1,\sigma_2}(x_1,x_2)\ . \end{aligned} \tag{2.49}$$

When the particles are well-separated, the problem immediately reduces to the one of two free fermions and we obtain the total energy of the system

$$E=-\left(2\cos k_1+2\cos k_2\right)-U+UL/4\ . \tag{2.50}$$

The interaction happens only when both particles occupy the same point in space $x_1=x_2=x$. The wavefunction will be different in the two spin ordering sectors, (σ_1,σ_2) and (σ_2,σ_1), but at their boundary it has to coincide

$$\begin{aligned} \psi_{\sigma_1,\sigma_2}(x,x)&=\left\{A_{\sigma_1\sigma_2}(k_1,k_2)-A_{\sigma_1\sigma_2}(k_2,k_1)\right\}\exp\left\{i(k_1+k_2)x\right\} \\ &=\left\{A_{\sigma_2\sigma_1}(k_2,k_1)-A_{\sigma_2\sigma_1}(k_1,k_2)\right\}\exp\left\{i(k_1+k_2)x\right\}\ , \end{aligned} \tag{2.51}$$

giving a constraint on the BA amplitudes. Additionally, the Schrödinger equation at the interaction point has to be fulfilled

$$\begin{aligned} &-e^{-ik_1}A_{\sigma_1\sigma_2}(k_1,k_2)+e^{-ik_2}A_{\sigma_1\sigma_2}(k_2,k_1)+e^{ik_2}A_{\sigma_2\sigma_1}(k_1,k_2)-e^{ik_1}A_{\sigma_2\sigma_1}(k_2,k_1) \\ &-e^{ik_2}A_{\sigma_1\sigma_2}(k_1,k_2)+e^{ik_1}A_{\sigma_1\sigma_2}(k_2,k_1)+e^{-ik_1}A_{\sigma_2\sigma_1}(k_1,k_2)-e^{-ik_2}A_{\sigma_2\sigma_1}(k_2,k_1) \\ &+U\left\{A_{\sigma_1\sigma_2}(k_1,k_2)-A_{\sigma_1\sigma_2}(k_2,k_1)\right\} \\ &=-2(\cos k_1+\cos k_2)\left\{A_{\sigma_1\sigma_2}(k_1,k_2)-A_{\sigma_1\sigma_2}(k_2,k_1)\right\}\ . \end{aligned} \tag{2.52}$$

Combining equations (2.51) and (2.52) we obtain a relationship which connects the amplitudes via an object which admits a natural interpretation of the scattering matrix S

$$A_{\sigma_1\sigma_2}(k_2,k_1)=\sum_{\tau_1,\tau_2\in\{\uparrow,\downarrow\}}S^{\tau_1\tau_2}_{\sigma_1\sigma_2}(k_1,k_2)A_{\tau_1\tau_2}(k_1,k_2)\ , \tag{2.53}$$

where the subscripts and superscripts of the S-matrix indicate the incoming and outgoing particles respectively. The scattering matrix is

$$\begin{aligned} S^{\tau_1\tau_2}_{\sigma_1\sigma_2}(k_1,k_2)=&\left(\sin k_1-\sin k_2-U/2i\right)^{-1} \\ &\left\{-U/2i\mathbb{I}^{\tau_1\tau_2}_{\sigma_1\sigma_2}(k_1,k_2)+(\sin k_1-\sin k_2)\mathbb{P}^{\tau_1\tau_2}_{\sigma_1\sigma_2}(k_1,k_2)\right\} \end{aligned} \tag{2.54}$$

where $\mathbb{I}^{\tau_1\tau_2}_{\sigma_1\sigma_2}=\delta^{\tau_1}_{\sigma_1}\delta^{\tau_2}_{\sigma_2}$ is the identity operator and $\mathbb{P}^{\tau_1\tau_2}_{\sigma_1\sigma_2}=\delta^{\tau_2}_{\sigma_1}\delta^{\tau_1}_{\sigma_2}$ is the permutation operator. Imposing the periodic boundary conditions we obtain additional constraints on the amplitudes

$$A_{\sigma_{Q_1}\sigma_{Q_2}}(k_{P_1},k_{P_2})=e^{ik_{P_1}L}A_{\sigma_{Q_2}\sigma_{Q_1}}(k_{P_2},k_{P_1})\ . \tag{2.55}$$

Now each magnetisation sector needs to be considered separately. The cases of both spins up or both spins down are equivalent under the particle-hole transformation which leaves the Hubbard Hamiltonian invariant. For both spins up we have $N = 2, M = 0$. The periodic boundary conditions lead to

$$e^{ik_j L} = 1 \ , \quad j = 1, 2 \tag{2.56}$$

and all the amplitudes equal to unity. The eigenfunction of the Hubbard Hamiltonian is therefore

$$\psi_{\sigma_1,\sigma_2}(x_1, x_2) = \begin{cases} e^{ik_1 x_1} - e^{ik_2 x_2} & \text{for} \quad x_1 < x_2 \ , \\ e^{ik_1 x_2} - e^{ik_2 x_1} & \text{for} \quad x_2 < x_1 \ . \end{cases} \tag{2.57}$$

For one spin up and one spin down we are in the sector $N = 2, M = 1$. In order to fully solve this case we need to first obtain the solutions to the inhomogenous Heisenberg model BAE on two-sites [79]. These give rise to another set of eigenvalues $\{\lambda_i\}$ called rapidities, with as many rapidity quantum numbers as the number of down spins M. In this case the inhomogenous Heisenberg model BAE are

$$1 = \prod_{j=1}^{2} \frac{\lambda - \sin k_j + iU/4}{\lambda - \sin k_j - iU/4} \ . \tag{2.58}$$

Combining these with the periodic boundary conditions leads to

$$e^{-iLk_j} = \frac{\lambda - \sin k_j + iU/4}{\lambda - \sin k_j - iU/4} \ , \quad j = 1, 2 \ . \tag{2.59}$$

Together, equations (2.58) and (2.59) form the BAE for Hubbard model in the two particle sector with one spin down. The corresponding wavefunction is

$$\psi_{\sigma_1,\sigma_2}(x_1, x_2) = \begin{cases} \frac{1}{\lambda - \sin k_s + iU/4} e^{ik_1 x_1 + ik_2 x_2} - \frac{1}{\lambda - \sin k_{\bar{s}} + iU/4} e^{ik_1 x_2 + ik_2 x_1} & \text{for} \quad x_1 < x_2 \ , \\ \frac{1}{\lambda - \sin k_s - iU/4} e^{ik_1 x_2 + ik_2 x_1} - \frac{1}{\lambda - \sin k_{\bar{s}} - iU/4} e^{ik_1 x_1 + ik_2 x_2} & \text{for} \quad x_2 < x_1 \ , \end{cases} \tag{2.60}$$

where $s = 1, 2$ is the position of the spin down in the chain and $\bar{s} = 2, 1$ is the position of spin up. This construction can be generalised to N-particles. Without proof, we state that the Hubbard model nested BAE for generic N and M are [74]

$$\begin{aligned} e^{-ik_j L} &= \prod_{i=1}^{M} \frac{\lambda_i - \sin k_j + iU/4}{\lambda_i - \sin k_j - iU/4} \ , \quad j = 1, \ldots, N \ , \\ \prod_{j=1}^{N} \frac{\lambda_i - \sin k_j + iU/4}{\lambda_i - \sin k_j - iU/4} &= \prod_{\substack{m=1 \\ m \neq i}}^{M} \frac{\lambda_i - \lambda_m + iU/4}{\lambda_i - \lambda_m - iU/4} \ , \quad i = 1, \ldots, M \ . \end{aligned} \tag{2.61}$$

2.4.2 String Hypothesis

BA reduces the problem of diagonalising the Hamiltonian to solving a set of coupled, non-linear equations for the rapidities. In practice, this task turns out to be difficult even for relatively small systems. The major issue that most standard numerical algorithms struggle to overcome is to identify the complex solutions to BAE. A saving grace could be the understanding of the structure of these solutions in order to improve the solving algorithm. It is generally agreed, although not proven, that the Bethe roots are arranged in string-like patterns in the rapidity plane [6, 81]. The hypothesised ideal string is centered around a real rapidity. Its remaining roots have the same real part as the string centre as well as imaginary parts symmetrically distributed with respect to the real axis. Such a structure is believed to describe the system accurately in the thermodynamic limit $L \to \infty$ and when the number of strings as well as their size is much smaller than the system size. Other solutions to BAE might still exist but they are believed not to contribute to the thermodynamic quantities in a significant manner. At the same time, it is known that the finite size effects introduce significant deviations from the ideal string pattern. Using the knowledge of the string pattern one can turn the BAE into coupled non-linear equations for the real centres of the strings. Restricting the discussion again to the case of the Hubbard model, its string hypothesis was first proposed by Takahashi [82]. For this model the string hypothesis provides exact results for thermodynamic quantities such as free energy per site and dispersions of excited states, provided that it is considered at infinite volume and at a finite density of Bethe roots [74].

By considering the structure of singularities in BAE, we can deduce the general form of the string solutions. The recipe is to complexify one of the spectral parameters in BAE (2.61) and take a limit of an infinite system size. As a result, the exponential part of the equation goes to infinity which tells us that the other side is close to a pole. The simplest example one can consider is the case of two spin-1/2 fermions, one with spin up and another with spin down. Such a system is described by three rapidities k_1, k_2, Λ. Complexifying the first one, we take $k_1 = k + i\kappa$, where $k \in \mathbb{R}$ and $\kappa \in \mathbb{R}^+$. Consider one of the BA equations defined in (2.61)

$$e^{-ik_1 L} = \frac{\Lambda - \sin k_1 + iU/4}{\Lambda - \sin k_1 - iU/4} \ . \tag{2.62}$$

Taking the limit $L \to \infty$, the left hand side of the equation goes to infinity and hence we deduce that there is a pole exponentially close to

$$\sin k_1 = \Lambda + iU/4 \ . \tag{2.63}$$

Plugging this into another BAE

$$\frac{\Lambda - \sin k_1 + iU/4}{\Lambda - \sin k_1 - iU/4} = \frac{\Lambda - \sin k_2 - iU/4}{\Lambda - \sin k_2 + iU/4} \ , \tag{2.64}$$

we expect there to also be a pole exponentially close to

$$\sin k_2 = \Lambda - iU/4 \ . \tag{2.65}$$

These are consistent with the third BAE

$$e^{-ik_2 L} = \frac{\Lambda - \sin k_2 + iU/4}{\Lambda - \sin k_2 - iU/4} \tag{2.66}$$

and ultimately allow us to determine that Λ is a real parameter, which completes the analysis.

For the Hubbard model, it has been shown that two different string configurations occur, Λ strings and $k - \Lambda$ strings, the former including only the rapidities Λ and the latter both the momenta k and the rapidities Λ [74]. The $k - \Lambda$ are particularly interesting as they do not occur in any simple integrable models [80]. In the case of the Hubbard model with multiple particles, roots forming the ideal Λ-strings are

$$\Lambda_\alpha^{'m,j} = \Lambda_\alpha^{'m} + i(m - 2j + 1)\frac{U}{4} \quad \text{for} \quad j = 1, \ldots, m \ , \tag{2.67}$$

where m roots form one string, there are α strings of length m, and j enumerates the roots in the α^{th} string of length m. $\Lambda_\alpha^{'m} \in \mathbb{R}$ and is the centre of the string. Roots forming the ideal $k - \Lambda$-strings are

$$\begin{aligned}
\Lambda_\alpha^{m,j} &= \Lambda_\alpha^m + i(m - 2j + 1)\frac{U}{4} \quad \text{for} \quad j = 1, \ldots, m \ , \\
k_\alpha^1 &= \pi - \arcsin\left(\Lambda_\alpha^m + im\frac{U}{4}\right) \ , \\
k_\alpha^2 &= \arcsin\left(\Lambda_\alpha^m + i(m-2)\frac{U}{4}\right) \ , \\
k_\alpha^3 &= \pi - k_\alpha^2 \ , \\
&\vdots \\
k_\alpha^{2m} &= \pi - \arcsin\left(\Lambda_\alpha^m - im\frac{U}{4}\right) \ ,
\end{aligned} \tag{2.68}$$

where m Λ-roots and $2m$ k-roots form one string. $\Lambda_\alpha^m \in \mathbb{R}$ and is the centre of the string. There also exist single real momentum k solutions corresponding to free particle excitations. Examples of the possible strings solutions to the Hubbard model BAE are shown in Figure 2.4.

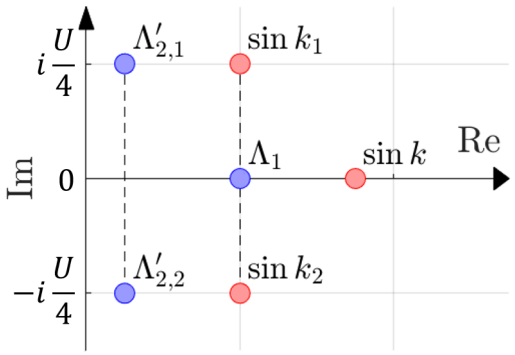


Figure 2.4: Examples of the possible string solutions to the Hubbard model BAE.

Strings consisting of multiple roots can be identified as bound states, although in the case of the Hubbard model, these are purely lattice effects. The discussion of the string hypothesis for the Hubbard model will become instructive later when complexified generalised Hubbard models are discussed.

2.4.3 Thermodynamic Bethe Ansatz

The thermodynamic properties of an integrable model were obtained from the BA for the first time by Yang and Yang for the Lieb-Liniger model of interacting bosons [65] and generalised to a relativistic case by Zamolodchikov [83]. Using the BA techniques to investigate thermodynamic properties has the advantage of reducing the problem to finding the energies of particle excitations and their statistical distributions. The derivation of the TBA equations themselves proceeds as follows. Consider a relativistic model of N particles on a ring of L sites. For simplicity, let us take these particles to be fermions with several flavours and only diagonal scattering. Energy and momentum in a Lorentz invariant system can be parametrised by a rapidity variable θ as defined in (2.19). In the limit of particles being well-separated, each of them is described by a plane wave. If we take one of these particles for a journey around the ring, it will acquire a kinematic phase related to the distance traveled as well as a scattering phase from interactions with each particle on the way. If, at the end, the ordering of particles is the same as the one we started with, the overall phase acquired needs to be equal to 1 for periodic boundary conditions and an odd number of particles in the system. From this condition, we obtain a relation for the phase change of the particle j, characterised by the rapidity θ_j, momentum k_j and flavour

(or other internal degree of freedom) a_j

$$e^{ik_jL}\prod_{\substack{m\neq j\\ m\in[1,N]}} S_{a_ja_m}(\theta_{jm}) = 1 \ , \tag{2.69}$$

where $\theta_{jm} \equiv \theta_j - \theta_m$ and the product over m includes all remaining particles in the system. Let us parametrise the scattering matrix in terms of its scattering phase $\tilde{\delta}$,

$$S_{ab}(\theta) = e^{i\tilde{\delta}_{ab}(\theta)} \ . \tag{2.70}$$

Accordingly, the logarithm of the quantisation condition (2.69) is

$$m_{a_j}\sinh\theta_j L + \sum_{\substack{m\neq j\\ m\in[1,N]}} \tilde{\delta}_{a_ja_m}(\theta_{jm}) = 2\pi I_j \ , \tag{2.71}$$

where $\{I_j\}$ is a set of integers and defines a branch of the logarithm. This set uniquely determines a Bethe state. The construction itself can be generalised to any other model by simply substituting the appropriate scattering matrix. Let us introduce a counting function

$$c_{a_j}(\theta_j) = \frac{1}{2\pi}m_{a_j}\sinh\theta_j + \frac{1}{2\pi L}\sum_{\substack{m\neq j\\ m\in[1,N]}} \tilde{\delta}_{a_ja_m}(\theta_{jm}) \ . \tag{2.72}$$

Comparing the counting function to the expression (2.71), it is clear that its roots correspond to rapidities such that $c(\theta_j) = I_j/L$. On the other hand, rapidity solutions which do not correspond to admissible quantum numbers $\{I_j\}$ can be identified with holes in the spectrum. Such forbidden quantum numbers arise because they simply do not feature in the physical state or violate the selection rules imposed by the particle statistics. A plot of the rescaled counting function $Lc_a(\theta)$ with a graphical solution is shown in Figure 2.5. Consider the thermodynamic limit $L\to\infty, N\to\infty$ at finite density, such that N/L is fixed. In this limit, we can define continuous density functions $\rho^r(\theta), \rho^h(\theta)$ for the roots and holes respectively, relative to the rapidity distribution. Then, $L\rho^{r/h}(\theta)\Delta\theta$ is the number of roots/holes with momentum between θ and $\theta+\Delta\theta$. Furthermore, we can replace sums over rapidities with integrals over densities

$$\frac{1}{L}\sum_j f(\theta_j) \to \int_{-\infty}^{\infty} \mathrm{d}\theta f(\theta)\rho^r(\theta) \ . \tag{2.73}$$

The thermodynamic counting function becomes

$$c_a(\theta) = \frac{1}{2\pi}m_a\sinh\theta + \sum_{\{b\}} \tilde{\delta}_{ab}\star\rho^r_a(\theta) \ , \tag{2.74}$$

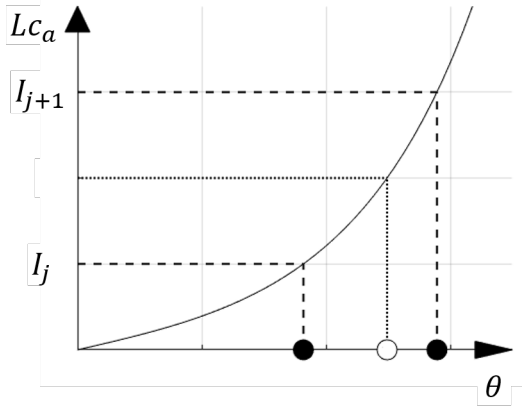


Figure 2.5: A rescaled counting function Lc_a versus rapidity θ. A graphical solution for three different integers is shown, where only two of them, I_j and I_{j+1}, are allowed quantum numbers. The roots and holes are marked with filled and empty circles respectively.

where $\sum_{\{b\}}$ sums over all particle types and $\star$ denotes the convolution

$$f \star g(\theta) = \int_{-\infty}^{\infty} \frac{\mathrm{d}\theta'}{2\pi} f(\theta - \theta') g(\theta') \ . \tag{2.75}$$

The total density $\rho_a(\theta)$ of species a is then obtained by taking a rapidity derivative of the corresponding counting function, which leads to the so-called thermodynamic limit of BAE

$$\rho_a(\theta) = \rho_a^r(\theta) + \rho_a^h(\theta) = \frac{\mathrm{d}}{\mathrm{d}\theta} c_a(\theta) = \frac{1}{2\pi} m_a \cosh\theta + \sum_{\{b\}} \varphi_{ab} \star \rho_a^r(\theta) \ , \tag{2.76}$$

where the scattering kernel is defined to be

$$\varphi_{ab}(\theta) = \frac{\mathrm{d}}{\mathrm{d}\theta} \tilde{\delta}_{ab}(\theta) \ . \tag{2.77}$$

To find a thermal state at temperature T, we need to minimise the free energy functional $f[\rho, \rho^r]$ with respect to two independent density variables ρ and ρ^r

$$f[\rho, \rho^r] = E[\rho^r] - T\mathcal{S}[\rho, \rho^r] \ , \tag{2.78}$$

where $E[\rho^r]$ and $\mathcal{S}[\rho, \rho^r]$ are the energy and entropy per unit length respectively. Without proof we state that the extremum condition reduces to a set of equations

$$\varepsilon_a(\theta) = \beta m_a \cosh\theta + \sum_{\{b\}} \varphi_{ab} \star F[\varepsilon_b](\theta) \ , \tag{2.79}$$

where $\beta = 1/T$ is the inverse temperature and $F[\varepsilon]$ is the free energy function which depends on the particle statistics. The free energy function is often referred to as

the TBA L-function and denoted by $L[\varepsilon]$. It is the latter notation we will use in the remainder of this work. Here, $\varepsilon_a(\theta)$ is a pseudo-energy defined by the density ratios

$$n_a(\theta) = \frac{\rho_a^r(\theta)}{\rho_a(\theta)} = \frac{e^{-\varepsilon_a(\theta)}}{1+e^{-\varepsilon_a(\theta)}} \ , \quad e^{-\varepsilon_a(\theta)} = \frac{\rho_a^r(\theta)}{\rho_a(\theta)-\rho_a^r(\theta)} \ . \tag{2.80}$$

The function $n_a(\theta)$ is often referred to as the occupation function or the filling function of particle a and its form reflects the particle statistics. The TBA equations suggest that the effective excitations of the theory are the so-called quasiparticles with "energies" given by $\varepsilon(\theta)/\beta$. Hence, in the presence of finite temperature, the physical properties of the system are dependent on these thermally modified excitations on top of the TBA ground state. Analogously to energy, thermodynamic limit corrections due to interactions apply to all conserved quantities. Consider an operator $W = \sum_i \beta_i Q_i$ with the corresponding rapidity dependent eigenfunctions

$$w(\theta) = \sum_i \beta_i h_i(\theta) \ , \tag{2.81}$$

where $h_i(\theta)$ is an eigenfunction of the conserved charge Q_i. Each quantity contributes to the partition function of the system not only the bare eigenfunction $h(\theta)$, but also a correction dependent on the scattering kernel. Equations for the generalised pseudo-energies $\varepsilon(\theta)$ which include these correction are the generalised TBA equations [84,85]

$$\varepsilon_a(\theta) = w_a(\theta) - \sum_{\{b\}} \varphi_{ab} \star L[\varepsilon_b](\theta) \ . \tag{2.82}$$

Formulation of the problem of finding the solutions to BAE in terms of integro-differential equation makes the thermodynamic properties of large systems numerically accessible, since the TBA equations can be solved by iterative algorithms.

2.4.3.1 Parity Violation

As it is of particular interest to our further considerations, we will present here a modification to the TBA equations in the absence of parity invariance. Immediately, we can expect that the scattering matrix will not be symmetric in the rapidity space.

Repeating the procedure from the beginning of this section, we can consider a system of particles on a ring. In the case of broken parity, a particle travelling around the system clockwise or anticlockwise are not equivalent situations. As a result, we obtain two equations for the phase change of the particle j

$$e^{ik_jL} \prod_{\substack{m\neq j \\ m\in[1,N]}} S_{a_ja_m}(\theta_{jm}) = 1 \ , \quad e^{-ik_jL} \prod_{\substack{m\neq j \\ m\in[1,N]}} S_{a_ma_j}(\theta_{mj}) = 1 \ . \tag{2.83}$$

Furthermore, we have two sets of TBA equations

$$\begin{aligned} \varepsilon_a^+(\theta) &= w_a(\theta) - \sum_{\{b\}} \varphi_{ab} \star L[\varepsilon_b^+](\theta) \ , \\ \varepsilon_a^-(\theta) &= w_a(\theta) - \sum_{\{b\}} \varphi_{ab} \star L[\varepsilon_b^-](\theta) \ , \end{aligned} \tag{2.84}$$

In general, $\varepsilon_a^+(\theta) \neq \varepsilon_a^-(\theta)$, but this symmetry can be recovered by restoring parity.

2.5 Equilibration in Integrable Systems

A description of quantum many-body systems challenges us to combine quantum and statistical approaches. Considering only the Hamiltonian time evolution of an isolated quantum system which does not interact with its environment, we expect no equilibration arising from its unitary time evolution. Indeed, this is the case for global properties of an isolated system, but not necessarily for local ones. In a generic system, if we measure a local operator that acts only on a finite subsystem, the remainder of the system acts as a bath and allows for relaxation [86]. In this section, by generic we mean a system satisfying the eigenstate thermalisation hypothesis [87–89]. To notable exceptions belong the integrable models, discussed in subsection 2.5.2, as well as systems displaying localisation in the presence of disorder, Anderson localisation in free models [90] and many-body localisation in interacting models [91–93]. A schematic of thermalisation in a generic isolated quantum system is presented in Figure 2.6.

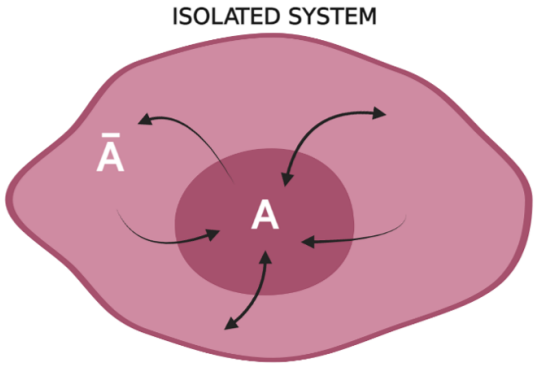


Figure 2.6: An isolated quantum system partitioned into a finite subsystem A and its complement $\bar{A}$ [94]. The subsystem interacts with the remainder of the system.

The entire isolated system is characterised by a density matrix ρ. The reduced density matrix ρ_A for the state of the subsystem A can be obtained by tracing out

the degrees of freedom of its complement

$$\rho_A = \mathrm{Tr}_{\bar{A}}\{\rho\} \ . \tag{2.85}$$

In the thermodynamic limit and at long times, such a subsystem will relax to a stationary density matrix $\rho_A(\infty)$ due to its interactions with the remainder of the system

$$\lim_{t\to\infty}\lim_{V\to\infty} \rho_A(t) = \rho_A(\infty) \ , \tag{2.86}$$

where V is the size of the entire system $A\cup\bar{A}$. Importantly, the thermodynamic limit has to be taken before the infinite time limit to avoid finite size effects. On this basis, we can define a stationary state of the system, which locally reproduces the steady state reduced density matrix for any finite subsystem

$$\lim_{V\to\infty} \mathrm{Tr}_{\bar{A}}\{\rho_{SS}\} = \rho_A(\infty) \ . \tag{2.87}$$

The stationary density matrix ρ_{SS} still does not describe global properties of an isolated system, but merely its local properties in the thermodynamic limit. Still, it is a useful object to work with when considering local observables and their expectation values.

2.5.1 Quench Dynamics

A quantum quench is a protocol of non-equilibrium state preparation and subsequent homogeneous time evolution of a quantum system [86, 95–98]. Examining quench dynamics gives an insight into relaxation properties and information spreading within the system. In the case of integrable models, crucial understanding of the entanglement spreading came from establishing the presence of so-called "quasiparticles" which are effectively the "carriers" of information. These are stable effective excitations and allow for spreading of correlations over macroscopic time and space scales. Such a unique ability to transport information has a potential application in quantum technologies [99].

The details of quench dynamics depend on the model in question as well as the initial state, which varies in different quench protocols. Consider a system prepared in an eigenstate $|\psi(0)\rangle$ of some Hamiltonian $H(\Delta)$, which depends on a quench parameter Δ. At time $t = 0$ we "quench" the Hamiltonian by changing the quench parameter to a new value Δ'. As the alteration is considered to be instantaneous, the

state at time $t = 0$ is still in an eigenstate of $H(\Delta)$, but in a case of a closed system it unitarily time-evolves with the new quench Hamiltonian $H(\Delta')$

$$|\psi(t)\rangle = e^{-iH(\Delta')t} |\psi(0)\rangle \ . \tag{2.88}$$

The initial state can be expanded in the basis of energy eigenstates of the quench Hamiltonian $H(\Delta')$. If in a large, finite volume the initial state has a non-zero overlap with an exponentially large number of those energy eigenstates, the expectation values of certain operators exhibit interesting quantum interference effects

$$\langle\psi(t)| \mathcal{O} |\psi(t)\rangle = \sum_{n,m} \langle\psi(0)|n\rangle \langle m|\psi(0)\rangle \langle n| \mathcal{O} |m\rangle e^{-i(E_m - E_n)t} \ , \tag{2.89}$$

where both $\{|n\rangle\}$ and $\{|m\rangle\}$ form a complete set of energy eigenstates of $H(\Delta')$ with eigenvalues $\{E_n\}$ and $\{E_m\}$ respectively. Global quench dynamics in closed quantum integrable models have been extensively investigated in [86].

2.5.2 Generalised Gibbs Ensemble

Despite the entirety of the system being isolated, it is conjectured that locally its equilibrium properties are described by a statistical ensemble. In the case of energy being the only conserved quantity, a generic system (i.e. not displaying localisation) locally thermalises to a Gibbs ensemble

$$\rho_{SS} \overset{\text{locally}}{=} \rho_{Gibbs} = \mathcal{Z}^{-1} e^{-\beta H} \ , \tag{2.90}$$

where $\mathcal{Z} = \operatorname{Tr} e^{-\beta H}$ is the partition function of the system and H is its Hamiltonian operator. The inverse temperature β is fixed by the energy density in the initial state at infinite volume

$$\lim_{V\to\infty} \frac{1}{V} \operatorname{Tr}\{\rho(t=0)H\} = \lim_{V\to\infty} \frac{1}{V} \operatorname{Tr}\{\rho_{Gibbs} H\} \ . \tag{2.91}$$

The distinguishing feature of integrable models is that their evolution towards a steady state must conserve all the local conservation laws of the model. Following the maximum entropy principle, integrable models are conjectured to locally relax to a so-called Generalised Gibbs Ensemble (GGE) [86, 100]

$$\rho_{GGE} = \mathcal{Z}^{-1} \exp\{-\sum_i \beta^i Q_i\} \ , \tag{2.92}$$

where the partition function is

$$\mathcal{Z} = \operatorname{Tr} \exp\{-\sum_i \beta^i Q_i\} \ . \tag{2.93}$$

In analogy to the non-integrable case, the Lagrange multipliers β_i are fixed so that the expectation values of the conserved quantities in the ensemble match those in the initial state

$$\langle Q_i \rangle_0 \equiv \langle \psi_0 | Q_i | \psi_0 \rangle = \mathrm{Tr}(\rho_{GGE} Q_i) \ . \tag{2.94}$$

In practice, it is challenging to identify all the relevant conservation laws required to reproduce a GGE [101, 102]. Apart from strictly local operators, one also needs to consider quasi-local charges whose support decays "quickly enough" in the thermodynamic limit [71, 101–105].

Numerical investigations corroborate the GGE description of thermalisation in integrable systems following a homogeneous quench. The presence of multiple conservation laws was shown to be consistent with the time evolution of theories such as the Hubbard model [106], the Lieb-Liniger model [107–109], integrable QFTs [84,110] and the XXZ spin chain [84, 111, 112]. Moreover, the steady state for these models carries substantially more memory of the initial state than a thermal state would. Experimentally, some evidence for GGEs have been observed by measuring correlation functions in a 1D Bose gas [113, 114]. For more details see the review [115].

2.6 Generalised Hydrodynamics

The understanding of equilibration processes in integrable models led to the development of a mathematical framework describing dynamics in spatially inhomogenous systems. The GHD formalism [18, 19] combines the well-established principles of hydrodynamics with the properties of integrable systems. For a recent review see [18], which largely informed this section. GHD is particularly useful in investigating non-equilibrium phenomena. It is applicable in a wide variety of integrable models, both classical and quantum, if the system variation is sufficiently smooth so that it can be coarse-grained into a collection of so-called "fluid-cells". Smooth variation allows for the separation of scales between the macroscopic description of the entire system, mesoscopic scale of the fluid-cells where the hydrodynamic description is valid, and the microscopic scale of single particles. More precisely, we require the typical inter-particle distance and the interaction lengths to be much smaller than the variation in the inhomogenous state.

The key principle of hydrodynamics is local entropy maximisation. In the case of an integrable model, this means that each of the fluid-cells is characterised by a local GGE, as outlined in subsection 2.5.2. Diagrammatically, this situation is presented in Figure 2.7.

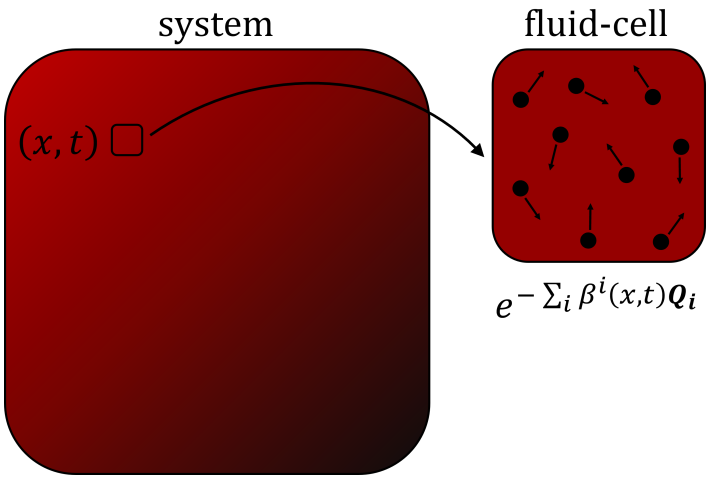


Figure 2.7: Mesoscopic scale of a fluid-cell. Figure reproduced after [18].

In the hydrodynamic approximation, the GGE characterising a fluid-cell approximately describes any observable across the entire cell. Hence, instead of time-dependent observables, we can work with time-independent operators averaged over the time-dependent state of the fluid-cell. This means shifting the spacetime dependence to the Lagrange multipliers characterising the local GGE

$$\langle \mathcal{O}(x,t) \rangle \approx \langle \mathcal{O}(0,0) \rangle_{\beta(x,t)} \ , \tag{2.95}$$

which makes the out-of-equilibrium dynamics more readily numerically accessible. In this approximation, we can write the continuity equation (2.5) as

$$\partial_t \mathtt{q}_i(x,t) + \partial_x \mathtt{j}_i(x,t) = 0 \ , \tag{2.96}$$

where $\mathtt{q}_i(x,t) \equiv \langle q_i \rangle_{\vec{\beta}(x,t)}$ and $\mathtt{j}_i(x,t) \equiv \langle j_i \rangle_{\vec{\beta}(x,t)}$ are averages over the fluid-cell. This form of a hydrodynamic equation shows a naturally emerging Euler (mesoscopic) scale dynamics, as it depends only on the number of conserved charges and the equations of state of the model, but not on any information of the microscopic details of the system.

A complete set of conserved charges at a given space-time coordinate $\{\mathtt{q}_i(x,t)\}$ uniquely determines the local GGE and the conserved currents $\{\mathtt{j}_i(x,t)\}$ can be expressed as their linear combination. As a result, the Euler hydrodynamic equation (2.96) can be diagonalised in terms of normal modes of the system dynamics, which can be shown be given by the TBA occupation functions (2.80). In this basis, the hydrodynamic equation is

$$\partial_t n_i(x,t) + v_i^{eff}(x,t) \partial_x n_i(x,t) = 0 \ , \tag{2.97}$$

where v_i^{eff} is the effective velocity with which the normal modes are transported. This quantity in general depends on all local normal mode densities $\{n_i(x,t)\}$ and contains important details about the interactions. Intuitively, we can imagine that particles propagate ballistically, but interactions "set them back", which effectively slows them down. Thus, the magnitude of the effective velocity carries the information about the number of collisions the particle on average experiences. Due to these interactions, the actual averages of local conserved quantities are "dressed" with the scattering kernel. Let us consider a derivative of the TBA equations (2.82) with respect to the local Lagrange multipliers β_i in a GGE (2.92). We obtain

$$h_i^{\mathrm{dr}}(x,t,\theta) = h_i(x,t,\theta) + \varphi \star [h_i^{\mathrm{dr}} n](x,t,\theta) \ , \tag{2.98}$$

where $n = \mathrm{d}L[\varepsilon]/\mathrm{d}\varepsilon$ is the occupation function dependent on the particle statistics, the dressed function is a derivative of the pseudoenergy $h_i^{\mathrm{dr}} = \mathrm{d}\varepsilon/\mathrm{d}\beta_i$ and superscript dr indicates a dressed quantity. It is important to note that the spacetime dependence of the conserved quantities does not mean a variation across a given fluid-cell, bu merely indicates a variation across a manifold of different local GGEs. In the following, the spacetime dependence of the quantities considered is suppressed for the clarity of notation and only the dependence or lack thereof on the rapidity θ is explicit. The GGE averages of local charge densities $\mathtt{q}_i$ and of their associated currents $\mathtt{j}_i$ can be expressed in terms of the dressed quantities

$$\mathtt{q}_i \ = \ \int_{-\infty}^{\infty} \frac{d\theta}{2\pi} p'(\theta) h_i^{\mathrm{dr}}(\theta) n(\theta) = \int_{-\infty}^{\infty} \frac{d\theta}{2\pi} (p')^{\mathrm{dr}}(\theta) h_i(\theta) n(\theta) \ , \tag{2.99}$$

and

$$\mathtt{j}_i \ = \ \int_{-\infty}^{\infty} \frac{d\theta}{2\pi} E'(\theta) h_i^{\mathrm{dr}}(\theta) n(\theta) = \int_{-\infty}^{\infty} \frac{d\theta}{2\pi} (E')^{\mathrm{dr}}(\theta) h_i(\theta) n(\theta) \ , \tag{2.100}$$

where $x' = \frac{\mathrm{d}x}{\mathrm{d}\theta}$ denotes a derivative with respect to the rapidity, $p(\theta), E(\theta)$ are the rapidity dependent bare momentum and energy respectively, and $h_i(\theta)$ is the eigenvalue of the conserved charge we are interested in as defined in (2.81). We have used here a symmetry of the equations that allows us to interchange the dressing operation inside the integral.

The average charge densities $\{\mathtt{q}_i\}$, the particle occupation functions $n(\theta)$, the eigenfunctions $w(\theta)$ as well as the pseudo-energies $\varepsilon(\theta)$ are valid coordinates of the GGE state manifold and are related to each other by in principle non-linear maps. The key for efficient computation of thermodynamic quantities is to choose the right

coordinate system, which for numerical calculations often turns out to be the particle occupation functions $n(\theta)$.

Some quantities of particular interest are the averages of the conserved particle charge and particle current. These are conventionally denoted with subscript 0. In the $n(\theta)$ basis, they are

$$\mathtt{q}_0 = \int_{-\infty}^{\infty} \frac{d\theta}{2\pi} (p')^{\mathrm{dr}}(\theta) n(\theta) \ , \tag{2.101}$$

$$\mathtt{j}_0 = \int_{-\infty}^{\infty} \frac{d\theta}{2\pi} (E')^{\mathrm{dr}}(\theta) n(\theta) \ . \tag{2.102}$$

Here, we implicitly use the one-particle eigenvalue $h_0(\theta) = 1$ which is the particle number. The dressed energy and momentum charges and currents are computed by substituting their one-particle eigenvalues $h_1(\theta) = E(\theta)$ and $h_2(\theta) = p(\theta)$ into formulae (2.99) and (2.100) respectively.

Alternatively, we can express the conserved charges in terms of the TBA root density, related to the occupation function via (2.80)

$$\frac{\rho^r(\theta)}{\rho(\theta)} = n(\theta) \ . \tag{2.103}$$

The root density $\rho^r(\theta)$ and the total density $\rho(\theta)$ are commonly referred to as the spectral and state density respectively and labelled as $\rho_p \equiv \rho^r, \rho_s \equiv \rho$. By definition, the GGE average of a conserved charge is

$$\mathtt{q}_i = \int \mathrm{d}\theta h_i(\theta) \rho_p(\theta) \ . \tag{2.104}$$

As a consequence of a continuity equation

$$\partial_t \rho_p(\theta) + \partial_x (v^{\mathrm{eff}} \rho_p(\theta)) = 0 \ , \tag{2.105}$$

the GGE average of the corresponding conserved current is

$$\mathtt{j}_i = \int \mathrm{d}\theta h_i(\theta) v^{eff}(\theta) \rho_p(\theta) \ . \tag{2.106}$$

Comparing this representation of the conserved quantities with equations (2.99) and (2.100), we then identify the effective velocity and spectral density to be

$$v^{eff}(\theta) = \frac{(E')^{\mathrm{dr}}(\theta)}{(p')^{\mathrm{dr}}(\theta)} \quad \text{and} \quad 2\pi\rho_p(\theta) = n(\theta)(p')^{\mathrm{dr}}(\theta) \ . \tag{2.107}$$

Then, employing the definition of the occupation function (2.103), we arrive at a formula for the state density

$$2\pi\rho_s(\theta)v^{eff}(\theta) = n(\theta)(p')^{\mathrm{dr}}(\theta) \ . \tag{2.108}$$

Combining this equation with the constitutive relation for the state density (2.76), we can show that the effective velocity is actually related to the group velocity via a dressing operation

$$v^{eff}(\theta) = v^g(\theta) + \int \mathrm{d}\alpha\varphi(\theta-\alpha)\rho_p(\alpha)\left[v^{eff}(\alpha) - v^{eff}(\theta)\right] \ , \tag{2.109}$$

where $v^g(\theta) = \mathrm{d}E(\theta)/\mathrm{d}\theta$ is the group velocity for a given rapidity. This form of the effective velocity equation resembles the hydrodynamic equation for a classical soliton gas [116]. Comparison with this classical model provides a useful geometric interpretation of GHD and allows us to define an effective interaction length scale for the quasiparticles [117]

$$d_{int} = \frac{\varphi(\theta)}{p'(\theta)} \ . \tag{2.110}$$

The Euler scale hydrodynamic description features a purely ballistic transport and is exact in the thermodynamic limit. Still, GHD models many systems accurately already at short timescales and gradient expansion corrections to the ballistic description have been conjectured to increase the precision of the GHD framework [118]. In principle, one also needs to include diffusive effects, where the diffusion can be understood as two-body scattering of the ballistic waves on top of the GGE [119–122]. The GHD formalism has also been extended to include bulk viscosity, leading to a generalised Navier-Stokes equation, as well as environment inhomogeneities, such as weakly varying force fields, temperature fields and other inhomogeneous external fields [123,124]. Nevertheless, these are phenomenological extensions and their regime of validity needs to be rigorously understood [118].

Experimentally, the development of GHD led to a successful explanation of the emblematic quantum Newton's Cradle [125]. In this experiment, two clouds of atoms governed by the Lieb-Liniger model interactions are released from a double well potential and time-evolve in a single quadratic well [24]. Instead of thermalising, as expected in the case of a generic system, the two clouds oscillate within the well due to restrictions imposed on the dynamics by the conservation laws. GHD has also been experimentally verified in an atom chip [126] and another ultracold atomic gas setup in an optical trap [34].

Chapter 3

Tales of Instability: Unstable Particles in an Integrable Quantum Field Theory

> *"Basically, I suppose the justification for studying these models is very simple: they are relevant and they can be solved, so why not do so and see what they tell us?" -Rodney J. Baxter*

Unstable particles in integrable systems sound like an oxymoron if one does not consider the asymptotic nature of the scattering framework. In the long time limit, integrability is indeed incompatible with the presence of decaying constituents. At intermediate timescales though, such excitations are allowed. The fact that they do not feature in the scattering states description makes them elusive and difficult to access. By employing the GHD formalism, we have achieved just that.

3.1 Out-of-Equilibrium Physics in Quantum Field Theory

Physics far from equilibrium offers a powerful way of studying strongly correlated many-body systems by bringing out properties that can be hidden in equilibrium situations. The most prominent example is emergence of life, which arises from complex dynamic processes allowing organisms to grow, reproduce, and evolve. In quantum systems out-of-equilibrium, an explosion of activity has taken place, particularly in one dimension [71,86,127–132]. Among them, much can be learned by looking through a non-equilibrium lens at QFTs. QFT is a basic mathematical framework of understanding elementary particles as well as quasiparticles in many-body systems. The

simplest non-equilibrium event characterising a QFT is a scattering process. Scattering theory describes how few particles interact and is a standard method of accessing the dynamics in QFTs [133–135]. However, scattering events mainly teach us about the vacuum state and what happens at low densities. Furthermore, scattering experiments for many-body systems are notoriously difficult to implement. Dynamics with finite energy and spatial particle densities can be argued to be more common and experimentally accessible, while simultaneously exhibiting a broader range of physical phenomena. A case in point is the spectrum of asymptotic particles. It is a basic ingredient of scattering theory, which is nevertheless not sufficient to fully understand finite-density physics. Other emergent structures of QFT may play an important role. One example is the phenomenon of confinement, which taps into the internal characteristics of asymptotic particles. As found in [136–138], this and other qualitatively similar [139] phenomena can be linked quite explicitly to the non-equilibrium dynamics that follow quantum quenches, defined in section 2.5. Another phenomenon, only indirectly observed in scattering events, is the existence of particles with finite life-times, which are absent from the asymptotic spectrum of an integrable theory, as explained in subsection 2.2.3. At high temperatures, physical intuition suggests that unstable particles are constantly formed and destroyed, and thus exist in finite proportions. As such, they may be expected to have a strong effect on the dynamics far from equilibrium and at finite densities. At the same time, since they are not part of the asymptotic spectrum, their presence is only felt through the effect they have on physical quantities associated either to the theory as a whole, such as scaling functions or correlation functions, or to the stable particles themselves, their energies and particle densities. Before resorting to a specific non-equilibrium setup, properties of unstable particles could be studied in finite density equilibrium states using dynamic structure factors [140, 141]. This is a well-established approach that also connects well to experimental investigations. In the following, we demonstrate that non-equilibrium setups at finite energy densities allow a more direct observation of unstable particles. We focus on a $(1 + 1)$D integrable QFT, which admits one unstable particle. By examining the propagation of nonlinear waves at finite energy densities with the GHD formalism, we show that the out-of-equilibrium dynamics of quantum integrable models lead to a new understanding of unstable excitations.

3.2 Homogeneous Sine-Gordon Models

3.2.1 General Features

In our work, we identify signatures of unstable particles by considering a particular example of a family of integrable QFTs referred to as the HSG models. Understanding their dynamical behaviour necessitates a discussion of how their action and scattering matrices have been derived. HSG models have been extensively studied in the group of the University of Santiago de Compostela [142–151] and the arguments in this section largely follow the PhD thesis of one of its previous members, O. A. Castro-Alvaredo [152]. HSG models belong to a family of Toda field theories [153, 154], which are field generalisations of classically integrable Toda lattice systems [155]. The latter describe n-particles on a 1D lattice interacting in a non-linear manner. If on top of the discreet coordinates of the lattice a continuous space and time dependence is imposed, such a function can be arranged into a field $h(x,t)$ which takes values in a certain Lie algebra g. Depending on the exact choice of this Lie algebra a further classification of Toda field theories follows. Of particular interest for this work is the case when g is non-abelian, giving rise to Non-Abelian Toda (NAT) field theories [143, 156–158]. These are classically integrable, but quantum integrability is a feature for only two subsets of NAT theories, HSG and symmetric space sine-Gordon models. An instance of the former is the main subject of this chapter. Significantly, for HSG models associated with simply-laced algebras the scattering matrix has been obtained explicitly [144]. Its form provided a further motivation for studying the HSG models. It is the first example of an integrable QFT in which the scattering amplitudes have a non-trivial rapidity dependence and which consistently incorporates both the parity breaking and the presence of unstable excitations, a rare feature in the currently known integrable QFTs. Moreover, HSG model admits a Lagrangian description, making it an intuitive model to study.

A $(1+1)$D QFT can be viewed as a perturbation to a Conformal Field Theory (CFT) by an operator of this CFT. CFTs are field theories which are conformally invariant, implying the same behaviour at all scales [159]. This symmetry restriction renders CFTs exactly solvable and of particular interest, especially in string theory and critical phenomena. The action of a perturbed CFT is

$$S = S_{CFT} + \lambda \int \mathrm{d}^2 x \Phi(x,t) \ , \tag{3.1}$$

where S_{CFT} is the unperturbed CFT, λ is a coupling constant, and Φ is a local field belonging to the CFT. Henceforth, we will refer to S_{CFT} as an underlying CFT of

the theory described by action S. Keeping in mind the underlying CFT of a model is an important validity check for computations, as in the ultraviolet limit the QFT reduces to the underlying CFT. It has been shown [160] that for a particular choice of perturbation, the resultant QFT retains the infinite number of local conservation laws despite the conformal symmetry breaking. Due to the intimate connection to CFT, the renormalisation group flow of an integrable QFT can be studied by investigating the Zamolodchikov's c-function [161], which is essentially an "off-critical" Virasoro central charge [162] and measures the effective number of light degrees of freedom of the theory at each energy scale.

The HSG models can be understood as massive perturbation of the Wess-Zumino-Novikov-Witten (WZNW) coset models [163–165]. Such WZNW models are conformally invariant theories based on cosets of a form $G_k/U(1)^l$, where G is a Lie group associated with a compact, finite, and semisimple algebra g, l is the rank of this algebra and k is the so-called "level" [163–165]. These theories are also known as G_k-parafermion theories. The action of the HSG models can be represented as

$$S = S_{WZNW} + \frac{m^2}{\pi\beta^2} \int \mathrm{d}^2x \left\langle \Lambda_+, h^\dagger \Lambda_- h \right\rangle \ , \tag{3.2}$$

where β^2 is the coupling constant, m is the mass scale, h is a field taking values in the Lie algebra g and $\Lambda_\pm$ take values in the Cartan subalgebra of g. The perturbing field in this case is $\Phi = \left\langle \Lambda_+, h^\dagger \Lambda_- h \right\rangle$, where $\langle\ ,\ \rangle$ is the bilinear form in g. The most commonly known example from the family of HSG theories is the complex sine-Gordon model [166, 167], which is constructed from the $su(2)$ Lie algebra. In this work, we will study the simplest non-trivial instance of an HSG model namely a $SU(3)_2$-HSG.

Resonance poles, which correspond to unstable excitations, have been found in not only the HSG models but also the roaming sinh-Gordon models [168–170] as well as roaming trajectory models [171–173]. What is special about the HSG family, is the simultaneous presence of a Lagrangian description of these theories [143] which allows for direct identification of the resonance poles with the unstable particles by means of a semi-classical analysis [144, 145]. The Lagrangian description lends itself to a very physical interpretation of the behaviour of the Zamolodchikov c-function. It has been shown that changing the mass-coupling relations in the HSG models leads to a characteristic "staircase" pattern in the RG flow of various thermodynamic quantities which is related to the onset of unstable particles [146, 147]. Each plateau of the c-function can be associated with an energy scale at which another degree of freedom is "unlocked", such as the formation of an unstable bound state. The richer

the asymptotic spectrum of the theory, the wider the variety of unstable boundstates that can be formed. In fact, the number of linearly independent resonance parameters, as described in the subsection 2.2.3, is dependent on the rank of the Lie algebra g and equal to $l-1$. HSG models corresponding to higher rank Lie groups have multiple unstable excitations, which lead to multiple plateaus and a more intricate behaviour of the theory at different energy scales.

3.2.2 $SU(3)_2$-Homogeneous Sine-Gordon Model

The model under study is the simplest non-trivial example of the HSG family and is known as the $SU(3)_2$-homogeneous sine-Gordon model, associated with the $SU(3)/U(1)^2$ coset. Interestingly, its underlying CFT, the $SU(3)_2$ parafermion theory [174], has found an application in construction of quantum Hall states carrying a spin and fractional charges [175, 176]. The $SU(3)_2$-HSG model has a spectrum of two stable, self-conjugate particles. As $su(3)$ algebra has rank $l=2$, we have a single resonance parameter for this model. Labelling the stable particles by $\pm$, the two-body scattering matrix of the theory has the simple form

$$S_{\pm\pm}(\theta) = -1 \qquad \text{and} \qquad S_{\pm\mp}(\theta) = \pm \tanh \frac{1}{2}\left(\theta \pm \sigma - \frac{i\pi}{2}\right) , \tag{3.3}$$

where $\sigma \in \mathbb{R}$ is the resonance parameter and θ is the rapidity difference between particles. The corresponding two-body scattering kernel for the $SU(3)_2$-HSG model is

$$\varphi_{\pm\pm}(\theta) = 0 \qquad \text{and} \qquad \varphi_{\pm\mp}(\theta) = \operatorname{sech}(\theta \pm \sigma) . \tag{3.4}$$

The scattering kernel is plotted in Figure 3.1. Clearly, the interaction is strongly peaked at $\theta = \mp\sigma$ for $\varphi_{\pm\mp}(\theta)$. Both the S-matrix and the scattering kernel can be immediately seen to break parity invariance, by not being invariant under the particle species exchange

$$S_{+-}(\theta) \neq S_{-+}(\theta) \quad \text{and} \quad \varphi_{+-}(\theta) \neq \varphi_{-+}(\theta) \quad \text{for} \quad \sigma \neq 0 . \tag{3.5}$$

Analysing the scattering matrix we deduce that the scattering process is always diagonal and particles of the same type interact like free fermions by acquiring only a phase upon interaction. More interestingly, interactions between particles of different types are non-trivial and rapidity dependent. For σ positive the scattering phases dictate that a particle $-/+$ has maximum interaction with a particle $+/-$ if it hits it from the right/left and their rapidity difference is of order $\theta = +\sigma/-\sigma$. This feature means that interaction for each particle is maximised for either positive or negative

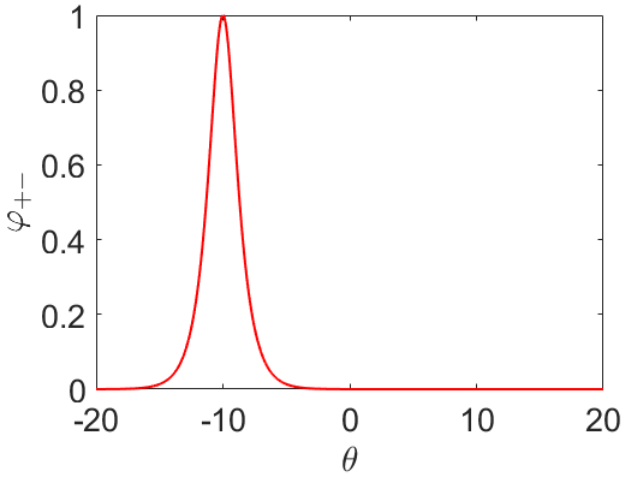


Figure 3.1: Two-body scattering kernel for the $SU(3)_2$-HSG model with $\sigma = 10$.

rapidities, whereas particles behave as free fermions otherwise. For finite σ, the scattering amplitudes $S_{\pm\mp}(\theta)$ have a pole outside the physical sheet at $\theta = \mp\sigma - \frac{i\pi}{2}$ in the strip $-\pi \leq \mathrm{Im}(\theta) \leq 0$. In the limit of $\sigma \to 0$ however, the excitation in the unphysical strip becomes virtual. On the other hand, for $\sigma \to +\infty$ the model reduces to a system of two free fermions. None of the scattering amplitudes has a pole inside the physical strip, hence creation of a bound state via fusing is forbidden.

From the Breit-Wigner formulae (2.33) and (2.34), it follows that the associated unstable particle has mass such that for $\sigma \gg 1$ and equal masses of the stable constituents $m_\pm = m$ the mass of the unstable particle scales as

$$M \sim \frac{1}{\sqrt{2}} m e^{\frac{|\sigma|}{2}} \ . \tag{3.6}$$

This energy scale plays the role of a threshold for the formation of the unstable particle, as can be seen in many physical quantities of interest. The decay width can be approximated by

$$\Gamma \sim \sqrt{2} m e^{\frac{|\sigma|}{2}} \ . \tag{3.7}$$

Therefore, the larger $|\sigma|$ is, the more massive and short-lived the unstable excitation becomes. From the RG viewpoint, starting in a Gibbs ensemble at temperature $T \gg e^{|\sigma|/2}$, the theory flows from a non-trivial CFT with a central charge $c = 6/5$, to a free fermion CFT with central charge $c = 1$ for $1 \ll T \ll e^{|\sigma|/2}$ [150]. The larger number of degrees of freedom at high temperatures is interpreted as signifying the presence of a finite proportion of unstable particles in the thermal state, allowed by the large energy. When studying RG-flows of different quantities and intermediate values

of σ, we observe that the flows approach these two fixed points in succession, giving rise to the staircase pattern, where the position and size of the steps are related to the value of σ. This is observed for the Zamolodchikov c-function (shown in Figure 3.2) but also for the scaled energy currents and energy densities in an out-of-equilibrium partitioning protocol [177]. The pattern reflects the onset of the unstable particle, which only takes place at sufficiently large energies, comparable to the mass M.

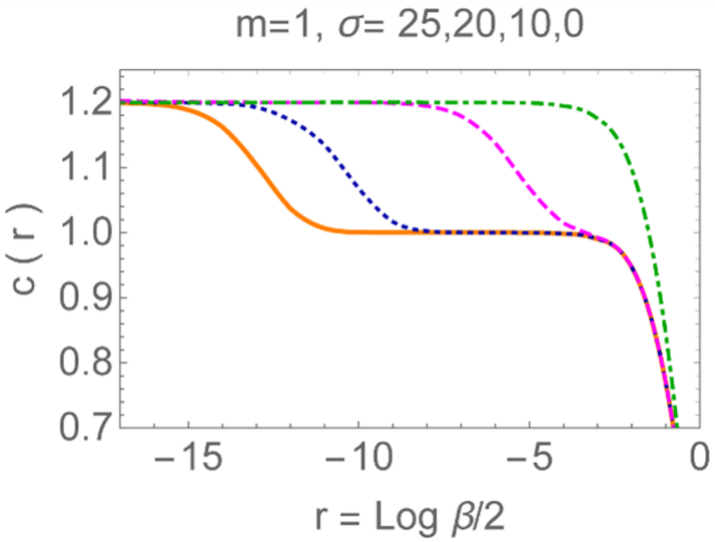


Figure 3.2: Zamolodchikov's c-function versus the logarithm of the inverse temperature $\beta = 1/T$. Each curve corresponds to the $SU(3)_2$-HSG model with the resonance parameter set to (in order from left to right) $\sigma = 25, 20, 10, 0$. The figure has been taken from [177].

3.2.2.1 Thermodynamic Bethe Ansatz and Generalised Hydrodynamics

Parity breaking and the presence of the unstable particle have many interesting effects both at and away from equilibrium. These effects are very clear when investigated in the context of GHD, that is, when looking at functions such as the effective velocities of stable particles, their associated densities and spectral densities. Some realisations in this subsection are a part of our ongoing study [178, 179] of the out-of-equilibrium dynamics in HSG models and, in particular, of the precise signatures related to the unstable particles.

In examining the $SU(3)_2$-HSG model, most generally we need to resort to the generalised TBA equations (2.84) as described in subsection 2.4.3.1. For this model, the TBA equations are

$$\varepsilon^{\pm}(x,t,\theta) = w(\theta,x,t) - \varphi_{\pm\mp} \star L^{\mp}(x,t,\theta)\,, \tag{3.8}$$

with the kernel $\varphi_{\pm\mp}(\theta)$ defined in (3.4). Here, the TBA L-function is associated with the Fermi-Dirac distribution

$$L^{\pm}(x,t,\theta) = \ln\Big(1 + e^{-\varepsilon^{\pm}(x,t,\theta)}\Big) \ . \tag{3.9}$$

The driving term $w(x,t,\theta)$ contains a sum over the one-particle eigenvalues of the conserved charges involved in the GGE. We call these eigenvalues $h_i(\theta)$ with $i = 0,1,2,\ldots$. In this case they are identical for both particle types so they carry no particle indices

$$w(x,t,\theta) = \sum_i \beta_i(x,t) h_i(\theta) \ , \tag{3.10}$$

where $\beta_i(x,t)$ are generalized inverse temperatures, which are fluid-cell dependent. For simplicity, we will take the mass of the particles to be $m = 1$ for the remainder of this work. As we can see, all quantities will generally be functions of both space and time and frequently also rapidity.

Consider equations (3.8) for our model in a Gibbs ensemble at equilibrium temperature $T = 1/\beta$

$$\varepsilon^{\pm}(\theta) = \beta \cosh\theta - \varphi_{\pm\mp} \star L^{\mp}(\theta) \ . \tag{3.11}$$

They can be mapped into an expression

$$\phi^{\pm}(\theta) = \beta \cosh\Big(\theta \mp \frac{\sigma}{2}\Big) - (\varphi \star K^{\mp})(\theta) \quad \text{with} \quad \varphi(\theta) = \text{sech}\theta \ , \tag{3.12}$$

for the shifted functions

$$\phi^{\pm}(\theta) = \varepsilon^{\pm}(\theta \mp \frac{\sigma}{2}) \quad \text{and} \quad K^{\pm}(\theta) = \log\Big(1 + e^{-\phi^{\pm}(\theta)}\Big) \ . \tag{3.13}$$

Note that under this shift and a change of variables in the convolution integral, the σ-dependence of the TBA kernel is eliminated so that it is now only explicit in the TBA driving term. Then, if σ or θ are large and positive, we can approximate

$$\phi_{\pm}(\theta) = \frac{\beta}{2} e^{\mp\theta + \frac{\sigma}{2}} - (\varphi \star K_{\mp})(\theta) = e^{\mp\theta - \kappa} - (\varphi \star K_{\mp})(\theta) \tag{3.14}$$

where

$$\kappa = \log(2T) - \frac{\sigma}{2} \ . \tag{3.15}$$

This shows that for σ large enough, the TBA equations and their solutions naturally depend on the variable κ. This observation extends to the out-of-equilibrium situation, as long as the initial state is defined by a temperature profile, and is crucial for our further considerations.

In GHD, asymptotic particles, characterised by their rapidity θ and species $\pm$, are dressed, within finite density states, into fluid modes as described in section 2.6

$$h_i^{\mathrm{dr},\pm}(x,t,\theta) = h_i(\theta) + \varphi_{\pm\mp} \star [h_i^{\mathrm{dr}} n^{\mp}](x,t,\theta) \ , \tag{3.16}$$

where the occupation functions associated with particles $\pm$ reflect the fermionic statistics

$$n^{\pm}(x,t,\theta) = \frac{1}{1+e^{\varepsilon^{\pm}(x,t,\theta)}} \ . \tag{3.17}$$

The state at any space-time point (x,t) is then described by an occupation function $n^{\pm}(x,t,\theta)$. The TBA equations (3.8) allow us to evaluate the initial condition $n^{\pm}(x,0,\theta)$ using the local density approximation. Of particular interest are three quantities, the spectral density of particles $\rho_p^{\pm}(x,t,\theta)$, the spatial particle density $\mathfrak{q}_0^{\pm}(x,t)$, and the effective velocity $v^{\mathrm{eff},\pm}(x,t,\theta)$, which is the fluid velocity of mode $(\theta,\pm)$. They are defined as

$$\begin{aligned} \rho_p^{\pm}(x,t,\theta) &= E^{\mathrm{dr},\pm}(x,t,\theta) n^{\pm}(x,t,\theta), & (3.18)\\ \mathfrak{q}_0^{\pm}(x,t) &= \int_{-\infty}^{\infty} \frac{d\theta}{2\pi} \rho_p^{\pm}(x,t,\theta), & (3.19)\\ v^{\mathrm{eff},\pm}(x,t,\theta) &= p^{\mathrm{dr},\pm}(x,t,\theta)/E^{\mathrm{dr},\pm}(x,t,\theta) \ . & (3.20) \end{aligned}$$

Here $E^{\pm}(\theta) = \cosh\theta$ is the energy, and $p^{\pm}(\theta) = \sinh\theta$ the momentum, as for any relativistic model. It is important to note that the conservation laws apply to the two particle species separately as well as combined, meaning that $h_i^{\mathrm{dr},\pm}(x,t,\theta)$ and $h_i^{\mathrm{dr,tot}}(x,t,\theta) = h_i^{\mathrm{dr},+}(x,t,\theta) + h_i^{\mathrm{dr},-}(x,t,\theta)$ are conserved. Because of the symmetry of the kernel $\varphi_{+-}(\theta) = \varphi_{-+}(-\theta)$, the functions above are not fully independent but rather satisfy the symmetry relations

$$\begin{aligned} \rho_p^{+}(x,t,\theta) &= \rho_p^{-}(-x,t,-\theta) \ , \\ \mathfrak{q}_0^{+}(x,t) &= \mathfrak{q}_0^{-}(-x,t) \ , \\ v^{\mathrm{eff},+}(x,t,\theta) &= -v^{\mathrm{eff},-}(-x,t,-\theta) \ . \end{aligned} \tag{3.21}$$

Thus, we concentrate in our analysis on particle $+$, bearing in mind that analogous statements apply to particle $-$.

3.3 Gaussian Quench Setup

To observe truly non-equilibrium behaviour of the $SU(3)_2$-HSG model, we initialised it in an environment with an inhomogenous Gaussian temperature profile of the form

$$T(x) = T_a + (T_m - T_a)e^{-x^2} \qquad \text{with} \qquad T_m > \frac{1}{2}e^{\frac{\sigma}{2}} > T_a \ , \tag{3.22}$$

where x is the space coordinate. From now on, we will refer to T_a as the bath temperature and T_m as the maximum or hot matter temperature. An example of a Gaussian temperature profile is plotted in Figure 3.3.

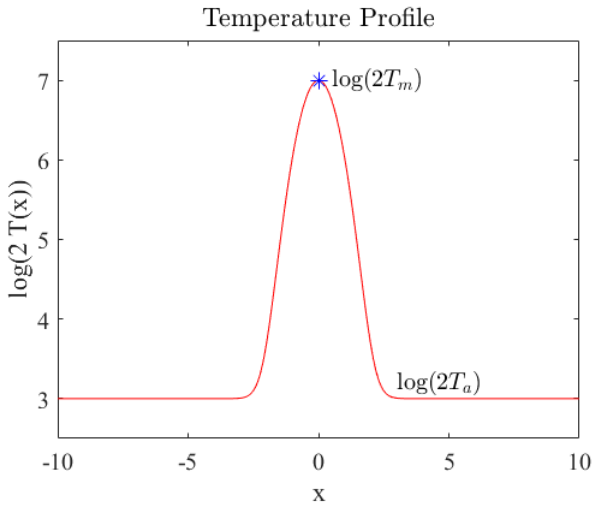


Figure 3.3: Initial temperature profile for $2T_m = e^7$ and $2T_a = e^3$.

We analyse the setup where a high-temperature region, with enough energy to form a large number of unstable particles at $\log 2T_m > \sigma/2$, is released into a colder environment with $\log 2T_a < \sigma/2$. The profile (3.22) also involves all temperatures $T_a \leq T \leq T_m$, so that there is an interplay of both the interacting and free regimes. Henceforth, we refer to the temperature required for the unstable particle formation

$$\log 2T = \sigma/2 \quad \text{or} \quad \kappa = 0 \tag{3.23}$$

as simply "the threshold". When letting the system evolve in time, we study the emitted waves by numerically solving the associated hydrodynamic equations. Subsequently, we find that at the energies considered the thermodynamic quantities corresponding to the asymptotic particles are drastically altered by the presence of unstable excitations.

Given the initial configuration (3.22), the system variation is of the order of $\xi \approx \mathcal{O}(1)$. For the temperatures chosen in this investigation, the inter-particle distance is of the order of $d = 1/\mathtt{q}_0 \approx \mathcal{O}(10^{-3}) - \mathcal{O}(1)$. In our case, the interaction distance defined in (2.110) is of the order $d_{int} \approx \mathcal{O}(10^{-5}) - \mathcal{O}(10^{-3})$. Hence, in most of the parameter space we are in the regime of smooth system variation $\xi \gg d, d_{int}$ and the dynamics can be computed using GHD. We approach the verge of the validity of the hydrodynamic description only in the small number of regions with a

low particle density. However, there exists extensive numerical work showing that large temperature densities within zero-temperature environment can be accurately described by hydrodynamics [180], in particular when compared to molecular dynamics simulations [34,125]. This gives us a reason to believe that the hydrodynamic theory provides an accurate description of the physics even in the low particle density regions.

In order to obtain numerical results, we adapted the iFluid package [181, 182], a MATLAB code that solves GHD equations for a wide range of conditions and models. The numerical algorithm follows a procedure:

1. Specify the model by inputting single-particle eigenvalues for energy h_1 and momentum h_2, their derivatives with respect to rapidity, two-particle scattering matrix elements $S_{i,j}$ and the initial conditions.

2. Calculate the initial thermal state $n_i(x, 0, \theta)$ from the equilibrium TBA using the local density approximation.

3. Solve the GHD equations (2.97) by iteratively computing single time-step propagation of the occupation function $n(x, t, \theta) \to n(x, t + \mathrm{d}t, \theta)$. To this end, an implicit solution to the GHD equations is used

$$n(x, t+\mathrm{d}t, \theta) = n(\tilde{x}(t+\mathrm{d}t, t), t, \theta) \ , \quad \tilde{x}(t', t) = x - \int_t^{t'} \mathrm{d}\tau v^{\mathrm{eff}}[\tilde{x}(\tau, t), \theta] \ , \tag{3.24}$$

   where the form given is valid in the absence of an external potential. The achieved accuracy is up to an order $\mathcal{O}(\mathrm{d}t^2)$. Each propagation step can be solved by numerical iteration. Although the convergence to a solution is not guaranteed a priori, this scheme shows good agreement with DMRG calculations [183].

4. Calculate the conserved charges and currents by solving the dressing equation (3.16).

This algorithm is known as the method of characteristics and is described in detail in [184]. More details of the numerical aspects of this work are presented in the Appendix A.

3.4 Free Fermions in a Gaussian Quench

To fully appreciate the complexity of the HSG model, it is instructive to examine first the dynamics in a free theory. In the setup proposed in (3.22), we deposit hot matter

at $x = 0, t = 0$ and let it evolve. In free relativistic theories, the effective velocity is

$$v^{\text{eff}}(x,t,\theta) = c\tanh\theta \ , \tag{3.25}$$

where c is the speed of light, set in the following to $c = 1$. The corresponding spectral density is described by an equation [180, 184, 185]

$$\rho_p^{\text{FF}}(x,t,\theta) = \frac{\cosh\theta}{1+e^{\beta(x,t,\theta)\cosh\theta}} \ , \tag{3.26}$$

where

$$\beta(x,t,\theta) = \frac{1}{(T_m - T_a)e^{-(x-t\tanh\theta)^2} + T_a} \tag{3.27}$$

is the time-dependent inverse temperature for the initial state (3.22) and velocity (3.25). Analysing the spectral density ρ_p^{FF} for large maximum temperature T_m and consequently large θ, we see that it features two identical local maxima at $x = 0$ and $\theta = \pm\log 2T_m$. When large rapidities are involved, asymptotic particles have velocities extremely near to the speed of light. Then, the standard picture, without unstable particles, is that after the splitting of the initial high-temperature region, long-lived, well-localised regions of higher energy density propagate at unit velocity in both directions. The same phenomenology of double-bump release applies to the particle density

$$\mathfrak{q}_0^{\text{FF}}(x,t) = \frac{1}{2\pi}\int_{-\infty}^{\infty}\rho^{\text{FF}}(x,t,\theta)\mathrm{d}\theta = \frac{1}{2\pi}\int_{-\infty}^{\infty}\frac{\cosh\theta}{1+e^{\beta(x,t,\theta)\cosh\theta}}\mathrm{d}\theta \ , \tag{3.28}$$

which is shown in Figure 3.4. Having such an explicit solution makes many analytic computations possible for free fermions and provides useful insights into some of the properties of the functions for the HSG model.

3.4.0.1 Decay

From the explicit form of equation (3.28), we can analyse how quickly do the two emitted waves separate at early times. For $x = 0$ we have

$$\begin{aligned} q_0^{\text{FF}}(0,t) &= \frac{1}{2\pi}\int_{-\infty}^{\infty}\frac{\cosh\theta}{1+e^{\beta_m e^{\tanh(\theta)^2 t^2}\cosh\theta}}\,d\theta \\ &= \frac{1}{2\pi}\sum_{n=0}^{\infty}\int_{-\infty}^{\infty}\cosh\theta(-1)^n e^{-(n+1)\beta_m e^{\tanh(\theta)^2 t^2}\cosh\theta} \ , \end{aligned} \tag{3.29}$$

where $\beta_m = 1/T_m$ and for simplicity we take $T_a = 0$. For large rapidities we can approximate $\tanh(\theta) \approx \pm 1$ and obtain

$$\frac{1}{\pi}\sum_{n=0}^{\infty}\int_0^{\infty}\cosh\theta(-1)^n e^{-(n+1)\beta_m e^{t^2}\cosh\theta} = \frac{1}{\pi}\sum_{n=0}^{\infty}(-1)^n K_1\left[(n+1)\beta_m e^{t^2}\right] \ , \tag{3.30}$$

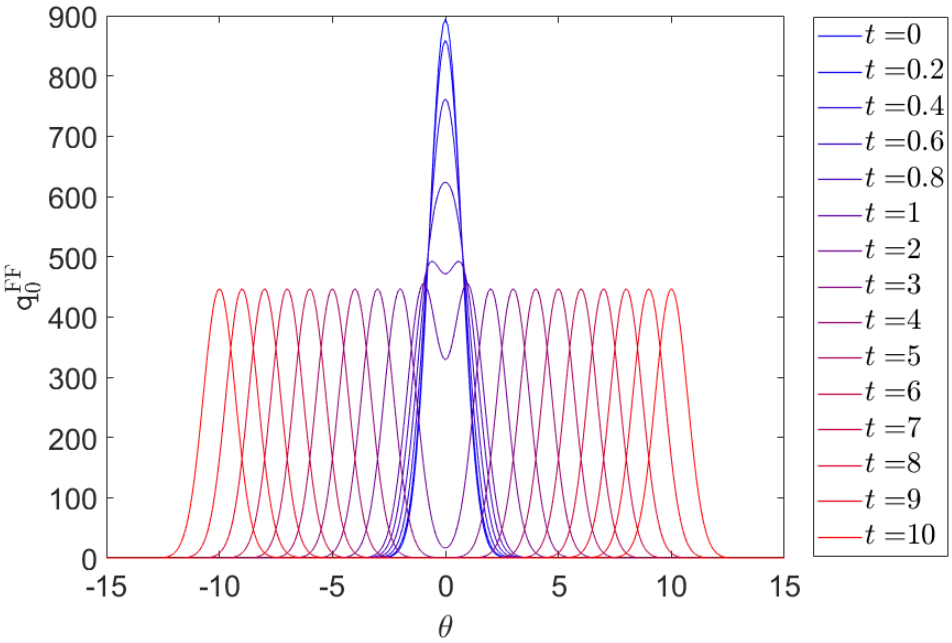


Figure 3.4: Free fermion particle density $\mathfrak{q}_0^{\rm FF}$ for a choice of parameters $\sigma = 10, \log 2T_m = 9, T_a = 0$ for a Gaussian temperature profile (3.22). After separating at $t = 0.8$, two identical peaks propagate in opposite directions at velocities ± 1.

where K_1 is the modified Bessel function of the second kind [186]. For high temperatures, this can be approximated by

$$q_0^{\rm FF}(0,t) \approx \frac{1}{\pi\beta_m e^{t^2}} \sum_{n=0}^{\infty} \frac{(-1)^n}{n+1} = \frac{\log 2}{\pi\beta_m e^{t^2}} = q_0^{\rm FF}(0,0)e^{-t^2} \ . \tag{3.31}$$

Thus, for small times the maximum of the free fermion density bump reduces as a Gaussian. A similar analysis gives

$$q_0^{\rm FF}(x,0) \approx q_0^{\rm FF}(0,0)e^{-x^2} \tag{3.32}$$

and the spatial profile of the particle density follows the temperature profile as expected.

For large temperature T_m, this result generalizes to interacting theories where $\log 2$ is replaced by the value $L(0)$ of the TBA L-function, as shown in Appendix B. Using similar arguments, we can show that the height of the two peaks that are produced after the release of the initial density bump in Figure 3.4 is exactly half that of the original bump

$$\lim_{t\to\infty} \mathfrak{q}_0(x = \pm t, t) = \frac{\mathfrak{q}_0(0,0)}{2} \ . \tag{3.33}$$

From this result it can be estimated that the bump splitting occurs roughly when $e^{-t^2} = \frac{1}{2}$, that is for $t = \sqrt{\log 2} \approx 0.83$. This value represents the end of the initial decay regime and although computed here for the free fermions, it gives a good indication of the order of magnitude for this process in an interacting theory.

Finally, when $T_a \neq 0$ the result (3.31) generalizes by replacing

$$e^{-t^2} \mapsto R + (1-R)e^{-t^2} \qquad \text{for} \qquad R = \frac{T_a}{T_m}\,. \tag{3.34}$$

3.5 Equilibrium Signatures of Unstable Particles

The equilibrium behaviour of the HSG model has been previously studied in [177]. There, the following signatures of unstable particle were identified.

- Particle densities and effective velocities develop *non-trivial patterns* as the temperature changes, which can be explained by the formation of unstable particles at energies beyond the temperature threshold (3.23).

- For temperatures beyond the threshold (3.23), the spectral densities of the stable particles develop *three peaks*, rather than the usual two primary peaks, centered around $\theta = \log(2T), \theta = -\log(2T)$ and a secondary peak $\theta = \pm\log(2T) \mp \sigma$ for particles $\pm$ and T the temperature defining the Gibbs ensemble.

- The secondary peak of particle $\pm$ and part of a primary peak of particle $\mp$ can be interpreted as representing densities of mutually interacting particles and, in effect, a *constant density of unstable particles*.

Therefore, already the equilibrium features of the HSG model are in clear contrast to the majority of known integrable QFTs. These equilibrium features are found again for the Gaussian profile (3.22) at time $t = 0$ for specific values of x. For each value of x we have in effect a Gibbs ensemble at temperature $T(x)$ for which all the observations above apply. Let us now consider the functions of interest for this situation of local equilibrium.

Substantial changes are observed in the effective velocity of the HSG model. Intermediate velocity plateaus are formed at energy scales away from the CFT limits. For particle $+$, the plateaus extend in the rapidity space between $-\sigma/2$ and 0 (or analogously 0 and $\sigma/2$ for particle $-$) and their height is temperature dependent. The extent of the maxima is closely related to the form of the HSG model TBA equations

under a $\sigma/2$ shift as explained in subsection 3.2.2.1. We argue that these additional plateaus are the effect of unstable bound state creation. The resultant particle "slow-down" is shown in Figure 3.5.

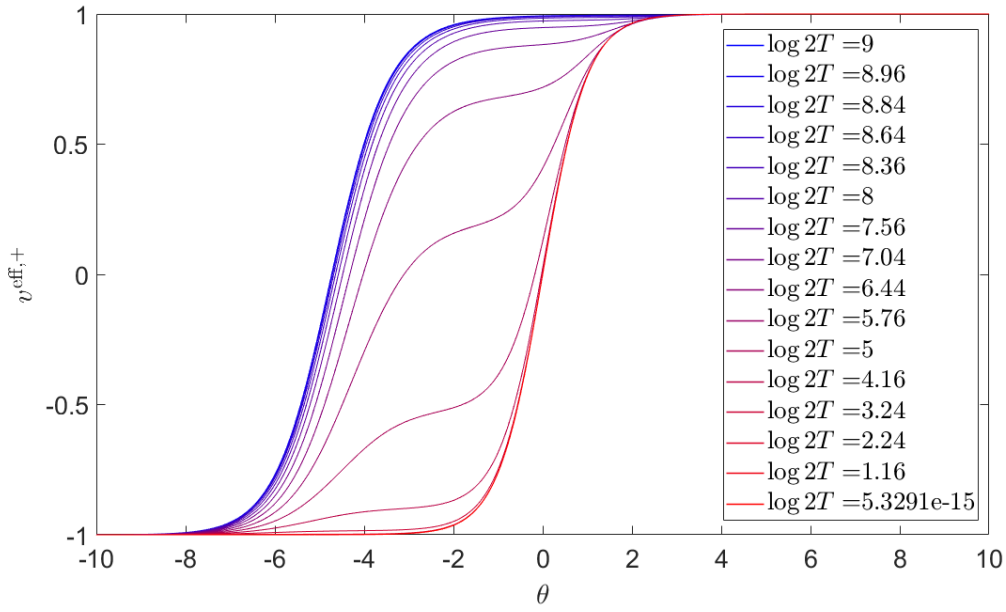


Figure 3.5: $SU(3)_2$-HSG effective velocity cuts $v^{\text{eff},+}$ as a function of rapidity θ for a choice of parameters $\sigma = 10, \log 2T_m = 9, T_a = 0$. Each cut is taken at a different position x corresponding to a different local equilibrium temperature in the Gaussian temperature profile $T(x)$. The temperature is the highest at $x = 0$ (red), with $\log 2T = 9$, and decays to $\log 2T = 0$ at $x \approx 3$ (blue).

Looking at the effective velocity in the rapidity-coordinate plane, a "tooth-like" feature develops, as in the example presented in Figure 3.6. For particle $+$, the effective velocity for positive rapidities is essentially the same as for a free theory, hence we name this region of rapidity space the free fermion region. The effective velocity for negative rapidities shows non-trivial differences with the free fermion case and thus we call it the interaction region. This distinction is consistent with the analysis of the scattering kernel (3.3), which indicates that the maximum interaction of particles $+$ with particles minus $-$ occurs for rapidity differences of the order of σ Particles $+$ in the free fermion region have simply no available particles $-$ to interact with, as there are no particles $-$ with extremely large negative rapidities.

The presence of unstable particles also modifies substantially the spectral density. In addition to the two primary maxima, a third secondary maximum is formed with no equivalent in a free theory. The position of the secondary peak is dictated by the

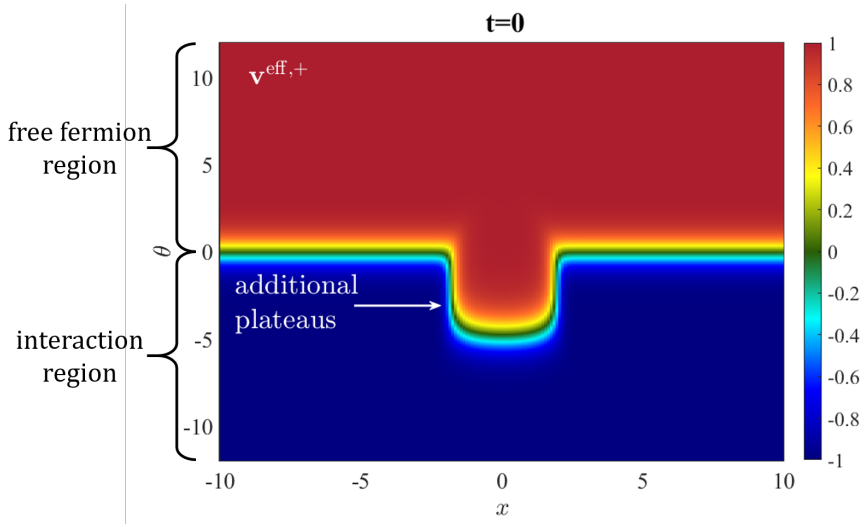


Figure 3.6: Local equilibrium ($t = 0$) effective velocity for the particle + in the HSG model initialised in a temperature profile (3.22) with a choice of parameters $\sigma = 10, \log 2T_m = 9, T_a = 0$.

maximum of interactions, $\theta \approx \log 2T_m - \sigma$ for particle +. At the same time, the primary maximum in the interaction region is larger than the one in the free region. It is precisely this excess of particles which are conjectured to be forming an unstable bound state and it has been shown that its volume is equal to the volume of the secondary peak [177]. The comparison on spectral density maxima between a free and HSG model is presented in Figure 3.7.

For ease of discussion, let us establish some nomenclature. The three local maxima in the initial state of the HSG model are shown in Figure 3.8. In the following, we refer to the local maximum in the free fermion region as a free peak. In the interacting region, we name the primary larger peak an interacting peak and the smaller secondary maximum a subsidiary peak. Note that the modifications in the effective velocity can be found around the location of the subsidiary peak.

Importantly, lack of the parity invariance leads to a breaking of left-right (x) and top-bottom (θ) symmetry in all quantities associated to a single particle. In our investigation, we have chosen temperatures that are large enough so that the presence of a continuum of fluid modes in integrable systems does not play an important role. The physics is dominated by the flow between a free ($c = 1$) and interacting ($c = 6/5$) conformal field theory, representing the formation and decay of unstable particles. Away from equilibrium, some of these features generalise in a natural fashion while new dynamics also come into play, notably the dynamics of unstable particle decay and that of persistent waves.

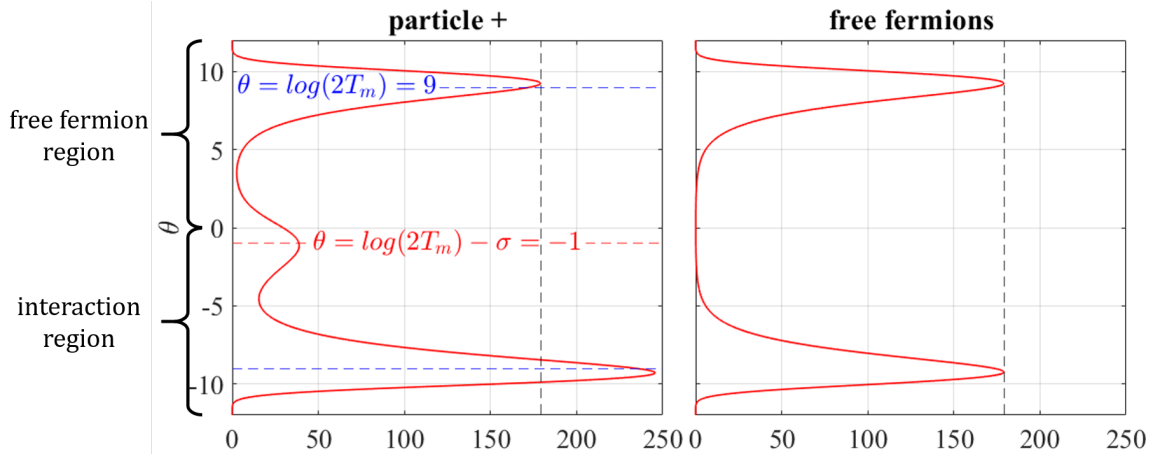


Figure 3.7: Cross-section of the spectral density for the HSG model particle + (left) and for free fermions (right) at $x = 0$ as a function of rapidity in a Gaussian temperature profile at local equilibrium ($t = 0$). The resonance parameter for the HSG model is $\sigma = 10$ and the temperatures in both cases were chosen to be $\log 2T_m = 9, T_a = 0$. We see that, in comparison to free fermions, a secondary maximum emerges in the spectral density of the HSG model and the height of a primary maximum in the interaction region is increased.

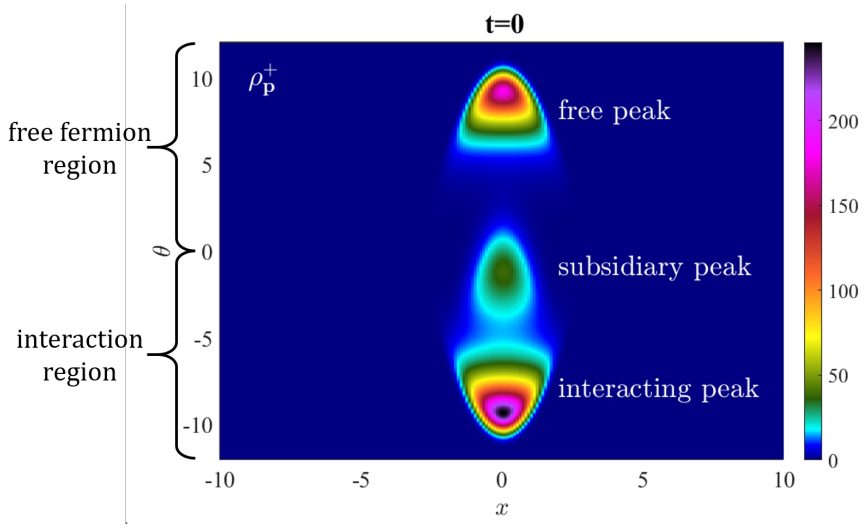


Figure 3.8: Spectral density for the HSG model at local equilibrium ($t = 0$) in a Gaussian temperature profile (3.22) and a choice of parameters $\sigma = 10, \log 2T_m = 9, T_a = 0$.

3.6 Non-Equilibrium Phenomenology of Unstable Particles

In our work [178,179], we uncovered the following main signatures of unstable particles emerging far from equilibrium

- The waves emitted from the initial hot matter deposit *partially decay* after the splitting of the initial high-temperature region rather than propagate undisturbed.
- *Long tails* of slower particles appear, trailing the well-localised high-density waves.
- In a finite-density environment, new *persistent waves* emerge, interpreted as being stable populations of unstable particles.

These distinct signatures of instability identified within GHD are explained via the combined phenomenology of unstable particles and hydrodynamics, and should reflect universal behaviours. In this section, we will consider a general non-equilibrium phenomenology of the $SU(3)_2$-HSG model for resonance parameter $\sigma = 10$ and a choice of temperatures $\log 2T_m = 7, T_a = 0$ for the zero-temperature environment and $\log 2T_m = 7, \log 2T_a = 3$ in the case with finite energy density in the background.

3.6.1 Time Evolution

Time evolution of various thermodynamic quantities in a zero-temperature environment is shown in Figure 3.9. The first row illustrates the behaviour of the spectral density of particle + as a function of time. At time $t = 0$ we observe many of the equilibrium features we would encounter for a Gibbs ensemble at the highest temperature T_m. There are three local maxima at rapidity positions dictated by the hot matter temperature. The maximum at $\theta \approx 7$ is the free fermion solution, at $\theta \approx -7$ we see a higher, interacting peak, and the subsidiary peak at $\theta \approx -3$ is a consequence of interaction with the interacting peak of particle $-$. The subsidiary peak represents the proportion of particles + involved in a bound state with particles $-$, our unstable particles. As we can see from the effective velocity plotted in the third row of Figure 3.9, for $t = 0$ the interacting peak moves at speed -1, the free fermion peak moves at speed $+1$ and the subsidiary peak contains a spectrum of positive and negative effective velocities, captured by the "rainbow" colouring and the presence of an intermediate plateau of the effective velocity centred at $\theta = -\sigma/4 = -2.5$.

Turning on time, the salient feature is that the subsidiary peak moves as per the initial splitting, but then falls apart, leaving behind a tail of slow particles. Unstable particles start moving at speed near $+1$, but, as they enter the zero-temperature environment, decay faster than they can form, and we see the particle + components un-binding and recovering their speeds near -1. Note that the initial spread of

effective velocities in the subsidiary peak, and the consequent dispersion, is not enough to explain its falling apart. It is the zero-temperature surrounding, with a very different effective velocity profile, which leads to the decay of unstable particles as the dominant effect. An in depth analysis of this phenomenon is presented in subsection 3.7.1.

As shown in the second row of Figure 3.9, the spatial particle density reflects this physics. After the initial splitting, the right-moving wave reduces in time, leaving just the free fermion contribution. After a period of initial decay, it remains unchanged for larger times, but features a tail linking it to the left-moving wave. The formation of tails and decay of local maxima in spatial densities are features that identify the presence of unstable particles.

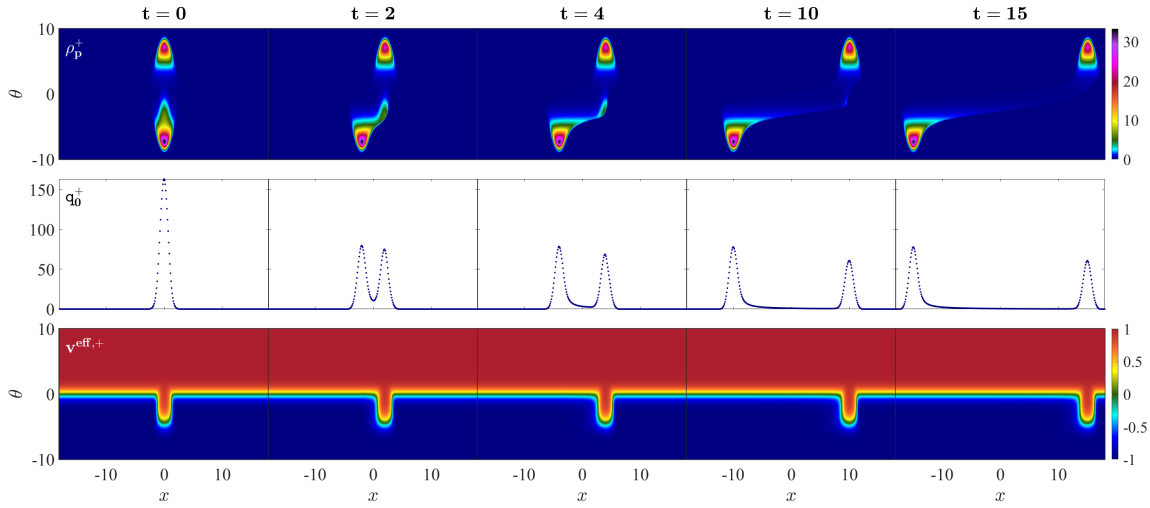


Figure 3.9: Particle + dynamics for various time snapshots. The parameters are $\sigma = 10$, $T_a = 0$ (no bath) and $2T_m = e^7$. Row 1: Spectral density exhibits three characteristic local maxima, the least of which decays in time leading to the formation of a tail. Row 2: Spatial particle density exhibits both a tail and decay. Row 3: Effective velocities are dominated by the values ± 1 but also exhibit intermediate plateaus in rapidity space which are correlated with the decaying peak position in the spectral density. The dynamics of particle $-$ follow from the relations (3.21). See also the video [187] for the time evolution of functions $\rho_p^+(x,t,\theta)$ and $v^{\text{eff},+}(x,t,\theta)$ in the presence of bath.

3.6.2 Bath Effects

Figure 3.10 shows the $x \geq 0$ part of the functions $\rho_p^{\pm}(x,t,\theta)$. In contrast to the zero-temperature case, two continuous, static ridges are formed centred around $\theta \approx \pm \log(2T_a) = \pm 3$, which is the free fermion equilibrium distribution for temperature

T_a. The availability of additional particles in the bath leads to a qualitatively different behaviour following the release of hot matter. The subsidiary peak observed at time $t = 0$ no longer fully disintegrates under time evolution. Instead, it largely persists, propagating on top of the $\theta = -3$ ridge. The presence of this persisting peak has a very interesting physical interpretation.

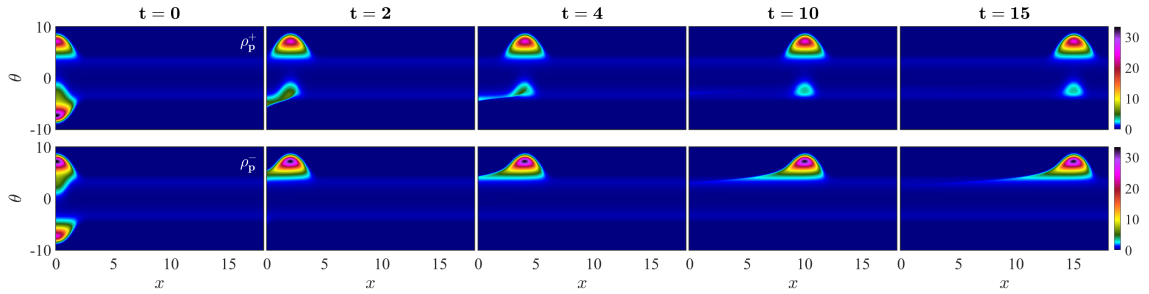


Figure 3.10: Time snapshots of the spectral densities $\rho_p^{\pm}(x, t, \theta)$ for $x \geq 0$ in the presence of a bath. The parameters are $\sigma = 10$, $2T_m = e^7$, $2T_a = e^3$. Recall that $\rho_p^+(x, t, \theta) = \rho_p^-(-x, t, -\theta)$. Whilst the interacting and free fermion peaks remain largely unchanged, the bath facilitates the formation of a persistent peak that travels at speed $+1$ "riding" on top of the bath. The two light-blue ridges are also due to the bath whose temperature is in the free fermion region of the theory. The ridges look "static" because they are uniformly distributed in space but actually propagate with opposite effective velocities ± 1. See also the video [188] for a spectral density comparison between the cases with and without a bath.

Because of the spread of velocities in the initial subsidiary peak, it cannot be explained by a large population of particles at constant velocity near $+1$. Instead, the large wave of particles $-$ in the interaction peak, traveling at velocity $+1$, interacts with particles $+$ in the bath, which are present around the rapidities of the subsidiary peak. The interacting peak forms unstable particles as it passes by and due to mutual interaction locally changes the density of the bath. This density wave then follows the $-$ particles in the interacting peak. The resulting effect is akin to having a fluid that is magnetic, and running a magnet past it. We see a wave that follows the magnet, but the fluid itself does not need to move. The interacting peak of particle $-$ serves as such a magnet and "pulls" along a deformation in the bath ridge of particle $+$, creating a persistent peak on top of it. This is a hydrodynamic effect never previously seen in the GHD context. It is also worth pointing out that the life-time of the unstable particles is of order $e^{-\frac{\sigma}{2}} \approx 0.007$ and what we observe as a persisting peak represents a constant density of unstable particles within which bound states are constantly created and destroyed albeit at balanced rate. Thus, despite the

unstable particles having very short life-time, their density can remain finite for large times.

The effect of the bath can also be clearly observed in the partial particle density defined as

$$\mathfrak{q}_0^+(x,t,\theta<0)=\int_{-\infty}^{0}\rho_p^+(x,t,\theta)\mathrm{d}\theta \tag{3.35}$$

for particle $+$. Leaving out $\theta>0$ is equivalent to subtracting the contribution of the free fermion peak which remains unchanged for all times. Figure 3.11 renders both the decay of the subsidiary peak in the absence of a bath (inset) and its persistence in the presence of a bath (main figure) evident.

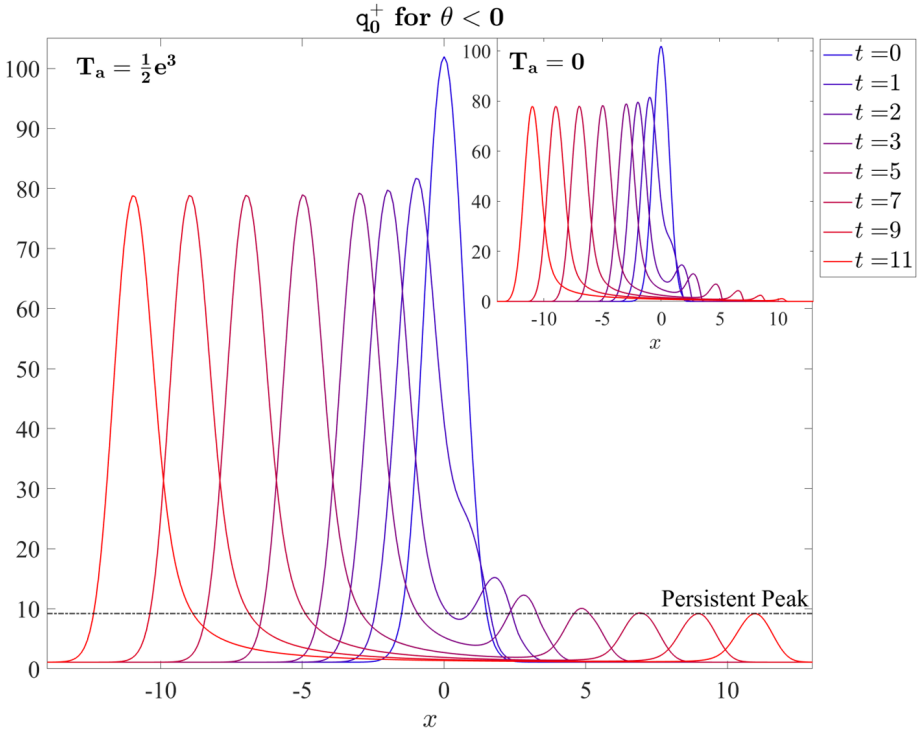


Figure 3.11: The partial spatial particle density $\mathfrak{q}_0^+(x,t,\theta<0)$ showing the decay in the absence of bath (inset) and persistence in the absence of bath (main figure) of the subsidiary peak. See also the video [188] for a spectral density comparison between the cases with and without a bath.

3.6.3 Comparison with Free Particle Evolution

An alternative way to look at the hallmarks of non-trivial interactions far from equilibrium is to compare our results with results obtained in the absence of interactions. Immediately, we can conclude that the presence of the persistent wave in a finite

energy density environment is purely an interaction effect, as for a free model no secondary local maxima are present in the first place.

It remains to consider whether the formation of tails and partial decay of peaks in both spectral and particle density can be reproduced by the velocity distribution alone, without any interaction. The comparison with free-particle evolution can be performed in a number of ways. One might consider the same quench problem, with the same initial temperature distribution but in a free theory. This, however, leads to a different initial density distribution, hence any comparison with the interacting case is not very meaningful.

Instead, one may compare with what would happen for a free-particle system initialised with the same spectral distribution of particles $\rho_p^{\pm}(x, 0, \theta)$ as an interacting model (see Figure 3.8) and evolving the density of particles with positions x and relativistic velocities $\tanh\theta$. This is a reasonable comparison as the initial distribution of positions and rapidities is a physically accessible quantity. In particular, the rapidities are well-defined asymptotic quantities, obtainable from expansion of spatial fluid-cells. Thus, the distribution can be taken as an initial condition under the evolution with either the interacting Hamiltonian, admitting unstable particles, or a free-particle evolution, where no unstable particles are formed. A comparison between the two cases for the particle densities $\mathfrak{q}_0^+$ is presented in Figure 3.12, where we see stark differences between free and interacting particle evolution.

Notably, the distribution of rapidities considered here is very different from that of the initial effective velocities. Particles + with negative rapidities that pertain to the subsidiary peak have negative, rather than positive effective velocities as in the case of an interacting model. Hence, with the free dynamics these particles will start moving towards the left instead of the right as observed with interactions. Thus, free-particle evolution according to the initial spectral distribution is significantly different from the outset, with peaks of very different sizes. Further, the distribution of rapidities leads to sharply defined velocities, which are all very near to ± 1. There is very little dispersion, and consequently no tail formation or decay is observed. Those are thus a stark indication of the presence of interaction. It is also striking to observe that in the case without bath, the decay under interacting evolution leads to a final right-moving wave that agrees precisely with the right-moving wave emitted from the initial distribution in the free evolution case. This indicates that all unstable particles, represented by the original subsidiary peak, have decayed. With a bath, there remains a finite density of particles, representing the population of unstable particles stabilised by the presence of the bath.

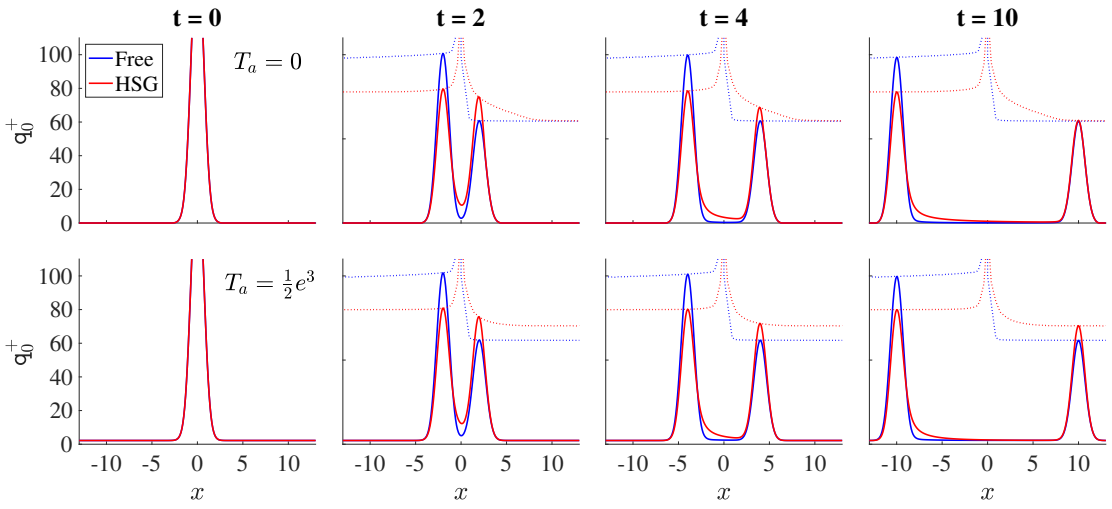


Figure 3.12: Particle density in the HSG model $\mathfrak{q}_0^+(x,t)$ (red) versus $\mathfrak{q}_0^+(x-t\tanh\theta,t)$ (blue). The top/bottom rows correspond to the absence/presence of a bath. The peak in the first column has been cut so as to show the remaining figures more clearly. The dotted curves represent the change in the height of the local maxima of the particle densities as function of time. Red and blue curves generally differ in the height of the local maxima as well as the presence (absence) of a tail.

Another way of testing the effect of interactions is to consider what happens to a free-particle system initialised with not only the same spectral distribution of particles $\rho_p^{\pm}(x,0,\theta)$ (Figure 3.8), but also the same velocity distribution $v^{\mathrm{eff},\pm}(x,0,\theta)$ (Figure 3.6) as an interacting model. This requires evolving the free particles at position x and rapidity θ with the effective velocity $v^{\mathrm{eff},\pm}(x,0,\theta)$. Such a setup is more difficult to justify physically, as the effective velocity already encodes nontrivial aspects of the interaction. However, it makes the free and interacting problems closer, as both the initial condition and its initial infinitesimal change are the same. This allows us to separate any features that are solely dependent on the initial state from features that are truly dependent on the nature of the interaction in the model. This is interesting because the initial density and effective velocity profiles are both non-trivial and in particular, there is a whole spectrum of effective velocities in the initial state. In this case we numerically implemented the free evolution using a Monte Carlo molecular dynamics simulation, in which classical particles are sampled out of a distribution describing the integrable quasiparticles [117, 189]. We start from an initial state determined by the quantum system and evolve it deterministically with the same interactions as for the quantum model. The resulting particle density $\mathfrak{q}_0^+(x,t)$ together with a comparison to our results is presented in Figure 3.13. The statistical nature of the Monte Carlo simulation introduces some noise in the free

particle evolution, yet it clearly preserves the main features.

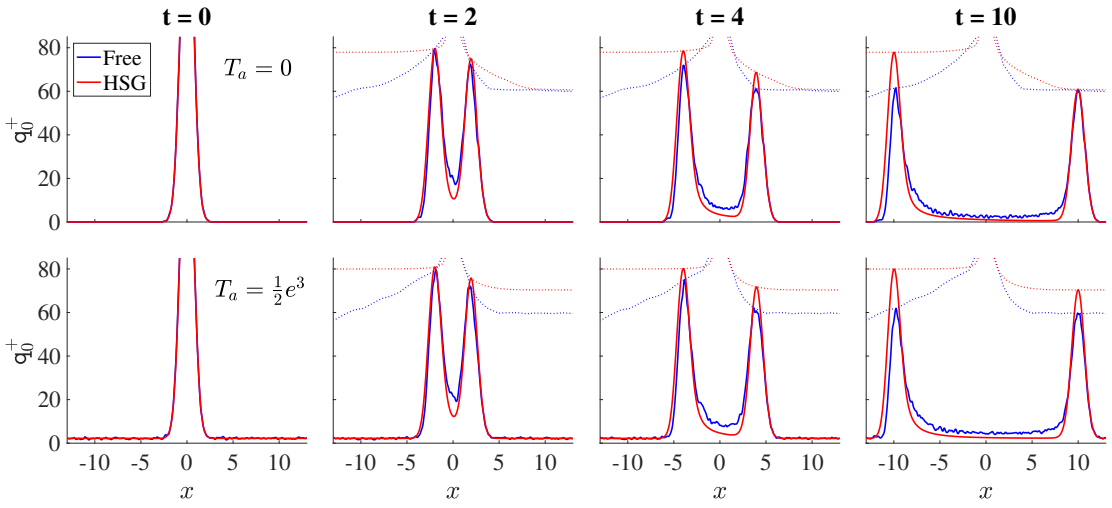


Figure 3.13: Particle density in the HSG model (red) compared to the particle density that would result from free evolution of the same initial conditions (blue). The top/bottom rows correspond to the absence/presence of a bath. The peak in the first column has been cut so as to show the remaining figures more clearly. The dotted curves represent the change in the height of the local maxima of the spectral densities as function of time.

First, a tail also appears for free evolution simply due to the presence of particles with intermediate velocities $-1 < v^{\text{eff}} < 1$. However, the shape of the tail is noticeably different. Indeed it contains a much higher density of particles than in the interacting model. This is due to the fact that in the interacting model even slower particles are carried forward by their interaction with particles of the opposite type so that their actual propagation velocity is higher than their effective velocity and the decaying process is slowed down. Essentially, this highlights the fact that unstable particles have a nonzero lifetime, and thus carry densities more coherently, limiting the dispersion due to the original velocity spectrum. Second, in the absence of interaction the left peak decays in time for all times we have reached numerically and continues to do so until, presumably, it eventually fully disintegrates due to the slower particles contained in it. Concurrently, the right peak experiences some decay only for early times. Instead, in the interacting model, the left peak experiences no reduction whereas there is some decay of the right peak which is however slower than for the free model, underlying again the slowing down of decay due to interactions. Finally, in the HSG model in the presence of a bath there is a magnetic effect that gives rise to a persistent particle density which contributes to the right peak of the

particle density. This effect is clearly absent for free evolution and as a result the red right peak is higher than the blue peak for large times in the second row, whereas they are equal in the top row. The extra density in the interacting model is a signature of the presence of a persisting population of unstable particles and is a specific characteristic of the interaction.

As a result, the signatures of instability, particle creation and decay that we have identified are robust features of the HSG model. They are strongly determined by interaction and are not found for other related scenarios involving free particle evolution.

3.7 Subsidiary Peak: Persistence versus Decay

Both the partial particle density in Figure 3.11 and the spectral density in Figures 3.9 and 3.10 exhibit a peak which either decays or persists for large times, depending on whether or not there is a bath. In this section, we examine the features of this peak in more detail. Naturally, the competition between the two phenomena depends on the parameters of the model, in particular the temperature profile in the initial state. For the clarity of notation, we define the exponents

$$\alpha_m = \log(2T_m) \quad \text{and} \quad \alpha_a = \log(2T_a) \ , \tag{3.36}$$

henceforth referred to as the maximum and the bath exponent respectively.

3.7.1 Propagation

Let us consider the velocity of particles both in the presence and in the absence of a bath. We will report on particle + with particle − admitting an analogous analysis. Importantly, two different velocities can be distinguished. The effective velocity $v^{\text{eff},+}$, as defined in (3.18), is the measure of the average number of interactions the particles experience within a given fluid-cell. It does not describe the speed with which we observe the macroscopic features propagating. In order to investigate the latter quantity, we define a propagation velocity

$$v^{p,+}(x,t,\theta[x,t]) = x/t \ , \tag{3.37}$$

where x, θ denote the position of a feature whose propagation we wish to examine and the rapidity coordinate, at which the propagation velocity is evaluated, depends on both space and time. Here, we concentrate on the physics of the subsidiary peak

and thus we consider the standard effective velocity $v^* \equiv v^{\text{eff},+}(x^*, t, \theta^*)$ evaluated at the maximum of the subsidiary peak $(x^*(t), \theta^*(t))$ as well as the propagation velocity, $v^{p,+}(x^*, t, \theta^*)$, that is the actual speed at which the maximum of the peak is seen to propagate. As a consequence of the non-trivial dynamics resulting from the unstable bound state formation, the two velocities differ from each other. Data facilitating this discussion in the case of $\sigma = 10, \alpha_m = 7$ and $\alpha_a = 3$ (finite bath) or $T_a = 0$ (zero-bath) for particle + is presented in Table 3.1. The choice of times $t \in [2, 12]$ in Table 3.1 was dictated by the time of clear separation of the subsidiary peak from the interacting peak at $t = 2$ and the time at which almost complete decay of the subsidiary peak is observed in a zero-temperature environment at $t = 12$. The most striking feature

	No bath					Bath				
t	x^*	θ^*	h^*	x^*/t	v^*	x^*	θ^*	h^*	x^*/t	v^*
2.00	1.90	-3.30	5.89	0.95	0.61	1.80	-3.44	5.89	0.90	0.54
3.00	2.80	-3.15	5.50	0.93	0.65	2.80	-3.07	5.47	0.93	0.67
4.00	3.80	-2.70	5.07	0.95	0.76	3.80	-2.70	5.03	0.95	0.76
5.00	4.90	-2.17	4.80	0.98	0.84	4.70	-2.54	4.53	0.94	0.77
6.00	5.70	-2.17	4.57	0.95	0.82	5.70	-2.24	4.06	0.95	0.81
7.00	6.50	-2.17	3.78	0.93	0.78	6.90	-2.39	3.42	0.99	0.81
8.00	7.50	-1.79	2.90	0.94	0.81	7.90	-2.39	3.41	0.99	0.81
9.00	8.40	-1.64	2.19	0.93	0.79	9.00	-2.39	3.41	1.00	0.81
10.00	9.40	-1.26	1.50	0.94	0.80	10.00	-2.39	3.41	1.00	0.81
11.00	10.30	-1.03	0.96	0.94	0.77	11.00	-2.39	3.42	1.00	0.81
12.00	11.30	-0.50	0.56	0.94	0.78	12.00	-2.39	3.42	1.00	0.81

Table 3.1: Numerical results for the subsidiary peak of the spectral density of particle + in the absence ($T_a = 0$) and presence ($\alpha_a = 3$) of a bath. The other parameters are fixed to $\sigma = 10$ and $\alpha_m = 7$. x^*, θ^* and h^* are respectively the phase-space coordinates and the height of the local maximum of the subsidiary peak and $v^* \equiv v^{\text{eff},+}(x^*, t, \theta^*)$. The quantity x^*/t represents the observed propagation velocity of the subsidiary peak of particle + resulting from its interaction with the interacting peak of particle − which propagates at speed +1. The numerical uncertainty of phase-space coordinates is $\Delta x^* = 0.10$ and $\Delta\theta^* = 0.07$ to 0.08, with lower rapidity resolution for less negative values of θ^*.

of the data in Table 3.1 is that the effective and propagation velocities are markedly different both in the presence and in the absence of a bath. Thus, even if the presence of a bath gives rise to the magnetic fluid phenomenon, that is, the emergence of a persisting peak that rides on top of the bath, the fact is that, in the absence of a bath, the interaction with particles of type − still has a huge influence on the propagation velocity of the subsidiary peak. The peak propagates faster than would be expected from its effective velocity distribution and this can only be attributed to non-trivial

interaction with particles of type − which is inextricably linked to the presence of unstable particles. This increase in velocity is however larger in the presence of a bath and for large times it reaches the maximum value of +1.

Several observations are befitting here. For early times, the data is very similar both in the presence and absence of a bath. Indeed, for times $t \in [2, 7]$ decay occurs whether or not there is a bath. We can see this decay most clearly from the height of the maximum which reduces from $h^* = 5.89$ at $t = 2$ to $h^* = 3.42$ at $t = 7$. The way in which this decay or particle loss occurs is asymmetric in θ and results in an "under-cut" in the shape of the subsidiary peak, with the lost particles contributing to a growing tail linking the subsidiary peak to the interacting peak of the same particle species, clearly visible in Figure 3.9. As a result, not only is the height of the maximum reduced but its position in phase-space shifts towards less negative values of θ.

In the absence of a bath, further asymmetric decay of the subsidiary peak continues until the peak disintegrates first into a front-like feature and ultimately into a section of the tail joining the free fermion and the interacting peak of the same species. It needs to be emphasised that the decay rate cannot be accounted for by the velocity profile alone, as shown in Figure 3.13. Since the propagation and the effective velocity are different, we know that interactions must play a fundamental role in this decay process.

In the presence of a bath, the subsidiary peak becomes persistent from time $t = 7$, with the rapidity space position fixed at $\theta^* = -2.39$, height $h^* = 3.42$ and propagation velocity $x^*/t = +1$. The fact that the subsidiary peak moves along the interacting peak at velocity +1 rather than the much slower effective velocity of its constituents is the embodiment of the "magnetic-fluid" mechanism. The subsidiary peak does not consist of the same particles propagating but instead of newly formed bound-states between the particles of the interacting peak of particle − and the particle reservoir of particle + available from the bath ridge. Nevertheless, the asymmetric decay process, being independent from the persistent feature, is still present in the case with bath. It is only masked by the dominant mechanism of the magnetic-fluid for times larger than $t = 7$. This coexistence of the two phenomena, decay and persistence, is shown in Figure 3.14. Up to time $t = 2$, the shape of the subsidiary peak is the same in both cases. At $t = 4$ though, the decaying part of the subsidiary peak, while remaining the same in the presence and absence of bath, lags behind the persistent part, featuring only on top of a bath ridge. With time, the decaying feature lags progressively further behind, uncovering an undisturbed, robust persistent peak in the presence of the bath.

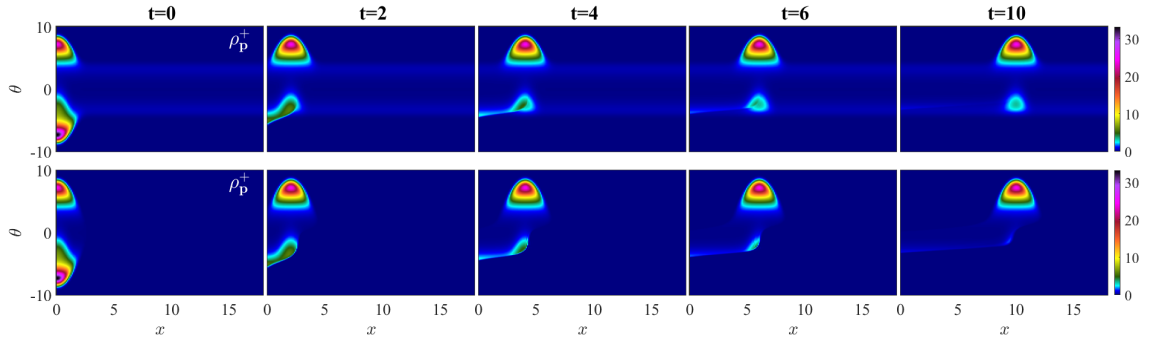


Figure 3.14: Time snapshots of the spectral density $\rho_p^+(x,t,\theta)$ for $x \geq 0$, $\sigma = 10$ and $\alpha_m = 7$, in the presence of a bath at temperature $\alpha_a = 3$ (row 1) and in the absence of bath (row 2). Both cases show qualitatively identical decay behaviour. In the case where a persistent peak on top of a bath ridge is present, it is superimposed onto the decaying feature. See also the video [188] for a comparison between the cases with and without a bath.

For time $t = 10$, a deeper understanding of the difference that the presence of the bath makes can be reached in conjunction with Figures 3.15 and 3.16. They show cross-sections of the effective velocity and spectral density of particles $\pm$ for the bath and no bath situations. In particular, the shape of the subsidiary peak, rather than solely its maximum, can be accessed more clearly through cross-sections at fixed space-time positions.

In Figure 3.15. the subsidiary peak of particle $+$, although very small compared to the free fermion peak, can still be seen to be highly asymmetric in both the x-coordinate and the rapidity space. In fact, it is more akin to a wave-front, with particles at the back slower than those at the front. As indicated by the data in Table 3.1, the effective velocity profile does not fully explain the decay and eventual disintegration of the peak. It is worth noticing that by time $t = 10$ the decaying peak is also significantly lagging behind the interacting peak of particle $-$, since its propagating velocity is $+0.94$ whereas for the interacting peak it is $+1$. Thus, the subsidiary peak $+$ eventually falls out of the interaction range of the interacting peak $-$. The physics changes significantly in the case of the persistent peak in Figure 3.16. Here, the subsidiary peak is symmetric in the coordinate space and is accompanied by a velocity profile symmetric with respect to its maximum. The maximum of the subsidiary peak of particle $+$ coincides in the coordinate space with the maximum of the interacting peak of particle $-$ and both can be found at $x = 10$ for $t = 10$. Despite slower effective velocity, the propagation velocity of the subsidiary peak equals that

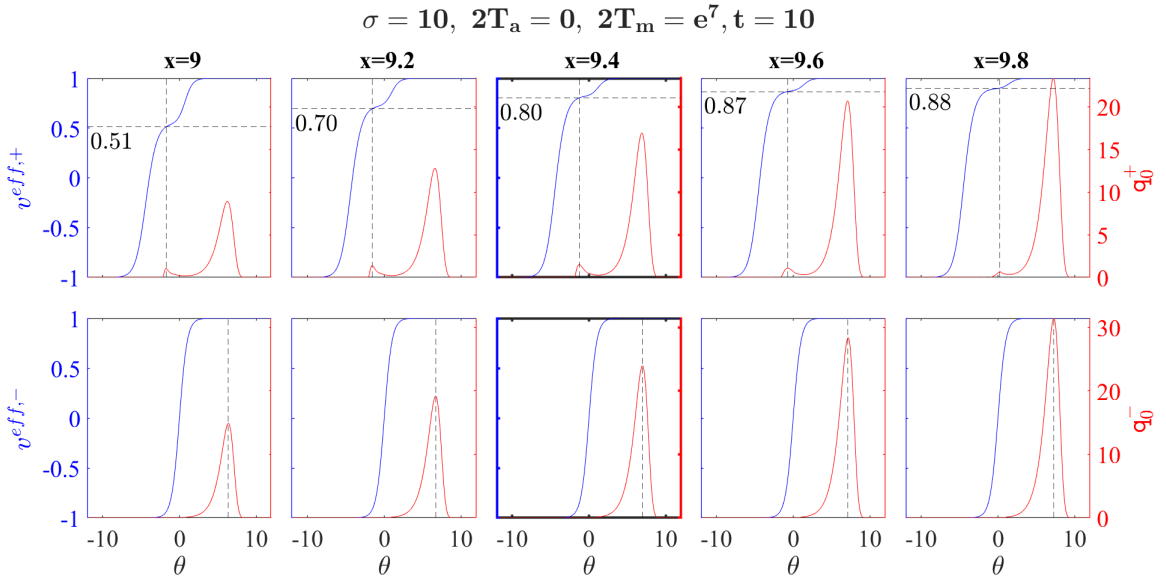


Figure 3.15: Effective velocities (left axis, blue) and spectral density cross-sections (right axis, red) of particle + in row 1 and − in row 2 at time $t = 10$ in the case without bath. For particle + we see the subsidiary (decaying) and free fermion peaks whereas for particle − we see the interacting peak. Columns shows these quantities sequentially for positions $x = 9, 9.2, 9.4, 9.6, 9.8$. The central emphasised column corresponds to $x = x^* = 9.4$, that is the position of the maximum of the subsidiary peak of particle +. The vertical dashed lines indicate the maximum of particle + subsidiary peak cut in row 1 and the maximum of particle − interacting peak cut in row 2. The horizontal dashed lines indicate the corresponding effective velocity of particle + and are annotated with the numerical values.

of the magnet-like interacting peak, which interacts with the bath and drags the subsidiary peak along. This is precisely the magnetic-fluid mechanism.

3.7.2 Quantifying Decay

The decay processes are most evident in the case of the subsidiary peak and it is this local maximum we paid particular attention to. In the subsidiary peak decay, three natural timescales emerge.

- Early Times: Between time zero and some small time $t_1 \approx 0.8$ (as explained in subsection 3.4.0.1) the dynamics are fully determined by the original Gaussian profile of temperatures and in particular the maximum exponent α_m, since $T_m \gg T_a$.

- Intermediate Times: For times between t_1 and some larger time t_2 we observe exponential decay. At this stage the decay process seems to mainly depend on

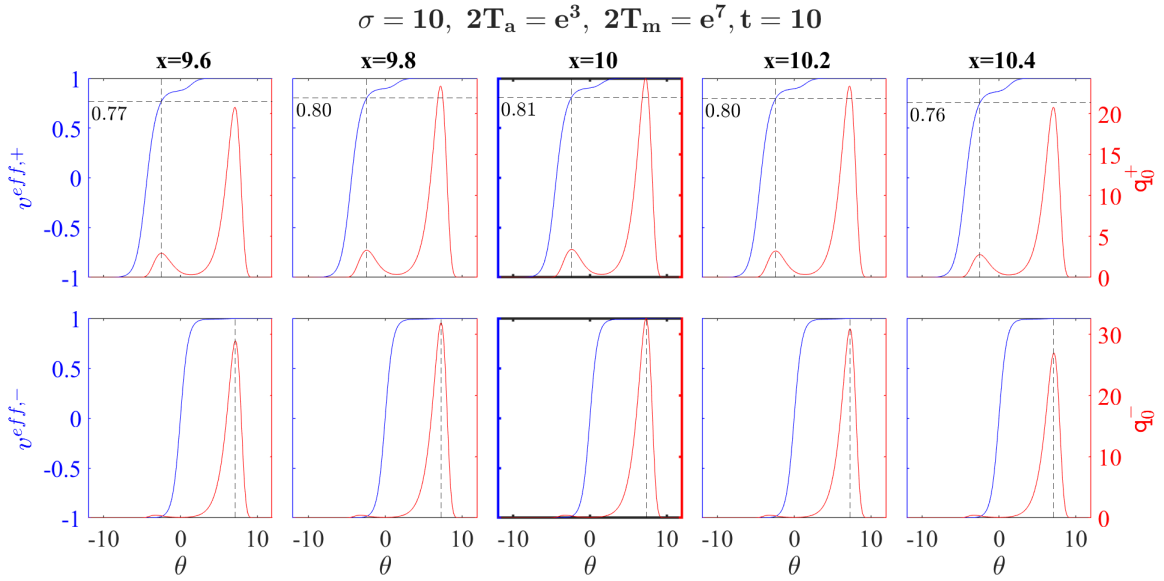


Figure 3.16: Effective velocities (left axis, red) and spectral density cross-sections (right axis, blue) of particle + in row 1 and − in row 2 at time $t = 10$ in the case with a bath at temperature $\log 2T_a = 3$. For particle + we see the subsidiary (persisting) and free fermion peaks whereas for particle − we see the (large) interacting peak and a very small bump corresponding to the bath (for particle + this is marked by the persisting peak sitting right on top). Columns show these quantities sequentially for positions $x = 9.6, 9.8, 10, 10.2, 10.4$. The emphasised central column corresponds to $x = x^* = 10$ the position of the maximum of subsidiary peak of particle +. The vertical dashed lines indicate the maximum of particle + subsidiary peak cut in row 1 and the maximum of particle − interacting peak cut in row 2. The horizontal dashed lines indicate the corresponding effective velocity of particle + and are annotated with the numerical values.

the energy scale $\kappa = \alpha_m - \frac{\sigma}{2}$, which provides the reference scale for the unstable particle formation.

- Late Times: After a larger time t_2, the exponential decay either accelerates in the absence of bath or eventually stops in its presence.

To clearly visualise the decay, we define a normalised particle density

$$\Delta \mathfrak{q}_0^{\pm}(x,t) = \mathfrak{q}_0^{\pm}(x,t) - \mathfrak{q}_0^{FF}(x,t). \tag{3.38}$$

Subtracting the free fermion contribution $\mathfrak{q}_0^{FF}$ is akin to removing the free fermion peak as well as the bath ridge from the spectral density and integrating only the remaining interacting peak and subsidiary peak contributions. The function of interest is the maximum of the decaying peak for $x > 0$ for the particle +

$$H_0^+(t) = \Delta \mathfrak{q}_0^+(x^*(t), t)\ , \tag{3.39}$$

where $x^*(t)$ is the position of the maximum and the definition for the particle $-$ is analogous. Example of the normalised particle density $\Delta\mathfrak{q}_0^+(x,t)$ time evolution with the decaying function $H_0^+(t)$ superimposed is shown in Figure 3.17.

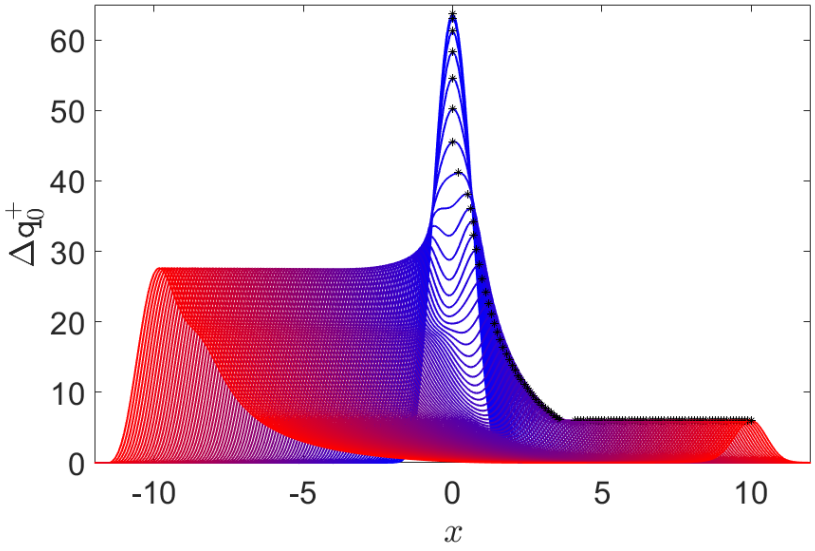


Figure 3.17: Time snapshots of the normalised particle density $\Delta\mathfrak{q}_0^+(x,t)$ for times from $t = 0$ (blue) to 10 (red). The function H_0^+ is plotted in black. The parameters are fixed to $\sigma = 12, \alpha_m = 7.5, \alpha_a = 3$.

Crucially for the later discussion, we have found that the phenomena of persistence and decay are largely separate, though superimposed in some regions of the coordinate and rapidity space. As a consequence, the rate of decay is mostly unaffected by the presence of the bath, as can be observed in Figure 3.18. There, we see that the initial quadratic decay and the intermediate linear decay of a logarithmic function $\log H_0^+(t)$ remain the same whether the hot matter is deposited in zero temperature environment or a bath at temperatures $\alpha_a = 2, 3, 4, 5$. Thereby, we have the freedom to consider the decay and persistence as separate phenomena in the subsequent analysis. A difference between cases of zero and finite background temperatures occurs only at late times when the decay continues more rapidly in the zero temperature environment or stabilises in the presence of the bath.

3.7.2.1 Early Times: Gaussian Decay

The properties of the function $H_0^+(t)$ for early times are fully determined by the initial state temperature profile (3.22). This can be shown analytically using equilibrium

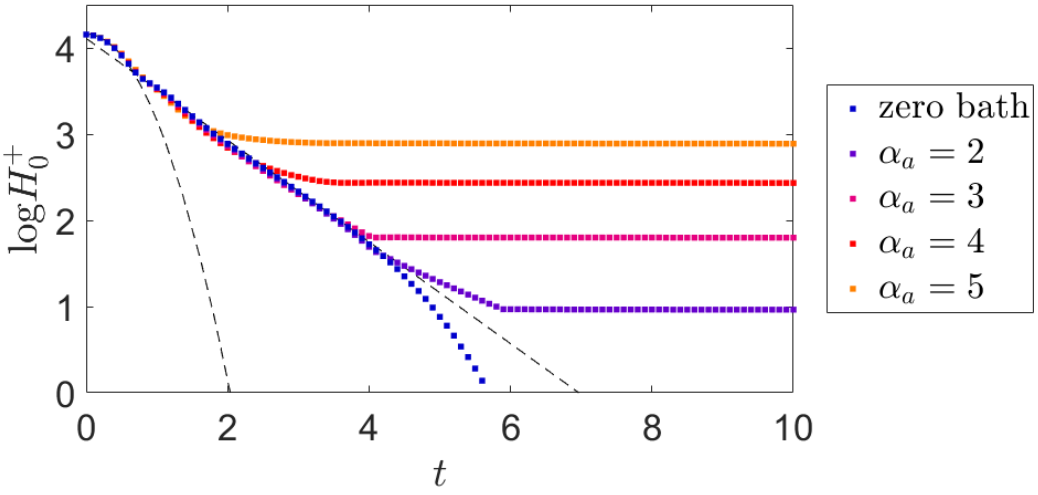


Figure 3.18: Logarithm of the normalised particle density subsidiary peak maximum $\log H_0^+(t)$ for parameters $\sigma = 12, \alpha_m = 7.5$ as well as zero bath or bath exponents $\alpha_a = 2, 3, 4, 5$. Early time quadratic fit and intermediate time linear fit are also plotted in a black dashed line.

TBA arguments presented in Appendix B. For $T_m \gg 1$, the initial particle density maximum is

$$\mathfrak{q}_0^{\pm}(0,0) = \frac{K^{\pm}(0)}{\pi\beta_m} \ , \tag{3.40}$$

where $K^{\pm}(0)$ represent the values of the shifted L-functions (3.13) at the centre of their plateau in the UV limit. For other parity-symmetric theories the plateau is centered around $\theta = 0$, that is $K(0)$ is simply replaced by $L(0)$. For the HSG model, the values of $K^{\pm}(0)$ are known to be [150]

$$K^{\pm}(0) = \log\left(\frac{3+\sqrt{5}}{2}\right) . \tag{3.41}$$

The free fermion result for the initial peak separation in the subsection 3.4.0.1 can be extrapolated to the interacting regime and the initial condition (3.22) to show that for early times we have

$$\mathfrak{q}_0^{\pm}(0,t) \approx \frac{1}{\pi}\log\left(\frac{3+\sqrt{5}}{2}\right) T_m e^{-t^2} \approx 0.15 e^{-t^2+\alpha_m} \ . \tag{3.42}$$

Similarly to the free fermion case, when $T_a \neq 0$ the result (3.31) generalizes by replacing

$$e^{-t^2} \mapsto R + (1-R)e^{-t^2} \qquad \text{for} \qquad R = \frac{T_a}{T_m} \ . \tag{3.43}$$

In our investigation $T_a \ll T_m$ and this rescaling has little impact onto the numerical solutions. The analytic prediction (3.42) is important because the local maximum of $\mathfrak{q}_0^{\pm}(x,t)$ for early times is located at $x^*(t) = 0$ and therefore the formula above can be matched to the numerical values of $H_0^+(t)$ for early times. In particular, for the case of $\alpha_m = 7.5$ presented in Figure 3.18 the numerical data gives us $\mathfrak{q}_0^{+,\mathrm{num}}(0,t) = 263.14e^{-t^2}$, which is consistent with the order of magnitude of the theoretical prediction $\mathfrak{q}_0^{+,\mathrm{th}}(0,t) \approx 271.21e^{-t^2}$. We found a better agreement between the theory and numerics for higher maximum temperature exponents. This is consistent with the high-temperature limit required for the derivation of the theoretical prediction (3.42). Importantly, formula (3.42) depends only on a single parameter of the theory, the maximum temperature exponent, though this dependence is physical only for very early times. For this reason, all curves in Figure 3.18 overlap in the Gaussian decay regime.

3.7.2.2 Intermediate Times: Exponential Decay

To understand the decay after peak separation, recall the natural scale (3.15) and the unstable bound state formation threshold (3.6) introduced earlier. Combining both, we can say that the scale κ provides a measure of where along the RG-flow the model is. A value $\kappa = 0$ corresponds exactly to the midpoint between the low energy behaviour, described by two free fermions, and the UV behaviour, characterised by the presence of the unstable particle. The larger κ is, the closer we are to the UV fixed point and the slower the decay rate. In particular, we can see in Figure 3.18 that the decay rate is largely independent of the bath temperature. We make an ansatz for the intermediate times decay

$$H_0^+(t)/H_0^+(0) = e^{-t/\tau + C} \ , \tag{3.44}$$

where τ is the characteristic timescale of the decay and C is a free parameter. The parameter κ has a defining role in determining the rate of the decay. In Figure 3.19 we plot the function $\log H_0^+(t)$ for different values of the resonance parameter σ and the maximum temperature exponent α_m, but a fixed parameter $\kappa = 1.5$. In all the cases presented in Figure 3.19, the subsidiary wave lifetime is $\tau(\kappa = 1.5) \approx 1.68$ and the free parameter $C(\kappa = 1.5) \approx -0.05$, which is consistent with the assumption of solely κ dependence. The linear fit data is shown in Table 3.2.

Examining the decay of a normalised function $\log H_0^+(t)/H_0^+(0)$ for a range of $\kappa = 1.25$ to 4 in Figure 3.20, we observe that the lifetime τ increases for larger κ. For certain values of κ, the intermediate exponential decay regime is difficult to capture

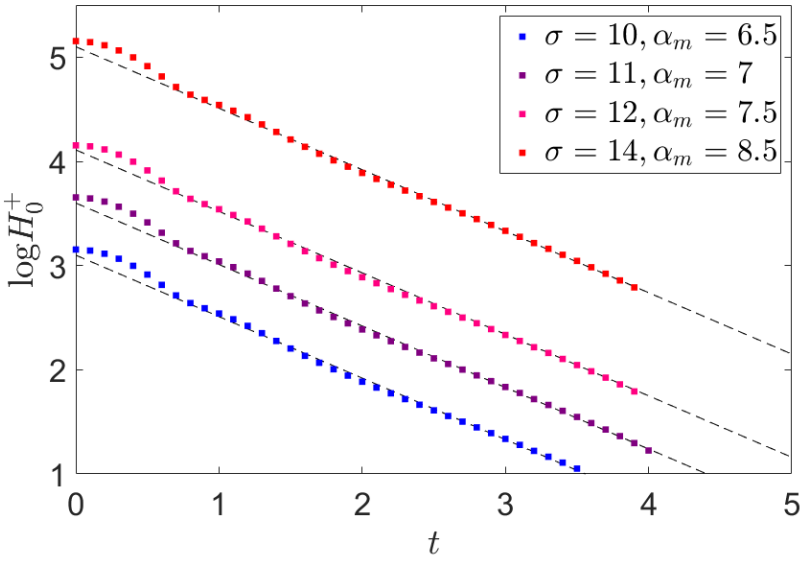


Figure 3.19: Logarithm of the particle density subsidiary peak maximum $\log H_0^+(t)$ for fixed $\kappa = 1.5$ in zero bath. Intermediate time linear fit follows a function $\log H_0^+(t) = -t/\tau + C + \log H_0^+(0)$, where $\tau \approx 1.68$ and $C \approx -0.05$.

σ	$\alpha_\mathbf{m}$	τ	$\Delta\tau$	C	ΔC	R^2
14	8.5	1.68	0.02	-0.05	0.02	0.9990
12	7.5	1.68	0.04	-0.05	0.02	0.9989
11	7	1.69	0.02	-0.04	0.02	0.9989
10	6.5	1.69	0.02	-0.05	0.02	0.9988

Table 3.2: Linear fit parameters $\log H_0^+(t)/H_0^+(0) = -t/\tau + C$ to the normalised particle density subsidiary peak maximum for particle + and fixed $\kappa = 1.5$ in zero bath. R^2 is the R-squared goodness of fit parameter.

because either it lasts very shortly ($\kappa < 1.5$) or requires exponentially long times impractical for the numerical computation. Hence, we analyse the data for $\kappa = 1.5$ to 2.5. The linear fit (3.44) parameters to the logarithmic data is presented in Table 3.3.

We have also investigated the dependence of the decay timescale on the distance from the energy threshold. In Figure 3.21 we see that the relation seems to be exponential and described by an equation

$$\log \tau = a_\kappa \kappa + b_\kappa \ . \tag{3.45}$$

Recall that the decay width of the unstable particles themselves (3.7) is exponentially dependent on the resonance parameter σ. The subsidiary peak consists of a finite population of unstable particles, yet it seems that the exponential dependence on an

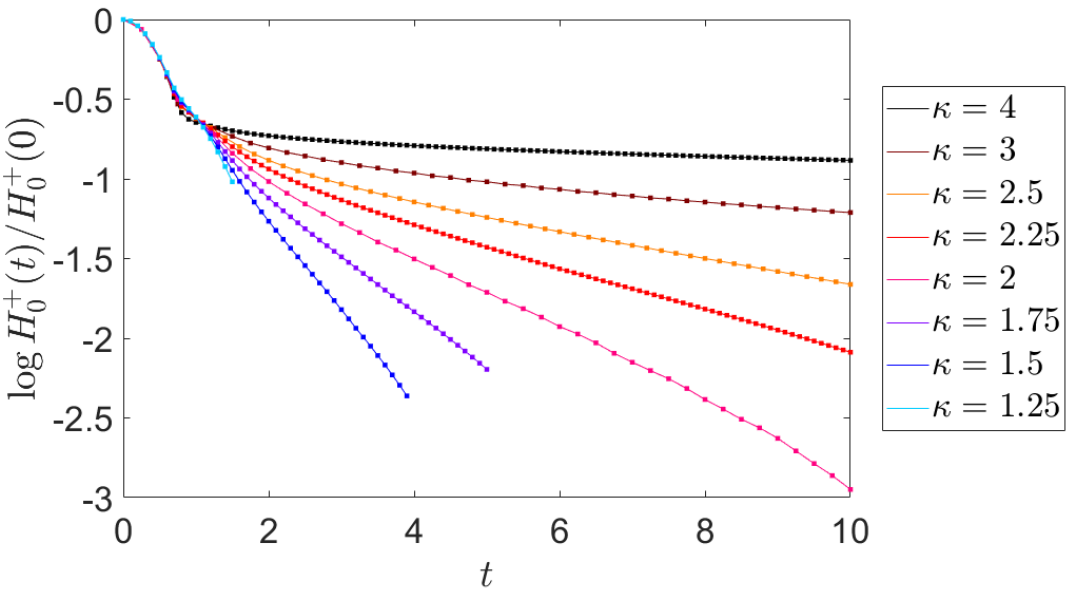


Figure 3.20: Logarithm of the normalised particle density subsidiary peak maximum $\log H_0^+(t)/H_0^+(0)$ for a range of κ values in zero bath.

energy scale applies in this case as well. The fit data is shown in Table 3.4. The results suggest that the function $H_0^+(t)$ decays for intermediate times exponentially as

$$H_0^+(t) = h_0 e^{t/\tau} \quad \text{with} \quad \tau \approx e^{2\kappa} = (2T_m/M)^2 \tag{3.46}$$

namely, as a function of the universal ratio T_m/M, where $M = e^{\sigma/2}$ is the mass scale of the unstable particle (3.6). This ratio is a measure of the energy available in the system relative to the energy required to form an unstable bound state. As expected, the larger this quantity, the closer we are to the UV regime, and the exponentially more stable the subsidiary wave and the population of unstable particles is. We have not found an analytic explanation for the exact scaling of the decay time, yet numerical investigation suggests it grows exponentially with the scale κ, that is, it is larger the closer the system is to its UV fixed point. In other words, we can say that for a given time in the interval described above, there exists a stable density of unstable particles that could itself be seen as an unstable excitation in an effective theory. The decay rate of this new unstable excitation takes the universal form (3.46).

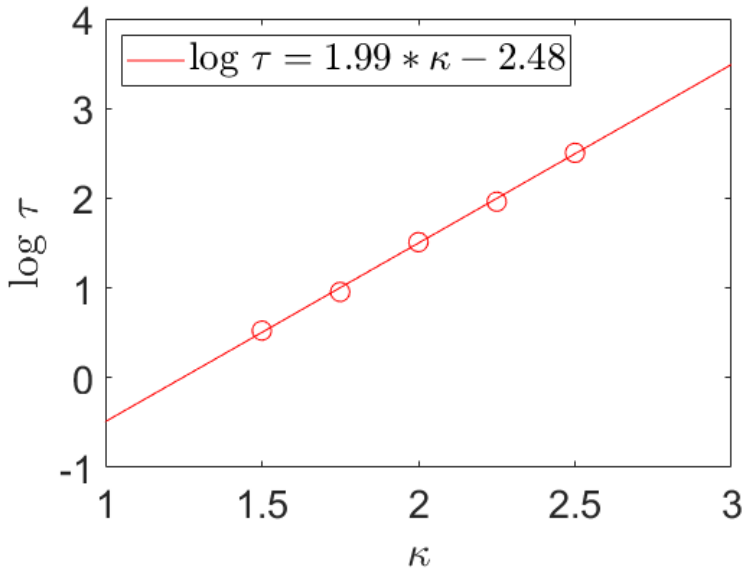


Figure 3.21: Logarithm of the subsidiary peak characteristic decay time τ versus the parameter κ. The linear fit follows a relation $\log \tau = a_\kappa \kappa + b_\kappa$

σ	$\alpha_{\mathbf{m}}$	κ	τ	$\Delta\tau$	C	ΔC	R^2
12	7.5	1.5	1.69	0.02	-0.05	0.02	0.9988
12	7.75	1.75	2.60	0.07	-0.31	0.03	0.9935
10	7	2	4.53	0.05	-0.61	0.02	0.9994
12	8.25	2.25	7.11	0.05	-0.726	0.004	0.9999
12	8.5	2.5	12.25	0.06	-0.85	0.02	0.9997

Table 3.3: Linear fit parameters $\log H_0^+(t)/H_0^+(0) = -t/\tau + C$ to the normalised particle density subsidiary peak maximum for particle + and a range of κ values in zero bath. R^2 is the R-squared goodness of fit parameter.

a_κ	Δa_κ	b_κ	Δb_κ	R^2
1.99	0.14	-2.48	0.29	0.9985

Table 3.4: Linear fit parameters $\log \tau = a_\kappa \kappa + b_\kappa$ to the subsidiary peak characteristic decay time τ and a range of κ values in zero bath. R^2 is the R-squared goodness of fit parameter.

3.8 Persistent Peak: Emergence of a Magnetic-Fluid

Intuitively, we expect that the persisting peak is only formed if there is some overlap in rapidity space between the subsidiary peak of the spectral density and the ridges associated with the bath. Since all these peaks are relatively broad, there is a wide range of temperatures for which overlap will take place. The positions of the peaks'

maxima are determined by the parameters of the model.

Data in Tables 3.5-3.7 provides a numerical in-depth study of the dependence of the persistent peak properties on the temperature exponents. The data presented describes the subsidiary peak of particle +, being representative for both particle species. In particular, we are interested in the maximum height of the persistent peak in the spectral density h_s and the volume of the subsidiary peak V_s. This last measure is computed by integrating the function $\Delta\mathfrak{q}_0^+(x,t)$ in the vicinity of the subsidiary peak maximum $(x^\star, t^\star)$ in the "long-time" limit, i.e. for $t^\star$ such that the subsidiary peak no longer decays

$$V_s = \int_{x^\star - \frac{\delta x_s}{2}}^{x^\star + \frac{\delta x_s}{2}} dx\ \Delta\mathfrak{q}_0^+(x, t^\star)\ , \tag{3.47}$$

where δx_s is the width of the subsidiary peak in the coordinate space. This has been determined on a case by case basis and depends on the initial conditions. Furthermore, we consider in the long-time limit the rapidity position of the persistent peak maximum $\theta^\star$ and its relation to the position of the bath ridge maximum θ_b as well as the position of the interaction maximum $\theta_{max} = \theta_i^\star - \sigma$ with $\theta_i^\star$ indicating the position of the interacting peak maximum of the opposite particle species.

We emphasize that the following numerical investigation indicates certain trends in the characteristics of the $SU(3)_2$-HSG model for different parameters rather than makes a definite statement about the analytic form of its behaviour. Nevertheless, in the range of parameters considered the fits presented provide the highest accuracy with the smallest number of parameters and give us an intuition for the influence of the competing factors of the bath and the deposited hot matter on the persistent peak.

3.8.1 Persistent Peak Position

Following the free fermion analysis in section 3.4, we expect that the maximum of interaction experienced by particle + is near rapidity $\theta_{max} \approx \alpha_m - \sigma$ as a consequence of the maximum of interacting peak of particle − being centered around $\theta_i^\star \approx \alpha_m$. The bath ridges are centered around $\theta_b \approx \pm\alpha_a$. These values are only approximate in the sense that they are based on equilibrium estimates at high temperatures, but they provide a good approximation in the first instance as we can see in Figure 3.7. The terminal position of the subsidiary peak maximum $\theta^\star$ is determined by the interplay between the availability of particles in the bath and the range of the interaction kernel. Before approaching the terminal position, the subsidiary peak

κ	α_m	h_s	V_s	$\theta_{\max}$	θ_b	$\theta^\star$
0	6.0	0.58	0.46	-5.65	-3.22	-3.22
0.5	6.5	0.82	1.26	-5.15	-3.22	-3.22
1	7.0	1.42	3.32	-4.66	-3.22	-3.15
1.5	7.5	2.84	8.33	-4.17	-3.24	-2.97
2	8.0	5.89	19.89	-3.71	-3.22	-2.78
2.5	8.5	11.99	45.00	-3.22	-3.22	-2.58
3	9.0	23.25	97.67	-2.70	-3.22	-2.39
3.5	9.5	53.93	222.19	-2.17	-3.22	-1.94
4	10.0	100.11	442.63	-1.71	-3.22	-1.83

Table 3.5: $\sigma = 12, \alpha_a = 3$ persistent peak data for a range of parameters α_m and κ. h_s is the height of the persistent peak in the spectral density and V_s is the volume of the subsidiary peak. We denote the rapidity position of the subsidiary peak maximum by $\theta^\star$, the bath ridge maximum by θ_b and the interaction maximum by θ_{max}.

κ	α_m	h_s	V_s	$\theta_{\max}$	θ_b	$\theta^\star$
0	5.0	0.57	0.48	-4.70	-3.22	-3.22
0.5	5.5	0.74	1.16	-4.20	-3.24	-3.11
1	6.0	1.13	2.75	-3.71	-3.22	-2.91
1.5	6.5	1.91	6.20	-3.16	-3.24	-2.71
2	7.0	3.41	13.33	-2.66	-3.22	-2.39
2.5	7.5	6.18	27.81	-2.23	-3.24	-1.98
3	8.0	10.78	53.82	-1.69	-3.22	-1.74

Table 3.6: $\sigma = 10, \alpha_a = 3$ persistent peak data for a range of parameters α_m and κ. h_s is the height of the persistent peak in the spectral density and V_s is the volume of the subsidiary peak. We denote the rapidity position of the subsidiary peak maximum by $\theta^\star$, the bath ridge maximum by θ_b and the interaction maximum by θ_{max}.

moves in rapidity space. An illustration of this in cases with and without a bath is shown in Figure 3.22. Without the bath the movement of the subsidiary peak in rapidity space can be explained by the convergence of it to a tail feature linking the interacting and free peaks, see the left panel of Figure 3.22. The formation of a tail itself is a hallmark of interactions, as discussed in subsection 3.6.3. With non-zero energy density in the background, the subsidiary peak is robust only on top of the available particle reservoir. The particles away from the bath ridge decay faster and as a result the subsidiary peak "hugs" the bath ridge. This phenomenon is plotted in the right panel of Figure 3.22.

α_a	h_b	h_s	V_s	θ_{max}	θ_b	$\theta^\star$
0.0	0.02	0.11	0.36	-4.17	-0.05	-0.52
0.5	0.04	0.24	0.71	-4.17	-0.33	-0.80
0.75	0.05	0.33	0.95	-4.17	-0.80	-1.08
1.0	0.06	0.45	1.23	-4.17	-1.27	-1.27
1.5	0.10	0.76	2.12	-4.17	-1.74	-1.74
2.0	0.16	1.24	3.47	-4.17	-2.25	-2.18
2.5	0.27	1.92	5.49	-4.17	-2.76	-2.58
3.0	0.45	2.84	8.33	-4.17	-3.24	-2.97
3.5	0.74	3.96	12.15	-4.17	-3.77	-3.31
4.0	1.22	5.19	16.96	-4.17	-4.23	-3.68
4.5	2.05	6.49	23.39	-4.25	-4.76	-4.05
5.0	3.52	7.77	32.51	-4.25	-5.30	-4.41
5.5	6.24	9.42	44.61	-4.25	-5.73	-4.94
5.75	8.35	10.43	54.70	-4.25	-5.99	-5.56

Table 3.7: $\sigma = 12, \alpha_m = 7.5, \kappa = 1.5$ persistent peak data for a range of parameters α_a. h_s is the height of the persistent peak in the spectral density and V_s is the volume of the subsidiary peak. We denote the rapidity position of the subsidiary peak maximum by $\theta^\star$, the bath ridge maximum by θ_b and the interaction maximum by θ_{max}.

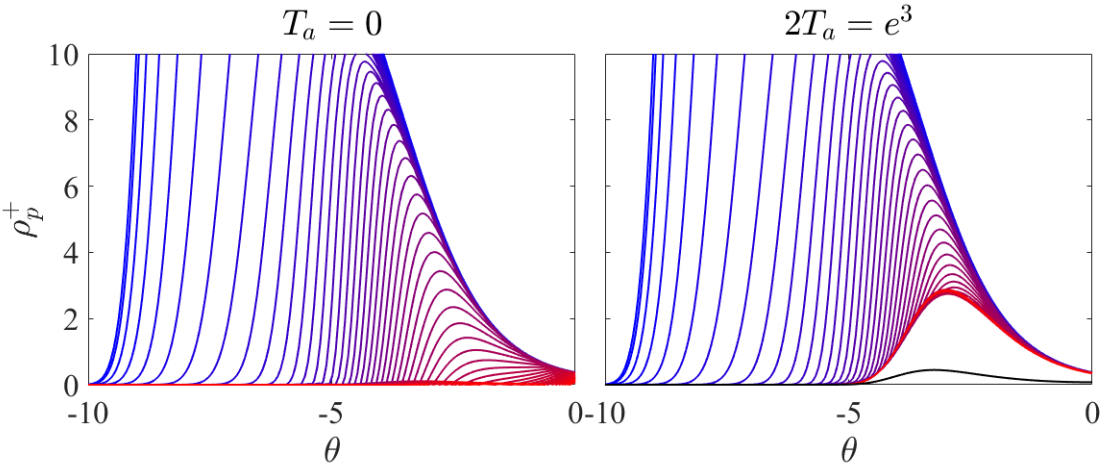


Figure 3.22: Cuts in the spectral density $\rho_p^+(x = t, t, \theta)$ across the subsidiary peak in the $x = t$ plane for different time steps from $t = 0$ (blue) to 5 (red). The parameters are $\sigma = 12, \alpha_m = 7.5, \kappa = 1.5$ and zero bath (on the left) or $\alpha_a = 3$ (on the right). The subsidiary peak decays in the absence of the bath (left panel) and persists in a shape that "hugs" the bath profile plotted in black (right panel).

In the long-time limit, when the subsidiary peak is entirely a persistent wave with no more decay, the analysis of the subsidiary peak position in the rapidity space provides an insight into the competition between the bath and the magnet (interacting

peak of the opposite species). The exact rapidity positions of interest at long times are presented in Tables 3.5-3.7. Studying the effects of varying the maximum temperature exponent α_m in Tables 3.5 and 3.6, we realise that the maximum of the subsidiary peak cannot venture beyond the bath and for $\alpha_a = 3$ we always have $|\theta^\star| \leq |\theta_b|$. This is consistent with the conjecture that the persistent wave propagates on top of the bath ridge and requires a finite particle reservoir not to disintegrate in the long-time limit. More specifically, for $\alpha_m \approx \sigma/2$ we have $\theta^\star = \theta_b$ as in this temperature regime the interacting peak is barely interacting and only a small number of unstable particles is formed. For $\alpha_m > \sigma/2$, we have $|\theta^\star| < |\theta_b|$. The interacting peak of particle $-$ moves towards larger rapidities $\theta_i^\star \approx \alpha_m$ and so does the persistent peak of particle $+$. Naively, we would expect the maximum of the interaction kernel to be where the subsidiary peak maximum is, $\theta^\star = \theta_{max}$, which is the case at thermal equilibrium. Left panel of Figure 3.23 suggests that out-of-equilibrium this is not the case and $\theta^\star$ is a non-trivial function of the maximum temperature exponent α_m and the corresponding interaction maximum θ_{max}. At the same time, it appears that the rapidity position of the subsidiary peak is largely independent of the resonance parameter σ for the same values of θ_{max} and any differences can be accounted for by the numerical precision.

Additionally, below the unstable particle production threshold $\alpha_m \leq \sigma/2$ the persistent peak still appears albeit very small. This reflects the fact that the RG flow is a smoothly varying function (see Figure 3.2) and already for $\alpha_m \lesssim \sigma/2$ we are away from the free fermion CFT. Still, in this region of the parameter space the physics of interest is not very pronounced and we have omitted it in further discussion.

We have also analysed the dependence of $\theta^\star$ on the bath ridge position θ_b based on the data in Table 3.7. We see that these values do not generally coincide and the right panel in Figure 3.23 shows that their relationship is non-trivial. The persistent peak maximum tends to be in between the bath ridges for larger bath temperatures $\alpha_a \in [2.5, 5.75]$, coincide with the bath maximum for intermediate temperatures $\alpha_a \in [1, 2]$, and move beyond it for low temperatures $\alpha_a \in [0, 0.75]$. This trend can be explained by considering the shape of the bath spectrum. There is a non-zero spectral density in between the two bath ridges for all bath temperatures considered and thus the number of particles available to interact with is not necessarily maximised on top of only one bath ridge. Phenomenologically, when the two bath ridges are evidently separate we have $\theta^\star \leq \theta_b$, but for low temperatures the two ridges effectively merge and then we have $\theta^\star > \theta_b$.

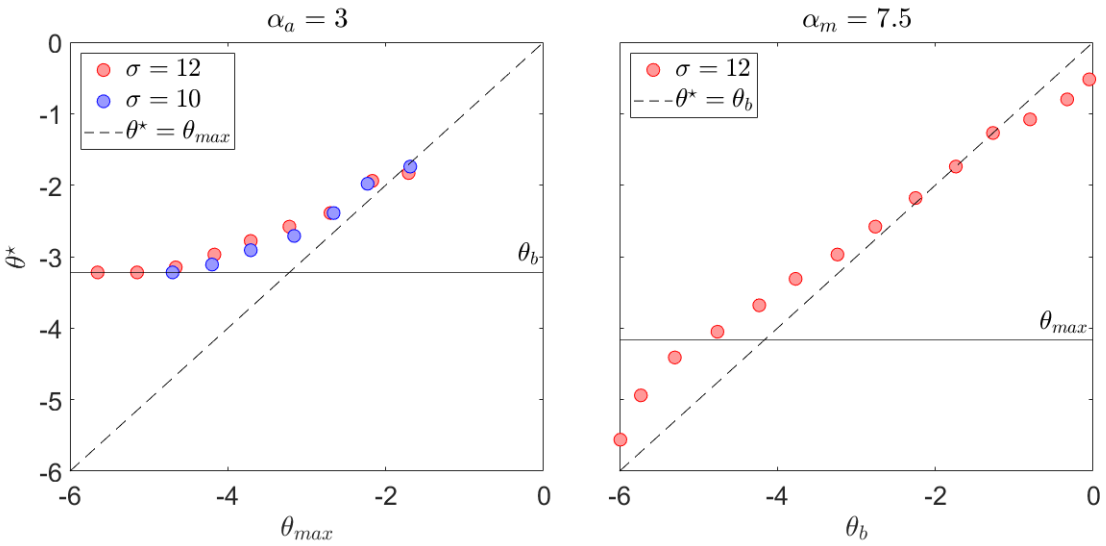


Figure 3.23: Left: Persistent peak of particle + position in the rapidity space $\theta^\star$ as a function of the interaction maximum $\theta_{max} = \theta_i^\star - \sigma$ with $\theta_i^\star$ indicating the position of the interacting peak maximum of particle $-$. Data is presented for two fixed parameters $\sigma = 12, 10$ and a fixed bath exponent $\alpha_a = 3$. Right: Persistent peak of particle + position $\theta^\star$ as a function of the bath maximum θ_b for a fixed parameter $\sigma = 12$ and a fixed maximum exponent $\alpha_m = 7.5$.

By comparing the range of $\theta^\star$ values taken by the subsidiary peak in the same range of θ_{max} and θ_b in Figure 3.23, we deduce that the position of the bath has a more decisive impact on the subsidiary peak position than does the interacting peak; maximising the availability of particles to interact with is more important than the strength of the interaction. This further supports the thesis of the persistent peak being a feature appearing only in the presence of an available particle reservoir.

The discrepancies between the equilibrium predictions and the observed quantities are clearly an effect of non-equilibrium time evolution. Interestingly, these deviations do not appear in the scale-invariant quench setup, such as a partitioning protocol [177]. Note that for the clarity of analysis we considered only the positions of the maxima of the peaks. This is a gross simplification, as all peaks have different geometries which additionally change over time. In particular, the interacting peak has a finite and asymmetric spread with respect to its maximum in the rapidity space. The actual position of the subsidiary peak is determined by the interaction with all the particles within the interacting peak, which are non-trivially distributed around the maximum. The exact relationship between the interacting and persistent peak position in a non-equilibrium setup remains out of reach analytically.

3.8.2 Persistent Peak Height and Volume

We expect the size of the persistent peak to grow for higher temperatures when higher energy density is available. However, this increase will depend on T_m and T_a in different ways. By comparing the two, we aim to determine which parameters have the most control over the formation of the secondary stable wave. In this section, we look at the height h_s and the volume V_s of the subsidiary peak in the spectral density ρ_s^+ in the long-time limit data shown in Tables 3.5-3.7.

The dependence of the persistent peak height on the maximum and bath temperature exponents is shown in row 1 of Figure 3.24. The subsidiary peak height shows an exponential dependence of the temperature exponents within the explored parameter space. The dependence on α_m resembles a function

$$h_s(\alpha_m) = \exp\big(a'_m \alpha_m^2 + b'_m\big) \tag{3.48}$$

and on α_a

$$h_s(\alpha_a) = \exp\big(a'_a \alpha_a^2 + b'_a \alpha_a + c'_a\big)\ . \tag{3.49}$$

The fit parameters are given in Table 3.8 and Table 3.9 respectively. Logarithm of the persistent peak height increases quadratically with both temperatures exponents, yet in the case of α_m the leading term is positive, whereas for α_a it is negative. In fact, for larger bath temperatures the persistent peak height seems almost stalled. We conclude that while the persistent peak can only be formed in the presence of a non-zero bath, the interacting peak of the opposite particle type has a much stronger influence on its height than the bath.

σ	a'_m	$\Delta a'_m$	b'_m	$\Delta b'_m$	R^2
12	0.084	0.004	-3.65	0.24	0.9979
10	0.078	0.005	-2.61	0.22	0.9970

Table 3.8: Parameter of the fit (3.48) for two values of the resonant parameter $\sigma = 12, 10$ and bath temperature exponent $\alpha_a = 3$. $\Delta a'_m, \Delta b'_m$ are the uncertainties of parameters a'_m, b'_m respectively. R^2 is the R-squared goodness of fit parameter.

σ	a'_a	$\Delta a'_a$	b'_a	$\Delta b'_a$	c'_a	$\Delta c'_a$	R^2
12	-0.12	0.01	1.41	0.05	-2.14	0.05	0.9995

Table 3.9: Parameter of the fit (3.49) for resonance parameter $\sigma = 12$ and maximum temperature exponent $\alpha_m = 7.5$. $\Delta a'_a, \Delta b'_a, \Delta c'_a$ are the uncertainties of the parameters a'_a, b'_a, c'_a respectively. R^2 is the R-squared goodness of the fit.

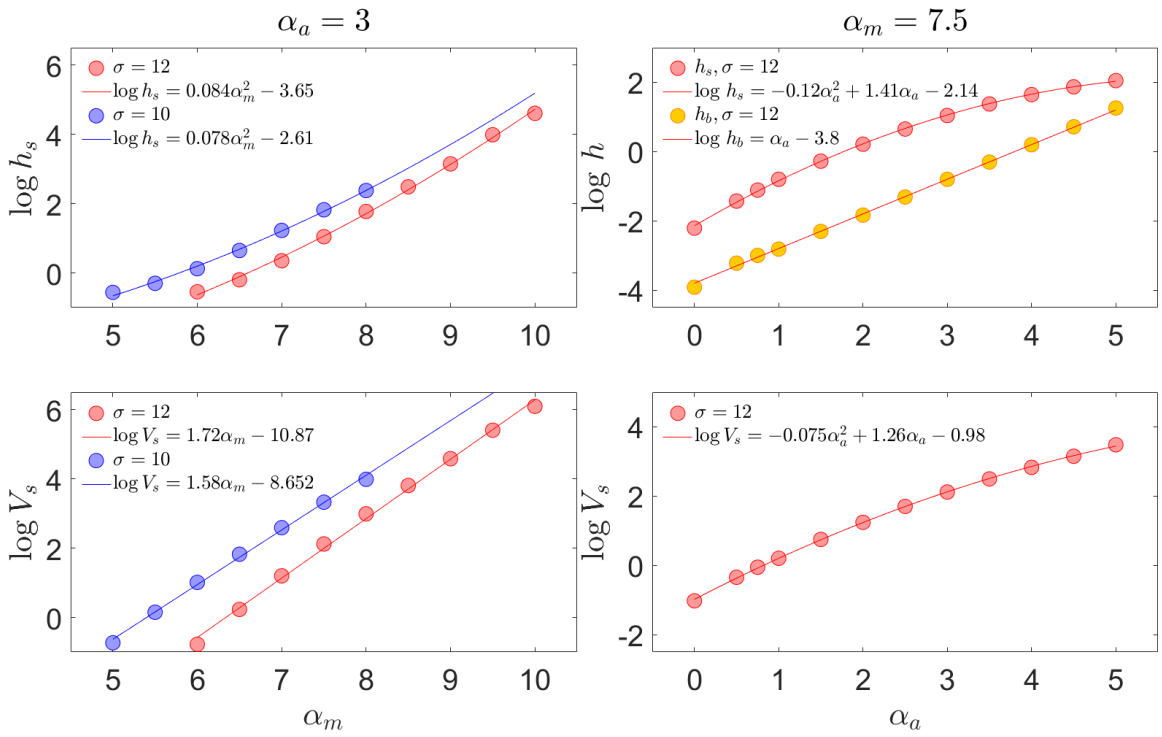


Figure 3.24: Column 1: Logarithm of the persistent peak height (top) and volume (bottom) as a function of the higher temperature exponent α_m for resonance parameters $\sigma = 12, 10$ and fixed bath temperature exponent $\alpha_a = 3$. Column 2: Logarithm of the persistent peak height (top) and volume (bottom) as a function of the bath temperature exponent α_a for resonance parameters $\sigma = 10$ and fixed bath temperature exponent $\alpha_a = 3$ as well as logarithm of the bath ridge height (top) for the same parameters.

For comparison, in the top right panel of Figure 3.24. we also plotted the numerical data for height h_b of the bath ridges in the spectral density $\rho_p^+(x, t, \theta)$ of particle $+$. The corresponding fit takes the form

$$h_b(\alpha_a) = \exp(\alpha_a + a_b') \ , \tag{3.50}$$

with fitting parameters given in Table 3.10. Immediately, it is clear that the persistent peak is indeed higher than the bath ridge and its height follows a different functional dependence on temperature, which signifies the key role of interactions in the process of the persistent peak formation. The dependence of the bath height on temperature can be derived analytically, as it is almost a free fermion solution at the temperature T_a.

For $T \gg 1$, the free fermion spectral density at constant temperature T is

$$\rho_p^{\mathrm{FF}}(\theta) = \frac{1}{2\pi} \frac{\cosh\theta}{1 + e^{\beta \cosh\theta}} \ , \tag{3.51}$$

where $\beta = 1/T$. It has two local maxima at $\theta = \pm\log(2T)$. Substituting these values back into (3.51) and expanding around T large we can obtain the leading dependence in T. Such expansion gives the height of the maxima

$$h = \rho_p^{\mathrm{FF}}(\pm\log(2T)) = \frac{T}{2\pi(1+e)} + \frac{1}{4\pi T(1+e)^2} + \mathcal{O}(T^{-2}) \ , \tag{3.52}$$

which is approximately

$$\log h \approx \log(2T) - \log(4\pi(1+e)) = \log(2T) - 3.8443 \ . \tag{3.53}$$

This analytic formula is in agreement with the numerically observed behaviour, providing an additional check for the suitability of the rapidity discretisation choice. Analytically obtained constant -3.8443 bears close resemblance, up to a numerical error, to the numerical fitting parameter in Table 3.10, $a_b' = -3.80 \pm 0.03$.

σ	a_b'	$\Delta a_b'$	R^2
12	-3.80	0.03	0.9991

Table 3.10: Parameter of the fit (3.50) for the resonant parameter $\sigma = 12$ and maximum temperature exponent $\alpha_m = 7.5$. $\Delta a_b'$ is the uncertainty of parameter a_b'. R^2 is the R-squared goodness of fit parameter.

Similarly, we investigated the dependence of the subsidiary peak volume on the temperature parameters. As shown in row 2 of Figure 3.24, it seems to depend exponentially on the temperature exponents

$$V_s(\alpha_m) = \exp(a_m''\alpha_m + b_m'') \qquad \text{and} \qquad V_s(\alpha_a) = \exp\left(a_a''\alpha_a^2 + b_a''\alpha_a + c_a''\right) \ . \tag{3.54}$$

The fit parameters for the volume dependence on the maximum exponent α_m and the bath exponent α_a are presented in Table 3.11 and 3.12 respectively. Again, by comparing the slopes of the fits to the $\log V_s$ data, we realise that the number of particles in the interacting peak available for the bound state formation is more important than the size of the particle reservoir. For large enough bath temperatures and fixed α_m, The persistent peak volume seems to saturate. This can be understood by considering the initial state, in which the subsidiary peak size is dependent largely on the hot matter temperature - without its presence, the subsidiary peak would not be formed at all as in the free fermion case. Then, although part of the subsidiary peak decays, the larger the interacting peak, the more efficiently it prevents the disintegration of the subsidiary peak. Although the rapidity space position of the subsidiary peak converges to that of the bath ridge, enough particles of the initial state are dragged along by the magnet to form a persistent wave commensurate with the size of the initial subsidiary peak.

σ	a''_m	$\Delta a''_m$	b''_m	$\Delta b''_m$	R^2
12	1.72	0.08	-10.87	0.66	0.9971
10	1.58	0.09	-8.52	0.58	0.9977

Table 3.11: Parameters of the fit (3.54) with respect to α_m for two values of the resonance parameter $\sigma = 12, 10$ and bath temperature exponent $\alpha_a = 3$. $\Delta a''_m, \Delta b''_m$ are the uncertainties of parameters a''_m, b''_m respectively. R^2 is the R-squared goodness of the fit.

σ	a''_a	$\Delta a''_a$	b''_a	$\Delta b''_a$	c''_a	$\Delta c''_a$	R^2
12	-0.075	0.008	1.26	0.04	-0.98	0.04	0.9998

Table 3.12: Parameters of the fit (3.54) with respect to α_a for resonance parameter $\sigma = 12$ and maximum temperature exponent $\alpha_m = 7.5$. $\Delta a''_a, \Delta b''_a, \Delta c''_a$ are the uncertainties of parameters a''_a, b''_a, c''_a respectively. R^2 is the R-squared goodness of the fit.

3.9 Other Temperatures Profiles

Additional insights into the out-of-equilibrium dynamics with unstable particles can be gained through exploring different initial conditions defined by temperature profiles which are distinct from (3.22). We will consider two examples

$$T(x) = (T_m - T_a)e^{-x^2} + T_a \ , \quad \text{for} \quad T_m, T_a \in \mathbb{R}^+ \quad \text{and} \quad \sigma > T_a > e^{\frac{\sigma}{2}} > T_m = 0 \ , \tag{3.55}$$

which we will refer to as an "inverted Gaussian profile" and

$$T(x) = (T_m - T_a)\left(\frac{e^{-(x-x_0)^2} + e^{-(x+x_0)^2}}{1 + e^{-4x_0^2}}\right) + T_a \ , \quad \text{for} \quad \sigma > T_m > e^{\frac{\sigma}{2}} > T_a \geq 0 \ , \tag{3.56}$$

with x_0 some real value. We call this a "double Gaussian profile". The normalization was chosen to ensure that $T(\pm x_0) = T_m$ and $T(\pm\infty) = T_a$

Similarly to the previous section, we present here the analysis concentrating on the particle $+$, with the properties of particle $-$ related by symmetry (3.21).

3.9.1 Inverted Gaussian Profile

Initialising the system in the inverted Gaussian profile (3.55) thermal state, we effectively consider a situation akin to a Gaussian "dip" in the otherwise high temperature environment. One may have expected that the results would be somehow reminiscent of those obtained for $T_m > T_a$, yet it is not the case. The bath region is now in the interacting regime and allows for the formation of unstable particles throughout the system. The resulting profiles reflect the fact that the low initial temperatures

around $x = 0$ are now just a small perturbation of an otherwise high temperature Gibbs ensemble. At local equilibrium at $t = 0$, the system is almost entirely in the interacting regime. The bath ridges can be found at positions predicted by the equilibrium computation $\theta_b = \pm\alpha_a = \pm 7$. However, now we observe that one of the bath ridges is interacting and higher than the other ridge. As a result, we observe unstable particle formation across the system as shown by the subsidiary ridge in the spectral density and intermediate plateaus in the effective velocity for all values of x except in the vicinity of the Gaussian dip. These features are shown in Figure 3.25, where the spectral density $\rho_p^+(x,t,\theta)$ (on the left) and the effective velocity $v_p^{\text{eff},+}(x,t,\theta)$ (on the right) equilibrium cuts for fixed coordinate x in the inverted Gaussian profile (3.55) are plotted. The parameters are fixed to $\sigma = 10, \alpha_a = 7, T_m = 0$, the inverse of the situation considered in section 3.6.

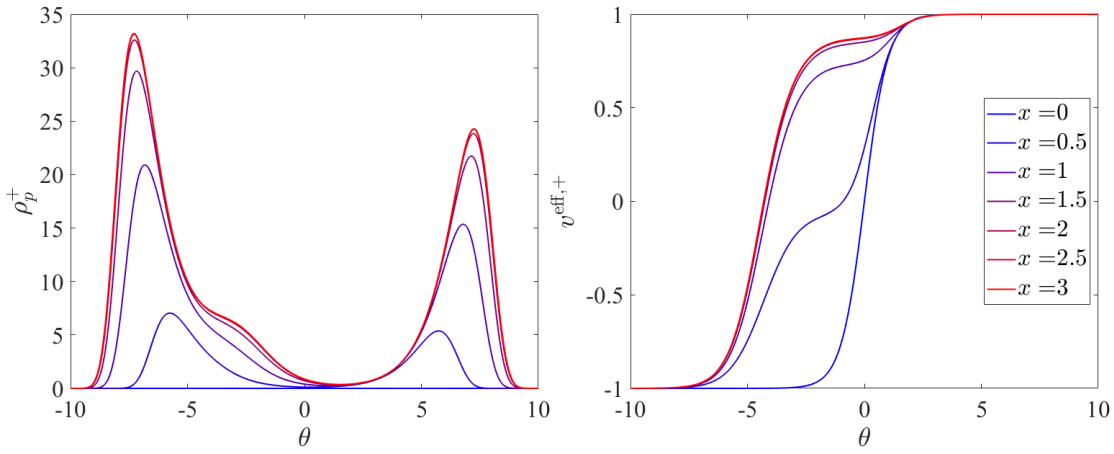


Figure 3.25: Spectral density $\rho_p^+(x,t,\theta)$ (on the left) and the effective velocity $v_p^{\text{eff},+}(x,t,\theta)$ (on the right) local equilibrium ($t = 0$) cuts for several values of x in the inverted Gaussian profile (3.55). The parameters are $\sigma = 10, \alpha_a = 7, T_m = 0$.

The out-of-equilibrium time evolution of the spectral density $\rho_p^+(x,t,\theta)$ and the effective velocity $v_p^{\text{eff},+}(x,t,\theta)$ are shown in Figure 3.26. We observe in row 1 that the effect of the low initial temperatures around $x = 0$ is the formation of a zero spectral density "filament". It originates from the middle region at $x = 0, t = 0$ and is carried away by the bath. In other words, the shape of this filament is precisely described by the function $\theta(x,t)$ which is obtained by solving the particle flow equation

$$v^{eff,+}(\theta) = x/t \ . \tag{3.57}$$

The particle flow profile is plotted in row 2 of Figure 3.26 and superimposed onto the effective velocity. It exactly matches the shape of the filament in the spectral density.

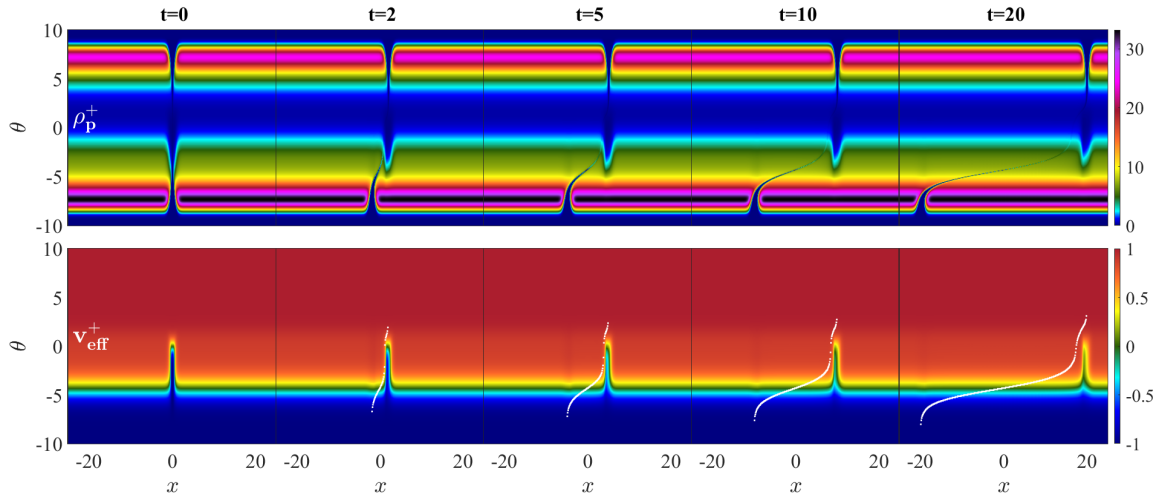


Figure 3.26: Row 1: Spectral density of particle + for different time snapshots in the case of an inverted Gaussian profile (3.55). Row 2: Effective velocity of particle + with the particle flow plotted in white. The parameters are $\sigma = 10, \alpha_a = 7, T_m = 0$.

With our normalisation, we have the velocity range $v^{eff,+}(\theta) \in [-1, 1]$ and hence the plotting range of the particle flow profile is $x \in [-t, t]$ for each time t.

Additionally, we observe that the Gaussian dip in the spectral density propagates at velocity +1. This is despite the fact that the particles in its surroundings have slower effective velocities, as indicated by the additional velocity plateaus in the right panel of Figure 3.25. This is again the magnetic-fluid mechanism in action. The magnet-like interacting bath ridge produces a stable population of unstable particles which is allowed to decay only within the "gap" in the magnet. As a result, the actual propagation velocity of the particles in the bound state is the same as that of the magnet.

3.9.2 Double Gaussian Profile

3.9.2.1 No Bath

In the case of a double Gaussian profile (3.56), we further explore the dependence between the size of the magnet (the interacting peak) and the persistent peak. At equilibrium, we observe a doubling of many of the same features found for the single Gaussian temperature profile (3.22). We now have two free fermion peaks, two interacting peaks and two subsidiary peaks as well as two tails for each particle species. To facilitate the discussion, the peaks in spectral density of particles ± are labelled with L and R and referred to as "left" and "right" respectively as indicated in Figure 3.27.

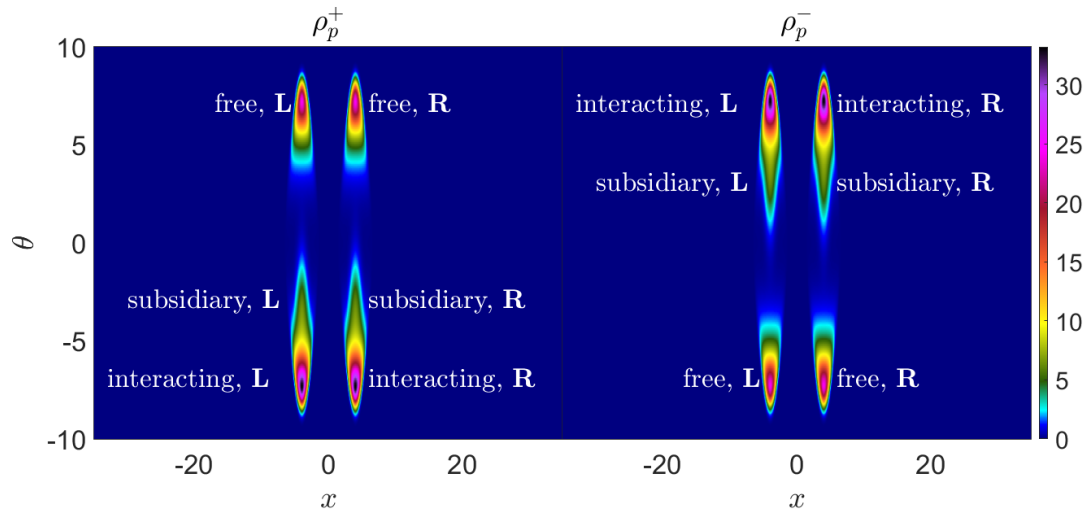


Figure 3.27: Local equilibrium ($t = 0$) spectral density of particle + (on the left) and the particle − (on the right) with the corresponding peak labelling.

Time evolution leads to additional interactions of some of these peaks and tails. Figures 3.28 and 3.29 show the spectral density $\rho_p^+(x, t, \theta)$ and the effective velocity $v^{\text{eff},+}(x, t, \theta)$ for the case with no bath. We consider an example with the parameters $\sigma = 10, \alpha_m = 7, T_a = 0$ and the initial peak position $x_0 = 4$ in expression (3.56).

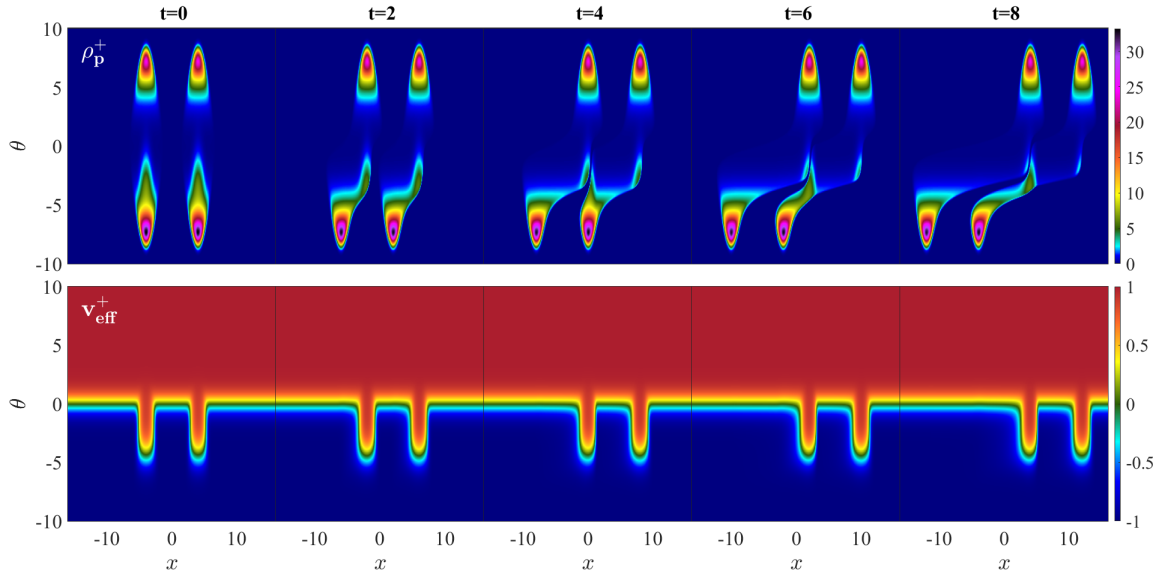


Figure 3.28: Spectral density of particle + (row 1) and its effective velocity (row 2) snapshots from time $t = 0$ to 8 for a double Gaussian initial temperature profile (3.56). The parameters are $\alpha_m = 7$, $T_a = 0$, $\sigma = 10$ and $x_0 = 4$. At early times, left magnet drags some of the particles from the left interacting peak into the left subsidiary peak.

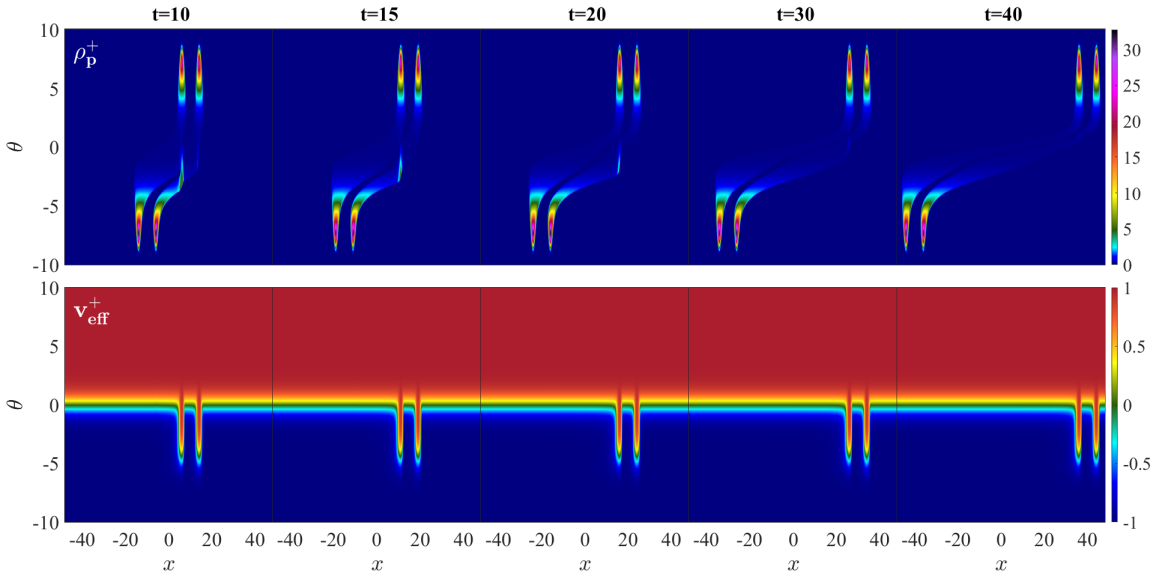


Figure 3.29: Spectral density of particle + (row 1) and its effective velocity (row 2) snapshot from time $t = 10$ to 40 for a double Gaussian initial temperature profile (3.56). The parameters are $\alpha_m = 7$, $T_a = 0$, $\sigma = 10$ and $x_0 = 4$. At late times, the decay of the left subsidiary peak lags behind the decay of the right subsidiary peak.

At time $t = x_0 = 4$ in Figure 3.28, the left interacting peak of particle $-$, the left magnet in this scenario, is aligned in the coordinate space with the right interacting peak of particle +. As their distance in the rapidity space is comparable to the resonance parameter σ, bound states between some of the particles in these two peaks are formed. Consequently, the left magnet drags along a matter wave originating from not only the left subsidiary peak of particle +, but also part of the right interacting peak of particle +. This process starts already at time $t \approx 2$ because of the finite spread of the peaks in the coordinate space.

The additional particles join the left subsidiary peak therefore the right interacting peak of particle + becomes smaller and remains smaller in the long-time limit. This can be visually ascertained by noticing, that the tail of the left interacting peak is much wider than the tail of the right interacting peak. The reversal of the travelling direction of particles redirected from the interacting peak to a subsidiary peak is accompanied by a negligible change in the velocity profile and hence is purely an interaction effect.

After the interacting peaks of both particle species separate, as shown in Figure 3.29, the two subsidiary peaks of particle + are dragged by the two magnets of the $-$ type. Since the left subsidiary peak spectral density was being replenished by

additional particles up until the time $t \approx 10$, this is approximately the timescale of the delay between the decay stages of the right and left subsidiary peaks.

Interestingly, there seems to occur a phenomenon reminiscent of "tail-shyness". In Figure 3.30 we show spectral density cuts for a fixed rapidity $\theta = -3$ illuminating this behaviour. We observe that the left and right tails avoid touching each other and leave a finite zero-density region between them. Referring to the magnetic-fluid analogy, the passing of the magnet leads density deformation wave on top of the available particles, but no particle transfer between the left and right tails takes place.

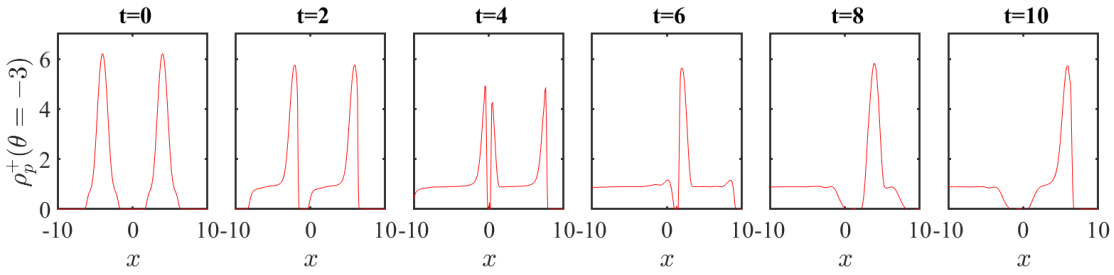


Figure 3.30: Spectral density cuts of particle + for $\theta = -3$ cutting across the subsidiary peaks. From time $t = 0$ to 10 we observe the decay of the right subsidiary peak and the transfer of the left subsidiary peak from the left tail to the right tail.

3.9.2.2 Finite Bath

New features are also present in the persistent peak characteristics. We consider a case with the bath temperature exponent $\alpha_a = 3$ in the double Gaussian profile (3.56) and the remaining parameters the same as in the subsection 3.9.2.1. The close ups of the spectral density $\rho_p^{\pm}(x, t, \theta)$ for both particle species are shown in Figure 3.31.

Looking at row 1 in Figure 3.31, we again observe the left subsidiary peak enlarged with additional particles at $t = 5$ and as a result decaying more slowly at $t = 10$ and 15. At $t = 20$, we seem to recover a familiar picture of persisting peaks riding on a bath ridge, only now involving two peaks. However, in this case the two magnets dragging them along are different sizes and this has profound consequences for the size of the persistent wave. This discussion is facilitated by Figure 3.32 where we plot the spectral density $\rho_p^+(x, t, \theta)$ and the effective velocity $v^{\text{eff},+}(x, t, \theta)$ cuts for a fixed rapidity.

Although the left subsidiary peak acquired more matter on the way and decayed slower, in the long time limit its history does not matter. The deciding factor is the size of the magnet. The left magnet of particle − lost some of its particles to a subsidiary peak of particle −. Therefore, it has fewer available particles to

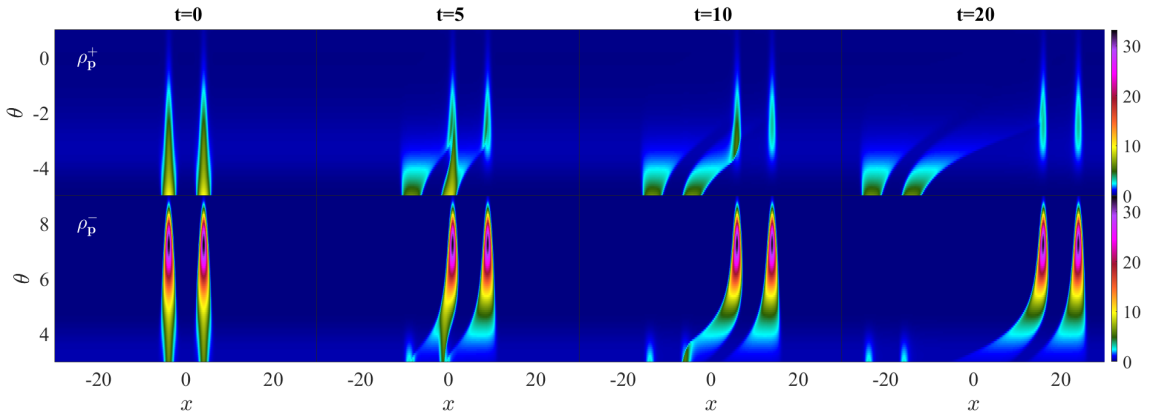


Figure 3.31: Spectral density close-ups of particle + (row 1) and particle − (row 2) for $\sigma = 10, \alpha_m = 7, \alpha_a = 3$ and $x_0 = 4$. $t = 0$: Two subsidiary peaks of particle + and two interacting peaks of particle − are identical. $t = 5$: The left subsidiary peak of particle + acquires additional particles from the right interacting peak of particle +. $t = 10$: The right subsidiary peak of particle + is persistent whereas the left one is still decaying. $t = 20$: The right persistent peak of particle + aligns in the coordinate space with a larger magnet, the right interacting peak of particle −. As a result, the right persistent peak of particle + is larger than the left one.

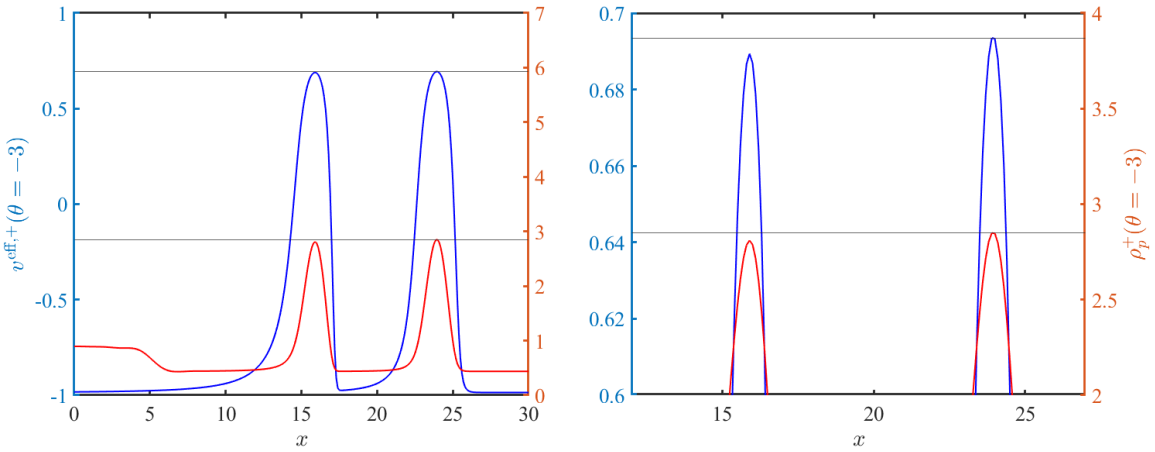


Figure 3.32: Spectral density and effective velocity cuts for particle + and $\theta = -3, t = 20$. Right-hand side is a close-up of the left-hand side figure. The right subsidiary peak, which aligns with a larger magnet, is both larger and has a higher effective velocity than the left subsidiary peak. The parameters chosen are $\alpha_m = 7$, $\alpha_a = 3$, $\sigma = 10$ and $x_0 = 4$.

interact with the subsidiary peak of particle +. As a result, the right magnet interacts with the bath more strongly and the right persistent peak of particle + is larger by $\Delta\rho_p^+ = 0.04 \pm 0.02$. Due to stronger interactions, it also has a higher effective velocity $\Delta v^{\text{eff},+} = 0.004 \pm 0.002$, although in the end both persistent peaks have a

propagation velocity equal to that of the magnets $x^*/t = 1$ in the case of particle $+$. This comparison of two magnets of different sizes, despite corresponding to the same temperature parameters, further underlines the crucial role of the interactions in the formation and properties of the persistent wave.

3.10 Discussion

Within the GHD framework, we have shown how unstable particles in integrable QFT can be observed both in a local equilibrium and in a truly dynamical setup. We have identified the key signatures of unstable excitations which may serve as hallmarks for the finite-lived bound states formation. In particular, we observed the emergence of additional local maxima in the spectral densities of the stable particles and the formation of intermediate plateaus in their effective velocity profiles. Our choice of a truly non-equilibrium quench protocol also led to an explicit observation of co-moving particle densities of opposite types. The real motion in space of the magnet and the corresponding persistent wave is the most direct observation of unstable particles up to date. An analysis of this local maximum and its disintegration shows that, after release into a zero- or low-temperature environment, unstable particles decay. In spatial density profiles, this is indicated by the slow decay of propagating waves and the formation of tails.

In our analysis of the subsidiary peak decay, we looked at the quantitative behaviour of local maxima in the particle density of the asymptotic particles. We have found that at early times the decay is fully governed by the initial temperature profile and follows a Gaussian time dependence. Importantly, we analytically derived the functional form of the decay using equilibrium TBA considerations. Numerical results were consistent with this theoretical prediction. At intermediate times, the subsidiary peak maximum was found to decay exponentially, allowing us to numerically determine the characteristic decay timescale of this density wave. The decay time was found to depend solely on the ratio of the thermal energy in the system and the unstable particle mass. At late times we found the decay to accelerate in the absence of the bath or cease in its presence.

Importantly, in the presence of a bath, a new hydrodynamic phenomenon comes into play. We find the long-time persistence of a small but significant wave of unstable particles "riding" on top of the bath, propelled by its interaction with the large wave of particles of the opposite type. Although we examined the HSG model only in particular temperatures, we found that it is a very robust feature. As all peaks

have a certain width and in addition are not symmetric (in particular they are not Gaussian), there is relatively wide range of temperatures for which this phenomenon is observed. We numerically examined the impact of the initial state temperatures on the persistent wave. It turns out that although a non-zero bath is essential for the persistent peak to exist, it subsequent characteristics are mostly determined by the size of the magnet, the interacting peak of the opposite type. Both the height and volume of the peak grow exponentially with the temperature exponents, yet the influence of the hot matter is always more significant than that of the bath. On the other hand, the position of the persistent wave changes more strongly with the position of the bath ridge than the position of the magnet. Here, the dependence is non-trivial in both cases.

The phenomena of persistence and decay were additionally explored in alternative quench setups with an inverted Gaussian and double Gaussian initial temperature profile. In the case of an inverted Gaussian profile we explicitly identify the features which are merely an effect of the velocity profile (the filament moving with the particle flow) and which ones are truly an interaction effect (propagation of a robust Gaussian dip). The double Gaussian temperature profile allowed us to confirm the key role of the magnet in determining the properties of a persistent wave. Despite both interacting peaks being initialised at the same temperature and with the same resonance parameter, one of them loses some of its particles during the time evolution. As a result, a smaller magnet gives rise to a smaller persistent wave on top of the bath ridge.

We have chosen temperatures that are large enough so that the presence of a continuum of fluid modes in integrable systems does not play an important role in our investigation. The physics in all cases considered is dominated by the RG flow from interacting ($c = 6/5$) to free ($c = 1$) CFT. Importantly, our results suggest that the decay of the population of unstable particles is a real-time dynamical implementation of this flow, an idea which has the potential for leading to a deeper understanding of non-equilibrium dynamics. The distinct signatures of instability identified within GHD are explained via the combined phenomenology of unstable particles and hydrodynamics, and should reflect universal behaviours.

Given how rich the dynamics of this simple model are, it would be very interesting to study other models where more unstable particles with tunable masses and decay widths are present. The complex phenomenology of the unstable excitations is worth also examining in a confining potential, which would form a more experimentally natural setup.

Chapter 4

Tales of Decay: Integrability in Open Quantum Systems

"The theory of exactly solvable models, perhaps more than any other subfield of many-body physics, has the distinct advantage of providing solid, reliable and long-lasting knowledge." -Michel Gaudin

Open quantum systems are characterised by the exchange of information with their environment. At first sight, a problem inherently involving gain and loss could have little to do with integrability. Yet, this counter-intuitive connection is the subject of this chapter and brought us several exciting results.

4.1 Importance of Open Quantum Systems

The mathematical description of quantum systems interacting with their environment is a problem of utmost importance. An isolated quantum system obeying perfectly unitary quantum dynamics is often just an idealisation which does not withstand an experimental trial. The high level of control over many-body quantum states and their dynamics, which is currently achievable in experiments, offers highly accurate measurements and necessitates a new mathematical toolbox. The theory derived to explain an idealised isolated system needs to be reconsidered in the light of the environmental impact. Open quantum systems appear with particular frequency in experiments in the fields of atomic, molecular and mesoscopic physics, as well as optomechanics [190, 191]. They are also closely related to problems in quantum computation. Coupling to a bath introduces unwanted decoherence in quantum information processing [192] but can also facilitate quantum computing and simulations [193], entanglement generation (competition between dissipation and coherent evolution can

induce an entanglement scaling transition [194]) or state preparation [195]. Moreover, open systems provide a fertile ground to study theoretically interesting phenomena such as pre-thermalisation [196, 197], non-equilibrium steady states [198–201] or the possibility of dynamical phase transitions [202]. Understanding the physical principles underlying open quantum systems is a crucial step in the advancement of these fields. Nevertheless, explicit predictions for the behaviour of open quantum systems are notoriously difficult to obtain. The body of research on open quantum systems is still significantly smaller than that on their isolated counterparts and up until the late 2010's, there were no known examples of analytic solutions for interacting many-body open systems. A search for these is motivated by a hope of finding paradigmatic examples, which shine more light onto open many-body interactions in general. A similar understanding in the case of closed systems was derived from integrable models, which provides an additional nudge to look again in this direction.

4.2 Markovian Open Quantum Systems

An analytic description for open time evolution is commonly obtained by considering a Markovian system with its dynamics averaged over the bath. It results in a well-defined mathematical description in a form of the Lindblad equation for the reduced density matrix [203, 204].

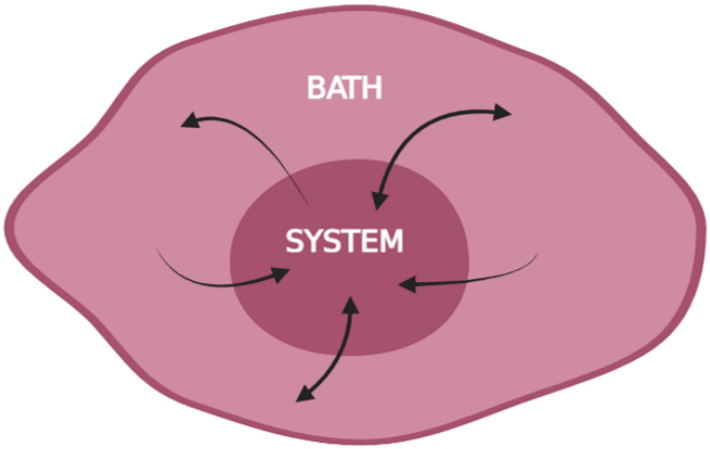


Figure 4.1: Open system diagram [94].

Consider a system coupled to a bath. The state of a combined system and bath is described by a statistical operator ρ, the density matrix. The dynamics of a closed system are governed by a unitary time evolution operator $U_{SB}(t, t_0)$, such that

$$\rho(t) = U_{SB}(t, t_0)\rho(t_0)U_{SB}^{\dagger}(t, t_0) \ , \tag{4.1}$$

where $U_{SB}(t,t_0) = T\exp\Big\{-i\int_{t_0}^{t} dsH_I(s)\Big\}$ is defined in terms of the interaction picture Hamiltonian $H_I(s)$ and T denotes time-ordering. The dynamics of a reduced density matrix ρ_S can be obtained by taking a partial trace over the degrees of freedom of the bath

$$\rho_S(t) = \mathrm{Tr}_B\{\rho(t)\} = \mathrm{Tr}_B\{U_{SB}(t,t_0)\rho(t_0)U_{SB}^{\dagger}(t,t_0)\} = V(t,t_0)\rho_S(t_0)\ . \tag{4.2}$$

In the above equation, $V(t,t_0)$ is a dynamical map which takes the Hilbert space of reduced density matrices $\mathcal{H}_{\mathcal{S}}$ into itself and is completely characterised by operators belonging to the space of endomorphisms on this space $\mathcal{O} \in \mathcal{E}nd(\mathcal{H}_{\mathcal{S}})$. There are several conditions which need to be imposed on the time evolution map in order to produce physical results. First of all, the map needs to be linear to retain the ensemble interpretation of the density matrix [205]. A valid density matrix has to be Hermitian and have unit trace to give a probabilistic interpretation of the master equation. Hence, the dynamical map needs to be trace and Hermiticity preserving. The ultimate requirement is the complete positivity of the map. This ensures that time evolution of a non-negative density matrix as well as its embeddings in an arbitrarily large Hilbert space produces a non-negative result. In general, effects such as strong system-environment coupling, initial state entanglement and finite bath size require the dynamical map to include long time environment memory effects [206]. This can be done by employing a projection superoperator $\mathcal{P}$, which acts on the complete set of states of the total system. $\mathcal{P}(\rho)$ then represents a simplified effective description of the system dynamics through a reduced set of variables. A closed equation for its dynamics can be obtained in the form of a Nakajima-Zwanzig equation, an integrodifferential equation with retarded memory kernel [207,208], or the time-convolutionless master equation, a differential equation involving a time-dependent generator [209]. However, in certain cases the problem reduces to a purely differential equation of motion with a time-independent generator. A crucial requirement for that to happen is a separation of timescales present in the problem. The measurements on the system can be done only with a coarse-grained time resolution δt_C which is much larger than the bath relaxation time δt_B, so that the environment memory effects can be ignored. This Markovian approximation is useful if the timescale of the dissipative dynamics δt_D is much larger than the resolution by which information about the system can be obtained. Overall, we require that

$$\delta t_B \ll \delta t_C \ll \delta t_D\ . \tag{4.3}$$

Switching on the interaction between the system and the bath at time $t = 0$, the combined density matrix of the two is initialised in a product state

$$\rho(0) = \rho_S(0) \otimes |0\rangle\langle 0|_B \ , \tag{4.4}$$

where $|0\rangle\langle 0|_B$ is a pure state in which the bath is initiated. The dynamics of the reduced density matrix ρ_S then become

$$\begin{aligned} \rho_S(t) = \mathrm{Tr}_B\, \rho(t) &= \sum_k \langle k|\, U_{SB}(t,t_0)(\rho_S(t_0) \otimes |0\rangle\langle 0|_B) U_{SB}^\dagger(t,t_0)\, |k\rangle \\ &= \sum_k M_k(t,t_0)\rho_S(t_0)M_k^\dagger(t,t_0) = V(t,t_0)\rho_S(t_0) \ , \end{aligned} \tag{4.5}$$

where $|k\rangle$ form a complete set of states spanning the Hilbert space of the bath and $M_k = \langle k|\, U_{SB}\, |0\rangle$ is an operator acting only on the Hilbert space of the system. This dynamical map is manifestly trace and Hermiticity preserving and the resultant density matrix is positive. In fact, the Kraus representation theorem states that any operator such that $\rho \to V(\rho)$ which is defined in a N^2-dimensional space and follows the requirement of linearity, Hermiticity and trace preservation as well as complete positivity, can be represented in the so-called Kraus representation [205]

$$V(\rho) = \sum_{k=1}^{K} M_k \rho M_k^\dagger \ , \tag{4.6}$$

where the Kraus operators M_k have a property $\sum_{k=1}^{K} M_k^\dagger M_k = \mathbb{1}$ and $K \leq N^2$ is a Kraus number. The Markovian approximation results in the time evolution of the reduced density matrix being governed by a continuous one-parameter set of dynamical maps satisfying a semigroup property $V(t_1)V(t_2) = V(t_1 + t_2)$, which reflects the lack of memory effects in Markovian systems as well as a defined arrow of time. The dynamics of a dissipative system are irreversible. A Markovian dynamical map can be represented in an exponential form $V(t) = \exp\{\mathcal{L}t\}$, where $\mathcal{L}$ is a semigroup generator. This representation leads to a differential quantum master equation

$$\frac{d}{dt}\rho_S(t) = \mathcal{L}\rho_S(t) \ . \tag{4.7}$$

To find an explicit expression for $\mathcal{L}$, consider a complete basis of orthonormal operators F_i, $i = 1, \ldots, N^2$, with N being the dimension of the system's Hilbert space, such that [210]

$$\mathrm{Tr}_S\{F_i^\dagger F_j\} = \delta_{ij} \ \ \forall F_i \in \mathcal{E}nd(\mathcal{H}_\mathcal{S}) \ . \tag{4.8}$$

For convenience, choose a basis in which $F_{N^2} = \sqrt{1/N}\mathbb{1}_S$, which implies $\mathrm{Tr}_S\{F_i\} = 0$ for $i \neq N^2$. By a completeness property, the Kraus operators can be rewritten in terms of this orthonormal set as

$$M_k(t) = \sum_{i=1}^{N^2} \mathrm{Tr}_S\{F_i^\dagger M_k(t)\} F_i \ . \tag{4.9}$$

Hence, the dynamical map itself can be represented as

$$V(t)\rho_s = \sum_{i,j=1}^{N^2} c_{ij}(t) F_i \rho_S F_j^\dagger \ , \tag{4.10}$$

where $c_{ij}(t) = \sum_k \mathrm{Tr}_S\{F_i^\dagger M_k(t)\}\,\mathrm{Tr}_S\{F_j M_k^\dagger(t)\}$ are the overlap coefficients between the two bases. Using the definition of a time derivative, the semigroup generator takes the form

$$\mathcal{L}\rho_S = \lim_{\epsilon\to 0} \frac{V(\epsilon)\rho_S - \rho_S}{\epsilon} = \frac{1}{N} a_{N^2N^2}\rho_S + \frac{1}{\sqrt{N}} \sum_{i=1}^{N^2-1} (a_{iN^2} F_i \rho_S + a_{N^2 i}\rho_S F_i^\dagger) + \sum_{i,j=1}^{N^2-1} a_{ij} F_i \rho_S F_j^\dagger \ . \tag{4.11}$$

where

$$a_{N^2N^2} = \lim_{\epsilon\to 0} \frac{c_{N^2N^2}(\epsilon) - N}{\epsilon} \ , \quad a_{iN^2} = \lim_{\epsilon\to 0} \frac{c_{iN^2}(\epsilon)}{\epsilon} \quad \text{and} \quad a_{ij} = \lim_{\epsilon\to 0} \frac{c_{ij}(\epsilon)}{\epsilon} \tag{4.12}$$

for $i, j \neq N^2$ and by definition, the coefficient matrix a_{ij} is Hermitian and positive. Define

$$F = \frac{1}{\sqrt{N}} \sum_{i=1}^{N^2-1} a_{iN^2} F_i \ , \quad G = \frac{1}{2N} a_{N^2N^2}\mathbb{1}_S + \frac{1}{2}(F^\dagger + F) \ , \quad H = \frac{1}{2i}(F^\dagger - F) \ . \tag{4.13}$$

In terms of those quantities, the equation of motion becomes

$$\mathcal{L}\rho_S = -i[H, \rho_S] + \{G, \rho_S\} + \sum_{i,j=1}^{N^2-1} a_{ij} F_i \rho_S F_j^\dagger \ . \tag{4.14}$$

The trace preservation property of the dynamical map implies

$$\mathrm{Tr}_S\{\mathcal{L}\rho_S\} = \frac{d}{dt}\mathrm{Tr}_S\{\rho_S\} = 0 \quad \Longrightarrow \quad G = -\frac{1}{2}\sum_{i,j=1}^{N^2-1} a_{ij} F_j^\dagger F_i \ . \tag{4.15}$$

Then, using a unitary transformation $\mathbf{u}$, which diagonalises the coefficient matrix a_{ij}, the quantum master equation can be recast into a diagonal form called the Lindblad equation

$$\mathcal{L}(\rho) = -i[H, \rho] + \sum_{\alpha=1}^{N^2-1} \gamma_\alpha (L_\alpha \rho L_\alpha^\dagger - \frac{1}{2}\{L_\alpha^\dagger L_\alpha, \rho\}) \ , \tag{4.16}$$

where the new operators are defined through $F_i = \sum_{\alpha=1}^{N^2-1} \mathbf{u}_{\alpha i} L_\alpha$ and γ_α are the eigenvalues of the coefficient matrix a_{ij}, which are real and non-negative. The first term in the Lindblad equation corresponds to a coherent evolution of the system. However, the Hermitian operator H is in general not the free Hamiltonian of the system itself and is renormalised by the contributions resulting from the coupling to the bath. The Lindblad operators L_α correspond to quantum "jumps" and hence are referred to as jump operators. They describe the dissipation due to interactions with the environment with corresponding dissipative rates γ_α. The Kraus representation of the Lindblad equation is not unique, as there exist transformations leaving it invariant. For this reason, one cannot immediately assign a physical meaning to the operators present in the diagonal Lindblad equation and such a correspondence has to be separately established. In contrast to the closed system dynamics, dissipative time evolution generated by a Liouvillian in general leads to a stationary state ρ_{SS}, defined by

$$\lim_{t\to\infty} \rho(t) = \rho_{SS} \ . \tag{4.17}$$

A stationary state corresponds to the right eigenmatrix of the Liouvillian with a zero eigenvalue and does not have to be unique. In analogy to classical stochastic systems, the left eigenmatrix with zero eigenvalue is a completely mixed state $\rho = \mathbb{1}$, which is a manifestation of probability conservation. Therefore, one has the properties [211]

$$\mathcal{L}(\rho_{SS}) = 0 \quad \text{and} \quad \mathcal{L}^\dagger(\mathbb{1}) = 0 \ , \tag{4.18}$$

where the left action is defined in terms of the adjoint Liouvillian

$$\mathcal{L}^\dagger(\rho) = i[H,\rho] + \sum_{\alpha=1}^{N^2-1} \gamma_\alpha (L_\alpha^\dagger \rho L_\alpha - \frac{1}{2}\{L_\alpha^\dagger L_\alpha, \rho\}) \ . \tag{4.19}$$

The form of the adjoint Lindblad operator makes it apparent that any system with Hermitian jump operators will equilibrate to the infinite temperature state. To consider the remaining spectrum of the Liouvillian, take a set of left and right eigenmatrices of $\mathcal{L}$, $\{R_i\}$ and $\{L_i\}$ respectively. Choosing a normalisation such that $\mathrm{Tr}\{L_i R_j\} = \delta_{ij}$, provided that $\{R_i, L_i\}$ are invertible, allows for the construction of a spectral decomposition of the Liouvillian applied to the statistical operator ρ [211]

$$\rho(t) = e^{t\mathcal{L}}(\rho_0) = \sum_i e^{t\lambda_i} \, \mathrm{Tr}\{L_i \rho_0\} R_i \ . \tag{4.20}$$

All the non-zero eigenvalues have a negative real part for the Liouvillians in the Lindblad form and decay exponentially in time. The eigenvalue with the smallest non-zero real part governs the asymptotic decay rate to the steady state and provides information about possible critical behaviour of the system [195].

4.3 Solutions to the Lindblad Equation

In spite of the linearity of the Lindblad equation, in practice it poses a significant challenge to analysis. Crucially, the Lindblad time evolution generator is non-Hermitian and requires more complicated algorithms to determine its complex spectrum. Initially explicit results were restricted to cases such as a single particle, single spin or harmonic oscillators [210]. For many-particle states, much progress has been made using perturbative techniques [212, 213], matrix product states methods [214–217] and even machine learning [218]. Yet, it is clearly desirable to explicitly analyse the structure of the open dynamics. For classical stochastic many-particle systems, such a solvable paradigm is the asymmetric simple exclusion process [219–223]. In the quantum case, we know that quadratic Lindblad equations, whether describing bosonic or fermionic excitations, can be solved by elementary means [195,224–226], yet with such methods, the interacting systems remained out of reach. A breakthrough appeared when the association with integrable models was realised [227]. This publication inspired not only our work, but afterwards also several others in which isolated examples of open quantum systems with links to integrability were analysed [228–236]. These seem to suggest that integrability is precisely the door through which we can access exact solutions for spectra and thermodynamic quantities of previously elusive interacting open quantum systems. Motivated by this association, we have constructed mappings between Lindblad systems and Yang-Baxter integrable Hamiltonians for a large family of models. The results described in this chapter were largely published in [237]. Following our work, an alternative approach to systematically establishing the equivalence between integrable and open problems has been published in [238]. In order to understand the significance of our results, I will review some stepping stones on the path of their achievement.

4.3.1 Tight Binding Hamiltonian with a Dephasing Noise

The first analytic solution to an interacting system with bulk dissipation appeared in the work of Medvedyeva, et al. in 2016 [239]. The authors considered a 1D lattice with N sites and periodic boundary conditions. The open system comprises a tight-binding Hamiltonian

$$H_{TB} = \sum_{j=1}^{N} \left(a_j^\dagger a_{j+1} + a_{j+1}^\dagger a_j \right) \ , \tag{4.21}$$

where $a_j^\dagger$ and a_j are canonical fermions creation and annihilation operators, and a dephasing noise in a form of local jump operators $L_j = \sqrt{2\gamma} a_j^\dagger a_j$.

The next step is to convert the Lindblad master equation into a so-called superoperator form, described in detail in section 4.4. The authors followed a particular construction introduced in [240, 241], which expresses the left and right acting operators in terms of two, mutually anticommuting species of fermionic superoperators, with raising and lowering operators $\hat{a}^\dagger, \hat{a}$ corresponding to the left acting fermionic operators in the original description, and $\tilde{a}^\dagger, \tilde{a}$ corresponding to the originally right acting operators. As a result, the Lindblad time-evolution superoperator for the system under consideration is

$$\mathcal{L}_{\mathcal{TB}} = -i\sum_{j=1}^{N}\left(\hat{a}_j^\dagger\hat{a}_{j+1} + \hat{a}_{j+1}^\dagger\hat{a}_j - \tilde{a}_j^\dagger\tilde{a}_{j+1} - \tilde{a}_{j+1}^\dagger\tilde{a}_j\right) + \gamma\sum_{j=1}^{N}\left(2\hat{a}_j^\dagger\hat{a}_j\tilde{a}_j^\dagger\tilde{a}_j - \hat{a}_j^\dagger\hat{a}_j - \tilde{a}_j^\dagger\tilde{a}_j\right) . \tag{4.22}$$

Under a unitary transformation

$$\mathcal{U} = \prod_{j=1}^{N}\exp\left\{i\pi\tilde{a}_j^\dagger\tilde{a}_j\right\} , \tag{4.23}$$

the Liouvillian $\mathcal{L}_{\mathcal{TB}}$ takes the form of a Hubbard Hamiltonian with imaginary interaction strength

$$\begin{aligned} H_{HUBB} = i\mathcal{U}^\dagger\mathcal{L}_{\mathcal{TB}}\mathcal{U} = &\sum_{\sigma=\uparrow,\downarrow}\sum_{j=1}^{N}\left(c_{j,\sigma}^\dagger c_{j+1,\sigma} + c_{j+1,\sigma}^\dagger c_{j,\sigma}\right) \\ &+ i\gamma\sum_{j=1}^{N}\left(2c_{j,\uparrow}^\dagger c_{j,\uparrow}c_{j,\downarrow}^\dagger c_{j,\downarrow} - c_{j,\uparrow}^\dagger c_{j,\uparrow} - c_{j,\downarrow}^\dagger c_{j,\downarrow}\right) , \end{aligned} \tag{4.24}$$

where $\gamma \in \mathbb{R}^+$. Here the two species of spinless fermions were canonically mapped onto a single speceis of spin-1/2 fermions with $\hat{a}_j \to c_{j,\uparrow}$ and $\tilde{a}_j \to c_{j,\downarrow}$. This model is BA solvable as presented in [239].

4.3.2 Other Known Results

A quadratic Liouvillian constitutes the simplest integrable model one can consider. Examples of (1 + 1)D free fermion Hamiltonians with linear jump operators were studied extensively in [195, 224] using a covariance matrix.

With the same method, some partial spectral analysis of non-quadratic Liouvillians, with a quadratic Hamiltonian and quadratic Hermitian jump operators, was also conducted in [195]. Such a system results in closed equations of motion for the covariance matrix and allows for a straightforward calculation of its steady state properties. Using first order perturbation theory, the largest non-zero eigenvalue was

also computed in this case, giving insight into the equilibration dynamics of this open quantum system. Nevertheless, the full spectrum could not be obtained with this method.

Instead of considering open quantum systems with the bath coupled to the entire bulk, one can look at interactions with the bath only at the boundary of the system. An example of the complete spectrum being analytically computed for a symmetric exclusion process with open, particle number non-conserving boundary conditions can be found in [242]. In this case the spectrum turned out to be equivalent to that of an open boundary spin-1/2 Heisenberg chain with a magnetic field coupled at the boundary. This is an integrable model, which allowed the authors to apply quantum integrability techniques to the original problem. Exact analytic results were also obtained in [243] for a boundary driven deterministic cellular automaton. The original idea for a closed system of a fully reversible deterministic cellular automaton is a two-state per site chain constituting a many-body interacting system, which admits non-trivially scattering solitons. As for its quantum version, spectral analysis was successful for two types of dissipative stochastic processes happening at the edges of the system, so-called conditional and Bernoulli boundary driving. The authors obtained exact results for a part of the spectrum through a set of Bethe-like equations and presented a conjecture for Bethe-like equations for the remaining part of the spectrum. For a wider range of boundary driven models, nonequilibrium steady states are known. For instance, a summary of a construction of steady states for a variety of locally interacting quantum chains with Markovian stochastic driving at the edges is described in [244]. Here, however, no information about the rest of the Liouvillian's spectrum was obtained. More recently, relaxation and equilibrium properties of boundary driven open systems have been investigated in [234] with the solutions obtained using BA techniques

In the case of bulk dissipation, connection to integrability has been established by various methods. A recipe similar to that presented in subsection 4.3.1 was followed in [229, 230, 233]. Alternatively, in [228] a spin chain with local couplings averaged over a stochastic noise results in a Bethe ansatz solvable form. Instead, [232] considered an already integrable Hamiltonian with purely triangle dissipation, which allows for straightforward computation of the spectrum of the model with BA techniques. Recently, an alternative approach of operator space fragmentation has also been employed [235, 236] and I elaborate on my contribution to this subject in section 4.8. An alternative approach to constructing integrable Liouvillians was followed by [238].

To ensure integrability, the authors considered solutions to the Yang-Baxter equation and imposed on them the requirements of the Lindblad equation structure.

4.4 Superoperator Formalism

The Lindblad equations are often analysed in a vectorised form. Vectorisation is a non-unique procedure the main ingredient of which is shifting the calculational focus from the space of states to a space of observables. The mapping also requires a transformation of the time evolution generator, which takes a superoperator form in the new basis. We have found it particularly instructive to design a vectorisation map in a basis of so-called Hubbard operators, which allows for systematic treatment of both bosonic and fermionic degrees of freedom. In the following, we will define the type of problems that can be treated with this basis choice and present details of the vectorisation map used in the subsequent sections.

4.4.1 Definitions

We consider 1D lattice models defined on a tensor product Hilbert space formed out of a direct product of identical copies of local Hilbert spaces, each corresponding to a single site of a chain. Unless otherwise stated, the problems considered have periodic boundary conditions. We allow for both bosonic as well as fermionic degrees of freedom. The states spanning the Hilbert space on site j are defined as

$$|\alpha\rangle_j \ , \quad \alpha = 1, \ldots, N+M \ , \tag{4.25}$$

where N bosonic and M fermionic quantum states are permitted. The fermion parity of the state $|\alpha\rangle_j$ is denoted by ϵ_α, such that

$$\epsilon_\alpha = \begin{cases} 0 & \text{if } \alpha \text{ is bosonic} \ , \\ 1 & \text{if } \alpha \text{ is fermionic} \ . \end{cases} \tag{4.26}$$

An orthonormal basis of the full Hilbert space $\mathcal{H}_L$ on an L-site chain is given by the states

$$|\boldsymbol{\alpha}\rangle \equiv \otimes_{j=1}^{L} |\alpha_j\rangle_j \ , \quad \alpha_j \in \{1, \ldots, N+M\}. \tag{4.27}$$

The fermion parity of these states is then defined by

$$\epsilon_{\boldsymbol{\alpha}} = \sum_{j=1}^{L} \epsilon_{\alpha_j} \ . \tag{4.28}$$

A complete set of operators acting on site j in the Hubbard operators' basis is

$$E_j^{\alpha\beta} = |\alpha\rangle_j \, {}_j\langle\beta|, \quad \alpha, \beta \in \{1, \ldots, N+M\} \ . \tag{4.29}$$

Their fermion parity can be determined from $\epsilon_\alpha + \epsilon_\beta$ mod 2. This means that Hubbard operators are fermionic if either only the state $|\alpha\rangle$ or only the state $|\beta\rangle$ is fermionic. The operators $E_n^{\alpha\beta}$ act non-trivially only on site n where they serve as projectors between the states α and β

$$\begin{aligned} E^{\alpha\beta}|\alpha^{'}\rangle &= \delta_{\beta,\alpha'} \, |\alpha\rangle \ , \\ \langle\alpha'|E^{\alpha\beta} &= \delta_{\alpha,\alpha'} \, \langle\beta| \ . \end{aligned} \tag{4.30}$$

When acting on the full Hilbert space of the chain, commutation relations between states of different parities have to be considered

$$\begin{aligned} E_n^{\alpha\beta}|\boldsymbol{\alpha}\rangle &= (-1)^{(\epsilon_\alpha+\epsilon_\beta)\sum_{j=1}^{n-1}\epsilon_{\alpha_j}} |\alpha_1\rangle_1 \ldots E_n^{\alpha\beta}|\alpha_n\rangle_n \ldots |\alpha_L\rangle_L \\ &= (-1)^{(\epsilon_\alpha+\epsilon_\beta)\sum_{j=1}^{n-1}\epsilon_{\alpha_j}} \delta_{\beta,\alpha_n} |\boldsymbol{\alpha'}\rangle \ , \quad \boldsymbol{\alpha'} = \alpha_1, \ldots, \alpha_{n-1}, \alpha, \alpha_{n+1}, \ldots, \alpha_L \ , \end{aligned} \tag{4.31}$$

which results in an overall phase. The operators themselves commute or anticommute on different sites depending on their parity

$$E_j^{\alpha\beta} E_k^{\gamma\delta} = (-1)^{(\epsilon_\alpha+\epsilon_\beta)(\epsilon_\gamma+\epsilon_\delta)} E_k^{\gamma\delta} E_j^{\alpha\beta} \ , \quad \text{for} \quad k \neq j. \tag{4.32}$$

In terms of the Hubbard operators, we can define a graded permutation operator on sites j and $j+1$

$$\Pi_{j,j+1} = \sum_{\alpha,\beta} (-1)^{\epsilon_\beta} E_j^{\alpha\beta} E_{j+1}^{\beta\alpha} \ . \tag{4.33}$$

It can be checked that it acts on states as

$$\Pi_{j,j+1}|\beta\rangle_j|\alpha\rangle_{j+1} = (-1)^{\epsilon_\alpha\epsilon_\beta}|\alpha\rangle_j|\beta\rangle_{j+1}, \tag{4.34}$$

hence it permutes the states and generates a minus sign if both states are fermionic as required. Of particular interest is a decomposition of the full Hilbert space $\mathcal{H}^{N+M}$ into a direct product of two identical Hilbert spaces $\hbar^n$, where the superscripts denote the dimensionality of the space. Such a decomposition is possible only for particular relations between the number of states spanning the initial Hilbert space and the decomposed subspaces. Physically, it means that we can treat the original problem by considering two copies of a smaller one and vice-versa. This possibility will nicely tie up with the later considerations of the structure of the vectorised Lindblad equation, where the use of a set of dual bases allows us to maintain a simple algebraic form for

the problem. Take N and M to be a number of respectively bosonic and fermionic states in $\mathcal{H}^{N+M}$, as defined in (4.25). Annotate these with n_B and n_F for the $\hbar_n$ subspace. If N and M are such that they can be expressed as

$$N = n_B^2 + n_F^2 \quad \text{and} \quad M = 2n_B n_F \tag{4.35}$$

for integer n_B, n_F, it is possible to express $\mathcal{H}^{N+M}$ as a graded tensor product of two $n = n_B + n_F$ dimensional spaces

$$\mathcal{H}^{N+M} = \hbar^n \otimes \hbar^n \ . \tag{4.36}$$

Denoting the basis of $\hbar^n$ by $\{|1\rangle, \ldots, |n\rangle\}$, we can express the $N + M$ basis states of $\mathcal{H}^{N+M}$ as

$$|\alpha\rangle = |\widetilde{\alpha}\rangle \otimes |\bar{\alpha}\rangle \ , \quad \alpha = 1, \ldots, N + M \ , \tag{4.37}$$

with the fermion parities of the states related by $\epsilon_\alpha = \epsilon_{\widetilde{\alpha}} \ + \ \epsilon_{\bar{\alpha}}$. The state labels in each subspace belong in the range $\bar{\alpha}, \widetilde{\alpha} \in [1, n]$ and are related to the labels α of the original vector space by

$$\bar{\alpha} = \alpha \bmod n + n\delta_{\alpha \bmod n, 0} \quad \text{and} \quad \widetilde{\alpha} = \left\lfloor \frac{\alpha}{n+1} \right\rfloor + 1 \ . \tag{4.38}$$

An inverse relation also holds

$$\alpha = n(\widetilde{\alpha} - 1) + \bar{\alpha} \ . \tag{4.39}$$

A new set of Hubbard operators can be defined to form a complete set of endomorphisms on each copy of $\hbar^n$

$$\widetilde{e}_j^{\widetilde{\alpha}\widetilde{\beta}} = |\widetilde{\alpha}\rangle_j \ {}_j\langle\widetilde{\beta}| \quad \text{and} \quad e_j^{\bar{\alpha}\bar{\beta}} = |\bar{\alpha}\rangle_j \ {}_j\langle\bar{\beta}| \ . \tag{4.40}$$

These can be related back to the complete set of operators acting on the initial Hilbert space

$$E_j^{\alpha\beta} = |\alpha\rangle\langle\beta| = |\widetilde{\alpha}\rangle|\bar{\alpha}\rangle\langle\bar{\beta}|\langle\widetilde{\beta}| = (-1)^{\epsilon_{\widetilde{\beta}}(\epsilon_{\bar{\alpha}} + \epsilon_{\bar{\beta}})} \ \widetilde{e}_j^{\widetilde{\alpha}\widetilde{\beta}} \ e_j^{\bar{\alpha}\bar{\beta}}. \tag{4.41}$$

In the case of solely bosonic states, the decomposition proceeds along the same steps with $M = 0$. This results in a dimensionality requirement $N = n^2$ with integer n. The new set of operators are then simply related by

$$E_j^{\alpha\beta} = \widetilde{e}_j^{\widetilde{\alpha}\widetilde{\beta}} \ e_j^{\bar{\alpha}\bar{\beta}}. \tag{4.42}$$

4.4.2 Vectorisation

The operation of vectorisation $\mathcal{V}$ derives its name from mapping state matrices onto state vectors according to a prescription

$$\mathcal{V}(\rho_{ij}) \to |\rho\rangle_{f_{ij}} \ , \tag{4.43}$$

where f_{ij} contains the details of the vectorisation procedure which in general is non-unique. An essential ingredient enabling such a mapping is the fact that the complete set of operators acting on a Hilbert space themselves span a Hilbert space. Thus, through vectorisation we map a space of endomorphisms $\mathcal{E}nd(\mathcal{H})$ acting on an N-dimensional Hilbert space $\mathcal{H}$ onto a space of states spanning an N^2-dimensional Hilbert space. This new enlarged Hilbert space, also called the Liouville space or superspace, comprises a direct product of two copies of the original Hilbert space. The operators acting on the Liouville space are the so-called superoperators. In this description, the action of the Lindblad equation on the density matrix is translated to

$$\mathcal{V}(\mathcal{L}(\rho)) \to \hat{\mathcal{L}}\,|\rho\rangle \ , \tag{4.44}$$

where $\hat{\mathcal{L}}$ is the superoperator Liouvillian in the Lindblad form. The vectorisation map also translates the action of the Hubbard operators to an N^2-dimensional superspace. In our prescription, the action of the right acting operators $E^{\alpha\beta}$ remains the same, while the left acting operators are mapped onto new, right acting operators $\tilde{E}^{\alpha\beta}$. We propose a vectorisation scheme mapping a space of operators in the original problem onto a space of vectors according to a recipe

$$\mathcal{V}'(|\alpha\rangle\langle\beta|_j) \to |\alpha\rangle_j\,|\beta\rangle\!\rangle_j \ , \tag{4.45}$$

leading to a 1D chain structure with every site's local superspace spanned by N^2-dimensional state vectors of the form

$$|\alpha_j\rangle_j\,|\beta_j\rangle\!\rangle_j \ , \quad \alpha_j, \beta_j \in [1, n] \ . \tag{4.46}$$

The action of E-matrices then translates to

$$\mathcal{V}'(E^{\alpha\beta}\,|a\rangle\langle b|\,E^{\gamma\delta}) \to E^{\alpha\beta}\,|a\rangle\,\tilde{E}^{\delta\gamma}|b\rangle\!\rangle = (-1)^{N(\epsilon_\gamma+\epsilon_\delta)}E^{\alpha\beta}\tilde{E}^{\delta\gamma}\,|a\rangle\,|b\rangle\!\rangle \tag{4.47}$$

where N is the number of fermionic sites in state $|a\rangle$.

Now, let us turn to the vectorised form of a Lindblad equation (4.16). We are interested in Lindbladians with a Hamiltonian H and jump operators L_a acting on

the space of states defined in (4.27). We are ultimately interested in cases where the Hamiltonian density and jump operators have local expansions in terms of the $E_j^{\alpha\beta}$ operators. Consider first a simplified case where all the jump operators are bosonic. The reduced density matrix can be expressed in terms of the basis states (4.27) as

$$\rho = \sum_{\boldsymbol{\alpha},\boldsymbol{\beta}} \rho_{\boldsymbol{\alpha},\boldsymbol{\beta}} |\boldsymbol{\alpha}\rangle\langle\boldsymbol{\beta}| \ . \tag{4.48}$$

The expansion coefficients are related to the Green's functions of the Hubbard operators

$$\rho_{\boldsymbol{\alpha},\boldsymbol{\beta}} = (-1)^{\sum_{j=1}^{L-1}\sum_{k=j+1}^{L}\epsilon_{\beta_j}\left(\epsilon_{\beta_k}+\epsilon_{\alpha_k}\right)} \ \mathrm{Tr}\left[\rho \ E_L^{\beta_L\alpha_L} \ldots E_1^{\beta_1\alpha_1}\right] \ . \tag{4.49}$$

To ensure the self-consistency of the vectorisation map, we use the Lindblad equation in terms of the matrix components as a benchmark for the correct action of the superoperator in the vectorised problem. In terms of components the Lindblad equation reads

$$\begin{aligned}
\frac{d}{dt}\rho_{\boldsymbol{\alpha},\boldsymbol{\beta}} &= i\sum_{\boldsymbol{\gamma}} \rho_{\boldsymbol{\alpha},\boldsymbol{\gamma}} H_{\boldsymbol{\gamma},\boldsymbol{\beta}} - H_{\boldsymbol{\alpha},\boldsymbol{\gamma}}\rho_{\boldsymbol{\gamma},\boldsymbol{\beta}} \\
&+ \sum_a \gamma_a \Big\{ \sum_{\boldsymbol{\gamma},\boldsymbol{\delta}} \left(L_a\right)_{\boldsymbol{\alpha},\boldsymbol{\gamma}} \rho_{\boldsymbol{\gamma},\boldsymbol{\delta}} \left(L_a^\dagger\right)_{\boldsymbol{\delta},\boldsymbol{\beta}} \\
&\quad -\frac{1}{2}\sum_{\boldsymbol{\gamma}} \left(L_a^\dagger L_a\right)_{\boldsymbol{\alpha},\boldsymbol{\gamma}} \rho_{\boldsymbol{\gamma},\boldsymbol{\beta}} + \rho_{\boldsymbol{\alpha},\boldsymbol{\gamma}} \left(L_a^\dagger L_a\right)_{\boldsymbol{\gamma},\boldsymbol{\beta}} \Big\},
\end{aligned} \tag{4.50}$$

where we have introduced the following notations for the matrix elements of an operator $\mathcal{O}$

$$\langle\boldsymbol{\alpha}|\mathcal{O}|\boldsymbol{\beta}\rangle = \mathcal{O}_{\boldsymbol{\alpha},\boldsymbol{\beta}} \ . \tag{4.51}$$

We can view the density matrix as a state vector in an N^{2L}-dimensional Hilbert space $\mathcal{H}_S = \mathcal{H}_L \otimes \mathcal{H}_L$ with basis states

$$|\boldsymbol{\alpha},\boldsymbol{\beta}\rangle = |\boldsymbol{\alpha}\rangle\,|\boldsymbol{\beta}\rangle\!\rangle = |\alpha_1\rangle_1 \ \ldots|\alpha_L\rangle_L \ |\beta_1\rangle\!\rangle_1 \ \ldots|\beta_L\rangle\!\rangle_L \ . \tag{4.52}$$

and a scalar product $\langle\boldsymbol{\alpha}',\boldsymbol{\beta}'|\boldsymbol{\alpha},\boldsymbol{\beta}\rangle = \delta_{\boldsymbol{\alpha},\boldsymbol{\alpha}'}\delta_{\boldsymbol{\beta},\boldsymbol{\beta}'}$. In this notation the vectorised density matrix is

$$|\rho\rangle = \sum_{\boldsymbol{\alpha},\boldsymbol{\beta}} \rho_{\boldsymbol{\alpha},\boldsymbol{\beta}} |\boldsymbol{\alpha}\rangle|\boldsymbol{\beta}\rangle\!\rangle \ . \tag{4.53}$$

The "wavefunctions" $\rho_{\boldsymbol{\alpha},\boldsymbol{\beta}}$ retain here their interpretation as correlators in the original problem and are an object of interest when investigating the vectorised problem. The quantum master equation (4.7) can be cast in the form

$$\frac{d|\rho\rangle}{dt} = \hat{\mathcal{L}}|\rho\rangle \ , \tag{4.54}$$

where the Liouvillian $\hat{\mathcal{L}}$ for bosonic jump operators is given by

$$\hat{\mathcal{L}} = -iH + i\bar{H} + \sum_a \gamma_a \left[L_a \overline{L_a^\dagger} - \frac{1}{2}\left(L_a^\dagger L_a + \overline{L_a^\dagger L_a} \right) \right] \ , \tag{4.55}$$

which is a so-called superoperator or Lindbladian form of the time evolution generator for Markovian open quantum systems. Here, we employ notations such that the leading superoperators $\mathcal{O} = \mathcal{O} \otimes 1$ originate from the right-acting operators, and their duals $\overline{\mathcal{O}} = 1 \otimes \overline{\mathcal{O}}$ derive from the originally left-acting operators. The dual set of superoperators is defined by

$$\langle\!\langle \boldsymbol{\gamma} | \overline{\mathcal{O}} | \boldsymbol{\beta} \rangle\!\rangle = \langle \boldsymbol{\beta} | \mathcal{O} | \boldsymbol{\gamma} \rangle \ . \tag{4.56}$$

These two sets of superoperators would be exchanged in their behaviour under the vectorisation map if an adjoint Lindblad problem was considered. In the space of endomorphisms on the superspace, the Hubbard superoperators are defined to be

$$E_n^{\alpha\beta} = \left(|\alpha\rangle_{n\ n}\langle\beta| \right) \otimes 1 \quad \text{and} \quad \widetilde{E}_n^{\alpha\beta} = 1 \otimes \left(|\alpha\rangle\!\rangle_{n\ n}\langle\!\langle\beta| \right) \tag{4.57}$$

for the leading and dual superoperators respectively. The action of the latter on the basis states of $\mathcal{H}_L$ is

$$\begin{aligned} \widetilde{E}_n^{\alpha\beta} |\boldsymbol{\alpha}\rangle |\boldsymbol{\beta}\rangle\!\rangle &= (-1)^{(\epsilon_\alpha + \epsilon_\beta)\epsilon_{\boldsymbol{\alpha}}} |\boldsymbol{\alpha}\rangle \ \widetilde{E}_n^{\alpha\beta} |\boldsymbol{\beta}\rangle\!\rangle \\ &= (-1)^{(\epsilon_\alpha + \epsilon_\beta)\epsilon_{\boldsymbol{\alpha}}} (-1)^{(\epsilon_\alpha + \epsilon_\beta) \sum_{j=1}^{n-1} \epsilon_{\beta_j}} \delta_{\beta,\beta_n} |\boldsymbol{\alpha}\rangle |\boldsymbol{\beta}'\rangle\!\rangle \ , \end{aligned} \tag{4.58}$$

where $|\boldsymbol{\beta}'\rangle\!\rangle = |\beta_1\rangle_1, \ldots, |\alpha\rangle_n, \ldots, |\beta_L\rangle_L$ and $\epsilon_{\boldsymbol{\alpha}}$ has been defined in (4.28). For an ultimate check of the validity of the above construction proposed, one needs to take a scalar product of (4.54) with the state $\langle\!\langle \boldsymbol{\beta} | \langle \boldsymbol{\alpha} |$. This directly reproduces (4.50), confirming the self-consistency of the scheme.

4.4.2.1 Fermionic Jump Operators

Interactions with the bath described by fermionic jump operators impose a need to modify the superoperator formalism. The overall parity of any term in the Lindblad equation is of essence here, because commuting it through the states in the vectorised density matrix can give rise to additional phases. Let us denote the fermion parity of the Hamiltonian H by ϵ_H and the jump operator L_a by ϵ_{L_a} both taking values in $\{0, 1\}$ as defined in (4.28). Dealing exclusively with the physically meaningful Hermitian Hamiltonians, we impose $\epsilon_H = 0$. Thus, the Hamiltonian part of the superoperator Lindbladian (4.55) remains the same as in the purely bosonic case.

Also, terms arising from the anticommutator in the Lindblad equation (4.16) are not altered, because $2\epsilon_{L_a} \bmod 2 = 0$ and the overall parity of these terms is bosonic. A modification to the superoperator Lindbladian has to be introduced only in the remaining part of the dissipative dynamics and the Liouvillian (4.55) is replaced by

$$\hat{\mathcal{L}} = -iH + i\bar{H} + \sum_a \gamma_a \left[(-i)^{\epsilon_{L_a}} L_a \overline{L_a^\dagger} - \frac{1}{2} \left(L_a^\dagger L_a + \overline{L_a^\dagger L_a} \right) \right]. \tag{4.59}$$

The state representing the density matrix is also modified and now takes the form

$$|\rho\rangle = \sum_{\boldsymbol{\alpha},\boldsymbol{\beta}} \rho_{\boldsymbol{\alpha},\boldsymbol{\beta}} \left[(-i)^{\epsilon_{\boldsymbol{\alpha}}} P_+ + i^{\epsilon_{\boldsymbol{\beta}}} P_- \right] |\boldsymbol{\alpha}\rangle |\boldsymbol{\beta}\rangle\rangle \ , \tag{4.60}$$

where $P_\pm$ are projection operators onto states with even and odd fermion parity respectively

$$P_\pm = \frac{1 \pm (-1)^F}{2} \ , \quad (-1)^F = \prod_{\ell=1}^{L} \prod_{\substack{\alpha=1 \\ \epsilon_\alpha = 1}}^{N+M} (1 - 2E_\ell^{\alpha\alpha})(1 - 2\widetilde{E}_\ell^{\alpha\alpha}). \tag{4.61}$$

Then, we have

$$(-1)^F |\boldsymbol{\alpha}\rangle |\boldsymbol{\beta}\rangle\rangle = (-1)^{\epsilon_{\boldsymbol{\alpha}} + \epsilon_{\boldsymbol{\beta}}} |\boldsymbol{\alpha}\rangle |\boldsymbol{\beta}\rangle\rangle. \tag{4.62}$$

Inserting the modified Lindblad superoperator (4.59) and the vectorised density matrix (4.60) into the equation for the Lindblad time evolution (4.54), we can again expand it in terms of components and recover precisely the correct Lindblad behaviour (4.50) as required. It is worth emphasising that in our construction both bosonic and fermionic jump operators can be accommodated as long as any given jump operator has a definite fermion parity.

4.5 Superoperator Lindblad Structure

Analysing the superoperator Liouvillian (4.55), we can differentiate between two types of terms, depending on their action onto the superspace $\mathcal{H}_S = \mathcal{H}_L \otimes \mathcal{H}_L$. Terms with solely left- or right-acting operators act only on one copy of the original Hilbert space $\mathcal{H}_L$, whereas terms which involve both types of operators act non-trivially on the entire Liouville space $\mathcal{H}_S$. We identify this structure as a "two-legged ladder". In this interpretation, each leg of the ladder corresponds to one copy of the original Hilbert space. Terms with only one type of superoperators are

$$-iH - \sum_a \frac{\gamma_a}{2} L_a^\dagger L_a \quad \text{and} \quad i\bar{H} - \sum_a \frac{\gamma_a}{2} \overline{L_a^\dagger L_a} \ , \tag{4.63}$$

and they act only on one leg of the ladder. The remainder of the Liouvillian has the form

$$\sum_a \gamma_a L_a \bar{L}_a^\dagger \tag{4.64}$$

and acts on the rungs of the ladder, meaning both copies of the original Hilbert space.

Having identified this structure, we want to find compatible Hamiltonians which are Yang-Baxter integrable. To this end, we have analysed the specific restrictions imposed by the Lindblad equation onto the form of the ladder and checked whether any of the large number of integrable Hamiltonians can be cast in the particular form of the vectorised Lindbladian (4.55). We are interested in Liouvillians with local interactions as the most experimentally feasible examples. We then consider Hamiltonians and jump operators acting either on a single site or on a single bond between the nearest-neighbour sites of a 1D lattice with periodic boundary conditions. Making an ansatz for a most general form of operators compatible with these assumptions, we derived constraints on integrable Hamiltonians which might have a Lindblad equivalent. Graphically, the interactions we investigated are shown in Figure 4.2. Single leg terms, as defined in (4.63), specify only the single site occupation energy u and a bond interaction within a leg, $J_=$. The rung terms (4.64) affect not only two-site interactions between the legs $J_{||}$ and J_X, but also plaquette interactions involving three or four sites, U_3 and U_4 respectively.

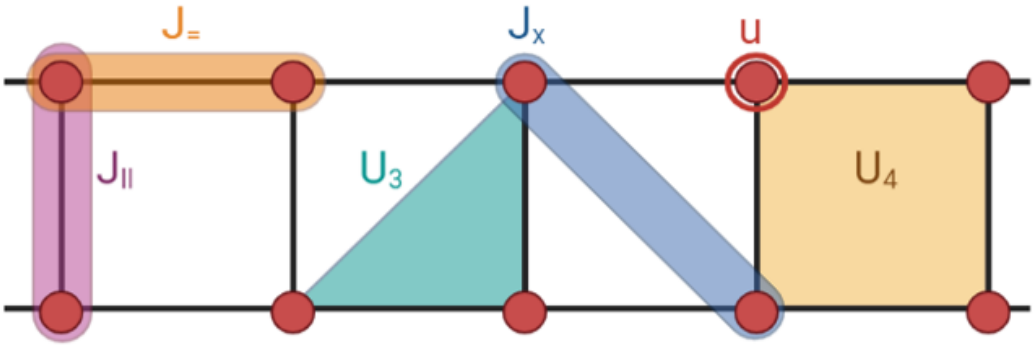


Figure 4.2: Ladder interactions accommodated by a Liouvillian with single-site and single-bond jump operators [94].

4.5.1 Single-Site Jump Operators

In translationally invariant situations the most general single-site jump operator can be written in the form

$$\ell_j = \sum_{\alpha,\beta} \lambda_{\alpha\beta} E_j^{\alpha\beta} \ , \tag{4.65}$$

where the sum is restricted so that the resultant jump operator has a definite fermion parity. In the case of a bosonic jump operator, subscripts on the coefficient matrix $\lambda_{\alpha\beta}$ can only be such that both $\epsilon_\alpha, \epsilon_\beta$ are 0 or 1. For a fermionic jump operator, ϵ_α and ϵ_β must have different values. The "interaction terms" generated in this way are of the form

$$\ell_j \overline{\ell_j^\dagger} = \sum_{\alpha\beta}{}' \sum_{\gamma\delta}{}' \lambda_{\alpha\beta}\ \lambda^*_{\gamma\delta}\ E_j^{\alpha\beta} \widetilde{E}_j^{\gamma\delta} \tag{4.66}$$

if the jump operator is bosonic and

$$\ell_j \overline{\ell_j^\dagger} = (-i) \sum_{\alpha\beta}{}'' \sum_{\gamma\delta}{}'' \lambda_{\alpha\beta}\ \lambda^*_{\gamma\delta}\ E_j^{\alpha\beta} \widetilde{E}_j^{\gamma\delta} \tag{4.67}$$

if it is fermionic. Here, the sums $\sum', \sum''$ imply respectively bosonic and fermionic constraints on the coefficients. $\lambda_{\alpha\beta}$ in the expressions for fermionic and bosonic interaction terms differ between each other because of these parity constraints. Furthermore, we obtain "generalized magnetic field terms", each acting on one of the two legs

$$\ell_j^\dagger \ell_j + \overline{\ell_j^\dagger \ell_j} = \sum_{\alpha,\beta,\gamma}{}' \left(\lambda^*_{\alpha\beta} \lambda_{\alpha\gamma} E_j^{\beta\gamma} + \lambda^*_{\alpha\gamma} \lambda_{\alpha\beta} \widetilde{E}_j^{\beta\gamma} \right) + \sum_{\alpha,\beta,\gamma}{}'' \left(\lambda^*_{\alpha\beta} \lambda_{\alpha\gamma} E_j^{\beta\gamma} + \lambda^*_{\alpha\gamma} \lambda_{\alpha\beta} \widetilde{E}_j^{\beta\gamma} \right) . \tag{4.68}$$

Comparing to the graphical representation in Figure 4.2, the single site jump operators affect only the interactions labelled with u and $J_{||}$.

4.5.1.1 2-State Fermionic Example

To visualise how restrictive the Lindblad structure is, consider a 2-state local Hilbert space for an open problem with one degree of freedom bosonic and one fermionic. The former can be identified with a vacuum state and the latter with a spinless fermion particle. The most general form of single-site jump operators one can obtain in this scenario are

$$\begin{aligned} b_j &= \lambda_{22} E_j^{22} \ , \\ f_j &= \lambda_{12} E_j^{12} + \lambda_{21} E_j^{21} \ , \end{aligned} \tag{4.69}$$

with rates γ_b and γ_f respectively. λ_{11} was omitted due to contributing only a constant term and thus cancelling in the Lindblad equation. In the vectorised form, the E-matrices can be mapped onto canonical spin-1/2 fermion creation and annihilation operators via a map

$$E_j^{11} \to 1 - n_{j,\uparrow} \ , \quad E_j^{22} \to n_{j,\uparrow} \ , \quad E_j^{12} \to c_{j,\uparrow}^\dagger \ , \quad E_j^{21} \to c_{j,\uparrow} \ , \tag{4.70}$$

with $\tilde{E}$-operators being mapped onto analogous spin down fermionic operators. The local density operator is defined as $n_{j,\sigma} = c^{\dagger}_{j,\sigma} c_{j,\sigma}$. The vectorised Liouvillain contains interactions

$$\begin{aligned}\hat{\mathcal{L}} = \sum_j & \gamma_b |\lambda_{22}|^2 n_{j,\uparrow} n_{j,\downarrow} - i\gamma_f \left(\lambda_{12} c^{\dagger}_{j,\uparrow} + \lambda_{21} c_{j,\uparrow}\right)\left(\lambda^*_{12} c^{\dagger}_{j,\downarrow} + \lambda^*_{21} c_{j,\downarrow}\right) \\ & + \left(\gamma_b |\lambda_{22}|^2 - \frac{\gamma_f}{2}|\lambda_{21}|^2 + \frac{\gamma_f}{2}|\lambda_{12}|^2\right)(n_{j,\uparrow} + n_{j,\downarrow}) - \gamma_f |\lambda_{12}|^2\end{aligned} \tag{4.71}$$

Here, the two-legged ladder structure is "folded" into a single chain in which the two copies of the original Hilbert space are identified with an internal degree of freedom and represented as spin-1/2 orientations. Single-site jump operators give rise to two- and four-body interactions. The Hubbard interaction $n_{j,\uparrow} n_{j,\downarrow}$ is completely independent from other four-point interactions, whereas the nearest neighbour spin flips as well as pair creation and pair annihilation terms are interdependent and can be manipulated only via two distinct parameters. Presence of each of these interactions implies an accompanying particle number operator term $N = \sum_j (n_{j,\uparrow} + n_{j,\downarrow})$.

4.5.2 Single-Bond Jump Operators

The most general bosonic jump operator acting on a bond between nearest neighbour sites takes the form

$$L_j = {\sum_{\alpha,\beta}}' \left(\lambda_{\alpha\beta} E^{\alpha\beta}_j + \lambda'_{\alpha\beta} E^{\alpha\beta}_{j+1}\right) + {\sum_{\alpha,\beta,\gamma,\delta}}' \mu_{\alpha\beta\gamma\delta}\ E^{\alpha\beta}_j E^{\gamma\delta}_{j+1}\ , \tag{4.72}$$

where the sums are restricted to ensure a definite parity of the jump operator. The extension to fermionic jump operators requires a different restriction on the sum and introduces only an additional phase in the final Lindblad equation. A single-bond jump operator gives rise to quartic, cubic and quadratic "interaction terms" between the two legs of the ladder

$$L_j \overline{L^{\dagger}_j} = \mathcal{I}^{(2)}_j + \mathcal{I}^{(3)}_j + \mathcal{I}^{(4)}_j\ , \tag{4.73}$$

where $\mathcal{I}^{(n)}_j$ involves n Hubbard operators $E^{\alpha\beta}_j$, $\widetilde{E}^{\alpha\beta}_j$. In relation to Figure 4.2, $\mathcal{I}^{(2)}_j$ contributes to the $J_{||}$ and J_X interactions, whereas $\mathcal{I}^{(3)}_j, \mathcal{I}^{(4)}_j$ determine the plaquette interactions U_3, U_4 respectively. The interaction along a single rung of the ladder arising from a single-bond jump operator is

$$\begin{aligned}\mathcal{I}^{(2)}_j = {\sum_{\substack{\alpha_1\beta_1 \\ \alpha_2\beta_2}}}' \Big(& \lambda_{\alpha_1\beta_1} \lambda^*_{\alpha_2\beta_2} E^{\alpha_1\beta_1}_j \widetilde{E}^{\alpha_2\beta_2}_j + \lambda_{\alpha_1\beta_1} \lambda'^*_{\alpha_2\beta_2} E^{\alpha_1\beta_1}_j \widetilde{E}^{\alpha_2\beta_2}_{j+1} \\ & + \lambda'_{\alpha_1\beta_1} \lambda^*_{\alpha_2\beta_2} E^{\alpha_1\beta_1}_{j+1} \widetilde{E}^{\alpha_2\beta_2}_j + \lambda'_{\alpha_1\beta_1} \lambda'^*_{\alpha_2\beta_2} E^{\alpha_1\beta_1}_{j+1} \widetilde{E}^{\alpha_2\beta_2}_{j+1} \Big)\ ,\end{aligned} \tag{4.74}$$

while the three and four point interactions on a given plaquette are given by

$$\begin{aligned}
\mathcal{I}_j^{(3)} &= \sum_{\substack{\alpha_1\beta_1\gamma_1\delta_1\\ \alpha_2\beta_2}}{}' \mu_{\alpha_1\beta_1\gamma_1\delta_1} E_j^{\alpha_1\beta_1} E_{j+1}^{\gamma_1\delta_1} \left(\lambda^*_{\alpha_2\beta_2} \widetilde{E}_j^{\alpha_2\beta_2} + \lambda'^*_{\alpha_2\beta_2} \widetilde{E}_{j+1}^{\alpha_2\beta_2}\right) \\
&+ \sum_{\substack{\alpha_1\beta_1\\ \alpha_2\beta_2\gamma_2\delta_2}}{}' \mu^*_{\alpha_2\beta_2\gamma_2\delta_2} \left(\lambda_{\alpha_1\beta_1} E_j^{\alpha_1\beta_1} + \lambda'_{\alpha_1\beta_1} E_{j+1}^{\alpha_1\beta_1}\right) \widetilde{E}_j^{\alpha_2\beta_2} \widetilde{E}_{j+1}^{\gamma_2\delta_2} \ , \\
\mathcal{I}_j^{(4)} &= \sum_{\substack{\alpha_1\beta_1\gamma_1\delta_1\\ \alpha_2\beta_2\gamma_2\delta_2}}{}' \mu_{\alpha_1\beta_1\gamma_1\delta_1} \mu^*_{\alpha_2\beta_2\gamma_2\delta_2} E_j^{\alpha_1\beta_1} E_{j+1}^{\gamma_1\delta_1} \widetilde{E}_j^{\alpha_2\beta_2} \widetilde{E}_{j+1}^{\gamma_2\delta_2} \ . \qquad (4.75)
\end{aligned}$$

There are also interaction terms along the two legs of the ladder

$$\begin{aligned}
L_j^\dagger L_j &= \sum_{\beta\gamma}{}' \big[\big(\sum_\alpha{}' \lambda_{\alpha\beta} \lambda^*_{\alpha\gamma} \big) E_j^{\gamma\beta} + \big(\sum_\alpha{}' \lambda'_{\alpha\beta} \lambda'^*_{\alpha\gamma} \big) E_{j+1}^{\gamma\beta} \big] + \sum_{\alpha\beta\gamma\delta}{}' \big[f_{\alpha\beta\gamma\delta} E_j^{\alpha\beta} E_{j+1}^{\gamma\delta} + \text{h.c.} \big] \ , \\
\overline{L_j^\dagger L_j} &= \sum_{\beta\gamma}{}' \big[\big(\sum_\alpha{}' \lambda^*_{\alpha\beta}{}' \lambda_{\alpha\gamma} \big) \widetilde{E}_j^{\gamma\beta} + \big(\sum_\alpha{}' \lambda'^*_{\alpha\beta} \lambda'_{\alpha\gamma} \big) \widetilde{E}_{j+1}^{\gamma\beta} \big] + \sum_{\alpha\beta\gamma\delta}{}' \big[f_{\beta\alpha\delta\gamma} \widetilde{E}_{j+1}^{\gamma\delta} \widetilde{E}_j^{\alpha\beta} + \text{h.c.} \big] \ , \qquad (4.76)
\end{aligned}$$

where

$$f_{\alpha\beta\gamma\delta} = \lambda^*_{\beta\alpha} \lambda'_{\gamma\delta} + \sum_\eta{}' \big[\lambda^*_{\eta\alpha} \mu_{\eta\beta\gamma\delta} + \lambda'^*_{\eta\gamma} \mu_{\alpha\beta\eta\delta} \big] + \frac{1}{2} \sum_{\eta\nu}{}' (-1)^{(\epsilon_\alpha+\epsilon_\beta)(\epsilon_\eta+\epsilon_\gamma)} \mu_{\nu\beta\eta\delta} \mu^*_{\nu\alpha\eta\gamma} \ . \qquad (4.77)$$

A 2-state fermionic example of this structure can be found in Appendix C.

4.5.3 Single-Bond Hamiltonian

The most general Hermitian Hamiltonian acting on a bond between nearest neighbour sites takes the form

$$\mathscr{H}_j = \sum_{\alpha,\beta}{}' \left(\chi_{\alpha\beta} E_j^{\alpha\beta} + \chi'_{\alpha\beta} E_{j+1}^{\alpha\beta} \right) + \sum_{\alpha,\beta,\gamma,\delta}{}' \xi_{\alpha\beta\gamma\delta} \ E_j^{\alpha\beta} E_{j+1}^{\gamma\delta} \ , \qquad (4.78)$$

where the sums are restricted to ensure that every term in the expansion is bosonic. We consider only Hamiltonians with local densities such that $H = \sum_j \mathscr{H}_j$. The Hamiltonian part of an open problem does not give rise to any "interaction terms", but solely to terms along each leg of the ladder. The coherent evolution part of the superoperator Liouvillian is of a form

$$\begin{aligned}
-i(\mathscr{H}_j - \widetilde{\mathscr{H}}_j) = &- i \sum_{\alpha,\beta}{}' \chi_{\alpha\beta} (E_j^{\alpha\beta} - \widetilde{E}_j^{\beta\alpha}) + \chi'_{\alpha\beta} (E_{j+1}^{\alpha\beta} - \widetilde{E}_{j+1}^{\beta\alpha}) \\
&- i \sum_{\alpha,\beta,\gamma,\delta}{}' \xi_{\alpha\beta\gamma\delta} \ (E_j^{\alpha\beta} E_{j+1}^{\gamma\delta} - \widetilde{E}_{j+1}^{\delta\gamma} \widetilde{E}_j^{\beta\alpha}) \ . \qquad (4.79)
\end{aligned}$$

In terms of spin-1/2 fermions, Hamiltonian can contribute only to on-site density operators, nearest-neighbour density interactions and nearest-neighbour hopping along the legs of the ladder. These are marked with u and $J_=$ in Figure 4.2.

4.5.4 Single-Bond Liouvillian

The vectorised Lindblad equation combines the Hamiltonian time evolution with the dissipative part. There is a parameter freedom in taking this linear combination through the dissipative rates γ_a as defined in (4.59), with a constraint that the rates are always real and non-negative. An added complication is that we should allow for general similarity transformations

$$\mathcal{L}' = S\mathcal{L}S^{-1}. \tag{4.80}$$

The spatial locality of the Hamiltonian density of the various integrable models imposes strong restrictions on the possible form of the transformation S, yet incorporating this parameter freedom into our discussion turned out not to be practical. In particular, transformations of the form

$$S = \prod_{j=1}^{L} S_j \ , \tag{4.81}$$

where S_j acts non-trivially only on site j are always compatible with the aforementioned local structure and should also be considered. A systematic way of implementing the similarity parameter freedom is to examine symmetries of the Yang-Baxter equation, as outlined in Chapter 12.2.5 in [74]. For example, given an R-matrix solution of the Yang-Baxter equation $R(\lambda, \mu) \in \mathcal{E}nd(C \otimes C)$, other solutions can be obtained as

$$\big[V(\mu) \otimes V(\lambda)\big] R(\lambda, \mu) \big[V^{-1}(\lambda) \otimes V^{-1}(\mu)\big], \tag{4.82}$$

where $V(\lambda)$ is an invertible $n \times n$ matrix. The resultant Hamiltonian will generally be non-Hermitian, but this is not a problem in the context of Lindblad equations.

4.6 Integrable Lindbladians

4.6.1 Generalized Hubbard Models

The mathematical structure that underlies the integrability of the Hubbard model leads to a connection with a Lindblad equation in a particularly clear manner. The Hubbard model was embedded into the general framework of the QISM [70] in seminal work by Shastry [245, 246]. This construction was subsequently generalized to other classes of integrable models [247–251]. Let us consider a free fermionic R-matrix $r_{jk}(\lambda)$ of a n-dimensional XX model. $r_{jk}(\lambda)$ acts on the tensor product of two graded

linear vector spaces $V \otimes V$ (labelled by j and k respectively) and depends on a spectral parameter λ. An explicit expression for $r_{jk}(\lambda)$ is given by

$$r_{jk}(\lambda) = \left[\cos^2\left(\frac{\lambda}{2}\right) - \sin^2\left(\frac{\lambda}{2}\right) C_j C_k\right] \Pi_{jk} + \frac{\sin(\lambda)}{2}\left[I - C_j C_k\right] \ , \tag{4.83}$$

where Π_{jk} is a graded permutation operator (4.33) acting on $V \otimes V$ and

$$C_j = 2\hat{\pi}_j - 1 \tag{4.84}$$

is a conjugation matrix acting on one copy of the vector space V (labelled with j) with $\hat{\pi}_j$ being a projection operator onto its subspace. Following [74, 249, 250], we constructed a generalised Hubbard model R-matrix from two copies of the free fermionic R-matrix. Without an interaction term, the new R-matrix operator is

$$\hat{R}_{jk}(\lambda) = r_{jk}(\lambda)\tilde{r}_{jk}(\lambda) \ , \tag{4.85}$$

where operators with and without a tilde act on two disjoint copies of the original vector space. As a result, $\hat{R}_{jk}(\lambda)$ acts on an enlarged vector space formed by taking a graded tensor product of two copies of the original vector space. In this case, the R-matrix fulfils not only the Yang-Baxter equation

$$\hat{R}_{12}(u-v)\hat{R}_{13}(u)\hat{R}_{23}(v) = \hat{R}_{23}(v)\hat{R}_{13}(u)\hat{R}_{12}(u-v) \ , \tag{4.86}$$

but also the "decorated" Yang-Baxter relation

$$\hat{R}_{12}(u+v)C_1\tilde{C}_1\hat{R}_{13}(u)\hat{R}_{23}(v) = \hat{R}_{23}(v)\hat{R}_{13}(u)\tilde{C}_1 C_1 \hat{R}_{12}(u+v) \ . \tag{4.87}$$

Consider taking a linear combination of the Yang-Baxter and the decorated Yang-Baxter equation in order to obtain from it a new Yang-Baxter relation

$$\begin{aligned} \left\{\alpha\hat{R}_{12}(u-v) + \beta\hat{R}_{12}(u+v)C_1\tilde{C}_1\right\}\hat{R}_{13}(u)\hat{R}_{23}(v) = \\ \hat{R}_{23}(v)\hat{R}_{13}(u)\left\{\alpha\hat{R}_{12}(u-v) + \beta\tilde{C}_1 C_1 \hat{R}_{12}(u+v)\right\} \ , \end{aligned} \tag{4.88}$$

with α, β being free parameters. This expression is fulfilled by a new R-matrix "glued" from two copies of the original, free-fermionic ones

$$R_{jk}(u,v) = \alpha\hat{R}_{jk}(u-v) + \beta\hat{R}_{jk}(u+v)C_j\tilde{C}_j \ . \tag{4.89}$$

To determine the appropriate coefficients, we need to consider an additional constraint in the form of the Yang-Baxter relation with an appropriate Lax operator

$$R_{12}(u,v)L_{a1}(u)L_{a2}(v) = L_{a2}(v)L_{a1}(u)R_{12}(u,v) \ . \tag{4.90}$$

In this case, the Lax operator has the form

$$L_{jk}(u) = \hat{R}_{jk}(u)e^{-h(u)C_j\tilde{C}_j} \ , \tag{4.91}$$

where $h(u)$ is a free parameter which depends on the spectral parameter u. Combining the constraints (4.88) and (4.90), we obtain the R-matrix of an integrable generalized Hubbard model

$$R_{jk}(u,v) = r_{jk}(u-v)\tilde{r}_{jk}(u-v) + \alpha(u,v)r_{jk}(u+v)C_j\tilde{r}_{jk}(u+v)\tilde{C}_j \ . \tag{4.92}$$

Here, the function $\alpha(\lambda,\mu)$ is given by

$$\alpha(\lambda,\mu) = \frac{\cos(\lambda-\mu)\sinh\big(h(\lambda)-h(\mu)\big)}{\cos(\lambda+\mu)\cosh\big(h(\lambda)-h(\mu)\big)} \ , \tag{4.93}$$

where $h(\lambda)$ is a solution of the equation

$$\sinh\big(2h(\lambda)\big) = U\sin(2\lambda) \ . \tag{4.94}$$

The local conserved charges of the model can then be computed in a standard fashion by taking derivatives of the transfer matrix. In particular, the Hamiltonian density can be obtained from

$$\begin{aligned} H_{jk} &= \frac{d}{d\lambda}\bigg|_{\lambda=u_0} \Pi_{jk}\widetilde{\Pi}_{jk}R_{jk}(\lambda,u_0) \\ &= \Pi_{jk}r'_{jk}(0) + \widetilde{\Pi}_{jk}\tilde{r}'_{jk}(0) + \alpha'(u_0,u_0)\Pi_{jk}r_{jk}(2u_0)C_j\widetilde{\Pi}_{jk}\tilde{r}_{jk}(2u_0)\tilde{C}_j \ , \end{aligned} \tag{4.95}$$

where primed quantities indicate a derivative with respect to the spectral parameter. This construction is a generalised version of [249] with the logarithmic derivative of the transfer matrix being taken at a shift-point u_0 following [252, 253]. This gives an additional parameter freedom in the resultant Hamiltonian. The Hamiltonian structure (4.95) is such that it always can be related to a Liouvillian of the Lindblad form. The two-legged ladder form becomes apparent when comparing the generalised Hubbard models to the vectorised Lindblad equation (4.55). Similarly to the Liouvillian, the generalised Hubbard Hamiltonians contain two types of terms. Terms involving only tilde or non-tilde operators in (4.95) can be identified with the single-leg ladder terms in the Lindblad description. Meanwhile, products between the two types of operators resemble the rung ladder terms.

4.6.2 $SU(2)$ Hubbard Model

The simplest example of the family of generalised Hubbard models is the $SU(2)$ Hubbard model which in terms of Hubbard operators takes a form

$$H(U) = -t\sum_j \left(e_j^{21}e_{j+1}^{12} + \widetilde{e}_j^{21}\widetilde{e}_{j+1}^{12} + \text{h.c.}\right) + U\sum_j \left(e_j^{22} - \frac{1}{2}\right)\left(\widetilde{e}_j^{22} - \frac{1}{2}\right) \ . \quad (4.96)$$

This is the first example of a Lindblad equation that was related to an interacting Yang-Baxter integrable model [227] as described in subsection 4.3.1. It can be incorporated into our vectorisation scheme by considering an open system consisting of a tight-binding model Hamiltonian

$$H_0 = -t\sum_j e_j^{12}e_{j+1}^{21} + \text{h.c.} \ , \quad (4.97)$$

coupled to an environment by jump operators

$$L_j = e_j^{22} \ . \quad (4.98)$$

In the superoperator formalism (4.55) the corresponding Liouvillian is

$$\mathcal{L}(\gamma) = it\sum_j [e_j^{12}e_{j+1}^{21} - \widetilde{e}_j^{12}\widetilde{e}_{j+1}^{21} + \text{h.c.}] + \sum_j \gamma\left[e_j^{22}\widetilde{e}_j^{22} - \frac{1}{2}(e_j^{22} + \widetilde{e}_j^{22})\right] \ . \quad (4.99)$$

This is related to the Hubbard Hamiltonian by

$$\mathcal{L}(\gamma) = -i\mathcal{U}^\dagger H(i\gamma)\mathcal{U} - \frac{\gamma L}{4} \ , \quad \mathcal{U} = \prod_{j=1}^{L/2}(\tilde{e}_{2j}^{11} - \tilde{e}_{2j}^{22}) \ . \quad (4.100)$$

Particularly significant is the presence here of a purely imaginary Hubbard interaction strength $U = i\gamma$, which turns out to be required for mappings between the generalised Hubbard models and Lindbladians in general. Since a Liouvillian is a non-Hermitian operator, via a unitary transformation it can be mapped only onto another non-Hermitian operator. This has profound consequences for the structure of the eigenstates, which is described in more detail in subsection 4.6.4.5.

4.6.2.1 Quench Dynamics

Quantum quench protocols, described in subsection 2.5.1, are a useful tool in investigating the non-equilibrium dynamics in open quantum systems. However, the theoretical picture of the information spreading is substantially more complicated in the presence of dissipation and there exists no general theoretical framework for

studying it. Only recently, there has been an attempt to incorporate the entanglement spreading in Markovian open systems into the quasiparticle framework in the case of free models [254]. Ultimately, the correlation functions are the main object of interest in the experiments. Hence, we add here a short discussion of the quench dynamics in the tight-binding model with a dephasing noise, which helps us to visualise some more physical properties of the model. To our knowledge, this has not been published before.

Let us consider the time evolution equation for a general n-point function in a Lindblad system written in the E-matrix basis

$$\frac{d}{dt}\langle E_{a_1}^{\alpha_1\beta_1} E_{a_2}^{\alpha_2\beta_2} \dots E_{a_n}^{\alpha_n\beta_n}\rangle = \mathrm{Tr}\left[\mathcal{L}(\rho) E_{a_1}^{\alpha_1\beta_1} E_{a_2}^{\alpha_2\beta_2} \dots E_{a_n}^{\alpha_n\beta_n}\right] \ . \tag{4.101}$$

Importantly, the E-matrices are locally orthonormal

$$\mathrm{Tr}\left\{E_j^{\alpha\beta}(E_j^{\mu\nu})^\dagger\right\} = \delta_{\alpha\mu}\delta_{\beta\nu} \ . \tag{4.102}$$

In conjunction with the density matrix decomposition in the Hubbard operator basis (4.49), we use this property to identify which "strings" of E-matrices $E_{a_1}^{\alpha_1\beta_1} E_{a_2}^{\alpha_2\beta_2} \dots E_{a_n}^{\alpha_n\beta_n}$, after being acted upon by the Liouville superoperator, will have diagonal elements and contribute non-trivially to the trace. Such considerations simplify the task of computing the equations of motion for correlators.

More specifically, consider a chain of N spinless fermions with a periodic boundary conditions Hamiltonian

$$H = \sum_{j=1}^{N} \left[a_j^\dagger a_{j+1} + a_{j+1}^\dagger a_j + \Delta(a_j^\dagger a_{j+1}^\dagger + a_j a_{j+1})\right] \ . \tag{4.103}$$

Initially, the system is prepared in a ground state of $H(\Delta)$. At time $t = 0$ the quench parameter Δ is set to zero and bulk-coupled dissipation is introduced through local dephasing jump operators $L_j = \sqrt{2\gamma} a_j^\dagger a_j$ acting on every site of the chain. The system is initialised out-of-equilibrium and dissipatively relaxes to a steady state. To investigate the thermalisation process, we examined the dynamics of one-particle Green's functions

$$F_{kl} = \langle a_k^\dagger a_l\rangle \quad \text{and} \quad G_{kl} = \langle a_k a_l\rangle \tag{4.104}$$

under the Lindblad evolution. The system considered is translationally invariant and thus depends only on the separation between the sites within a chain, $F_{kl} \equiv F_{k-l}$ and

$G_{kl} \equiv G_{k-l}$. Direct computation of the time evolution of these correlators leads to equations of motion

$$\frac{d}{dt}F_s(t) = -2\gamma F_s(t)(1-\delta_{s,0}) \ , \tag{4.105}$$

$$\frac{d}{dt}G_d(t) = -2i(G_{d-1}(t)+G_{d+1}(t)) - 2\gamma G_d(t) \ . \tag{4.106}$$

For zero separation, $F_0(t) = F_0(0)$ is a constant and $G_0(t) = 0$ disappears by anti-symmetry. Subsequently, we Fourier transformed the equations of motion in order to diagonalise them. The Fourier transform is defined to be

$$F_s = \frac{1}{N}\sum_{q=0}^{N-1} e^{2\pi iqs/N}\tilde{F}_q \ , \tag{4.107}$$

where $\frac{2\pi q}{N} = Q$ is the quantised momentum. The inverse Fourier transform is

$$\tilde{F}_Q = \sum_{s=0}^{N-1} e^{iQs}F_s \ . \tag{4.108}$$

Following [86], the initial conditions for the Fourier transformed Green's functions were taken to be the expectations values of the correlators in question in the ground state of $H(\Delta)$

$$\tilde{F}_Q(t=0) = \frac{1}{2}\left[1 + \frac{\cos Q}{\sqrt{\cos Q^2 + \Delta^2 \sin Q^2}}\right] \ , \tag{4.109}$$

$$\tilde{G}_Q(t=0) = \frac{i\Delta \sin Q}{2\sqrt{\cos Q^2 + \Delta^2 \sin Q^2}} \ . \tag{4.110}$$

We numerically examined the analytic expressions for the time dependence of the one-particle Green's functions using the MATHEMATICA software. Their time evolution with and without dissipation is shown in Figures 4.3 -4.8.

In Figures 4.3-4.4, data points at $s = 0$ for the F_{kl} correlator give a very large and constant in time contribution regardless of dissipation. These points were removed from the figures for clarity of presentation. In the absence of dissipation, the F_{kl} correlator in Figure 4.3 has no time dependence for all separation values. Therefore, the spatially symmetric initial state remains as such at later times and the Green's function remains real. Non-zero magnitude of correlation appears here only for odd values of separation. The presence of dissipation introduces exponential suppression of the correlator's magnitude for separations $s \neq 0$, as shown in Figure 4.4.

For the G_{kl} Green's function, the results are separated into the real and imaginary parts of the Green's function in Figures 4.5, 4.7 and 4.6, 4.8 respectively. In these

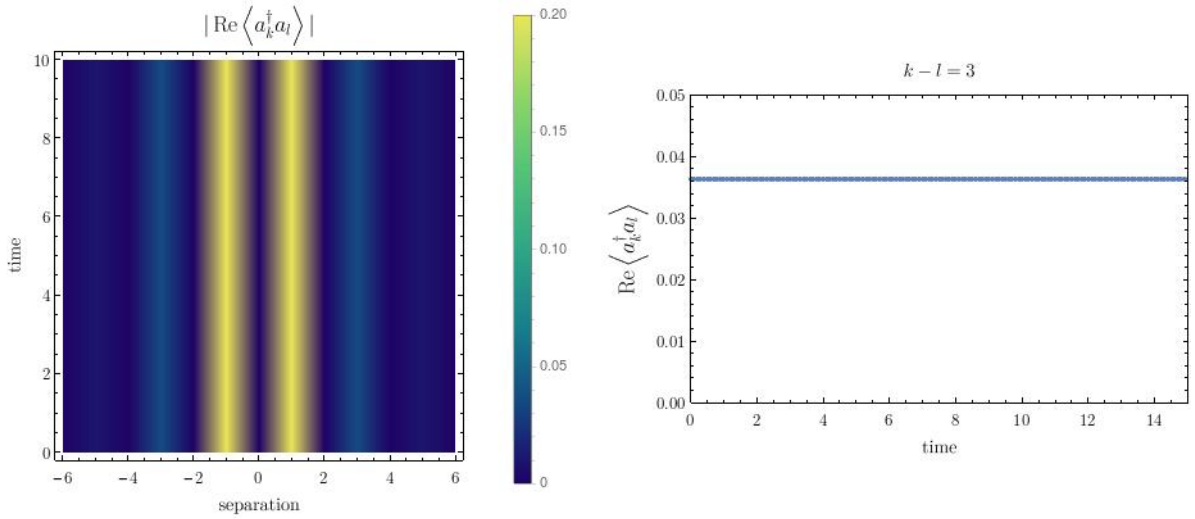


Figure 4.3: Quench dynamics of $\mathrm{Re}\,[F_{k-l}(t)]$. Non-zero correlation appears only for odd separation values. No time-dependence is present.

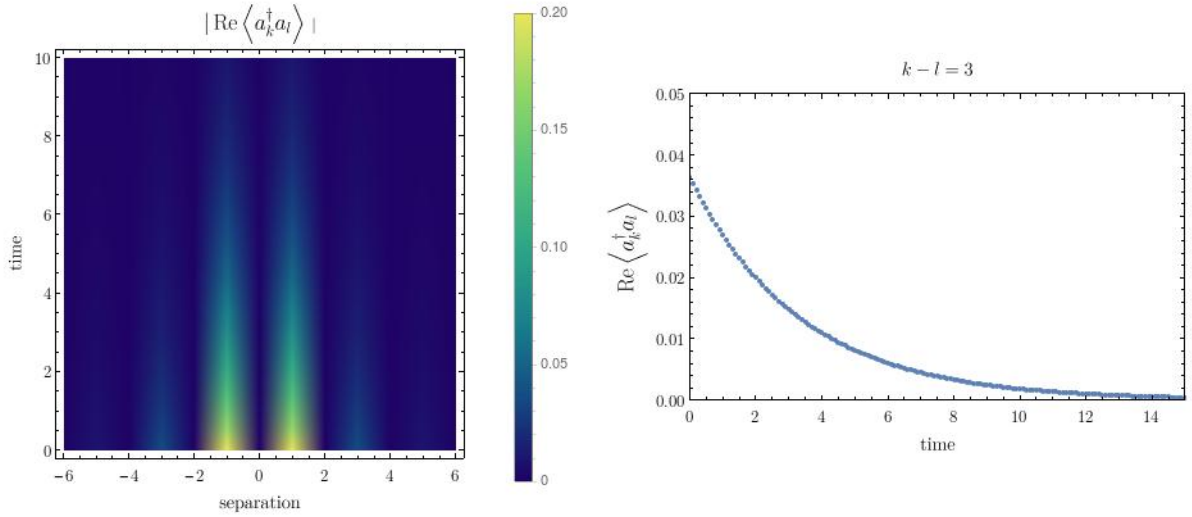


Figure 4.4: Quench dynamics of $\mathrm{Re}\,[F_{k-l}(t)]$ with additional dissipation. Non-zero correlation appears only for odd separation values. Dephasing introduces an exponential suppression of the Green's function's magnitude.

plots an absolute value is taken for clarity of presentation. The actual magnitude is antisymmetric in space and takes both positive and negative values. The non-

zero magnitude of G_{kl} oscillates here between being purely real for odd values of separation and purely imaginary for even values. In all density plots the lightcone effect is clearly visible. As described in [86], immediately after the global quench the post-quench Hamiltonian creates fermionic quasiparticle excitations throughout the system. In this case, the correlations between them are exponentially small and they can be treated as free fermions. The quasiparticle propagation velocity is bounded by the maximal group velocity dictated by the post-quench Hamiltonian $H(0)$ and it determines the slope of the lightcone visible in Figures 4.5 - 4.8. Moreover, as advertised in equation (2.89), quantum interference effects are visible in both the dissipative and non-dissipative case. Similarly to F_{kl}, introduction of dissipation leads here to the exponential in time suppression of the function's magnitude, visible in Figures 4.7 and 4.8.

There is an important difference between the system with and without the dephasing present. For a closed system with a quadratic Hamiltonian, one-particle Green's functions determine all the higher-point correlators as a consequence of the Wick's theorem [255]. Conversely, when quadratic jump operators are present the two-particle and higher order Green's functions are expected to yield qualitatively different results. We computed the equation of motion for a two-particle Green's function $C_{klmn} = \langle a_k^\dagger a_l^\dagger a_m a_n \rangle$,

$$\begin{aligned}\frac{d}{dt}C_{klmn} =& i(C_{k+1,lmn} + C_{k-1,lmn} + C_{k,l+1,mn} + C_{k,l-1,mn} - C_{kl,m+1,n} - C_{kl,m-1,n} \\ &- C_{klm,n+1} - C_{klm,n-1}) + 2\gamma(\delta_{km} + \delta_{kn} + \delta_{lm} + \delta_{ln} - 2)C_{klmn} \ .\end{aligned} \tag{4.111}$$

Remarkably, the time evolution of a four-point correlator does not depend on the higher- point functions and an exact analytic computation is possible. Its behaviour remains to be investigated in future work.

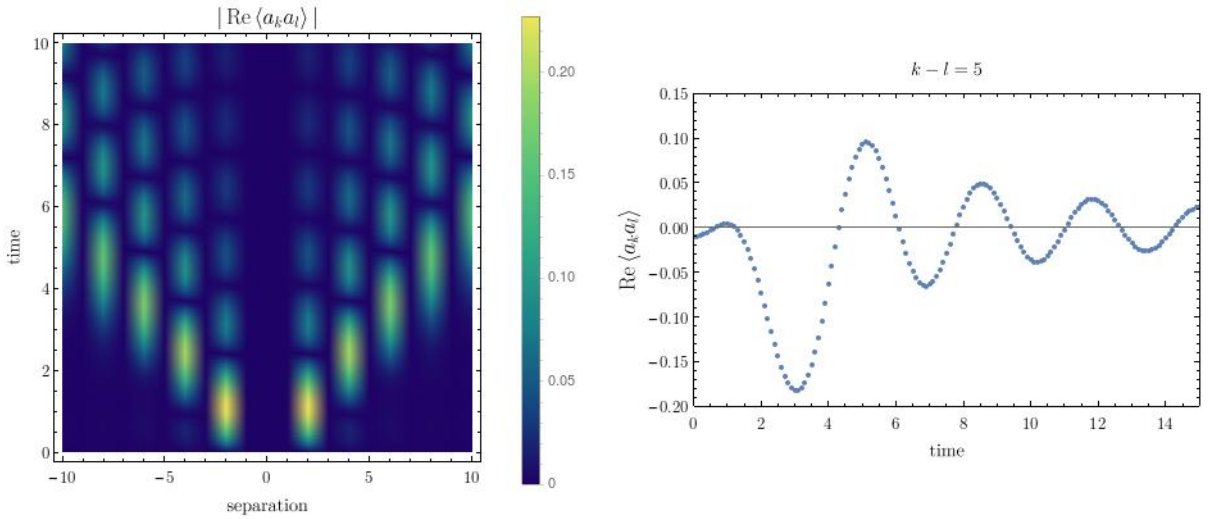


Figure 4.5: Quench dynamics of $\mathrm{Re}\,[G_{k-l}(t)]$. Non-zero correlation appears only for odd separation values. Time-dependent quantum interference effects are present.

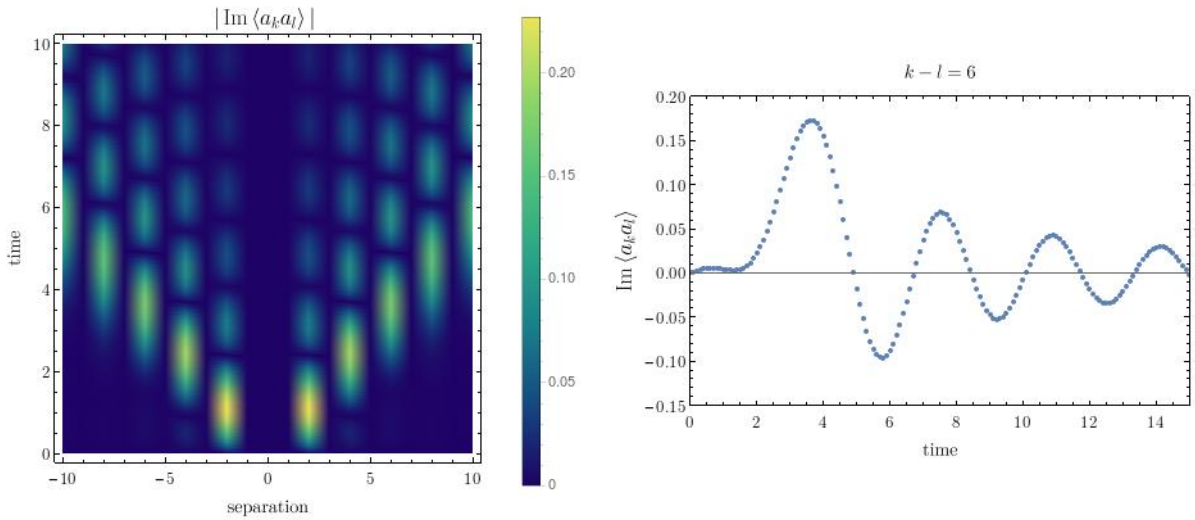


Figure 4.6: Quench dynamics of $\mathrm{Im}\,[G_{k-l}(t)]$. Non-zero correlation appears only for even separation values. Time-dependent quantum interference effects are present.

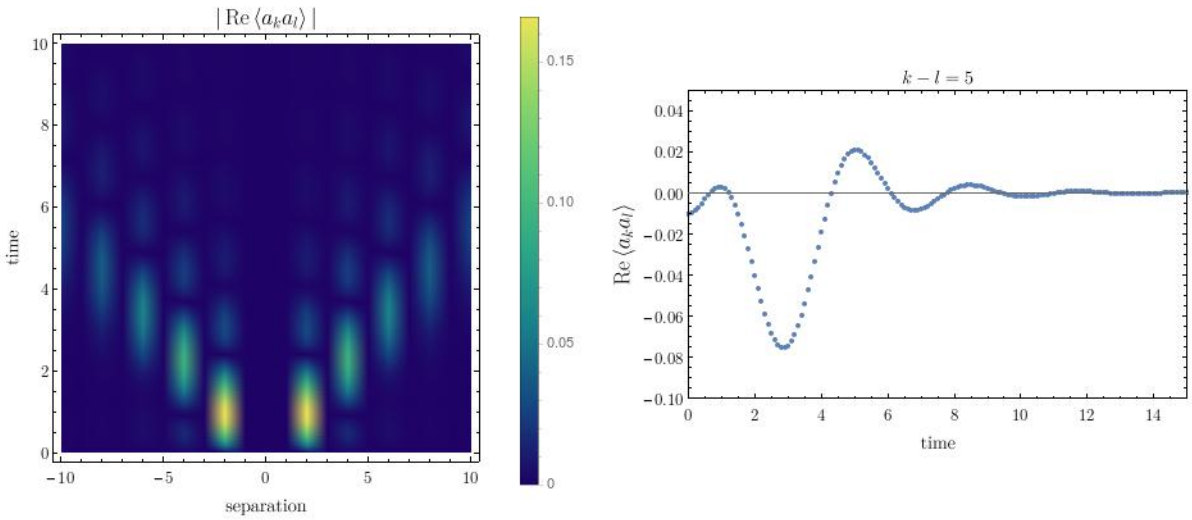


Figure 4.7: Quench dynamics of $\mathrm{Re}\,[G_{k-l}(t)]$ with additional dissipation. Non-zero correlation appears only for odd separation values. Time-dependent quantum interference effects are present, as well as an exponential suppression of the Green's function's magnitude due to dephasing.

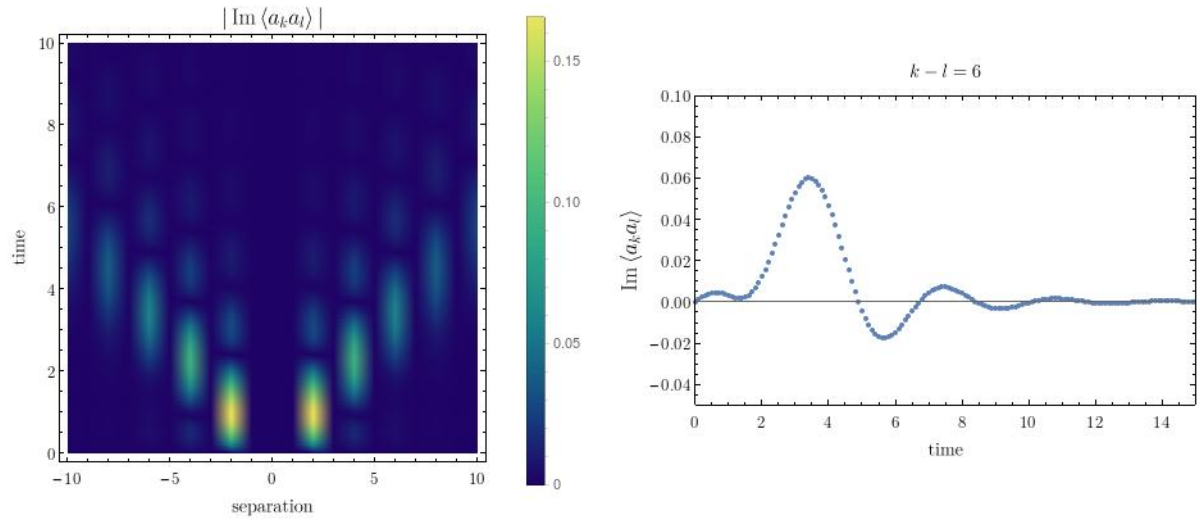


Figure 4.8: Quench dynamics of $\mathrm{Im}\,[G_{k-l}(t)]$ with additional dissipation. Non-zero correlation appears only for even separation values. Time-dependent quantum interference effects are present, as well as an exponential suppression of the Green's function's magnitude due to dephasing.

4.6.3 USW Model

As the first example of newly discovered integrable Lindbladians, we present a model which can be associated with the Umeno-Shiroishi-Wadati (USW) integrable Hamiltonian [253]. The USW model belongs to the family of generalised Hubbard models and can be derived from equation (4.95) by taking the Hubbard model R-matrix, with the logarithmic derivative evaluated at a non-zero value of the spectral parameter [252]. The Hamiltonian of this model is of the form

$$H_{\mathrm{USW}}(U) = -\sum_j \left[e_j^{21}e_{j+1}^{12} + \widetilde{e}_j^{21}\widetilde{e}_{j+1}^{12} + \mathrm{h.c.}\right] + \frac{U}{\cosh\left(2h(u_0)\right)}\sum_j B_{j,j+1}\tilde{B}_{j,j+1} \ , \tag{4.112}$$

where

$$B_{j,j+1} = \left[\cos^2(u_0)\left(e_j^{11} - e_j^{22}\right) - \sin^2(u_0)\left(e_{j+1}^{11} - e_{j+1}^{22}\right) + \sin(2u_0)\left(e_j^{21}e_{j+1}^{12} - e_{j+1}^{21}e_j^{12}\right)\right] \tag{4.113}$$

and $\tilde{B}_{j,j+1}$ is obtained from $B_{j,j+1}$ by replacing $e_n^{\alpha\beta} \to \tilde{e}_n^{\alpha\beta}$. Here, u_0 is a free (complex) parameter and the function $h(u)$ is fixed by the requirement

$$\sinh\left(2h(u_0)\right) = U\sin(2u_0) \ . \tag{4.114}$$

In comparison to the $SU(2)$ Hubbard model, additional structure appears in the terms associated with the ladder rung interactions, as expected from equation (4.95). Apart from the on-site density-density interaction, the USW model also features correlated hopping interactions. We note that the operators $e_j^{\alpha\beta}$ are related to spinful fermion creation and annihilation operators by

$$c_{j,\uparrow}^\dagger = e_j^{21} \ , \quad c_{j,\downarrow}^\dagger = \widetilde{e}_j^{21} \ , \quad n_{j,\uparrow} = e_j^{22} \ , \quad n_{j,\downarrow} = \widetilde{e}_j^{22} \ . \tag{4.115}$$

The Hamiltonian (4.112) is $SO(4)$ symmetric [253] and in particular commutes with the total particle number

$$\hat{N} = \sum_{j=1}^{L} e_j^{22} + \tilde{e}_j^{22}. \tag{4.116}$$

4.6.3.1 Associated Lindblad Equation

The USW model is related to a Lindblad equation with a tight-binding Hamiltonian

$$H_0 = -\sum_j e_j^{12}e_{j+1}^{21} + \mathrm{h.c.} \ , \tag{4.117}$$

and jump operators

$$L_j = B_{j,j+1}, \tag{4.118}$$

where the parameter u_0 is taken to be purely imaginary. In the superoperator formalism the corresponding Liouvillian (4.55) is

$$\mathcal{L}(\gamma) = i\sum_j \left[e_j^{12}e_{j+1}^{21} - \widetilde{e}_j^{12}\widetilde{e}_{j+1}^{21} + \text{h.c.}\right] + \gamma\sum_j \left[B_{j,j+1}\tilde{B}^*_{j,j+1} - \cos^2(2u_0)\right]. \tag{4.119}$$

This is related to the USW Hamiltonian by

$$\mathcal{L}(\gamma) = -i\mathcal{U}^\dagger H_{\text{USW}}(\mathfrak{u})\mathcal{U} - \gamma\cos^2(2u_0)L\ , \tag{4.120}$$

where the unitary transformation $\mathcal{U}$ is given by (4.100) and the parameter $\mathfrak{u}$ is purely imaginary and related to γ by

$$\gamma = -i\frac{\mathfrak{u}}{\cosh\big(2h(u_0)\big)}. \tag{4.121}$$

4.6.3.2 Correlation Functions

Since the jump operators are Hermitian, the Lindblad equation implies the following time evolution for expectation values of time independent operators

$$\frac{d}{dt}\text{Tr}\left[\rho(t)\mathcal{O}\right] = -i\text{Tr}\left(\rho(t)[\mathcal{O}, H_0]\right) + \frac{\gamma}{2}\sum_j \text{Tr}\left(\rho(t)\ [[L_j, \mathcal{O}], L_j]\right)\ . \tag{4.122}$$

The jump operators leading to the USW model (4.118) fulfil a relation

$$\begin{aligned}[L_n, c_j] &= 2\delta_{n,j-1}\sin(u_0)\big(\cos(u_0)c_{j-1} - \sin(u_0)c_j\big) \\ &+ 2\delta_{n,j}\cos(u_0)\big(\cos(u_0)c_j - \sin(u_0)c_{j+1}\big)\ .\end{aligned} \tag{4.123}$$

This shows that n-particle Green's functions follow closed time evolution equations, similarly to the case of the imaginary-U Hubbard model [227]. For example, the single-particle Green's function

$$G_{j,k}(t) = \text{Tr}\left[\rho(t)c_j^\dagger c_k\right] \tag{4.124}$$

has the following equation of motion

$$\begin{aligned}
\frac{d}{dt}G_{j,k} &= \sum_{\ell,m} K^{\ell,m}_{j,k} G_{\ell,m} \ , \\
K^{\ell,m}_{j,k} &= \delta_{j,\ell}\delta_{k-1,m}\left[i - \frac{\gamma\sin(4u_0)}{2}\right] + \delta_{j,\ell}\delta_{k+1,m}\left[i + \frac{\gamma\sin(4u_0)}{2}\right] \\
&- \delta_{j-1,\ell}\delta_{k,m}\left[i - \frac{\gamma\sin(4u_0)}{2}\right] - \delta_{j+1,\ell}\delta_{k,m}\left[i + \frac{\gamma\sin(4u_0)}{2}\right] \\
&- 4\gamma\delta_{j,\ell}\delta_{k,m}\cos^2(2u_0) - 4\gamma\delta_{j,k}\left[\sin^2(u_0)M^{\ell,m}_{j-1} - \cos^2(u_0)M^{\ell,m}_{j}\right] \\
&- 4\gamma\left[\delta_{j-1,k}\sin(u_0)\cos(u_0)M^{\ell,m}_{j-1} - \delta_{j,k-1}\sin(u_0)\cos(u_0)M^{\ell,m}_{j}\right] . \quad (4.125)
\end{aligned}$$

Here, we have defined

$$M^{\ell,m}_{j} = \cos^2(u_0)\delta_{\ell,j}\delta_{m,j} - \sin(u_0)\cos(u_0)\left[\delta_{\ell,j}\delta_{m,j+1} - \delta_{\ell,j+1}\delta_{m,j}\right] - \sin^2(u_0)\delta_{\ell,j+1}\delta_{m,j+1}. \quad (4.126)$$

This result is remarkable because we are dealing with a non-Gaussian theory and, as pointed out in subsection 4.6.2.1, the Wick's theorem does not apply here. In such cases, even for Yang-Baxter integrable models, correlators are typically defined in terms of an infinite number of coupled differential equations and perturbative techniques need to be used to truncate this series [256]. Instead, we observe a decoupling of the hierarchy of correlators. As a result, we can solve the time evolution equations for the Green's functions exactly by means of Fourier transform and then directly study their physics, which remains to be reported on in future work.

4.6.4 Maassarani Models

In [257,258] Maassarani introduced a class of integrable n-state models that generalize the Hubbard models along the lines set out in subsection 4.6.1 above. Maassarani models can be thought of as "higher-dimensional" Hubbard model. A basis of their local Hilbert space is given by the tensor product

$$|a\rangle \otimes |\tilde{a}\rangle \ , \quad a, \tilde{a} = 1, \ldots, n, \quad (4.127)$$

which gives n^2 states per site (two copies of n-dimensional Hilbert space). Here, all states are bosonic and a basis of operators acting on these states is then given by the product of two species of bosonic Hubbard operators, $e^{ab}_j \tilde{e}^{\tilde{a}\tilde{b}}_j$. While these models a priori are generalized spin models, they can be related to interacting fermion models by Jordan-Wigner transformations [259]. In particular, the $SU(2)$ Hubbard model

corresponds to a transformed 2-state Maassarani model. The Maassarani Hamiltonian reads

$$H_{\mathrm{Ma,n}}(U) = \sum_{j=1}^{L} P_{j,j+1}^{(n)} + \widetilde{P}_{j,j+1}^{(n)} + U\big(C_j^{(n)}\widetilde{C}_j^{(n)} - 1\big), \tag{4.128}$$

where

$$\begin{aligned} P_{j,j+1}^{(n)} &= \sum_{a\in A}\sum_{b\in B} x_{ab} e_j^{ba} e_{j+1}^{ab} + x_{ab}^{-1} e_j^{ab} e_{j+1}^{ba} \ , \\ C_j^{(n)} &= \sum_{a\in A} e_j^{aa} - \sum_{b\in B} e_j^{bb} \ . \end{aligned} \tag{4.129}$$

Here the two sets A and B form an arbitrary partition of $\{1,\ldots,n\}$ such that $A\cap B = \varnothing$. Parameters x_{ab} are arbitrary complex variables and in the following we will simply set them equal to 1. The operators $\widetilde{P}_{j,j+1}^{(n)}$ and $\widetilde{C}_j^{(n)}$ are of the same forms as $P_{j,j+1}^{(n)}$ and $C_j^{(n)}$ respectively but with the replacement $e_j^{ab} \to \widetilde{e}_j^{ab}$.

4.6.4.1 Associated Lindblad Equation

Maassarani models are related to Lindblad equations with Hamiltonians

$$H_0^{(n)} = -\sum_j \left[\sum_{a\in A}\sum_{b\in B} e_j^{ba} e_{j+1}^{ab} + e_j^{ab} e_{j+1}^{ba}\right], \tag{4.130}$$

and jump operators

$$L_j = c - C_j^{(n)}, \tag{4.131}$$

where $c \in \mathbb{R}$ is a free parameter. Such systems can be viewed as nearest-neighbour hopping between the degrees of freedom belonging to sets A and B with dephasing dissipation. In the superoperator formalism the corresponding Liouvillian is

$$\mathcal{L}_{\mathrm{Ma,n}}(\gamma) = -i(H_0^{(n)} - \widetilde{H}_0^{(n)}) + \gamma \sum_j \left[C_j^{(n)}\widetilde{C}_j^{(n)} - 1\right], \tag{4.132}$$

where $\widetilde{H}_0^{(n)}$ is of the same form as $H_0^{(n)}$ but with e_j^{ab} replaced by $\widetilde{e}_j^{ab}$. This is related to Maassarani Hamiltonian by a unitary transformation

$$\mathcal{L}_{\mathrm{Ma,n}}(\gamma) = i\mathcal{U} H_{\mathrm{Ma,n}}(-i\gamma)\mathcal{U}^\dagger \ , \quad \mathcal{U} = \prod_{j=1}^{L/2} \widetilde{C}_{2j}^{(n)} \ . \tag{4.133}$$

As previously remarked, the interaction parameter of the equivalent Hamiltonian is purely imaginary.

4.6.4.2 3-State Maassarani Model

One of the simplest Maassarani model is obtained by considering a local Hilbert space of three bosonic states. Choosing a decomposition $A = \{1\}$, $B = \{2, 3\}$ gives at the level of the Lindblad equation a Hamiltonian

$$H_0^{(3)} = -\sum_j e_j^{21} e_{j+1}^{12} + e_j^{31} e_{j+1}^{13} + \text{h.c.} \tag{4.134}$$

and jump operators

$$L_j = c + e_j^{22} + e_j^{33} - e_j^{11} \ . \tag{4.135}$$

In this basis, one can identify the degree of freedom labelled with 1 as a vacuum reference state, and interpret the system as having two types of bosonic particles labelled with 2 and 3. Then, the Hamiltonian is simply the nearest-neighbour hopping of the two species of bosons and the dissipation has a form of local dephasing. In order to fermionise this model, we embed it into an enlarged Hilbert space with four states per site, and then employ the results of subsection 4.4.1. This gives

$$e_j^{12} = \mathfrak{e}_j^{12}\, \tilde{\mathfrak{e}}_j^{11} \ , \qquad e_j^{13} = \mathfrak{e}_j^{11} \tilde{\mathfrak{e}}_j^{12} \ . \tag{4.136}$$

Finally, we Jordan-Wigner transform the two species of E-matrices into two fermion species labelled by spin-1/2 degrees of freedom

$$\mathfrak{e}_j^{21} = \prod_{\ell=1}^{j-1} (1 - 2n_{\ell,\uparrow}) c_{j,\uparrow}^\dagger \ , \qquad \tilde{\mathfrak{e}}_j^{21} = \prod_{\ell=1}^{L} (1 - 2n_{\ell,\uparrow}) \prod_{\ell=1}^{j-1} (1 - 2n_{\ell,\downarrow}) c_{j,\downarrow}^\dagger \ . \tag{4.137}$$

After these transformations the Hamiltonian $H_0^{(3)}$ can be written in the form

$$H_0^{(3)} = -\mathcal{P} \sum_{j,\sigma} \left[c_{j+1,\sigma}^\dagger c_{j,\sigma} + \text{h.c.} \right] \mathcal{P}, \tag{4.138}$$

where

$$\mathcal{P} = \prod_{j=1}^{L} (1 - n_{j,\uparrow} n_{j,\downarrow}) \tag{4.139}$$

is a projection operator that ensures that all sites are at most singly occupied. This guarantees that an effective number of degrees of freedom at every site is indeed three. The Hamiltonian (4.138) can be viewed as the infinite interaction strength ($U \to \infty$) limit of the $SU(2)$ Hubbard model and is sometimes referred to as the $t - 0$ model. In terms of the fermionic operators the jump operator takes the form

$$L_j = 1 - 2(1 - n_{j,\uparrow})(1 - n_{j,\downarrow}) + c. \tag{4.140}$$

Choosing $c = 1$ we have

$$L_j|0\rangle = 0 \ , \quad L_j c^\dagger_{j,\sigma}|0\rangle = 2c^\dagger_{j,\sigma}|0\rangle, \tag{4.141}$$

which shows that the bath acts on the charge degrees of freedom. The Hamiltonian part $H_0^{(3)}$ has a free fermionic spectrum [260, 261], but the creation operators of the non-interacting fermion degrees of freedom are related to the $c^\dagger_{j,\sigma}$ in a non-local way [262, 263]. As a result, the single-particle Green's function does not obey a simple evolution equation. The time evolution is again given by the general expression (4.122), where the relevant commutators are

$$\begin{aligned} [[L_n, c_{j,\sigma}], L_n]\mathcal{P} &= -4c_{j,\sigma}\delta_{j,n}\ \mathcal{P} \ , \\ \mathcal{P}[c_{j,\sigma}, H_0^{(3)}]\mathcal{P} &= -\mathcal{P}\big[(c_{j+1,\sigma} + c_{j-1,\sigma}) + c^\dagger_{j,\bar\sigma}c_{j,\sigma}(c_{j+1,\bar\sigma} + c_{j-1,\bar\sigma})\big]\mathcal{P}. \end{aligned} \tag{4.142}$$

These imply that correlators of different rank are coupled to each other and generate an infinite number of coupled differential equations, in a stark contrast to the simple form achieved for the USW model in section 4.6.3.

4.6.4.3 4-State Maassarani Model

In the 4-state case we can use the decomposition (4.41) and express operators $\mathfrak{e}^{ab}_j, \tilde{\mathfrak{e}}^{ab}_j$ in terms of two species of Pauli operators

$$\begin{aligned} \sigma^z &= \mathfrak{e}^{11} - \mathfrak{e}^{22} \ , \qquad \sigma^+ = \mathfrak{e}^{12} \ , \qquad \sigma^- = \mathfrak{e}^{21} \ , \\ \tau^z &= \tilde{\mathfrak{e}}^{11} - \tilde{\mathfrak{e}}^{22} \ , \qquad \tau^+ = \tilde{\mathfrak{e}}^{12} \ , \qquad \tau^- = \tilde{\mathfrak{e}}^{21} \ . \end{aligned} \tag{4.143}$$

Choosing $A = \{1, 2, 3\}$ and $B = \{4\}$, we can then interpret $H_0^{(4)}$ in the Lindblad equation as the Hamiltonian of a two-legged spin ladder model

$$\begin{aligned} H_0^{(4)} = \sum_{j=1}^{L} \Big[&\sigma^+_j\sigma^-_{j+1}\tau^+_j\tau^-_{j+1} + \sigma^-_j\sigma^+_{j+1}\tau^-_j\tau^+_{j+1} + \frac{1}{4}(\sigma^+_j\sigma^-_{j+1} + \sigma^-_j\sigma^+_{j+1})(1-\tau^z_j)(1-\tau^z_{j+1}) \\ &+\frac{1}{4}(\tau^+_j\tau^-_{j+1} + \tau^-_j\tau^+_{j+1})(1-\sigma^z_j)(1-\sigma^z_{j+1})\Big] \ . \end{aligned} \tag{4.144}$$

The jump operators become (setting again $c = 1$ in (4.131))

$$L_j = \frac{1}{2}(1-\sigma^z_j)(1-\tau^z_j) \ . \tag{4.145}$$

Choosing the dissipation channel rate as U, the corresponding vectorised Liouvillian is a four spin-1/2 species integrable ladder model with $SU(4)$ symmetry

$$\begin{aligned}\mathcal{L}_{rot} = \sum_{j=1}^{N} & -i[\sigma_j^+\sigma_{j+1}^-\tau_j^+\tau_{j+1}^- + \frac{1}{4}\sigma_j^+\sigma_{j+1}^-(1-\tau_j^z)(1-\tau_{j+1}^z) + \frac{1}{4}\tau_j^+\tau_{j+1}^-(1-\sigma_j^z)(1-\sigma_{j+1}^z)] \\ & + i[\sigma_j^-\sigma_{j+1}^+\tau_j^-\tau_{j+1}^+ + \frac{1}{4}\sigma_j^-\sigma_{j+1}^+(1-\tau_j^z)(1-\tau_{j+1}^z) + \frac{1}{4}\tau_j^-\tau_{j+1}^+(1-\sigma_j^z)(1-\sigma_{j+1}^z)] \\ & + i[\tilde{\sigma}_j^-\tilde{\sigma}_{j+1}^+\tilde{\tau}_j^-\tilde{\tau}_{j+1}^+ + \frac{1}{4}\tilde{\sigma}_j^-\tilde{\sigma}_{j+1}^+(1-\tilde{\tau}_j^z)(1-\tilde{\tau}_{j+1}^z) + \frac{1}{4}\tilde{\tau}_j^-\tilde{\tau}_{j+1}^+(1-\tilde{\sigma}_j^z)(1-\tilde{\sigma}_{j+1}^z)] \\ & - i[\tilde{\sigma}_j^+\tilde{\sigma}_{j+1}^-\tilde{\tau}_j^+\tilde{\tau}_{j+1}^- + \frac{1}{4}\tilde{\sigma}_j^+\tilde{\sigma}_{j+1}^-(1-\tilde{\tau}_j^z)(1-\tilde{\tau}_{j+1}^z) + \frac{1}{4}\tilde{\tau}_j^+\tilde{\tau}_{j+1}^-(1-\tilde{\sigma}_j^z)(1-\tilde{\sigma}_{j+1}^z)] \\ & + U[(1-\sigma_j^z)(1-\tau_j^z)(1-\tilde{\sigma}_j^z)(1-\tilde{\tau}_j^z) - 2(1-\sigma_j^z)(1-\tau_j^z) - 2(1-\tilde{\sigma}_j^z)(1-\tilde{\tau}_j^z)] \ . \end{aligned} \tag{4.146}$$

For comparison, consider a partition $A = \{1, 2\}$ and $B = \{3, 4\}$. We again obtain a two-legged spin ladder, but now $H_0^{\prime(4)}$ is asymmetric in the two Pauli operator species

$$H_0^{\prime(4)} = \sum_{j=1}^{L} \left(\sigma_j^+\sigma_{j+1}^- + \sigma_j^-\sigma_{j+1}^+\right) \left[\tau_j^+\tau_{j+1}^- + \tau_j^-\tau_{j+1}^+ + \frac{1}{2}(1+\tau_j^z\tau_{j+1}^z)\right] , \tag{4.147}$$

as are the jump operators (with $c = 1$ in (4.131))

$$L_j = 1 - \sigma_j^z \ . \tag{4.148}$$

4.6.4.4 Bethe Ansatz Solution

The Maassarani models have been solved by BA in [264]. Without loss of generality, we restrict our discussion to the case where the sets A and B in (4.129) are given by

$$A = \{1, 2, \ldots, p\} \ , \qquad B = \{p+1, p+2, \ldots, n\} \ . \tag{4.149}$$

This notation explicitly indicates that the underlying symmetry algebra of the model is $gl(p) \oplus gl(n-p) \oplus gl(p) \oplus gl(n-p)$. The exact eigenstates of $H_{\mathrm{Ma,n}}(U)$ are then labelled by eigenvalues of the operators

$$Q^a = \sum_{j=1}^{L} e_j^{aa} \ , \qquad \tilde{Q}^a = \sum_{j=1}^{L} \tilde{e}_j^{aa} \ , \qquad a = 1, \ldots, n \ , \tag{4.150}$$

which commute with $H_{\mathrm{Ma,n}}(U)$ and with one another. Hence, their eigenvalues N_a, $\tilde{N}_a$ can be used as good quantum numbers. The Maassarani Hamiltonian has four particle species, $N_a, \widetilde{N}_a$ particles associated with set A and $N_b, \widetilde{N}_b$ particles belonging

to set B. These species have "colours" $\{1,\ldots,p\}$ and $\{p+1,\ldots,n\}$ respectively. Let us choose a reference "vacuum" state to be the non-trivial eigenvector of the operator $\sum_j e_j^{11}\tilde{e}_j^{11}$. All the other operators then appear as "excitations". The conserved quantum numbers labelling the number of particles in the system are

$$N_A=\sum_{a=2}^{p}N_a\ ,\quad N_B=\sum_{a=p+1}^{n}N_a\ ,\quad \tilde{N}_A=\sum_{a=2}^{p}\tilde{N}_a\ ,\quad \tilde{N}_B=\sum_{a=p+1}^{n-1}\tilde{N}_a\ , \tag{4.151}$$

with $N\geq N_A+N_B+\tilde{N}_A+\tilde{N}_B$. We then define sets

$$\begin{aligned}\mathcal{M}_A &= \{1,\ldots,N_A\}\ ,\quad \mathcal{M}_B=\{N_A+1,\ldots,N_A+N_B\}\ ,\\ \tilde{\mathcal{M}}_A &= \{N_A+N_B+1,\ldots,N_A+N_B+\tilde{N}_A\}\ ,\\ \tilde{\mathcal{M}}_B &= \{N_A+N_B+\tilde{N}_A+1,\ldots,N_A+N_B+\tilde{N}_A+\tilde{N}_B\}\ ,\end{aligned} \tag{4.152}$$

and finally introduce two non-intersecting ordered sets of integers $1\leq a_j\leq N\leq L$

$$\mathbb{A}_A=\{a_j|j\in\mathcal{M}_A\}\ ,\quad \tilde{\mathbb{A}}_A=\{a_j|j\in\tilde{\mathcal{M}}_A\}\ ,\quad \mathbb{A}_A\cap\tilde{\mathbb{A}}_A=\varnothing\ ,\quad \mathbb{A}_A\cup\tilde{\mathbb{A}}_A\equiv\mathbb{A}. \tag{4.153}$$

By ordered we mean that $a_j<a_{j+1}$ if $a_j,a_{j+1}\in\mathbb{A}_A$ and similarly for $\tilde{\mathbb{A}}_A$. The eigenstates of the Liouvillian $\mathcal{L}_{\mathrm{Ma,n}}(\gamma)$ are then given in terms of rapidities $\{k_1,\ldots,k_N\}$, $\{\Lambda_j|j\in\mathcal{M}_B\}$, $\{b_m|m\in\tilde{\mathcal{M}}_B\}$ and integers $\{n_1,\ldots,n_{\tilde{N}_B-\tilde{N}_{n-1}}\}$, $\{\bar{n}_1,\ldots,\bar{n}_{N_B-N_n}\}$ subject to the following set of BAE [264]

$$\begin{aligned}e^{ik_jL} &= e^{2\pi i\Phi}\prod_{l\in\mathcal{M}_B}\frac{\Lambda_l-\sin k_j+\gamma}{\Lambda_l-\sin k_j-\gamma}\ ,\quad j\in[1,N]\backslash\mathbb{A},\\ \prod_{\substack{j=1\\ j\notin\mathbb{A}}}^{N}\frac{\Lambda_m-\sin k_j+\gamma}{\Lambda_m-\sin k_j-\gamma} &= e^{2\pi i\Psi}\prod_{\substack{l\in\mathcal{M}_B\\ l\neq m}}\frac{\Lambda_m-\Lambda_l+2\gamma}{\Lambda_m-\Lambda_l-2\gamma}\ ,\quad m\in\mathcal{M}_B\ ,\end{aligned} \tag{4.154}$$

$$\begin{aligned}b_\ell^{\tilde{N}_B+\tilde{N}_n} &= \prod_{j=1}^{\tilde{N}_B-\tilde{N}_{n-1}}e^{2\pi i\frac{n_j}{\tilde{N}_B}}\ ,\quad 1\leq n_1<\cdots<n_{\tilde{N}_B-\tilde{N}_{n-1}}\leq\tilde{N}_B\ ,\ \ell\in\tilde{M}_B\ ,\\ e^{ik_j(L-N_B)} &= (-1)^{N_A-1}e^{2\pi i\frac{m_\alpha}{N_A}}\ ,\quad m_\alpha\in[1,N_A]\ ,\quad j\in\mathbb{A}_A\ ,\\ e^{ik_j(L-\tilde{N}_B-\tilde{N}_n)} &= (-1)^{\tilde{N}_A-1}e^{2\pi i\frac{\tilde{m}_\alpha}{\tilde{N}_A}}\ ,\quad \tilde{m}_\alpha\in[1,\tilde{N}_A]\ ,\quad j\in\tilde{\mathbb{A}}_A\ ,\end{aligned} \tag{4.155}$$

where we require $\arg(b_\ell)<\arg(b_{\ell+1})$ and the phases Φ and Ψ are given by

$$\begin{aligned}e^{2\pi i\Phi} &= (-1)^{\tilde{N}_B+\tilde{N}_n-1}\prod_{m\in\tilde{M}_B}b_m\prod_{j\in\tilde{M}_A}e^{-ik_{a_j}}\ ,\\ e^{2\pi i\Psi} &= (-1)^{N-N_A-\tilde{N}_A}\prod_{j\in M_A}e^{-ik_{a_j}}\prod_{m\in\tilde{M}_A}e^{ik_{a_m}}\prod_{\ell\in\tilde{M}_B}b_\ell^{-1}\prod_{s=1}^{N_B-N_n}e^{2\pi i\frac{\bar{n}_s}{N_B}}\ ,\\ &\quad 1\leq\bar{n}_1<\cdots<\bar{n}_{N_B-N_n}<N_B.\end{aligned} \tag{4.156}$$

Although we expect n-level nesting of BAE for an n-state model, in this particular case the hierarchy of equations collapses. In particular, equations (4.154) are the same as for the Hubbard model with imaginary interaction strength and twisted boundary conditions, with the remaining BAE imposing constraints on the twist phases in (4.156). The eigenvalues of $\mathcal{L}_{\mathrm{Ma,n}}(\gamma)$ for a given set of quantum numbers are

$$E = 2i \sum_{j \in \mathcal{M}_B \cup \tilde{\mathcal{M}}_B} \cos k_j - 2\gamma(N_B + \tilde{N}_B + \tilde{N}_n). \tag{4.157}$$

For an imaginary interaction parameter, the BAE solutions change substantially. The scattering phases have magnitudes different from unity and the eigenstates corresponding to Bethe strings acquire a non-trivial structure which remains to be better understood.

4.6.4.5 String Solutions and the Liouvillian Gap

As a consequence of BAE in (4.154) being the same as for the imaginary-U Hubbard model, the k-Λ string solutions constructed in [227] and discussed in subsection 2.4.2 are valid solutions for the n-state Maassarani models as well. A k-Λ string of length m corresponds to the following pattern of rapidities

$$\begin{aligned} k_{\alpha,j}^{(m)} &= \arcsin\big(i\Lambda_\alpha^{(m)} - (m-2j+2)\gamma'\big), \\ k_{\alpha,j+m}^{(m)} &= \pi - \arcsin\big(i\Lambda_\alpha^{(m)} + (m-2j+2)\gamma'\big), \\ \Lambda_{\alpha,j}^{(m)} &= i\Lambda_\alpha^{(m)} + \gamma(m+1-2j)\ , \qquad 1 \le j \le m \end{aligned} \tag{4.158}$$

and bears a clear resemblance to the string pattern of the Hubbard model (2.68). Here the string centres $\Lambda_\alpha^{(m)}$ are real and $\gamma' = -\gamma\ \mathrm{sgn}(\Lambda_\alpha^{(m)})$. As a consequence of the imaginary interaction strength, the string pattern is rotated by $\pi/2$ in the complex plane with respect to the pattern described in subsection 2.4.2. Now, the string centers are along the imaginary rapidity axis with the remaining roots having symmetrically distributed finite real parts. This change is shown in Figure 4.9.

We now take $N_A = \tilde{N}_A = 0$ and consider a Bethe Ansatz state with a single k-Λ string of length $m \ll L$. The corresponding eigenvalue of the Liouvillian is

$$\epsilon = 4\mathrm{Im}\sqrt{1 - (i|\Lambda_\alpha^{(m)}| - m\gamma)^2} - 4\gamma m. \tag{4.159}$$

In the framework of the string hypothesis the equation that fixes the allowed positions of the string centres $\Lambda_\alpha^{(m)}$ is obtained by "multiplying out the string". This procedure gives

$$\exp\left(iL\sum_{j=1}^{2m} k_j^{(m)}\right) = e^{2\pi i m(2\Phi+\Psi)}. \tag{4.160}$$

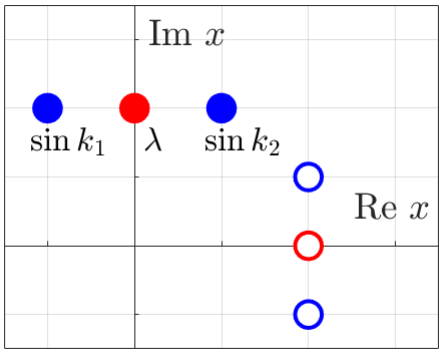


Figure 4.9: Sketch of the string pattern for the Maassarani Bethe roots. Empty circles represent the case of real interaction strength whereas the solid circles correspond to the case considered in this chapter, with imaginary interaction strength. Figure reproduced after [227].

By taking logarithms, this can be cast in the form

$$\mathrm{sgn}(\Lambda^{(m)})\big[\pi - \arcsin(i\Lambda^{(m)} + m\gamma) + \arcsin(i\Lambda^{(m)} - m\gamma)\big] = \frac{2\pi}{L}\big(J_\alpha^{(m)} + \varphi\big), \quad (4.161)$$

where we have defined

$$\varphi = m(2\Phi + \Psi) \bmod 1. \quad (4.162)$$

For even lattice lengths L, the $J_\alpha^{(m)}$ are integers with range

$$-\frac{L+1-2m}{2} - \varphi < J^{(m)} < \frac{L+1-2m}{2} - \varphi\ . \quad (4.163)$$

We now focus on the particular sequence of string states characterized by integers

$$J_\alpha^{(m)} = \frac{L}{2} - m - \alpha\ , \quad \alpha = 1, 2, \cdots \ll L\ . \quad (4.164)$$

In the limit of large system sizes $L \gg 1$, the corresponding string centres follow from (4.161)

$$\Lambda_\alpha^{(n)} = \frac{m\gamma L}{\pi(m + \alpha - \varphi)} + \mathcal{O}(1). \quad (4.165)$$

Substituting this into expression (4.159) for the eigenvalue of the Liouvillian gives

$$\epsilon_\alpha^{(m)} = -\frac{2\pi^2}{m\gamma L^2}(m + \alpha - \varphi)^2 + \mathcal{O}(L^{-4}). \quad (4.166)$$

This shows that in the large L limit we have a band of Liouvillian eigenstates with eigenvalues that scale as L^{-2}. This establishes that the Liouvillian gap vanishes in the thermodynamic limit. Moreover, the scaling with system size suggests that the corresponding eigenmodes are diffusive. Our calculation does not rule out the existence of eigenstates with gaps that approach zero faster than L^{-2}.

4.6.5 $GL(N,M)$ Maassarani Models

The Shastry-Maassarani construction described in subsection 4.6.1 can be generalized to graded magnets based on $GL(N,M)$. Following [249], we consider the class of Hamiltonians

$$H_{\rm gMa}(U) = \sum_j \Pi^{(n)}_{j,j+1} + \widetilde{\Pi}^{(n)}_{j,j+1} + U\big[C_j\widetilde{C}_j - 1\big], \tag{4.167}$$

where

$$\begin{aligned}\Pi^{(n)}_{j,j+1} &= \sum_{k\neq N,K}\Big[E^{kN}_j E^{Nk}_{j+1} - E^{kK}_j E^{Kk}_{j+1} + (-1)^{\epsilon_k}(E^{Nk}_j E^{kN}_{j+1} + E^{Kk}_j E^{kK}_{j+1})\Big],\\ C_j &= 1 - 2E^{KK}_j - 2E^{NN}_j\ , \qquad K = N+M\ ,\end{aligned} \tag{4.168}$$

and the operators with a tilde $\widetilde{\Pi}^{(n)}_{j,j+1}, \widetilde{C}_j$ are obtained by taking respectively $\Pi^{(n)}_{j,j+1}, C_j$ and replacing $E^{\alpha\beta}_j \to \widetilde{E}^{\alpha\beta}_j$. Such a model has $2M$ fermionic and $2N$ bosonic degrees of freedom for each species on every site, which gives a total of $2K$ local degrees of freedom per operator species. We can relate this to a Lindblad equation with Hamiltonian

$$H_0 = -\sum_j \Pi^{(n)}_{j,j+1}, \tag{4.169}$$

and jump operators

$$L_j = 1 - C_j. \tag{4.170}$$

4.6.5.1 3-State $GL(1,2)$ Model

The simplest example is the 3-state model based in $GL(1,2)$. Like in the case of the 3-state Maassarani model considered above, we may represent the Hamiltonian in terms of canonical spin-1/2 fermion creation and annihilation operators by identifying the three states per site as

$$|1\rangle_j = |0\rangle_j\ , \quad |2\rangle_j = c^\dagger_{j,\uparrow}|0\rangle_j\ , \quad |3\rangle_j = c^\dagger_{j,\downarrow}|0\rangle_j\ . \tag{4.171}$$

Consequently, H_0 can be represented as

$$H_0 = -\mathcal{P}\sum_{j=1}^{L}\big(c^\dagger_{j,\uparrow}c_{j+1,\uparrow} - S^+_j S^-_{j+1} + \text{h.c.}\big)\mathcal{P}, \tag{4.172}$$

where $\mathcal{P}$ is the projection operator on singly occupied sites (4.139) and $S^+_j = c^\dagger_{j,\uparrow}c_{j,\downarrow}$. This model describes correlated hopping of the spin up fermions, whereas the spin down fermions can only move through spin-flip processes. The jump operators lead to dephasing of only the spin up fermions

$$L_j = 2n_{j,\uparrow} - 1\ . \tag{4.173}$$

4.6.5.2 4-State $GL(2,2)$ Model

Similarly, consider a canonical spin-1/2 fermion representation of 4-state graded $GL(2,2)$ Maassarani model with a basis identification

$$|1\rangle_j = |0\rangle_j \ , \quad |2\rangle_j = c^\dagger_{j,\uparrow}|0\rangle_j \ , \quad |3\rangle_j = c^\dagger_{j,\downarrow}|0\rangle_j \ , \quad |4\rangle_j = c^\dagger_{j,\downarrow}c^\dagger_{j,\uparrow}|0\rangle_j \ . \tag{4.174}$$

Then, the open system Hamiltonian H_0 can be represented as

$$\begin{aligned} H_0 = \sum_{j=1}^{L} \Big[\Big(c^\dagger_{j,\uparrow}c_{j+1,\uparrow} + c^\dagger_{j+1,\uparrow}c_{j,\uparrow} \Big) (n_{j,\downarrow} + n_{j+1,\downarrow} - 1) + S^+_j S^-_{j+1} + S^+_j S^-_{j+1} \\ + c^\dagger_{j,\uparrow}c^\dagger_{j,\downarrow}c_{j+1,\uparrow}c_{j+1,\downarrow} + c^\dagger_{j+1,\uparrow}c^\dagger_{j+1,\downarrow}c_{j,\uparrow}c_{j,\downarrow} \Big] \ , \end{aligned} \tag{4.175}$$

where $S^+_j = c^\dagger_{i,\uparrow}c_{j,\downarrow}$. In comparison to the 3-state Maassarani case described in subsection 4.6.5.1, this model features correlated hopping of the spin up fermions, spin-flip processes, and additionally simultaneous hopping of both spin species. The jump operators here lead to dephasing of only the spin up fermions (4.173) exactly as in the 3-state Maassarani case.

4.6.6 Other Integrable Two-Legged Ladder Models

The generalized Hubbard models considered above are all related to Lindblad equations with a single jump operator on each bond by virtue of their integrability structure. Yet, integrable models which can be associated with a Lindbladian do not end there. In the following, we present several more examples of families of integrable models with a two-legged ladder structure of Lindblad type. At the same time, we provide some details of integrable models with ladder structure but no Lindblad equivalent in Appendix D.

4.6.7 $GL(N^2)$ Magnets

Consider generalized spin models on a local Hilbert space with N^2 bosonic states. A well-known class of integrable models is obtained by taking [265, 266]

$$H_{GL(N^2)} = \sum_{j=1}^{L} \sum_{\alpha,\beta=1}^{N^2} E^{\alpha\beta}_j E^{\beta\alpha}_{j+1} \ , \tag{4.176}$$

where $P_{j,j+1} = \sum_{\alpha,\beta=1}^{N^2} E^{\alpha\beta}_j E^{\beta\alpha}_{j+1}$ is a permutation operator acting on nearest-neighbour lattice sites

$$P_{j,j+1}|\gamma\rangle_j|\delta\rangle_{j+1} = |\delta\rangle_j|\gamma\rangle_{j+1} \ . \tag{4.177}$$

The Hamiltonian H is $GL(N^2)$ symmetric and hence

$$[H, Q^{\alpha,\beta}] = 0 \ , \quad \alpha, \beta \in [1, N^2] \ , \quad \text{where} \quad Q^{\alpha,\beta} = \sum_{j=1}^{L} E_j^{\alpha\beta} \ . \tag{4.178}$$

The permutation models can be viewed as two-legged ladders by employing the decomposition of section 4.41 for $M = N$. This provides a representation of the permutation operator as a tensor product

$$P_{j,j+1} = \left[\sum_{\alpha,\beta=1}^{N} \widetilde{e}_j^{\alpha\beta} \ \widetilde{e}_{j+1}^{\beta\alpha} \right] \left[\sum_{\gamma,\delta=1}^{N} e_j^{\gamma\delta} \ e_{j+1}^{\delta\gamma} \right] \tag{4.179}$$

and immediately leads to

$$[H, J^{\alpha\beta}] = 0 = [H, \widetilde{J}^{\alpha\beta}] = 0 \ , \tag{4.180}$$

where

$$\widetilde{J}^{\alpha\beta} = \sum_{j=1}^{L} \widetilde{e}_j^{\alpha\beta} \ , \quad J^{\alpha\beta} = \sum_{j=1}^{L} e_j^{\alpha\beta} \ , \qquad \alpha, \beta = 1, \dots N. \tag{4.181}$$

These operators are related to the $GL(N^2)$ symmetry generators by

$$J^{\alpha\beta} = \sum_{\gamma=1}^{N} Q^{N(\gamma-1)+\alpha, N(\gamma-1)+\beta} \ , \quad \widetilde{J}^{\alpha\beta} = \sum_{\gamma=1}^{N} Q^{N(\alpha-1)+\gamma, N(\beta-1)+\gamma} \ , \tag{4.182}$$

in analogy to the superscript relations in (4.38).

4.6.7.1 Associated Lindblad Equation

Consider now a Lindblad equation with Hamiltonian H_0 and two sets of jump operators $\{L_j\}$ and $\{\ell_j^{\alpha\beta}\}$

$$H_0 = \sum_{\alpha,\beta=1}^{N} \lambda_{\alpha\beta} J^{\alpha\beta} \ , \quad L_j = \sum_{\bar{\alpha},\bar{\beta}=1}^{N} e_j^{\bar{\alpha}\bar{\beta}} \ e_{j+1}^{\bar{\beta}\bar{\alpha}} \ , \quad \ell_j^{\alpha\beta} = e_j^{\alpha\beta} \ . \tag{4.183}$$

with corresponding dissipative rates γ and $\gamma_{\alpha,\beta}$. Noting that $L_j^\dagger L_j = 1$, we conclude that the corresponding Liouvillian is

$$\mathcal{L} = \sum_{\alpha,\beta=1}^{N^2} f_{\alpha\beta} Q^{\alpha,\beta} + \gamma \sum_{j=1}^{L} \left(P_{j,j+1} - 1 \right) \ , \tag{4.184}$$

where

$$\sum_{\alpha,\beta=1}^{N^2} f_{\alpha\beta} Q^{\alpha,\beta} = \sum_{\bar{\alpha},\bar{\beta}=1}^{N} -i\lambda_{\bar{\alpha}\bar{\beta}} [J^{\bar{\alpha}\bar{\beta}} - \widetilde{J}^{\bar{\alpha}\bar{\beta}}] + \gamma_{\bar{\alpha}\bar{\beta}} \left[Q^{N(\bar{\alpha}-1)+\bar{\alpha}, N(\bar{\beta}-1)+\bar{\beta}} - \frac{J^{\bar{\beta}\bar{\beta}} + \widetilde{J}^{\bar{\beta}\bar{\beta}}}{2} \right] \ . \tag{4.185}$$

By construction, the first term in (4.184) commutes with the second, which is equal to the integrable Hamiltonian $H_{GL(N^2)}$. As $H_{GL(N^2)}$ is invariant under all global $GL(N^2)$ rotations U, we conclude that Liouvillian (4.184) is integrable for choices of $\gamma_{\alpha\beta}$ and $\lambda_{\alpha\beta}$ such that

$$U\left[\sum_{\alpha,\beta=1}^{N^2} f_{\alpha\beta}Q^{\alpha,\beta}\right]U^\dagger = \sum_{\alpha=1}^{N^2} g_\alpha Q^{\alpha,\alpha}\ , \quad g_\alpha \in \mathbb{C}\ . \tag{4.186}$$

4.6.7.2 Twisting the Boundary Conditions

In general, we need to consider similarity transformations when trying to ascertain whether a Lindblad equation is related to an integrable Hamiltonian. A simple example is provided by considering a Lindblad equation with vanishing Hamiltonian and jump operators

$$L_j = \left[\sum_{\bar\alpha,\bar\beta=1}^{N} e^{i(\varphi_{\bar\beta}-\varphi_{\bar\alpha})}e_j^{\bar\alpha\bar\beta}\ e_{j+1}^{\bar\beta\bar\alpha}\right]\ , \quad \varphi_{\bar\alpha}\in\mathbb{R}. \tag{4.187}$$

The corresponding Liouvillian is

$$\begin{aligned}\mathcal{L} &= \gamma\sum_{j=1}^{L}\left[\sum_{\widetilde\alpha,\widetilde\beta,\bar\alpha,\bar\beta=1}^{N} e^{i(\varphi_{\bar\beta}-\varphi_{\bar\alpha}-\varphi_{\widetilde\beta}+\varphi_{\widetilde\alpha})}e_j^{\bar\alpha\bar\beta}\ e_{j+1}^{\bar\beta\bar\alpha}\ \widetilde e_j^{\widetilde\alpha\widetilde\beta}\ \widetilde e_{j+1}^{\widetilde\beta\widetilde\alpha} - 1\right] \\ &= \gamma\sum_{j=1}^{L}\sum_{\alpha,\beta=1}^{N^2}\left[E_j^{\alpha\beta}E_{j+1}^{\beta\alpha}e^{i(\phi_\beta-\phi_\alpha)} - 1\right],\end{aligned} \tag{4.188}$$

where we have used the inverse of the decomposition (4.41) and fixed the phases ϕ_α by

$$\phi_\beta - \phi_\alpha = \varphi_{\bar\beta} - \varphi_{\bar\alpha} + \varphi_{\widetilde\alpha} - \varphi_{\widetilde\beta}\ , \tag{4.189}$$

in accordance with the rules derived in (4.38). To relate this to the $GL(N^2)$ Hamiltonian we consider the canonical transformation

$$UE_j^{\alpha\beta}U^\dagger = E_j^{\alpha\beta}e^{-i(\phi_\alpha-\phi_\beta)j}\ , \tag{4.190}$$

under which the Liouvillian transforms as

$$U\mathcal{L}U^\dagger = \sum_{j=1}^{L}\sum_{\alpha,\beta=1}^{N^2}\left[E_j^{\alpha\beta}E_{j+1}^{\beta\alpha} - 1\right]\ . \tag{4.191}$$

Here it was necessary to impose twisted boundary conditions

$$E_{L+1}^{\beta\alpha} = E_1^{\beta\alpha}e^{-i(\phi_\alpha-\phi_\beta)L}\ . \tag{4.192}$$

As a result, we show that the Liouvillian is related to the integrable $GL(N^2)$ Hamiltonian with twisted boundary conditions

$$U\mathcal{L}U^\dagger = \gamma H_{GL(N^2)}\Big|_{\text{twisted bc}} . \tag{4.193}$$

The integrability of such models has been shown in [9, 267, 268].

4.6.7.3 $GL(4)$ Spin Ladder

As a specific example let us consider the $GL(4)$ case

$$H = J\sum_{j=1}^{L} P_{j,j+1} + \frac{h}{2}\left[Q^{1,1} + Q^{2,3} + Q^{3,2} + Q^{4,4}\right], \tag{4.194}$$

where we have added a particular generalized magnetic field term. Using the decomposition (4.41) and a mapping (4.143), we can express this in terms of two species of Pauli operators

$$H = \frac{1}{4}\sum_{j=1}^{L} J\left(\sigma_j.\sigma_{j+1}+1\right)\left(\tau_j.\tau_{j+1}+1\right) + h\left(\sigma_j.\tau_j+1\right) . \tag{4.195}$$

The associated Lindblad equation has no Hamiltonian and two sets of jump operators

$$L_j = \frac{1}{2}\sum_{a=x,y,z}\sigma_j^a\sigma_{j+1}^a + 1 , \quad \{\ell_j^{(a)} = \sigma_j^a | a = x,y,z\} . \tag{4.196}$$

The corresponding Liouvillian is

$$\mathcal{L} = \gamma\sum_{j=1}^{L}(P_{j,j+1}-1) + \gamma'\sum_{j=1}^{L}(\sigma_j^x\widetilde{\sigma}_j^x - \sigma_j^y\widetilde{\sigma}_j^y + \sigma_j^z\widetilde{\sigma}_j^z - 3). \tag{4.197}$$

After a local basis rotation around the y-axis by an angle of π

$$\tau_j^x = -\widetilde{\sigma}_j^x , \quad \tau_j^y = \widetilde{\sigma}_j^y , \quad \tau_j^z = -\widetilde{\sigma}_j^z , \tag{4.198}$$

this maps onto (4.195) (up to a constant contribution) if we identify $\gamma = J/4$ and $h = -\gamma'$. Additionally, we can extend the open problem by a Hamiltonian involving local magnetic fields

$$H_0 = \sum_{j=1}^{L}\left(h_z\sigma_j^z + h_+\sigma_j^+ + h_-\sigma_j^-\right) , \tag{4.199}$$

where h_z, h_+, h_- are free parameters. In the vectorised description and after the y-axis rotation (4.198), the contribution to the integrable Hamiltonian takes a form

$$H_{add} = -i \sum_{j=1}^{L} h_z \left(\sigma_j^z + \tau_j^z\right) + h_+ \left(\sigma_j^+ + \tau_j^+\right) + h_- \left(\sigma_j^- + \tau_j^-\right) \tag{4.200}$$

and thus adds imaginary magnetic fields while still preserving integrability of the Hamiltonian (4.195). In the E-matrix description, this Hamiltonian part has a form

$$\begin{aligned} H_{add} = -i \Big[& 2h_z \left(Q^{1,1} + Q^{4,4}\right) + h_+ \left(Q^{1,3} + Q^{1,2} + Q^{2,4} + Q^{3,4}\right) \\ & + h_- \left(Q^{3,1} + Q^{2,1} + Q^{4,2} + Q^{4,3}\right) \Big] \ . \end{aligned} \tag{4.201}$$

4.6.7.4 $GL(4)$ Anisotropic Spin Ladder

To implement the anisotropy, consider adding a twist parameter to the Lindblad equation with dissipation governed by one jump operator per site

$$L_j = e^{i\theta} \sigma_j^+ \sigma_{j+1}^- + e^{-i\theta} \sigma_j^- \sigma_{j+1}^+ + \frac{1}{2}(1 + \sigma_j^z \sigma_{j+1}^z) \ , \tag{4.202}$$

where $\theta \in \mathbb{R}$ is a free parameter. After vectorisation and y-axis rotation as defined in (4.198), the associated Liouvillian corresponds to an integrable Hamiltonian studied in [269, 270]

$$\begin{aligned} H_= \sum_j & \sigma_j^+ \sigma_{j+1}^- [\frac{t_1^{-1}}{4}(1+\tau_j^z)(1+\tau_{j+1}^z) + \frac{t_2}{4}(1-\tau_j^z)(1-\tau_{j+1}^z)] \\ & + \sigma_j^- \sigma_{j+1}^+ [\frac{t_1}{4}(1+\tau_j^z)(1+\tau_{j+1}^z) + \frac{t_2^{-1}}{4}(1-\tau_j^z)(1-\tau_{j+1}^z)] \\ & + \tau_j^- \tau_{j+1}^+ [\frac{t_1}{4}(1+\sigma_j^z)(1+\sigma_{j+1}^z) + \frac{t_2^{-1}}{4}(1-\sigma_j^z)(1-\sigma_{j+1}^z)] \\ & + \tau_j^+ \tau_{j+1}^- [\frac{t_1^{-1}}{4}(1+\sigma_j^z)(1+\sigma_{j+1}^z) + \frac{t_2}{4}(1-\sigma_j^z)(1-\sigma_{j+1}^z)] \\ & + t_3 \sigma_j^+ \sigma_{j+1}^- \tau_j^+ \tau_{j+1}^- + t_3^{-1} \sigma_j^- \sigma_{j+1}^+ \tau_j^- \tau_{j+1}^+ + \sigma_j^+ \sigma_{j+1}^- \tau_j^- \tau_{j+1}^+ + \sigma_j^- \sigma_{j+1}^+ \tau_j^+ \tau_{j+1}^- \\ & + \frac{1}{4}(1+\sigma_j^z \sigma_{j+1}^z)(1+\tau_j^z \tau_{j+1}^z) \ . \end{aligned} \tag{4.203}$$

The equivalence holds when the free parameters of the integrable Hamiltonian are fixed to be $t_1 = t_2^{-1} = e^{-i\theta}$ and $t_3 = e^{2i\theta}$.

4.6.8 $GL(n_B^2 + n_F^2|2n_B n_F)$ Magnets

We now turn to particular graded magnets, where we have $n_B^2 + n_F^2$ bosonic and $2n_B n_F$ fermionic states at a given site of the lattice, where $n_{B,F} \in \mathbb{N}_0$. A much studied family of integrable models is given by [266, 271–276]

$$H = \sum_j \Pi_{j,j+1} + \sum_j \sum_\alpha \lambda_\alpha E_j^{\alpha\alpha} \ , \tag{4.204}$$

where $\Pi_{j,j+1}$ is a graded permutation operator (4.33) and λ_α are generalized chemical potentials. The case $n_B = n_F = 1$ gives the EKS model (supersymmetric extended Hubbard model [273]). We now employ the decomposition (4.41) which leads to the following form of the graded permutation operator

$$\Pi_{j,j+1} = \left[\sum_{\widetilde{\alpha},\widetilde{\beta}=1}^{n_B+n_F} (-1)^{\epsilon_{\widetilde{\beta}}} \widetilde{e}_j^{\widetilde{\alpha}\widetilde{\beta}} e_{j+1}^{\widetilde{\beta}\widetilde{\alpha}} \right] \left[\sum_{\bar{\alpha},\bar{\beta}=1}^{n_B+n_F} (-1)^{\epsilon_{\bar{\beta}}} e_j^{\bar{\alpha}\bar{\beta}} e_{j+1}^{\bar{\beta}\bar{\alpha}} \right] . \tag{4.205}$$

4.6.8.1 Associated Lindblad Equation

Consider now a Lindblad equation with no Hamiltonian and Hermitian jump operators

$$L_j = \sum_{\bar{\alpha},\bar{\beta}=1}^{N} (-1)^{\epsilon_{\bar{\beta}}} e_j^{\bar{\alpha}\bar{\beta}} \ e_{j+1}^{\bar{\beta}\bar{\alpha}} \ . \tag{4.206}$$

Noting that

$$L_j^\dagger L_j = 1 \ , \tag{4.207}$$

we conclude that the corresponding Liouvillian is

$$\mathcal{L} = \gamma \sum_{j=1}^{L} (\Pi_{j,j+1} - 1) \ . \tag{4.208}$$

We can generalize this by following the construction for the $GL(N^2)$ case and adding an open system Hamiltonian

$$H_0 = \sum_{\bar{\alpha}=1}^{n_B+n_F} \lambda_{\bar{\alpha}} \sum_{j=1}^{L} e_j^{\bar{\alpha}\bar{\alpha}} \ , \tag{4.209}$$

which relates to the generalised chemical potentials in the vectorised description. Necessarily, these potentials constitute an imaginary contribution to the integrable Hamiltonian.

4.6.9 Generalised Integrable Spin Ladder

The Hamiltonian of this model can be cast in the form of a two-legged spin ladder [277–279]

$$\begin{aligned} H(J) &= \frac{1}{4}\sum_{j=1}^{L}\Big[\left(\sigma_j.\sigma_{j+1}+1\right)\left(\tau_j.\tau_{j+1}+1\right)+J\left(\sigma_j.\tau_j+1\right) \\ &\quad +\left(\sigma_j.\tau_j+1\right)\left(\sigma_{j+1}.\tau_{j+1}+1\right)-\left(\sigma_j.\tau_{j+1}+1\right)\left(\tau_j.\sigma_{j+1}+1\right)\Big] \end{aligned} \tag{4.210}$$

or in terms of bosonic E-matrices

$$\begin{aligned} H(J) &= \sum_{j=1}^{L} P_{j,j+1}+\frac{J}{2}\sum_{\alpha,\beta=1}^{2} e_j^{\alpha\beta}\widetilde{e}_j^{\beta\alpha} \\ &\quad +\sum_{\alpha,\beta,\gamma,\delta=1}^{2} e_j^{\alpha\beta}\widetilde{e}_j^{\beta\alpha}e_{j+1}^{\gamma\delta}\widetilde{e}_{j+1}^{\delta\gamma}-e_j^{\alpha\beta}\widetilde{e}_{j+1}^{\beta\alpha}e_{j+1}^{\gamma\delta}\widetilde{e}_j^{\delta\gamma}\ . \end{aligned} \tag{4.211}$$

4.6.9.1 Associated Lindblad Equation

The Hamiltonian (4.210) is related to a Lindblad equation with no Hamiltonian part and a set of Hermitian jump operators

$$L_j=\sigma_j\cdot\sigma_{j+1}+1\ ,\quad A_j^{(a)}=\sum_{b,c}\epsilon_{abc}\sigma_j^b\sigma_{j+1}^c\ ,\quad B_j^{(a)}=\sigma_j^a+\sigma_{j+1}^a\ ,\quad a=x,y,z. \tag{4.212}$$

After a local basis rotation

$$\tau_j^a\to\tau_j^y\tau_j^a\tau_j^y\ ,\quad a=x,y,z \tag{4.213}$$

and setting the γ parameters to be equal for all jump operator terms we arrive at a Liouvillian

$$\mathcal{L}=4\gamma H(-4)-12L\gamma. \tag{4.214}$$

4.7 Scaling Limits of the Lindbladian

A standard way of generating integrable QFTs is by taking appropriate scaling limits of integrable lattice models. A paradigmatic example is the scaling limit of the Hubbard model, which gives rise to the integrable Yang-Gaudin model. An interesting question is whether we can carry out an analogous construction for our integrable Liouvillians and arrive at non-unitary integrable QFTs. The answer seems to be negative. Let us consider a lattice model with Hamiltonian

$$H_0=-t\sum_j c_j^\dagger c_{j+1}+c_{j+1}^\dagger c_j\ , \tag{4.215}$$

where c_j and $c_j^\dagger$ are annihilation and creation operators of spinless fermions, and jump operators

$$L_j = n_j = c_j^\dagger c_j \ . \tag{4.216}$$

They give rise to a Liouvillian associated with the Hubbard model with imaginary interaction strength

$$H = -t \sum_{\sigma\in\{\uparrow,\downarrow\}} \sum_{j=1}^{L} \left(c_{j,\sigma}^\dagger c_{j+1,\sigma} + c_{j+1,\sigma}^\dagger c_{j,\sigma} \right) + i\gamma \sum_{j=1}^{L} (n_{j,\uparrow} - \frac{1}{2})(n_{j,\downarrow} - \frac{1}{2}) \ . \tag{4.217}$$

The discrete spinful fermion operators can be mapped onto spinful fermionic fields

$$c_{j,\sigma} = \sqrt{a}\psi_\sigma(x_j) \ , \tag{4.218}$$

where $x_j = ja$ and a is the lattice constant. Taking a continuum limit of the lattice Hamiltonian

$$\begin{aligned} H &= \lim_{a\to 0}\{-at \sum_{\sigma\in\{\uparrow,\downarrow\}} \sum_{j=1}^{L} \left(\psi_\sigma^\dagger(x_j)\psi_\sigma(x_{j+1}) + \psi_\sigma^\dagger(x_{j+1})\psi_\sigma(x_j) \right) + ia^2\gamma \sum_{j=1}^{L} \rho_\uparrow(x_j)\rho_\downarrow(x_j)\} \\ &= \lim_{a\to 0}\{-t \sum_{\sigma\in\{\uparrow,\downarrow\}} \int dx \left(\psi_\sigma^\dagger(x)\psi_\sigma(x+a) + \psi_\sigma^\dagger(x+a)\psi_\sigma(x) \right) + ia\gamma \int dx \rho_\uparrow(x)\rho_\downarrow(x)\} \ , \end{aligned} \tag{4.219}$$

where we used the fact that

$$\lim_{a\to 0}\{a \sum_j f(x_j)\} = \int dx f(x) \ . \tag{4.220}$$

Taylor expanding the fermionic fields in the small parameter a, we get

$$\psi_\sigma^\dagger(x+a) = \psi_\sigma^\dagger(x) + a\frac{\partial\psi_\sigma^\dagger(x')}{\partial x'}\Big|_{x'=x} + \frac{a^2}{2}\frac{\partial^2\psi_\sigma^\dagger(x')}{\partial x'^2}\Big|_{x'=x} + \mathcal{O}(a^3) \ . \tag{4.221}$$

The nearest-neighbour hopping terms in the Hamiltonian then behave as

$$\begin{aligned} \mathcal{O}(a^0) \text{ terms} &: -2t \sum_\sigma \int dx \rho_\sigma(x) \rightarrow \text{ total number of particles is a conserved quantity,} \\ \mathcal{O}(a^1) \text{ terms} &: -at \sum_\sigma \int dx \frac{\partial}{\partial x}(\rho_\sigma(x)) \rightarrow \text{ surface term does not contribute,} \\ \mathcal{O}(a^2) \text{ terms} &: -\frac{ta^2}{2} \sum_\sigma \int dx \{\psi_\sigma^\dagger(x)\frac{\partial^2\psi_\sigma(x)}{\partial x^2} + \frac{\partial^2\psi_\sigma^\dagger(x)}{\partial x^2}\psi_\sigma(x)\} \\ &= ta^2 \sum_\sigma \int dx \frac{\partial\psi_\sigma^\dagger(x)}{\partial x}\frac{\partial\psi_\sigma(x)}{\partial x} \rightarrow \text{ kinetic energy term.} \end{aligned} \tag{4.222}$$

The Liouvillian becomes

$$\begin{aligned} H = &- \left(2t + i\frac{\gamma}{2}\right) \sum_{\sigma} \int dx \rho_{\sigma}(x) + i\gamma a \int dx \rho_{\uparrow}(x)\rho_{\downarrow}(x) \\ &- \frac{1}{2}ta^2 \sum_{\sigma\in\{\uparrow,\downarrow\}} \int dx \left\{ \psi_{\sigma}^{\dagger}(x) \frac{\partial^2 \psi_{\sigma}(x)}{\partial x^2} + \frac{\partial^2 \psi_{\sigma}^{\dagger}(x)}{\partial x^2} \psi_{\sigma}(x) \right\} . \end{aligned} \tag{4.223}$$

In analogy to the steps obtaining the Yang-Gaudin model as a scaling limit of the Hubbard model, we now consider the scaling limit

$$t \to \infty \, , \gamma \to \infty \, , a \to 0, \quad \text{with} \quad ta^2, \gamma a \quad \text{fixed.} \tag{4.224}$$

In this limit, we regularise the kinetic energy as well as the density-density interaction terms, but a problem occurs with the first term in equation (4.223). If γ were purely imaginary, as is the case for the Hubbard model, we could tune the chemical potential in such a way to ensure that the prefactor remains finite in the scaling limit. This would leave us with a Yang-Gaudin model at a finite density, but with imaginary interaction strength. However, given that γ is real and positive, as dictated by the Lindblad equation, we cannot take $\gamma \to i\infty$. This means that the only scaling limit requires $\gamma = 0$ and leads to a trivial case of no interactions. Analogously, it can be checked that the same holds when generalising the open quantum systems corresponding to higher-dimensional Hubbard extensions. This would appear to be a more general feature, independent of integrability.

4.8 Operator Space Fragmentation in Lindblad Dynamics

Recently, an alternative way of analysing Lindbladians has been established [235,236]. It turns out that certain vectorised Lindbladians exhibit strictly local conservation laws. Starting with a vectorised Lindblad equation as defined in (4.55), we can identify them with non-dynamical degrees of freedom acting as "defects" within the system. By fixing the occupation of each species of these defects we define "sectors" of the Lindbladian and in each sector the non-dynamical degrees of freedom result in the so-called "operator space fragmentation". This means that the Liouville space is partitioned into a direct sum of subspaces

$$\mathcal{H} \otimes \mathcal{H} \to \oplus_{\alpha} \mathcal{K}_{\alpha} \, , \tag{4.225}$$

which are invariant under the dissipative time evolution.

In our discussion, we concentrate on 1D spin chains with periodic boundary conditions as a representative example. The Lindblad projection onto subsystem sites in between two defects is independent from the rest of the system if the interactions are local (single-site or single-bond interactions). The static degrees of freedom effectively isolate certain sites of the chain from the rest of the system. Hence, we can consider the spectrum of the Lindbladian in each subspace separately and add these contributions for a complete spectral analysis in a given sector. Graphical representation of a system with defects is sketched in Figure 4.10.

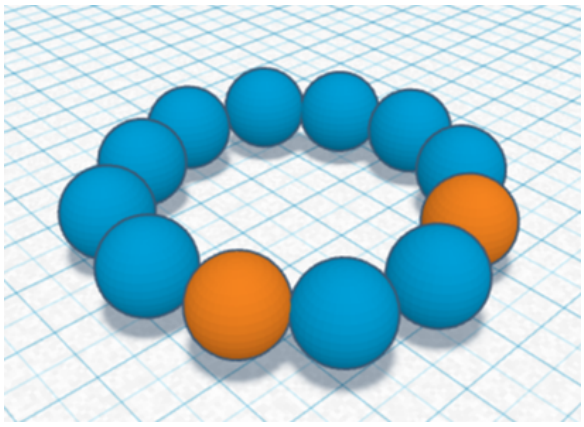


Figure 4.10: A 1D lattice with periodic boundary conditions. Lattice sites are occupied by dynamic (blue) or static (orange) degrees of freedom. Linbladian projections onto each subspace (blue sites separated from others by defects) have an independent spectrum for Lindblad operators with only single-site and single-bond interactions.

Consider an invariant subspace $\mathcal{K}_\alpha$ consisting of q sites with d-dimensional Hilbert space of the dynamical degrees of freedom at every site. Within the invariant subspace $\mathcal{K}_\alpha$, let us project the Liouvillian onto the reduced Hilbert space of purely the dynamical excitations. This means projecting out the defects and results in a Liouvillian form

$$\mathcal{L}|_{\mathcal{K}_\alpha} = \mathcal{B}_{\alpha_1} + \sum_{j=1}^{q-1} \mathcal{L}_{\alpha_j,\alpha_{j+1}} + \mathcal{B}_{\alpha_q} \ , \quad \dim(\mathcal{K}_\alpha) = d^q \ , \tag{4.226}$$

where $\mathcal{L}_{\alpha_j,\alpha_{j+1}}$ is the action of the Liouvillian on the dynamical degrees of freedom within the subsystem and $\mathcal{B}_{\alpha_{1/q}}$ are the boundary terms arising from the interactions of the dynamical excitations with the boundary defects. The projection reduces the number of degrees of freedom in the subspace of interest only to the dynamical degrees of freedom and in general leads to a form different to the two-legged ladder structure considered earlier. In analogy to section 4.6, we can look for integrable

Hamiltonians which can be mapped onto this open problem. Crucially, the structure of the projected Liouvillian is not the same as of the original Lindblad equation and hence a potentially wider range of integrable Hamiltonians can be found to have a Lindblad equivalent. Then, integrability techniques can assist us in determining the spectrum in each subspace, which combined give us the Lindbladian spectrum for a given sector with a fixed number of defects. Still, entanglement between the sectors generally exists if the density matrix describing the state of the system is entangled. This makes determining the dynamics of observables in a system with operator space fragmentation a highly non-trivial problem, analysed in detail only in the free fermion case [236].

In the following, we will review some of the results published in [235, 236] and present some contributions to this field done in close collaboration with the authors of these works.

4.9 Spin-1/2 Dissipative Chains

We present several examples of spin-1/2 open quantum systems which admit operator space fragmentation in their vectorised form and have a correspondence to an integrable XXZ Hamiltonian. Consider a purely dissipative Liouvillian with four jump operators per site

$$L_j^{(1)} = \sigma_j^+ \sigma_{j+1}^- \ , \ L_j^{(2)} = \sigma_j^- \sigma_{j+1}^+ \ , \ L_j^{(3)} = \sigma_j^+ \sigma_{j+1}^+ \ , \ L_j^{(4)} = \sigma_j^- \sigma_{j+1}^- \ , \tag{4.227}$$

and rates J_1, J_2, J_3 and J_4 respectively. We assume periodic boundary conditions unless otherwise stated. In the vectorised form, we arrive at two species of spin-1/2 operators (4.143), which can be mapped onto four-dimensional Hubbard operators according to a prescription

$$\sigma_j^+ \tau_j^+ = E_j^{14}, \quad \frac{1}{2}(\sigma_j^z + \tau_j^z) = E_j^{11} - E_j^{44}, \quad \frac{1}{2}(\sigma_j^z - \tau_j^z) = E_j^{22} - E_j^{33} \ . \tag{4.228}$$

The vectorised Liouvillian is explicitly block-diagonal in this basis and takes a form

$$\begin{aligned}\mathcal{L} =& \sum_{j=1}^{L} J_1 E_j^{14} E_{j+1}^{41} + J_2 E_j^{41} E_{j+1}^{14} - J_1 E_j^{44} E_{j+1}^{11} - J_2 E_j^{11} E_{j+1}^{44} \\ &-\frac{1}{2}\sum_{j=1}^{L} \left(E_j^{22} + E_j^{33}\right)\left(J_1 E_{j+1}^{11} + J_2 E_{j+1}^{44}\right) + \left(E_{j+1}^{22} + E_{j+1}^{33}\right)\left(J_2 E_j^{11} + J_1 E_j^{44}\right) \\ &-\frac{1}{2}\sum_{j=1}^{L} (J_1 + J_2)\left(E_j^{22} E_{j+1}^{33} + E_j^{33} E_{j+1}^{22}\right) \\ &+\sum_{j} J_3 E_j^{14} E_{j+1}^{14} + J_4 E_j^{41} E_{j+1}^{41} - J_3 E_j^{44} E_{j+1}^{44} - J_4 E_j^{11} E_{j+1}^{11} \\ &-\frac{1}{2}\sum_{j=1}^{L} \left(E_j^{22} + E_j^{33}\right)\left(J_4 E_{j+1}^{11} + J_3 E_{j+1}^{44}\right) + \left(E_{j+1}^{22} + E_{j+1}^{33}\right)\left(J_4 E_j^{11} + J_3 E_j^{44}\right) \\ &-\frac{1}{2}\sum_{j=1}^{L} (J_3 + J_4)\left(E_j^{22} E_{j+1}^{22} + E_j^{33} E_{j+1}^{33}\right) \ .\end{aligned} \tag{4.229}$$

This Liouvillian conserves the number of excitations 2 and 3 at each site, which can be checked directly

$$[\mathcal{L}, E_j^{22}] = [\mathcal{L}, E_j^{33}] = 0 \ , \tag{4.230}$$

so we identify these degrees of freedom as static defects. The vectorised problem in equation (4.229) has four degrees of freedom per site. Yet, as two of them do not participate in the dynamics, we can project them out and reduce the problem to an effective Hamiltonian with again only two degrees of freedom per site. In the sector with no defects, the Liouvillian projection onto the space of dynamical excitations $\{1, 4\}$ takes a form

$$\begin{aligned}\mathcal{L}_{\{1,4\}} = \sum_{j=1}^{L} \Big\{ & J_1 E_j^{14} E_{j+1}^{41} + J_2 E_j^{41} E_{j+1}^{14} - J_1 E_j^{44} E_{j+1}^{11} - J_2 E_j^{11} E_{j+1}^{44} \\ & + J_3 E_j^{14} E_{j+1}^{14} + J_4 E_j^{41} E_{j+1}^{41} - J_3 E_j^{44} E_{j+1}^{44} - J_4 E_j^{11} E_{j+1}^{11} \Big\} \ .\end{aligned} \tag{4.231}$$

Let us denote the reduced local Hilbert space states by

$$|1\rangle \to \left|\tilde{1}\right\rangle \ , \ |4\rangle \to \left|\tilde{2}\right\rangle \ . \tag{4.232}$$

The reduced Liouvillian can then be recast in the basis of canonical Pauli matrices and regain the interpretation as a spin-1/2 chain with periodic boundary conditions

$$\begin{aligned}\mathcal{L}_{\{1,4\}} = &\sum_{j=1}^{L}\Big\{ J_1\sigma_j^+\sigma_{j+1}^- + J_2\sigma_j^-\sigma_{j+1}^+ + J_3\sigma_j^+\sigma_{j+1}^+ + J_4\sigma_j^-\sigma_{j+1}^-\Big\} \\ &+\frac{1}{4}\sum_{j=1}^{L}\Big\{ (J_1+J_2-J_3-J_4)\sigma_j^z\sigma_{j+1}^z - (J_1+J_2+J_3+J_4) + 2(J_3-J_4)\sigma_j^z\Big\} \ .\end{aligned} \tag{4.233}$$

The same procedure can be repeated in the sectors with the non-dynamical degrees of freedom occupied. Consider defects of type either 2 or 3 located on sites α_1 and α_q. The Liouvillian acting on the sites in between the defects (an invariant subspace) is an open boundary chain of the form

$$\begin{aligned}\mathcal{L}_{\{1,4\}}^{[\alpha_1,\alpha_q]} = &\sum_{j=1}^{q-1}\Big\{ J_1\sigma_j^+\sigma_{j+1}^- + J_2\sigma_j^-\sigma_{j+1}^+ + J_3\sigma_j^+\sigma_{j+1}^+ + J_4\sigma_j^-\sigma_{j+1}^-\Big\} \\ &+\frac{1}{4}\sum_{j=1}^{q-1}\Big\{ (J_1+J_2-J_3-J_4)\sigma_j^z\sigma_{j+1}^z - (J_1+J_2+J_3+J_4) + 2(J_3-J_4)\sigma_j^z\Big\} \\ &-\frac{1}{2}(J_1+J_2+J_3+J_4) \ .\end{aligned} \tag{4.234}$$

The complete Liouvillian is a sum of these open chains of different lengths and a constant contribution from any two or more consecutive $\{2,3\}$ defect sites

$$\begin{aligned}\mathcal{L}_{\{2,3\}}^{[\beta_1,\beta_r]} = -\frac{1}{2}\sum_{j=1}^{r-1}\Big\{ &(J_1+J_2)\left(E_j^{22}E_{j+1}^{33} + E_j^{33}E_{j+1}^{22}\right) \\ &+(J_3+J_4)\left(E_j^{22}E_{j+1}^{22} + E_j^{33}E_{j+1}^{33}\right)\Big\} \ ,\end{aligned} \tag{4.235}$$

where $r \geq 2$ is the number of consecutive defect sites and $\beta_1, \ldots, \beta_r$ label the defect sites. The constant contribution makes it apparent that the more blocks of two or more consecutive defects are in the sector, the quicker the state is going to decay in the open system time evolution. We determined numerically that a state corresponding to the zero eigenvalue can be found in the sector with only excitation of 1 and 4 type, as in equation (4.233). The other sectors, with non-zero 2 and 3 occupancy, have a gap at least of the order of

$$\lambda_{gap} = -\frac{J_1+J_2+J_3+J_4}{2} \ . \tag{4.236}$$

4.9.1 Asymmetric Simple Exclusion Process

First, consider the case of only asymmetric hopping jump operators studied in [235]. This requires setting the rates in equation (4.227) to

$$J_3 = 0, \quad J_4 = 0 \ , \tag{4.237}$$

while keeping J_1, J_2 as free parameters. Projecting out the defect degrees of freedom, the Liouvillian can be identified with a spin-1/2 model with periodic boundary conditions

$$\mathcal{L}_{ASEP} = \sum_{j=1}^{L} \left\{ J_1 \sigma_j^+ \sigma_{j+1}^- + J_2 \sigma_j^- \sigma_{j+1}^+ + \frac{1}{4}(J_1 + J_2)(\sigma_j^z \sigma_{j+1}^z - 1) \right\} \tag{4.238}$$

in a sector with no defects. This is an Asymmetric Simple Exclusion Process (ASEP), which is known to be integrable by virtue of mapping it onto an XXZ Hamiltonian [280]. The required similarity transformation is

$$S = \prod_j S_j \ , \quad S_j = \begin{pmatrix} 1 & 0 \\ 0 & Q^{j-1} \end{pmatrix}_j \ , \tag{4.239}$$

with $Q = \sqrt{J_1/J_2}$. The spin-1/2 operators map under this transformation to

$$S^{-1}\sigma_j^+ S \to Q^{j-1}\sigma_j^+ \ , \quad S^{-1}\sigma_j^{+-} S \to Q^{1-j}\sigma_j^- \ , \quad S^{-1}\sigma_j^z S \to \sigma_j^z \ . \tag{4.240}$$

The Liouvillian in a sector with no defects becomes

$$\begin{aligned} S^{-1}\mathcal{L}_{ASEP} S =& \frac{J}{8} \sum_{j=1}^{L-1} \left\{ \sigma_j^x \sigma_{j+1}^x + \sigma_j^y \sigma_{j+1}^y + \Delta \left(\sigma_j^z \sigma_{j+1}^z - 1 \right) \right\} \\ &+ \frac{J}{4} \left(Q^L \sigma_L^+ \sigma_1^- + Q^{-L} \sigma_L^- \sigma_1^+ \right) + \frac{J\Delta}{8} \left(\sigma_L^z \sigma_1^z - 1 \right), \end{aligned} \tag{4.241}$$

where

$$J = 4\sqrt{J_1 J_2}, \quad \Delta = \frac{J_1 + J_2}{4\sqrt{J_1 J_2}} \ . \tag{4.242}$$

This is XXZ Hamiltonian on a ring with twisted boundary conditions, which preserve integrability [280].

In the sectors with defects present, the Liouvillian acting on each subspace transforms as ASEP with open boundary conditions

$$\begin{aligned} S^{-1}\mathcal{L}_{ASEP}^{[\alpha_1,\alpha_q]} S = & \frac{J}{8} \sum_{j=1}^{q-1} \sigma_j^x \sigma_{j+1}^x + \sigma_j^y \sigma_{j+1}^y + \Delta \left(\sigma_j^z \sigma_{j+1}^z - 1 \right) \\ &+ \frac{J}{8} \sqrt{\Delta^2 - 1/4} \left(\sigma_1^z - \sigma_L^z \right) \ , \end{aligned} \tag{4.243}$$

leading to an open XXZ chain with diagonal boundary fields, also an integrable model.

4.9.1.1 Additional Terms

We considered introducing additional jump operators as well as a Hamiltonian to the open system defined in (4.237) under a condition they commute with the remainder of the Liouvillian and thus do not break the integrability of the ASEP. Starting from an ansatz in a vectorised form

$$\mathcal{L}_{add} = \sum_{j=1}^{L} \left\{ f_{\alpha\beta} E_j^{\alpha\alpha} E_{j+1}^{\beta\beta} + h_{\alpha\beta} E_j^{\alpha\beta} \right\} \ , \tag{4.244}$$

we discovered that the additional jump operators fulfilling this critarion are

$$L_j \in \{\sigma_j^z, \sigma_j^z + \sigma_{j+1}^z, \sigma_j^z \sigma_{j+1}^z\} \ . \tag{4.245}$$

All of them result in only density-density interactions between different excitations species.

Moreover, without breaking integrability we can accommodate a jump operator

$$L_j^{(5)} = \sigma_j^+ \sigma_{j+1}^- + \sigma_j^- \sigma_{j+1}^+ \tag{4.246}$$

with rate J_5. Together with jump operators $L_j^{(1)}, L_j^{(2)}$ defined in equation (4.227), the vectorised Liouvillian for such a model is

$$(1 + J_5)\mathcal{L} + J_3 \sum_j \left\{ E_j^{23} E_{j+1}^{32} + E_j^{32} E_{j+1}^{23} \right\} \ , \tag{4.247}$$

where $\mathcal{L}$ is the original ASEP Liouvillian with only two jump operators $L_j^{(1)}, L_j^{(2)}$. Hence, one can add to the Liouvillian an independent Symmetric Simple Exclusion Process (SSEP) in the $2, 3$ particle sector. SSEP is simply an ASEP with equal hopping rates and is similarly integrable.

Furthermore, the following Hamiltonian can be accommodated

$$H^{(1)} = \lambda \sum_{j=1}^{L} \sigma_j^z \ . \tag{4.248}$$

Only in the presence of defects it contributes to the vectorised Liouvillian an imaginary conserved term

$$\mathcal{L}_{add}^{(1)} = -2i\lambda \sum_{j=1}^{L} (E_j^{22} - E_j^{33}) \ . \tag{4.249}$$

Alternatively, consider a Hamiltonian

$$H^{(2)} = \lambda \sum_{j=1}^{L} \sigma_j^z \sigma_{j+1}^z \ . \tag{4.250}$$

As part of a vectorised Liouvillian, it contributes density-density interactions

$$\mathcal{L}^{(2)}_{add} = -2i\lambda \sum_{j=1}^{L} \left\{ (E^{22}_j - E^{33}_j)(E^{11}_{j+1} - E^{44}_{j+1}) + (E^{22}_{j+1} - E^{33}_{j+1})(E^{11}_j - E^{44}_j) \right\} \ . \tag{4.251}$$

These give non-zero contribution to the dynamics only in the sectors with defects and result in imaginary boundary fields for an open ASEP in each subspace

$$\mathcal{L}^{(2),[\alpha_1,\alpha_q]}_{add} = -2i\lambda \left\{ (\delta_{i,2} - \delta_{i,3})(E^{11}_1 - E^{44}_1) + (\delta_{f,2} - \delta_{f,3})(E^{11}_l - E^{44}_l) \right\} \ , \tag{4.252}$$

where by i, f we have denoted the species of the initial and final defect constraining the subspace. Carrying out the similarity transformation (4.239), the contribution to the XXZ Hamiltonian is of the form of boundary diagonal fields with imaginary values

$$\mathcal{L}^{(2),[\alpha_1,\alpha_q]}_{add} = -2i\lambda \left\{ (\delta_{i,2} - \delta_{i,3})\sigma^z_1 + (\delta_{f,2} - \delta_{f,3})\sigma^z_l \right\} \ , \tag{4.253}$$

which preserve integrability.

4.9.2 Symmetric Simple Exclusion Process with Balanced Particle Creation and Annihilation

As a second case, consider jump operators describing symmetric hopping together with particle creation and annihilation at equal rates. This requires setting the rates in equation (4.227) to

$$J_1 = J_2 = J', \quad J_3 = J_4 = \gamma' \ . \tag{4.254}$$

When no defects are present, the Liouvillian in the reduced Hilbert space is a chain of two level sites. Mapped onto spin-1/2 basis it takes a form

$$\mathcal{L}_{SSEP} = \frac{1}{2} \sum_{j=1}^{L} \left[(J' + \gamma')\sigma^x_j \sigma^x_{j+1} + (J' - \gamma') \left(\sigma^y_j \sigma^y_{j+1} + \sigma^z_j \sigma^z_{j+1} - 1 \right) \right] \ . \tag{4.255}$$

Applying a unitary transformation

$$U = \prod_j U_j \ , \quad U_j = \frac{1}{\sqrt{2}} \begin{pmatrix} 1 & 1 \\ 1 & -1 \end{pmatrix}_j \ , \tag{4.256}$$

the transformed Liouvillian is again an XXZ chain with periodic boundary conditions

$$U^\dagger \mathcal{L}_{SSEP} U = \frac{J}{4} \sum_{j=1}^{L} \left[\sigma^x_j \sigma^x_{j+1} + \sigma^y_j \sigma^y_{j+1} + \Delta \sigma^z_j \sigma^z_{j+1} \right] - \frac{L+1}{2}(J' + \gamma') \ , \tag{4.257}$$

where

$$J = 2\left(J' - \gamma'\right), \qquad \Delta = \frac{J' + \gamma'}{J' - \gamma'} \ . \tag{4.258}$$

The dynamics of this model can be studied by examining the solutions to BAE for the XXZ Hamiltonian. In sectors with defects, the dynamics in each subspace are governed by an open XXZ model with diagonal boundary conditions

$$U^{\dagger}\mathcal{L}_{SSEP}^{[\alpha_1,\alpha_q]}U = \frac{J}{4}\sum_{j=1}^{q-1}\left[\sigma_j^x\sigma_{j+1}^x + \sigma_j^y\sigma_{j+1}^y + \Delta\sigma_j^z\sigma_{j+1}^z\right] - \frac{q+1}{2}(J' + \gamma') \ . \tag{4.259}$$

This model also admits a free fermion point when all the rates considered are equal

$$J_1 = J_2 = J_3 = J_4 \ . \tag{4.260}$$

The model with this choice of rates has been studied in depth in [236].

4.9.3 Correlated Hopping with Correlated Particle Creation and Annihilation

Alternatively, one can also consider a Liouvillian with two jump operators per site

$$l_j^{(1)} = \sigma_j^+\sigma_{j+1}^- + \sigma_j^-\sigma_{j+1}^+ \ , \ l_j^{(2)} = \sigma_j^+\sigma_{j+1}^+ + \sigma_j^-\sigma_{j+1}^- \ , \tag{4.261}$$

and rates γ_1 and γ_2 respectively. The resultant vectorised Liouvillian mapped onto E-matrices via (4.228) is

$$\begin{aligned}\mathcal{L} = \sum_{j=1}^{L}\Big\{&\gamma_1\left[E_j^{14}E_{j+1}^{41} + E_j^{41}E_{j+1}^{14} + E_j^{23}E_{j+1}^{32} + E_j^{32}E_{j+1}^{23}\right] \\ &+ \gamma_2\left[E_j^{14}E_{j+1}^{14} + E_j^{41}E_{j+1}^{41} + E_j^{23}E_{j+1}^{23} + E_j^{32}E_{j+1}^{32}\right] - (\gamma_1 + \gamma_2) \\ &+ \frac{\gamma_1 - \gamma_2}{2}\left[(E_j^{11} - E_j^{44})(E_{j+1}^{11} - E_{j+1}^{44}) + (E_j^{22} - E_j^{33})(E_{j+1}^{22} - E_{j+1}^{33})\right]\Big\}\end{aligned} \tag{4.262}$$

and corresponds to two independent XXZ chains in $\{1,4\}$ or $\{2,3\}$ particle species. In sectors with only $\{1,4\}$ or $\{2,3\}$ occupancy, the Liouvillian projection onto a reduced Hilbert space is

$$\mathcal{L} = \frac{1}{2}\sum_{j=1}^{L}\left[(\gamma_1 + \gamma_2)(\sigma_j^x\sigma_{j+1}^x - 1) + (\gamma_1 - \gamma_2)\left(\sigma_j^y\sigma_{j+1}^y + \sigma_j^z\sigma_{j+1}^z\right)\right] \ . \tag{4.263}$$

4.9.4 XXZ Bethe Ansatz

All of the discussed Lindbladians with operator space fragmentation can be studied by investigating the spectrum of the XXZ model. XXZ BAE differ depending on the boundary conditions and an appropriate form of the equations needs to be used in each case. As an example, let us consider the vectorised Liouvillian (4.259) acting on a subspace in between defects. It has a structure of an open boundaries XXZ chain of length N

$$H_{XXZ} = \frac{J}{4}\sum_{j=1}^{N-1}\left[\sigma_j^x\sigma_{j+1}^x + \sigma_j^y\sigma_{j+1}^y + \Delta\sigma_j^z\sigma_{j+1}^z\right] \ . \tag{4.264}$$

As a reference state, choose a chain with all N spins up. Its eigenvalue is

$$E_0 = \frac{N-1}{4}J\Delta \ . \tag{4.265}$$

In a sector of M flipped spins, the relevant Bethe Ansatz Equations are [281]

$$\begin{aligned}\left[\frac{\sinh\left[\gamma\left(u_j+\frac{i}{2}\right)\right]}{\sinh\left[\gamma\left(u_j-\frac{i}{2}\right)\right]}\right]^{2N}&\left[\frac{\cosh\left[\gamma\left(u_j-\frac{i}{2}\right)\right]}{\cosh\left[\gamma\left(u_j+\frac{i}{2}\right)\right]}\right]^{2}\\ &= \prod_{k\neq j}^{M}\frac{\sinh\left[\gamma\left(u_j-u_k+i\right)\right]\sinh\left[\gamma\left(u_j+u_k+i\right)\right]}{\sinh\left[\gamma\left(u_j-u_k-i\right)\right]\sinh\left[\gamma\left(u_j+u_k-i\right)\right]} \ ,\end{aligned} \tag{4.266}$$

where $\gamma = \arccos\Delta$. The roots of BAE are related to the momenta through

$$e^{ik_j} = \frac{\sinh\left[\gamma\left(u_j+\frac{i}{2}\right)\right]}{\sinh\left[\gamma\left(u_j-\frac{i}{2}\right)\right]} \tag{4.267}$$

and the energy of each solution is

$$E = E_0 + J\sum_{j=1}^{M}\frac{\sin^2\gamma}{\cos\gamma-\cosh\left(2\gamma u_j\right)} = E_0 + J\sum_{j=1}^{M}\left(\cos k_j - \Delta\right) \ . \tag{4.268}$$

For a complete spectral analysis of the Liouvillian described in section 4.9.2, the BA for the XXZ model with periodic boundary conditions also needs to be considered.

4.9.5 Higher Dimensional Generalisation

Let us consider a generalisation of the Liouvillian described by the jump operators (4.227), in which the dimension of the local Hilbert space is $n_A + n_B = n$. Let us partition the state vector labels into two, disjoint sets $A \cap B = \varnothing$

$$A = \{\alpha_1, \ldots, \alpha_{n_A}\} \ , \qquad B = \{\beta_1, \ldots, \beta_{n_B}\} \ . \tag{4.269}$$

Now, consider a Liouvillian with $2n_An_B$ jump operators per site

$$L_j^{\alpha\beta} = e_j^{\alpha\beta} e_{j+1}^{\beta\alpha} \ , \ L_j^{\beta\alpha} = e_j^{\beta\alpha} e_{j+1}^{\alpha\beta} \tag{4.270}$$

and different rates, J_1 for $L_j^{\alpha\beta}$ operators and J_2 for $L_j^{\beta\alpha}$ operators. The vectorised Liouvillain takes a form

$$\begin{aligned}\mathcal{L} = \sum_{j=1}^{L} \sum_{\alpha\in A} \sum_{\beta\in B} \Big\{ & J_1 \left[e_j^{\alpha\beta} \tilde{e}_j^{\alpha\beta} e_{j+1}^{\beta\alpha} \tilde{e}_{j+1}^{\beta\alpha} - \frac{1}{2} \left(e_j^{\beta\beta} e_{j+1}^{\alpha\alpha} + \tilde{e}_j^{\beta\beta} \tilde{e}_{j+1}^{\alpha\alpha} \right) \right] \\ & + J_2 \left[e_j^{\beta\alpha} \tilde{e}_j^{\beta\alpha} e_{j+1}^{\alpha\beta} \tilde{e}_{j+1}^{\alpha\beta} - \frac{1}{2} \left(e_j^{\alpha\alpha} e_{j+1}^{\beta\beta} + \tilde{e}_j^{\alpha\alpha} \tilde{e}_{j+1}^{\beta\beta} \right) \right] \Big\}.\end{aligned} \tag{4.271}$$

The two species of the Hubbard operators can be represented as a single species of higher dimensional Hubbard operators acting on the entire local superspace

$$e_j^{\alpha\beta} \tilde{e}_j^{\gamma\delta} = E_j^{ab} \ , \tag{4.272}$$

such that $a = n(\alpha - 1) + \gamma$ and $b = n(\beta - 1) + \delta$. Consider partitioning the labels of the new superstate vectors into disjoint sets

$$\begin{aligned} A_1 &= \{a_1, \ldots, a_{n_A}\} : \forall_i \, |\alpha_i\rangle \, |\alpha_i\rangle\!\rangle = |a_i\rangle \ , \\ B_1 &= \{b_1, \ldots, b_{n_B}\} : \forall_i \, |\beta_i\rangle \, |\beta_i\rangle\!\rangle = |b_i\rangle \ , \\ A_2 &= \{a'_1, \ldots, a'_{(n_A-1)n_A}\} : |\alpha_i\rangle \, |\alpha_j\rangle\!\rangle = |a'_k\rangle \quad \text{if} \quad i \neq j \ , \\ B_2 &= \{b'_1, \ldots, b'_{(n_B-1)n_B}\} : |\beta_i\rangle \, |\beta_j\rangle\!\rangle = |b'_k\rangle \quad \text{if} \quad i \neq j \ , \\ C_1 &= \{c_1, \ldots, c_{n_An_B}\} : \forall_{i,j} \, |\alpha_i\rangle \, |\beta_j\rangle\!\rangle = |c_k\rangle \ , \\ C_2 &= \{c'_1, \ldots, c'_{n_An_B}\} : \forall_{i,j} \, |\beta_i\rangle \, |\alpha_j\rangle\!\rangle = |c'_k\rangle \ . \end{aligned} \tag{4.273}$$

The superspace Liouvillian density acting on each site of the chain is then

$$\begin{aligned}\mathcal{L}_j = & \sum_{a\in A_1} \sum_{b\in B_1} \left\{ J_1 E_j^{ab} E_{j+1}^{ba} + J_2 E_j^{ba} E_{j+1}^{ab} - J_1 E_j^{bb} E_{j+1}^{aa} - J_2 E_j^{aa} E_{j+1}^{bb} \right\} \\ & - \sum_{a'\in A_2} \sum_{b'\in B_2} \left\{ J_1 E_j^{b'b'} E_{j+1}^{a'a'} + J_2 E_j^{a'a'} E_{j+1}^{b'b'} \right\} - \sum_{a\in A_1} \sum_{b'\in B_2} \left\{ J_1 E_j^{b'b'} E_{j+1}^{aa} + J_2 E_j^{aa} E_{j+1}^{b'b'} \right\} \\ & - \sum_{a'\in A_2} \sum_{b\in B_1} \left\{ J_1 E_j^{bb} E_{j+1}^{a'a'} + J_2 E_j^{a'a'} E_{j+1}^{bb} \right\} \\ & - \frac{1}{2} \left\{ \sum_{c\in C_1} E_j^{cc} + \sum_{c'\in C_2} E_j^{c'c'} \right\} \left\{ J_1 \left(\sum_{a\in A_1} E_{j+1}^{aa} + \sum_{a'\in A_2} E_{j+1}^{a'a'} \right) + J_2 \left(\sum_{b\in B_1} E_{j+1}^{bb} + \sum_{b'\in B_2} E_{j+1}^{b'b'} \right) \right\} \\ & - \frac{1}{2} \left\{ \sum_{c\in C_1} E_{j+1}^{cc} + \sum_{c'\in C_2} E_{j+1}^{c'c'} \right\} \left\{ J_2 \left(\sum_{a\in A_1} E_j^{aa} + \sum_{a'\in A_2} E_j^{a'a'} \right) + J_1 \left(\sum_{b\in B_1} E_j^{bb} + \sum_{b'\in B_2} E_j^{b'b'} \right) \right\} \\ & - \frac{1}{2} \sum_{c\in C_1} \sum_{c'\in C_2} (J_1 + J_2) \left\{ E_j^{cc} E_{j+1}^{c'c'} + E_j^{c'c'} E_{j+1}^{cc} \right\} \ .\end{aligned} \tag{4.274}$$

The only dynamical degrees of freedom can be found in the set $A_1 \cup B_1$. The Liouvillian projection onto the reduced Hilbert space of only the dynamical excitations is

$$\mathcal{L}_{A_1\cup B_1} = \sum_{j=1}^{L} \sum_{a\in A_1} \sum_{b\in B_1} \left\{ J_1 E_j^{ab} E_{j+1}^{ba} + J_2 E_j^{ba} E_{j+1}^{ab} - J_1 E_j^{bb} E_{j+1}^{aa} - J_2 E_j^{aa} E_{j+1}^{bb} \right\} \tag{4.275}$$

in the sector with no defects. In sectors with a finite number of defects, the Liouvillian projection within each subspace becomes an open chain with boundary fields. The exact form of the Liouvillian depends on the flavour of the defects that form the subspace boundary.

If the dimension of set A_1 or B_1 is 1, then the Liouvillian in equation (4.275) takes a form of multispecies ASEP. This model is not integrable, but has been studied extensively both in the case of periodic [282,283] and open [284] boundary conditions relevant here. Using a matrix product ansatz, the authors of [282, 283] determined the stationary state for an ASEP with an arbitrary number of particle species and additionally the spectrum and eigenvectors in the totally asymmetric case. In the case of open boundary conditions, only the stationary state is known which also has a matrix product form [284].

4.9.6 XYZ Model in Operator Space Fragmentation

We have considered whether a dissipative Liouvillian can lead to an anisotropic spin-1/2 chain referred to as the XYZ Hamiltonian [8, 72]

$$H_{XYZ} = \sum_{j=1}^{L} \left[\Delta_Z (\sigma_j^z \sigma_{j+1}^z - 1) + \Delta_Y \sigma_j^y \sigma_{j+1}^y + \Delta_X \sigma_j^x \sigma_{j+1}^x \right] . \tag{4.276}$$

To this end, we applied the inverse of the similarity transformation defined in (4.239). The result in the Hubbard operator basis is

$$\begin{aligned} S H_{XYZ} S^{-1} = &- \frac{\Delta_X + \Delta_Y}{\sqrt{J_1 J_2}} \sum_{j=1}^{L} \Bigg\{ J_1 E_j^{14} E_{j+1}^{41} + J_2 E_j^{41} E_{j+1}^{14} \\ &+ \frac{\Delta_X - \Delta_Y}{\Delta_X + \Delta_Y} \left[J_1 \left(\frac{J_2}{J_1} \right)^j E_j^{14} E_{j+1}^{14} + J_2 \left(\frac{J_1}{J_2} \right)^j E_j^{41} E_{j+1}^{41} \right] \\ &+ \frac{\Delta_Z}{\Delta_X + \Delta_Y} \left(E_j^{11} - E_j^{44} \right) \left(E_{j+1}^{11} - E_{j+1}^{44} \right) \Bigg\} . \end{aligned} \tag{4.277}$$

For $\Delta_X \neq \Delta_Y$, we necessarily have the terms with site-dependent pre-factors. One could attempt incorporating them into site-dependent rates for the jump operators

in the Liouvillian. Unfortunately, the corresponding jump operators also produce integrability breaking diagonal terms multiplied by the same rates. We conclude that it is impossible to obtain an XYZ Hamiltonian from a Liouvillian with operator-space fragmentation using this form of a similarity transformation.

4.10 Discussion

We have focused on translationally invariant situations where jump operators act on bonds or sites of a 1D chain and derived a superoperator representation for lattice models with both fermionic and bosonic degrees of freedom. In this representation, the Lindblad equation takes the form of an imaginary time Schrödinger equation with a non-Hermitian "Hamiltonian", which can be thought of in terms of a two-legged ladder model of interacting spins or fermions. Most prominently, we discovered that a wide class of generalized Hubbard models can be interpreted as Liouvillians of Lindblad equations and this fact can be traced back to their integrability structure. Some of the corresponding dissipative models are highly physically interesting, an example being the infinite-U Hubbard model subject to on-site dephasing noise. As the jump operators in this class of models are Hermitian, the completely mixed state is a steady state in all cases. Using the BA solution we have shown for a subclass of generalized Hubbard models that the Liouvillian gap vanishes like L^{-2} as the thermodynamic limit is approached. The eigenstates closest to the gap correspond to particle-like "excitations" with quadratic dispersions, which suggests that the late-time behaviour in these models is likely to be diffusive.

We have also identified Yang-Baxter integrable Lindblad equations that are not generalized Hubbard models by showing that certain known integrable Hamiltonians can be cast in the form of Liouvillians associated with a Lindblad equation. However, in many cases considered, such mappings are not possible. To help identify these incompatible cases, an analysis of several unsuccessful mappings is presented. We stress that in this work we have focused on a particular "direct" relation between Liouvillians of Lindblad equations and Hamiltonians of Yang-Baxter integrable models. There are known cases where it is possible to establish such relationships by means of more complicated, non-local maps [229]. Moreover, as we pointed out in subsection 4.239, one ought to allow for similarity transformations that maintain locality of the Hamiltonian density in integrable models when trying to establish relations with Lindblad equations.

We have only briefly explored using methods of quantum integrability to obtain physical properties of a subgroup of the generalised Hubbard models and a broader investigation into this issue is required. Building on our work, it would be interesting to determine the spectrum of the Liouvillians given in terms of the solutions of the relevant BAE. It is well understood that the nature of solutions to BAE changes quite substantially when a parameter is made complex, and even in the simplest case of the Hubbard model the structure of Bethe roots appears to be non-trivial. Ultimately one would like to determine the dynamics of general Green's functions from a given initial density matrix $\rho(0)$. In some of the cases discussed above this is relatively simple because the equations of motion for these Green's functions decouple and for two-point functions can thus either be integrated numerically or determined from the exact Liouvillian eigenstates in the two-particle sector [285]. In subsection 4.6.2.1, we presented an example of such an analysis for the time evolution of the single-particle Green's functions in the case of a $SU(2)$ Hubbard model via direct integration. To our knowledge, this has not been explored before. Still, in cases like the 3-state Maassarani model a more involved analysis is required and it would be informative to investigate it in more detail.

At the same time, the operator space fragmentation approach opens a new door to look for integrable models without the ladder structure yet still related to Lindblad dynamics. In particular, we showed that certain open systems can be related in each sector to the integrable XXZ Hamiltonian and in these cases spectra of the Lindbladian can be determined with BA methods. Unfortunately, with the same type of mapping we could not accommodate the physically richer XYZ model. We have also found a Lindblad open system whose dynamics in every sector are described by a multispecies ASEP, a model that is not integrable, but is of physical interest and its spectrum is known in special cases [282].

Chapter 5

Conclusion and Outlook

In this work, we investigated dynamical properties of specific many-body, interacting quantum systems. Employing the techniques of integrability, we have obtained new insight into representative processes of instability and decay.

We uncovered novel features of unstable excitations in the context of an integrable QFT. Since decaying particles are not part of the asymptotic spectrum, their presence is only felt through the effect they have on physical quantities associated either to the theory as a whole, such as scaling and correlation functions, or to the stable particles themselves. Concentrating on the dynamical behaviour of thermodynamic quantities, we demonstrated that the presence of unstable excitations dramatically and permanently alters the features of the densities and effective velocities associated to the stable constituents. Within the GHD framework, we identified dynamic signatures of the presence of unstable particles, such as the formation of tails and partial decay of the primary peaks in quantities such as spectral density and particle density. Additionally, in the presence of a finite energy density background, a new hydrodynamic phenomenon comes into play. We find the long-time persistence of a small but significant wave of unstable particles "riding" on top of the bath, propelled by its interaction with the large wave of particles of the opposite type. We expect the signatures identified to be universal.

The next step in further understanding the physics of unstable excitations in QFTis to look at theories with higher particle content in the spectrum and multiple species of unstable excitations. Integrable examples of these are the HSG models associated with higher rank Lie algebras. There, we expect to find even more intricate structures for the observables and intriguing relations between unstable particles of different types.

Another avenue to pursue is the investigation of the scattering processes between the unstable particles themselves. By constructing a suitable quench protocol, one

can attempt to numerically measure their relative scattering phases and in doing so construct an effective theory for the unstable particles.

Making a link between open systems and integrable models opens up access to the powerful machinery of integrability and allows us to employ it in the service of understanding the dissipative quantum dynamics. This work established such a link in a number of representative cases as well as presented some analysis of the physical properties enabled by this connection. It is worth emphasizing that the examples presented are not merely isolated instances, but entire families of models whose algebraic structure is the basis of establishing the Lindblad-integrability mapping. Having a number of Lindbladians that can now be better analytically understood increases their potential relevance to experiments.

Our findings in the field of Lindblad systems leave an open question of what other physical properties can now be explored within our framework. The most natural choice would be the study of higher point Green's functions in non-Gaussian theories and determination of whether signatures of integrability can be observed in their time evolution.

Another direction to explore is the issue of entanglement spreading in Lindblads with links to integrability. It is firmly established that for integrable Hamiltonians the quasiparticle interpretation of the entanglement spreading produces accurate analytic predictions for the entanglement time evolution [95–98]. The quasiparticle description has also been recently extended to Lindblad open quantum systems describing free particles [254]. It is a matter of curiosity whether any variation of this interpretation applies to interacting open models, particularly when they have a connection to integrability.

Furthermore, it would be interesting to investigate the possibility of extending the mapping between open quantum systems and integrable models to field theories. Following [213], one can construct the path integral description of an open QFT by adding to its Schwinger-Keldysh action an influence functional term of the Lindblad form. Recent progress has shown that such scalar theories are renormalisable to the first loop order [286]. Establishing a connection with integrability would potentially provide some informative insights into their analytic behaviour.

The methods of integrability provide a unique level of scrutiny we can apply to many-body quantum dynamics even in the case of interacting systems. Building on the results presented in this thesis, we reiterate the point that an integrable perspective is able to elucidate the intricacies of many relevant physical questions.

Appendix A

Numerical Generalised Hydrodynamics Investigation of the $SU(3)_2$-Homogeneous Sine-Gordon Model

A.1 Generalities

In our study of the non-equilibrium behaviour of the $SU(3)_2$-HSG model we have employed the open-source, MATLAB based framework called iFluid (integrable-Fluid, version 1.1.0) [181,182]. It is specifically designed for solving GHD equations in integrable models and thus perfect for our purposes. Thanks to a tensor-based numerical environment, iFluid boasts high efficiency and high process running speed. Additionally, a new model can be easily implemented by extending the iFluid package with a model-specific class. Such implementation can be done by following the instructions provided in [181]. However, the $SU(3)_2$-HSG model requires additional modifications and we have implemented them in this study.

The quantities studied feature in the `iFluidCore` class, which provides solutions to the TBA equations and inputs for the GHD equations. By default, the definition of spatial particle density included in the `iFluidCore` class depends on the type-array. It is a fundamental property of the class and is included in the model implementation as a one-dimensional array composed of integers which label the particle types. In massive integrable QFTs with more than one particle in the spectrum, this definition of the particle density introduces multiplicative factors in its type components, which can lead to wrong results. We have instead implemented the definition that reproduces the total spatial particle density $\mathtt{q}_0(x,t) = \mathtt{q}_0^+(x,t) + \mathtt{q}_0^-(x,t)$ and leads to a correct result. Moreover, in our implementation of the model, some `iFluidCore` functions

have been modified to output the contributions from each particle type to a given quantity separately such as the functions $\mathtt{q}_0^{\pm}(x,t)$. In iFluid, the propagation of the GHD quantities is computed via `iFluidSolver` class. In numerical simulation we have employed the `SecondOrderSolver` solver, whose details can be found in section 3.2 in [181].

To the best of our knowledge, our work provides the first application of the iFluid package to a system which is initially prepared in a state involving temperatures $T \gg 1$. The convergence of the iterative procedure of numerically solving the TBA equations improves at lower temperatures [83]. Earlier examples provided with the iFluid package were tested for temperatures $T \approx 1$. We have successfully ensured the convergence of the TBA equations evaluated by the `iFluidCore` class for temperatures up to $\mathcal{O}(e^{10})$ and checked the consistency of our results in several ways.

A.2 Precision and Consistency Checks

A preliminary check was done on the initial state, which is given by the solution of the equilibrium TBA equations for a given fixed temperature $T(x)$ for each value of x. In the iFluid code, the precision is controlled by two parameters, namely, the tolerance and the maximal number of iterations allowed. In order to guarantee the highest accuracy, we set the former to 10^{-32} and the latter to 5000. We made these choices in part by comparing the outputs of iFluid in the initial state to results obtained for the same functions with a Mathematica code used in [177], a work by some of the authors analysing the scale invariant GHD of the $SU(3)_2$-HSG model. In this way, we established that for the choices above we achieved higher precision with iFluid.

A similar check was performed by evaluating the TBA scaling function $c(T)$ over a range of temperatures, especially at high temperatures, and seeing that plateaus at the expected values of the central charge [150] where reproduced. Likewise we computed the energy densities and currents in the UV limit, reproducing once more the results of [177].

Having established that the ground state is accurately described, we then turned to consistency checks of dynamical quantities and calculated the total particle density Q_0. As it should be conserved in time, its computation for various time steps provides a consistency check for numerical solutions of the GHD equations. In Table A.1 we have reported the numerical values of the total particle density evaluated in the case of no-bath, $T_a = 0$. Q_0 is confirmed to be conserved, up to a numerical variation

on the first decimal place, which is the order of the grid spacing implemented in the simulation, see Table A.2 for details. Finally, we performed other consistency checks

t	0	3	6	9	12
Q_0	561.2520	561.2541	561.1937	561.1511	561.1156

Table A.1: Numerical values of the total particle density Q_0 at several times. Here, the parameters are $\sigma = 10$, $\log(2T_m) = 7$ and $T_a = 0$ (no bath). To evaluate Q_0, we have computed $\mathfrak{q}_0^{\pm}$ and performed a cubic spline interpolation for the integration, implementing additional grid points whose spacing in x is $\Delta x = 1. \times 10^{-5}$. Q_0 is numerically conserved, up to a variation on the first decimal place, which can be attributed to the discretisation procedure.

which exploit the connection of our model with free theories. In particular, for $T \ll e^{|\sigma|/2}$ our model reduces to two Majorana free fermions. Consequently, performing numerics for the $SU(3)_2$-HSG model with $\sigma = 20$ and the choice of temperatures $T_m = \frac{1}{2}e^7, T_a = \frac{1}{2}e^3$, we should obtain results which are fully in the free fermion regime where the GHD equations can be solved exactly. Thus, in this regime numerical results from iFluid can be compared to analytical solutions. We have confirmed that they are in good agreement.

A.3 Space and Rapidity Discretisations

Besides convergence of the numerical solution of the TBA equations, we have established that the key source of numerical error is the choice of space discretisation. Examples of the values adopted in our computations are given in Table A.2.

	$\Delta_{\mathbf{max}}$	**No. Points**	**Max. Val.**	**Quadrature**
t	0.2500	61	15.	Rectangular
x	0.1000	441	22.	Rectangular
θ	0.0762	700	17.	Gauss-Legendre

Table A.2: Representative discretisation parameters and quadratures chosen for the numerical simulations discussed in section 3.6. From the left, the columns indicate (respectively for t, x, θ): the variable, the lowest resolution (i.e. the largest spacing between two grid points $\Delta_{\mathbf{max}}$), the number of grid points, the largest absolute value the variable takes, and the type of quadrature implemented. In the rectangular quadrature we have implemented equidistant grid points with fixed spacing $\Delta_{\mathbf{max}}$.

We have devoted special attention to the discretisation of the rapidity interval. iFluid employs Gauss-Legendre quadrature integration, which has excellent convergence properties for integrals over a finite interval [287,288]. However, this quadrature

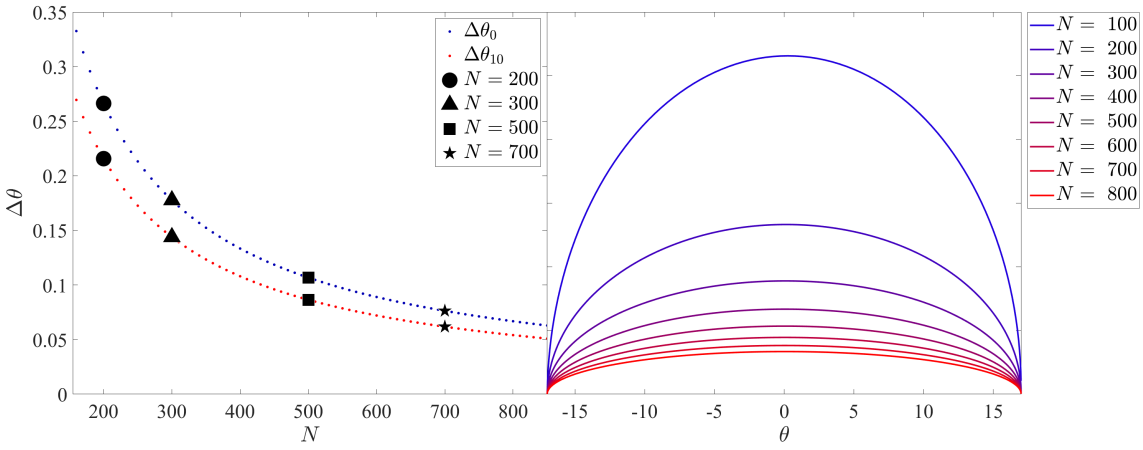


Figure A.1: Right: The rapidity discretisation interval as a function of rapidity for different numbers of points in a fixed rapidity interval $\theta \in [-17, 17]$. The markers indicate the values of N that are considered in Figure A.2. Left: Comparison of the rapidity discretisation interval in the middle and towards the edges of the interval with non-trivial dynamics for the choice of parameters considered in this thesis. $\Delta\theta_0$ and $\Delta\theta_{10}$ are defined to be the rapidity discretisation intervals for $\theta = 0$ and $\theta = 10$ respectively.

is optimised for minimising boundary errors. This means that the number of data intervals is lowest in the middle of the region of interest, precisely where we find the non-trivial behaviour of the thermodynamic quantities of interest. The dependence of the size of the rapidity intervals, $\Delta\theta$ on the rapidity θ and the number of points N in the interval considered for a fixed range of rapidities is shown in Figure A.1.

As a point of reference, we have chosen to compare the resolution at $\theta = 0$ and 10, as a primary region with non-trivial dynamics in many cases investigated. Although the discretisation interval for $\theta = 0$ remains the largest for any value of N, the distribution quickly flattens out when the number of points is increased. Investigating the range of N values from 200 to 700, we achieve an order of magnitude increase in resolution for both $\theta = 0$ and 10. Significantly smaller is also the difference between these two quantities, which is consistent with the flattening of the curve in the right panel of Figure A.1. The numerical values of the size of the discretisation interval for a chosen numbers of points in the rapidity interval are included in Table A.3.

In order to obtain the averages of conserved charges in the $SU(3)_2$-HSG model, it is necessary to integrate over the rapidity variable. This integration procedure leads to the "accumulation" of any numerical errors present in the original function and to the formation of regular structures that could be easily mistaken for genuine

N	$\Delta\theta_0$	$\Delta\theta_{10}$	$\Delta\theta_0 - \Delta\theta_{10}$
200	0.2664	0.2157	0.0506
300	0.1777	0.1439	0.0338
500	0.1067	0.0864	0.0203
700	0.0762	0.0617	0.0145

Table A.3: Numerical values of the rapidity discretisation intervals $\Delta\theta$, for a given number of rapidity points N in the range of rapidities $\theta \in [-17, 17]$.

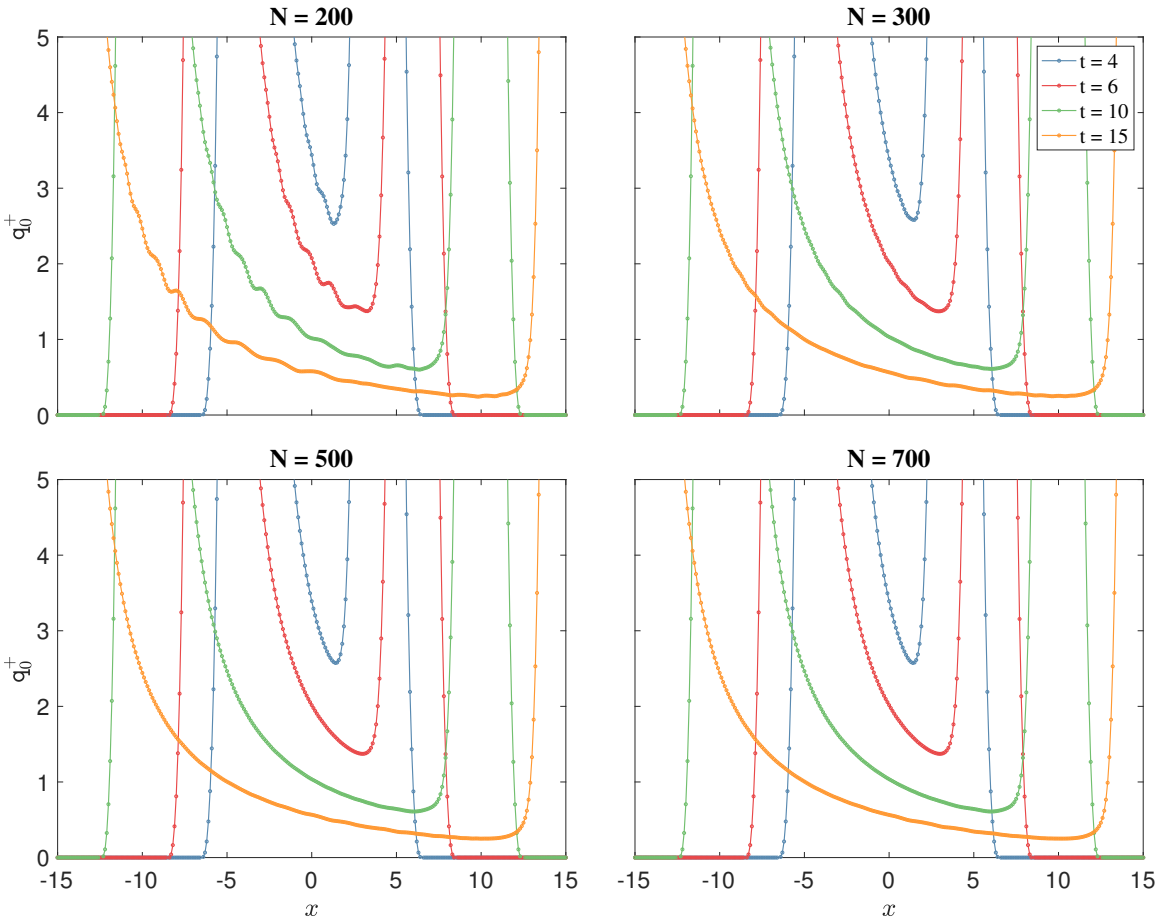


Figure A.2: Particle density of particle + for different numbers of points in the fixed rapidity interval $\theta \in [-17, 17]$. The $N = 200$ panel shows regular oscillations. The oscillations persist for $N = 300$, disappear around $N = 500$ and are consistently absent for higher numbers of points, such as $N = 700$. Variations of space and time discretisation parameters have not produced any significant changes in the same functions.

physical phenomena. An example of this effect can be seen in the particle density associated to particle + computed with different rapidity discretisations, as shown in Figure A.2. As expected, the problem arises from the middle of the rapidity interval

where resolution is lowest. By changing N we can identify a large enough value that guarantees a stable solution for the spatial particle density. The quantities not integrated over the rapidity integral did not exhibit any unusual behaviour even for the values of N as low as 200. Interestingly, this also applies to the spectral density, which then produces spatial particle density when integrated over rapidity. This further confirms that the emergence of the oscillations seen in the top left panel of Figure A.2 is genuinely a numerical effect arising due to integration.

Appendix B

Analytic Computation of $\mathfrak{q}_0(0,0)$

Let us look at the particle density at equilibrium at temperature T for a simple interacting QFT with single particle type and a diagonal S-matrix. By definition

$$\mathfrak{q}_0(0,0) = \frac{1}{2\pi}\int_{-\infty}^{\infty} n(\theta)E^{\rm dr}(\theta)d\theta \ , \tag{B.1}$$

where $n(\theta)$ is the occupation function, $E^{\rm dr}(\theta)$ the dressed energy and θ the rapidity variable. For later use, define a variable

$$y = \log\frac{2}{\beta} = \log(2T) \ . \tag{B.2}$$

Our aim is to study the asymptotics of $\mathfrak{q}_0(0,0)$ as a function of temperature for $y \to \infty$, that is $T \gg 1$. Let us rewrite it as

$$\begin{aligned}\mathfrak{q}_0(0,0) &= \frac{1}{2\pi}\int_{-\infty}^{0} n(\theta)E^{\rm dr}(\theta)d\theta + \frac{1}{2\pi}\int_{0}^{\infty} n(\theta)E^{\rm dr}(\theta)d\theta \\ &= \frac{1}{2\pi}\int_{-\infty}^{y} n(\theta-y)E^{\rm dr}(\theta-y)d\theta + \frac{1}{2\pi}\int_{-y}^{\infty} n(\theta+y)E^{\rm dr}(\theta+y)d\theta \end{aligned} \tag{B.3}$$

For a generic theory with a single particle, we can compute the pseudo-energy $\varepsilon(\theta \pm y) \equiv \varepsilon_\pm(\theta)$ in the limit of y large. Note that here the $\pm$ indices are not related in any way to the HSG model particles. The TBA equations are

$$\varepsilon(\theta) = \beta\cosh(\theta) - (\varphi \star L)(\theta) = e^{\theta-y} + e^{-\theta-y} - (\varphi\star L)(\theta) \ , \tag{B.4}$$

so that

$$\varepsilon_\pm(\theta) = e^{\theta-y\pm y} + e^{-\theta-y\mp y} - (\varphi\star L)(\theta\pm x) \approx e^{\pm\theta} - (\varphi\star L_\pm)(\theta) \ , \quad \text{for} \quad y \gg 1 \ . \tag{B.5}$$

Differentiating this equation with respect to rapidity, we get

$$\varepsilon'_\pm(\theta) = \pm e^{\pm\theta} - (\varphi'\star L_\pm)(\theta) \approx \pm e^{\pm\theta} - (\varphi\star L'_\pm)(\theta) \ , \tag{B.6}$$

where the last step follows from integration by parts, using the fact that $\varphi(\theta)$ should vanish at $\pm\infty$, and the identity $\frac{d}{d\theta}\varphi(\theta-\theta') = -\frac{d}{d\theta'}\varphi(\theta-\theta')$. The TBA L-function is defined as

$$L'_{\pm}(\theta) = -n_{\pm}(\theta)\varepsilon'_{\pm}(\theta)\ . \tag{B.7}$$

For large rapidities, we can take the derivatives of pseudo-energies to be

$$\varepsilon'_{\pm}(\theta) = [\pm e^{\pm\theta}]^{\mathrm{dr}}\ . \tag{B.8}$$

Then, equation (B.7) becomes exactly the equation for the dressing of the function $\pm e^{\pm\theta}$. On the other hand, the equation for the dressing of the energy is very similar to (B.6)

$$E^{\mathrm{dr}}(\theta) = \cosh\theta + (\varphi \star nE^{\mathrm{dr}})(\theta)\ , \tag{B.9}$$

and if we shift the rapidity by y as above we have that, for $y \gg 1$,

$$E^{\mathrm{dr}}_{\pm}(\theta) \approx \frac{e^{\pm\theta+y}}{2} + (\varphi \star n_{\pm}E^{\mathrm{dr}}_{\pm})(\theta)\,. \tag{B.10}$$

Consequently, (B.6) and (B.9) are essentially identical if we identify $\varepsilon'_{\pm}(\theta) = \pm\beta e^{\mathrm{dr}}_{\pm}(\theta)$. This realisation leads to the following replacement in the particle density

$$\begin{aligned}
\mathrm{q}_0(0,0) &= \frac{1}{2\pi}\int_{-\infty}^{y} n(\theta-y)e^{\mathrm{dr}}(\theta-y)\,d\theta + \frac{1}{2\pi}\int_{-y}^{\infty} n(\theta+y)e^{\mathrm{dr}}(\theta+y)\,d\theta \\
&\approx \frac{e^y}{4\pi}\int_{-\infty}^{y} n(\theta-y)[-e^{-\theta}]^{\mathrm{dr}}\ d\theta + \frac{e^y}{4\pi}\int_{-y}^{\infty} n(\theta+y)[e^{\theta}]^{\mathrm{dr}}\ d\theta \\
&\approx -\frac{e^y}{4\pi}\int_{-\infty}^{y} n(\theta-y)\varepsilon'(\theta-y)\ d\theta + \frac{e^y}{4\pi}\int_{-y}^{\infty} n(\theta+y)\varepsilon'(\theta+y)\,d\theta \\
&\approx \frac{1}{2\beta\pi}\int_{-\infty}^{y} L'(\theta-y)\ d\theta - \frac{1}{2\beta\pi}\int_{-y}^{\infty} L'(\theta+y)\,d\theta = \\
&= \frac{1}{2\beta\pi}(L(0) - L(-\infty-y) - L(\infty+y) + L(0))\ .
\end{aligned} \tag{B.11}$$

For $y \to \infty$, we have that $L(\pm\infty \pm y) \to 0$, as the L-functions typically go to zero at $\pm\infty$ and have a plateau between $-y$ and y. The final result is

$$\mathrm{q}_0(0,0) \approx \frac{L(0)}{\beta\pi}\,. \tag{B.12}$$

We can argue that $L(\pm\infty) = 0$, so for y large $L(y) = 0$. $L(0)$ for y large is the middle of the plateau of the L-function, so it will be model-dependent. It can be shown that $L(0) = \log 2$ for free fermions, as described in subsection 3.4.0.1. The result (B.12) generalizes to the case when the inverse temperature β is a function of x leading to the formula (3.40).

Appendix C

Single-Bond Jump Operator

C.1 2-State Fermionic Example

To interpret the ansatz (4.72) for a single-bond jump operator in terms of spinless fermions, consider a two-dimensional local Hilbert space with one degree of freedom bosonic and one fermionic. Taking $E^{11}_j E^{11}_{j+1}$ to represent the reference vacuum state, the most general single-bond jump operators are

$$\begin{aligned} B_j =&\lambda_{22} E^{22}_j + \lambda'_{22} E^{22}_{j+1} + \mu_{1212} E^{12}_j E^{12}_{j+1} + \mu_{2121} E^{21}_j E^{21}_{j+1} \\ &+ \mu_{1221} E^{12}_j E^{21}_{j+1} + \mu_{2112} E^{21}_j E^{12}_{j+1} + \mu_{2222} E^{22}_j E^{22}_{j+1} \ , \\ F_j =&\lambda_{12} E^{12}_j + \lambda'_{12} E^{12}_{j+1} + \lambda_{21} E^{21}_j + \lambda'_{21} E^{21}_{j+1} \\ &+ \mu_{1222} E^{12}_j E^{22}_{j+1} + \mu_{2122} E^{21}_j E^{22}_{j+1} + \mu_{2212} E^{22}_j E^{12}_{j+1} + \mu_{2221} E^{22}_j E^{21}_{j+1} \ . \end{aligned} \tag{C.1}$$

Interaction terms generated in this way are

$$\begin{aligned} B_j \overline{B^\dagger_j} =&(\lambda_{22} n_{j,\uparrow} + \lambda'_{22} n_{j+1,\uparrow} + \mu_{1212} c^\dagger_{j,\uparrow} c^\dagger_{j+1,\uparrow} + \mu_{2121} c_{j,\uparrow} c_{j+1,\uparrow} \\ &+ \mu_{1221} c^\dagger_{j,\uparrow} c_{j+1,\uparrow} + \mu_{2112} c_{j,\uparrow} c^\dagger_{j+1,\uparrow} + \mu_{2222} n_{j,\uparrow} n_{j+1,\uparrow}) \\ &\times(\lambda^*_{22} n_{j,\downarrow} + \lambda'^*_{22} n_{j+1,\downarrow} + \mu^*_{1212} c^\dagger_{j,\downarrow} c^\dagger_{j+1,\downarrow} + \mu^*_{2121} c_{j,\downarrow} c_{j+1,\downarrow} \\ &+ \mu^*_{1221} c^\dagger_{j,\downarrow} c_{j+1,\downarrow} + \mu^*_{2112} c_{j,\downarrow} c^\dagger_{j+1,\downarrow} + \mu^*_{2222} n_{j,\downarrow} n_{j+1,\downarrow}) \ , \end{aligned} \tag{C.2}$$

$$\begin{aligned} F_j \overline{F^\dagger_j} =&(\lambda_{12} c_{j,\uparrow} + \lambda'_{12} c_{j+1,\uparrow} + \lambda_{21} c^\dagger_{j,\uparrow} + \lambda'_{21} c^\dagger_{j+1,\uparrow} + \mu_{1222} c_{j,\uparrow} n_{j+1,\uparrow} \\ &+ \mu_{2122} c^\dagger_{j,\uparrow} n_{j+1,\uparrow} + \mu_{2212} n_{j,\uparrow} c_{j+1,\uparrow} + \mu_{2221} n_{j,\uparrow} c^\dagger_{j+1,\uparrow}) \\ &\times(\lambda^*_{12} c_{j,\downarrow} + \lambda'^*_{12} c_{j+1,\downarrow} + \lambda^*_{21} c^\dagger_{j,\downarrow} + \lambda'^*_{21} c^\dagger_{j+1,\downarrow} + \mu^*_{1222} c_{j,\downarrow} n_{j+1,\downarrow} \\ &+ \mu^*_{2122} c^\dagger_{j,\downarrow} n_{j+1,\downarrow} + \mu^*_{2212} n_{j,\downarrow} c_{j+1,\downarrow} + \mu^*_{2221} n_{j,\downarrow} c^\dagger_{j+1,\downarrow}) \ . \end{aligned} \tag{C.3}$$

Hence, in the vectorised Liouvillian we have 105 interaction terms acting on the rungs of the two-legged ladder dependent on only 15 independent parameters, which gives us a sense of how restrictive the Lindblad structure is. Necessarily, the rung

interactions are accompanied by the single-leg interactions. These do not contribute any new independent parameters and may destroy the potential integrability of the rung interaction terms. In the case considered, the single leg terms are

$$B_j^\dagger B_j + \overline{B_j^\dagger B_j} + F_j^\dagger F_j + \overline{F_j^\dagger F_j} = \mathcal{S}_{j,j+1}^{(\uparrow)} + \mathcal{S}_{j,j+1}^{(\downarrow)*} \ , \tag{C.4}$$

where

$$\begin{aligned}
\mathcal{S}_{j,j+1}^{(\sigma)} &= c_{j,\sigma}^\dagger c_{j+1,\sigma}^\dagger \left[\lambda_{21}^* \left(\lambda_{12}^{'} + \mu_{2212}\right) - \lambda_{21}^{'*} \left(\lambda_{12} + \mu_{1222}\right) - \mu_{2121}^* \left(\lambda_{22} + \lambda_{22}^{'} + \mu_{2222}\right)\right] \\
&+ c_{j,\sigma}^\dagger c_{j+1,\sigma} \left[\lambda_{21}^* \left(\lambda_{21}^{'} + \mu_{2221}\right) - \lambda_{12}\lambda_{12}^{'*} + \mu_{2122}^* \left(\lambda_{21}^{'} + \mu_{2221}\right) - \mu_{2112}^* \lambda_{22} + \mu_{1221}\lambda_{22}^{'*}\right] \\
&+ \frac{1}{2} n_{j,\sigma} \left[|\lambda_{22}|^2 + |\lambda_{12}|^2 - |\lambda_{21}|^2 + |\mu_{1221}|^2 - |\mu_{2121}|^2 + |\mu_{2221}|^2 + \mu_{2221}^* \lambda_{21}^{'} + \mu_{2221}\lambda_{21}^{'*}\right] \\
&+ \frac{1}{2} n_{j+1,\sigma} \left[|\lambda_{22}^{'}|^2 + |\lambda_{12}^{'}|^2 - |\lambda_{21}^{'}|^2 + |\mu_{2112}|^2 - |\mu_{2121}|^2 + |\mu_{2122}|^2 + \mu_{2122}^* \lambda_{21} + \mu_{2122}\lambda_{21}^*\right] \\
&+ \frac{1}{2} n_{j,\sigma} n_{j+1,\sigma} \Big[|\mu_{1212}|^2 + |\mu_{2121}|^2 - |\mu_{1221}|^2 - |\mu_{2112}|^2 + |\mu_{1222}|^2 + |\mu_{2212}|^2 \\
&\quad - |\mu_{2122}|^2 - |\mu_{2221}|^2 - |\lambda_{22}|^2 - |\lambda_{22}^{'}|^2 + \left(\lambda_{22} + \lambda_{22}^{'} + \mu_{2222}\right)\left(\lambda_{22}^* + \lambda_{22}^{'*} + \mu_{2222}^*\right) \\
&\quad + \lambda_{12}\mu_{1222}^* + \lambda_{12}^*\mu_{1222} + \lambda_{12}^{'}\mu_{2212}^* + \lambda_{12}^{'*}\mu_{2212} - \lambda_{21}\mu_{2122}^* - \lambda_{21}^*\mu_{2122} - \lambda_{21}^{'}\mu_{2221}^* - \lambda_{21}^{'*}\mu_{2221}\Big] \\
&+ \frac{1}{2}\left[|\mu_{2121}|^2 + |\lambda_{21}|^2 + |\lambda_{21}^{'}|^2\right] + \text{h.c} \ .
\end{aligned} \tag{C.5}$$

Appendix D

Some Unsuccessful Lindblad Maps

Most of the integrable ladder models we have considered cannot be associated in a straightforward way with Lindblad equations. In the following, we present some representative examples together with useful basis transformations.

D.1 Perk-Schultz Models

As an example we consider the $N = 4$ Perk-Schultz model [289, 290]

$$H_{\rm PS} = J\sum_j\sum_\alpha \cosh(\eta) E_j^{\alpha\alpha}E_{j+1}^{\alpha\alpha} + J\sum_j\sum_{\alpha\neq\beta} E_j^{\beta\alpha}E_{j+1}^{\alpha\beta} + \mathrm{sgn}(\alpha-\beta)\sinh\eta\ E_j^{\alpha\alpha}E_{j+1}^{\beta\beta}\ . \tag{D.1}$$

This can be viewed as a q-deformation of the $GL(4)$ two-legged ladder Hamiltonian considered in subsection 4.6.7 and is an integrable model. Using the decomposition (4.41), we can rewrite $H_{\rm PS}$ as

$$\begin{aligned} H_{\rm PS} &= J\sum_j P_{j,j+1} + \frac{\cosh(\eta)-1}{4}\big(1+\sigma_j^z\sigma_{j+1}^z\big)\big(1+\tau_j^z\tau_{j+1}^z\big) \\ &\quad + \frac{J\sinh(\eta)}{4}\sum_j\big(\sigma_{j+1}^z-\sigma_j^z\big)\big(1+\tau_j^z\tau_{j+1}^z\big). \end{aligned} \tag{D.2}$$

As the spectra of $\sigma_{j+1}^z - \sigma_j^z$ and $1+\tau_j^z\tau_{j+1}^z$ are different, the term in the second line cannot be related to Lindblad jump operator terms in this representation.

D.2 Higher Conservation Laws

A well-known way of obtaining integrable spin-ladder models is by considering higher conservation laws [70, 291]. In case of the spin-1/2 Heisenberg XXX chain, higher

conservation laws $H^{(k+1)}$ can be obtained from the transfer matrix by taking logarithmic derivatives at the "shift point". By construction, we have $[H^{(k)}, H^{(l)}] = 0$. The Hamiltonian we want to consider here is $H(b) = H^{(2)} + bH^{(4)} + \text{const}$ [291–293], which takes the form

$$\begin{aligned} H(b) &= 4\sum_{j=1}^{L}\Big[(1-b)\mathbf{S}_j\cdot\mathbf{S}_{j+1} + \frac{b}{2}\mathbf{S}_j\cdot\mathbf{S}_{j+2} + 2b\,(\mathbf{S}_{j-1}\cdot\mathbf{S}_{j+1})\,(\mathbf{S}_j\cdot\mathbf{S}_{j+2}) \\ &\qquad -2b\,(\mathbf{S}_{j-1}\cdot\mathbf{S}_{j+2})\,(\mathbf{S}_j\cdot\mathbf{S}_{j+1})\Big]. \end{aligned} \tag{D.3}$$

This can be viewed as a zig-zag ladder model by associating all even/odd sites with the first/second leg of a ladder, which gives

$$\begin{aligned} H(b) &= \sum_{j=1}^{L/2}(1-b)\boldsymbol{\sigma}_j\cdot[\boldsymbol{\tau}_j+\boldsymbol{\tau}_{j+1}] + \frac{b}{2}\Big\{\boldsymbol{\sigma}_j\cdot\boldsymbol{\sigma}_{j+1}[\boldsymbol{\tau}_j\cdot\boldsymbol{\tau}_{j+1}+\boldsymbol{\tau}_{j+1}\cdot\boldsymbol{\tau}_{j+2}] \\ &+ \boldsymbol{\sigma}_j\cdot\boldsymbol{\sigma}_{j+1} + \boldsymbol{\tau}_j\cdot\boldsymbol{\tau}_{j+1} - \boldsymbol{\tau}_j\cdot\boldsymbol{\sigma}_{j+1}\,\boldsymbol{\sigma}_j\cdot\boldsymbol{\tau}_{j+1} - \boldsymbol{\sigma}_j\cdot\boldsymbol{\tau}_{j+2}\,\boldsymbol{\sigma}_{j+1}\cdot\boldsymbol{\tau}_{j+1}\Big\} \end{aligned} \tag{D.4}$$

This expression is asymmetric under leg exchange in a way that precludes a direct relation with a Lindblad equation.

Alternatively, one can use a non-local transformation of the form

$$\begin{aligned} S^x_{2j-1} &= (-1)^j\left\{\prod_{m=1}^{j-1}\tau^z_m\right\}\sigma^x_j\ , \\ S^x_{2j} &= (-1)^j\left\{\prod_{m=1}^{j}\tau^z_m\right\}\sigma^x_j \\ S^y_{2j-1} &= (-1)^{j-1}\tau^x_j\left\{\prod_{m=j}^{N}\sigma^z_m\right\}\ , \\ S^y_{2j} &= (-1)^j\tau^x_j\left\{\prod_{m=j+1}^{N}\sigma^z_m\right\}\ , \\ S^z_{2j-1} &= \left\{\prod_{m=1}^{j-1}\tau^z_m\right\}\sigma^y_j\tau^x_j\left\{\prod_{m=j+1}^{N}\sigma^z_m\right\}\ , \\ S^z_{2j} &= \left\{\prod_{m=1}^{j-1}\tau^z_m\right\}\sigma^x_j\tau^y_j\left\{\prod_{m=j+1}^{N}\sigma^z_m\right\}\ . \end{aligned} \tag{D.5}$$

This transformation renders the Hamiltonian symmetric under leg exchange, yet still

incompatible with the Lindblad structure

$$
\begin{aligned}
H(b) = 4\sum_{j=1}^{L/2}(1-b)\left(\sigma_j^x\sigma_{j+1}^x\tau_j^x\tau_{j+1}^x + \tau_j^x\tau_{j+1}^x - \sigma_j^x\sigma_{j+1}^x\right) \\
- \frac{b}{2}\left(\sigma_j^x\sigma_{j+1}^y\tau_j^x\tau_{j+1}^y + \sigma_j^x\sigma_{j+1}^x\tau_{j+1}^z + \sigma_{j+1}^z\tau_j^x\tau_{j+1}^x\right) \\
+ 2b\big(- \sigma_j^y\sigma_{j+1}^y\tau_j^z + \sigma_j^z\tau_j^y\tau_{j+1}^y - \sigma_j^y\sigma_{j+1}^y\tau_{j+1}^z - \sigma_{j+1}^z\tau_j^y\tau_{j+1}^y \\
- \sigma_j^x\sigma_{j+1}^x\tau_j^y\tau_{j+1}^y - \sigma_j^y\sigma_{j+1}^y\tau_j^x\tau_{j+1}^x + \sigma_j^y\sigma_{j+1}^y\tau_j^z\tau_{j+1}^z - \sigma_j^z\sigma_{j+1}^z\tau_j^y\tau_{j+1}^y \\
+ \sigma_j^y\sigma_{j+1}^x\tau_j^x\tau_{j+1}^y + \sigma_j^x\sigma_{j+1}^y\tau_j^y\tau_{j+1}^x + \sigma_j^y\sigma_{j+1}^y - \tau_j^y\tau_{j+1}^y\big) \ .
\end{aligned}
\tag{D.6}
$$

The way to realise the incompatibility is by examining the single species "components" of every term in the above Hamiltonian. Presence of terms of a type $a\tilde{b}$ and $b\tilde{a}$ also requires terms $a\tilde{a}, b\tilde{b}$ with appropriate proportionality constants. In this case, the Lindblad compatibility is precluded by the absence of terms proportional to

$$
\sigma_j^y\sigma_{j+1}^y\tau_j^y\tau_{j+1}^y,\ \sigma_j^y\sigma_{j+1}^x\tau_j^y\tau_{j+1}^x,\ \sigma_j^z\sigma_{j+1}^z\tau_j^z\tau_{j+1}^z,\ \sigma_j^z\tau_j^z,\ \sigma_{j+1}^z\tau_{j+1}^z \ . \tag{D.7}
$$

D.3 Alcaraz-Bariev Model

The Alcaraz-Bariev two-parameter families of integrable models [294] come in two classes denoted by $A^{\pm}$ and $B^{\pm}$ respectively. The $B^{\pm}$ family contains the Hubbard model as a special limit and this is the only case in which we succeeded in obtaining an interpretation in terms of a Lindblad equation. We now discuss why such a relation does not seem to exist in general for the $A^{\pm}$ family of models. The Hamiltonian of the $A^{\pm}$ family can be cast in the form

$$
H_A^{(\epsilon)} = \sum_j T_{j,j+1} + T_{j,j+1}^{(1)} + T_{j,j+1}^{(2)} + gT_{j,j+1}^{(3)} + \cos\theta[S_{j,j+1} - \epsilon T_{j,j+1}^{(p)} + V_{j,j+1} - \epsilon U_{j,j+1}] \ , \tag{D.8}
$$

where $g = (1+\epsilon)(1-\sin\theta)$ and

$$
\begin{aligned}
T_{j,j+1} &= -e_j^{21}e_{j+1}^{12} + \widetilde{e}_j^{21}\widetilde{e}_{j+1}^{12} + \text{h.c.}, \\
T_{j,j+1}^{(1)} &= -(e_j^{21}e_{j+1}^{12} - e_j^{12}e_{j+1}^{21})\widetilde{e}_j^{22}(\epsilon\sin\theta - 1) + (\widetilde{e}_j^{21}\widetilde{e}_{j+1}^{12} - \widetilde{e}_j^{12}\widetilde{e}_{j+1}^{21})e_j^{22}(\sin\theta - 1), \\
T_{j,j+1}^{(2)} &= -(e_j^{21}e_{j+1}^{12} - e_j^{12}e_{j+1}^{21})\widetilde{e}_{j+1}^{22}(\sin\theta - 1) + (\widetilde{e}_j^{21}\widetilde{e}_{j+1}^{12} - \widetilde{e}_j^{12}\widetilde{e}_{j+1}^{21})e_{j+1}^{22}(\epsilon\sin\theta - 1), \\
T_{j,j+1}^{(3)} &= -e_j^{21}e_{j+1}^{12}\widetilde{e}_j^{22}\widetilde{e}_{j+1}^{22} + \widetilde{e}_j^{21}\widetilde{e}_{j+1}^{12}e_j^{22}e_{j+1}^{22} + \text{h.c.}, \\
S_{j,j+1} &= e_j^{21}e_{j+1}^{12}\widetilde{e}_j^{12}\widetilde{e}_{j+1}^{21} + \text{h.c.}, \\
T_{j,j+1}^{(p)} &= -e_j^{21}e_{j+1}^{12}\widetilde{e}_j^{21}\widetilde{e}_{j+1}^{12} + \text{h.c.} \ , \\
V_{j,j+1} &= e^{-2\eta}e_j^{22}\widetilde{e}_{j+1}^{22} + e^{2\eta}\widetilde{e}_j^{22}e_{j+1}^{22}, \\
U_{j,j+1} &= e_j^{22}\widetilde{e}_j^{22} + e_{j+1}^{22}\widetilde{e}_{j+1}^{22}.
\end{aligned}
\tag{D.9}
$$

Here, we have carried out a unitary transformation

$$Ue_j^{ab}U^\dagger = e_j^{ab}(-1)^{j(a-b)} \tag{D.10}$$

on the Hamiltonian given in [294] in anticipation of relating it to a Lindbladian. We start by noting that we require $g = 0$ for such an interpretation to be possible. The reason is that the only way to generate $T^{(3)}_{j,j+1}$ is as a "cross-term" in $\ell_j\overline{\ell_j^\dagger}$ with

$$\ell_j = ae_j^{21}e_{j+1}^{12} + be_j^{12}e_{j+1}^{21} + ce_j^{22}e_{j+1}^{22}. \tag{D.11}$$

However, such jump operators would also generate an unwanted contribution

$$|c|^2 e_j^{22}e_{j+1}^{22}\widetilde{e}_j^{22}\widetilde{e}_{j+1}^{22}. \tag{D.12}$$

As this cannot be cancelled by introducing additional jump operators and does not feature in $H_A^{(\epsilon)}$ we conclude that we must have $g = 0$. Next we turn to the cubic terms $T^{(1)}_{j,j+1}$. These must arise from jump operators of the form

$$L_j = ae_j^{21}e_{j+1}^{12} + be_j^{12}e_{j+1}^{21} + ce_j^{22}. \tag{D.13}$$

These jump operators give rise to inter-species interactions

$$\begin{aligned} L_j\overline{L}_j^\dagger &= |a|^2 e_j^{21}e_{j+1}^{12}\widetilde{e}_j^{21}\widetilde{e}_{j+1}^{12} + ab^* e_j^{21}e_{j+1}^{12}\widetilde{e}_j^{12}\widetilde{e}_{j+1}^{21} + a^*be_j^{12}e_{j+1}^{21}\widetilde{e}_j^{21}\widetilde{e}_{j+1}^{12} \\ &+ |b|^2 e_j^{12}e_{j+1}^{21}\widetilde{e}_j^{12}\widetilde{e}_{j+1}^{21} + |c|^2 e_j^{22}\widetilde{e}_j^{22} + c^*(ae_j^{21}e_{j+1}^{12} + be_j^{12}e_{j+1}^{21})\widetilde{e}_j^{22} \\ &+ ce_j^{22}(a^*\widetilde{e}_j^{21}\widetilde{e}_{j+1}^{12} + b^*\widetilde{e}_j^{12}\widetilde{e}_{j+1}^{21}), \end{aligned} \tag{D.14}$$

and intra-species interactions

$$\begin{aligned} L_j^\dagger L_j &= |a|^2(1-e_j^{22})e_{j+1}^{22} + |b|^2 e_j^{22}(1-e_{j+1}^{22}) + |c|^2 e_j^{22} - a^*ce_j^{12}e_{j+1}^{21} + c^*ae_j^{21}e_{j+1}^{12}\ , \\ \overline{L_j^\dagger L_j} &= |a|^2(1-\widetilde{e}_j^{22})\widetilde{e}_{j+1}^{22} + |b|^2\widetilde{e}_j^{22}(1-\widetilde{e}_{j+1}^{22}) + |c|^2\widetilde{e}_j^{22} - ac^*\widetilde{e}_j^{12}\widetilde{e}_{j+1}^{21} + ca^*\widetilde{e}_j^{21}\widetilde{e}_{j+1}^{12}\ . \end{aligned} \tag{D.15}$$

In order to produce the cubic terms in $H_A^{(\epsilon)}$ we require

$$a = -b\ , \quad ac^* = 1 - \epsilon\sin\theta\ , \quad ca^* = \sin\theta - 1. \tag{D.16}$$

Combining these with the requirement that $g = 0$ leads to

$$\epsilon = \sin\theta = 1. \tag{D.17}$$

In this case the $A^\pm$ model reduces to free fermions.

We have also investigated whether carrying out a similarity transformation $SH_A^{(\epsilon)}S^{-1}$, with

$$S = \prod_{j=1}^{L}\exp\left[\varphi e_j^{22}\widetilde{e}_j^{22} + j\left(\varphi_1 e_j^{11} + \varphi_2 e_j^{22} + \tilde{\varphi}_1\widetilde{e}_j^{11} + \tilde{\varphi}_2\widetilde{e}_j^{22}\right)\right], \tag{D.18}$$

may facilitate a Lindblad interpretation. The answer appears to be negative.

D.4 Spin-1/2 Ladder Models

Using an ansatz of jump operators, the following integrable spin-1/2 ladder models given by V. Gritsev and D. Baeriswyl [277] could not be recast into a valid Lindblad equation. To simplify the description, the models are described by the types of interactions they include: single-leg $S_j.S_{j+1}$, rung $S_j.T_j$, diagonal $S_j.T_{j+1}$, leg-leg $(S_j.S_{j+1})(T_j.T_{j+1})$, rung-rung $(S_j.T_j)(S_{j+1}.T_{j+1})$, and diagonal-diagonal $(S_j.T_{j+1})(T_j.S_{j+1})$. Here, S_j and T_j are canonical spin-1/2 operators which act on site j of the first and second leg of the ladder respectively.

1. Single-leg and leg-leg interactions

$$H_L = \sum_j [4(S_j.S_{j+1})(T_j.T_{j+1}) - S_j.S_{j+1} - T_j.T_{j+1}] \ . \tag{D.19}$$

2. Diagonal and diagonal-diagonal interactions

$$H_D = \sum_j [4(S_j.T_{j+1})(S_{j+1}.T_j) - S_j.T_{j+1} - T_j.S_{j+1}] \ . \tag{D.20}$$

3. Single-leg, diagonal, leg-leg and diagonal-diagonal interactions (first type)

$$\begin{aligned} H_{LD1} = \sum_j [&4(S_j.S_{j+1})(T_j.T_{j+1}) - 4(S_j.T_{j+1})(S_{j+1}.T_j) \\ &+ S_j.T_{j+1} + S_{j+1}.T_j + S_j.S_{j+1} + T_j.T_{j+1}] \ . \end{aligned} \tag{D.21}$$

4. Single-leg, diagonal, leg-leg and diagonal-diagonal interactions (second type)

$$\begin{aligned} H_{LD2} = \sum_j [&4(S_j.S_{j+1})(T_j.T_{j+1}) + 4(S_j.T_{j+1})(S_{j+1}.T_j) \\ &- S_j.S_{j+1} - T_j.T_{j+1} - S_j.T_{j+1} - T_j.S_{j+1}] \ . \end{aligned} \tag{D.22}$$

5. Single-leg, diagonal, leg-leg and diagonal-diagonal interactions (third type)

$$\begin{aligned} H_{LD3} = \sum_j [&-2(S_j.S_{j+1})(T_j.T_{j+1}) + 2(S_j.T_{j+1})(S_{j+1}.T_j) \\ &+ \frac{3}{2}(S_j.T_{j+1} + S_{j+1}.T_j + S_j.S_{j+1} + T_j.T_{j+1})] \ . \end{aligned} \tag{D.23}$$

6. Single-leg, diagonal, leg-leg and diagonal-diagonal interactions (fourth type)

$$\begin{aligned} H_{LD4} = \sum_j [&2(S_j.S_{j+1})(T_j.T_{j+1}) + 2(S_j.T_{j+1})(S_{j+1}.T_j) \\ &+ \frac{1}{2}(S_j.T_{j+1} + S_{j+1}.T_j + S_j.S_{j+1} + T_j.T_{j+1})] \ . \end{aligned} \tag{D.24}$$

7. Single-leg, rung, diagonal, leg-leg and rung-rung interactions

$$H_{LRD1} = \sum_j [(2S_j.S_{j+1} + \frac{1}{2})(2T_j.T_{j+1} + \frac{1}{2}) + J_R S_j.T_j \\ - 4(S_j.T_j)(S_{j+1}.T_{j+1}) - S_j.T_{j+1} - S_{j+1}.T_j - S_j.S_{j+1} - T_j.T_{j+1}] \ , \tag{D.25}$$

where J_R is a free parameter.

8. Single-leg, rung, diagonal, leg-leg, rung-rung and diagonal-diagonal interactions

$$H_{LRD2} = \sum_j [(2S_j.S_{j+1} + \frac{1}{2})(2T_j.T_{j+1} + \frac{1}{2}) + (J_R + 2)S_j.T_j \\ 4(S_j.T_j)(S_{j+1}.T_{j+1}) - 4(S_j.T_{j+1})(S_{j+1}.T_j) - (S_j.T_{j+1}) - (S_{j+1}.T_j)] \ , \tag{D.26}$$

where J_R is a free parameter.

D.4.1 Dzyaloshinsky-Moriya Spin Chain

The integrable Hamiltonian considered is a spin-1/2 chain [295]

$$H = \sum_{j=1}^{N} \Big\{ \vec{S}_{2j}.\vec{S}_{2j-1} + \vec{S}_{2j+1}.\vec{S}_{2j} + 2b^2(\vec{S}_{2j+2}.\vec{S}_{2j} + \vec{S}_{2j+1}.\vec{S}_{2j-1}) \\ - b\Big\{ \vec{S}_{2j+2}.(\vec{S}_{2j+1} \times \vec{S}_{2j}) + \vec{S}_{2j+1}.(\vec{S}_{2j-1} \times \vec{S}_{2j}) \Big\} \Big\} \ . \tag{D.27}$$

As the Hamiltonian is not-symmetric under odd-even site exchange, the interpretation of this model as a zig-zag ladder is not compatible with the Lindblad equation. Using the non-local spin transformation (D.5), the Hamitonian takes a form

$$H = \sum_{j=1}^{N} \Big\{ (\sigma_j^z + 1)(\tau_j^z - 1) + (\sigma_j^x \sigma_{j+1}^x + 1)(\tau_j^x \tau_{j+1}^x - 1) \\ - 2b^2\{\sigma_j^x \sigma_{j+1}^x(\tau_j^z + \tau_{j+1}^x) + (\sigma_j^z + \sigma_{j+1}^z)\tau_j^x \tau_{j+1}^x + \sigma_j^y \sigma_{j+1}^x \tau_j^y \tau_{j+1}^x + \sigma_j^x \sigma_{j+1}^y \tau_j^x \tau_{j+1}^y\} \\ - b\{-\sigma_j^x \sigma_{j+1}^y(\tau_j^x \tau_{j+1}^x + 1) + (\sigma_j^x \sigma_{j+1}^x - 1)\tau_j^x \tau_{j+1}^y + \sigma_j^y \sigma_{j+1}^x(\tau_j^z - 1) - (\sigma_j^z + 1)\tau_j^y \tau_{j+1}^x \\ + \sigma_{j+1}^z \tau_j^x \tau_{j+1}^y + \sigma_j^x \sigma_{j+1}^y \tau_{j+1}^z - \sigma_j^x \sigma_{j+1}^x \tau_j^y \tau_{j+1}^x + \sigma_j^y \sigma_{j+1}^x \tau_j^x \tau_{j+1}^x\} \Big\} \ . \tag{D.28}$$

In order to reproduce the interaction terms present, the most general ansätze for jump operators are

$$L_j^{(1)} = \alpha_1 \sigma_j^x \sigma_{j+1}^x + \beta_1 \sigma_j^y \sigma_{j+1}^x + \gamma_1 \sigma_j^z \ , \\ L_j^{(2)} = \alpha_2 \sigma_j^x \sigma_{j+1}^x + \beta_2 \sigma_j^x \sigma_{j+1}^y + \gamma_2 \sigma_{j+1}^z \ . \tag{D.29}$$

Considering the coefficients in front of the terms proportional to

$$\sigma_j^x \sigma_{j+1}^x \tau_j^x \tau_{j+1}^y \ , \quad \sigma_j^x \sigma_{j+1}^y \tau_{j+1}^z \ , \quad \sigma_j^x \sigma_{j+1}^x \tau_{j+1}^z \ , \tag{D.30}$$

we require

$$\alpha_2 \beta_2^* = b \ , \quad \beta_2 \gamma_2^* = b \ , \quad \alpha_2 \gamma_2^* = -2b^2 \ . \tag{D.31}$$

Combining these conditions gives

$$\frac{b}{\beta_2^*} \frac{b}{\beta_2} = -2b^2 \quad \Rightarrow \quad |\beta_2|^2 = -\frac{1}{2} \ , \tag{D.32}$$

which is a contradiction. Thus, in this basis the model is incompatible with the Lindblad structure.

Bibliography

[1] A. M. Kaufman, M. E. Tai, A. Lukin, M. Rispoli, R. Schittko, P. M. Preiss, and M. Greiner, "Quantum thermalization through entanglement in an isolated many-body system," *Science*, vol. 353, no. 6301, p. 794–800, 2016.

[2] Y. O. Nakagawa, M. Watanabe, H. Fujita, and S. Sugiura, "Universality in volume-law entanglement of scrambled pure quantum states," *Nature Communications*, vol. 9, no. 1635, 2018.

[3] R. Ma, B. Saxberg, C. Owens, N. Leung, Y. Lu, J. Simon, and D. I. Schuster, "A dissipatively stabilized Mott insulator of photons," *Nature*, vol. 566, no. 7742, p. 51–57, 2019.

[4] C. S. Gardner, J. M. Greene, M. D. Kruskal, and R. M. Miura, "Method for Solving the Korteweg-deVries Equation," *Physical Review Letters*, vol. 19, p. 1095, 1967.

[5] M. A. Ablowitz and P. A. Clarkson, *Solitons, Nonlinear Evolution Equations and Inverse Scattering*. London Mathematical Society Lecture Note Series, Cambridge University Press, 1991.

[6] H. Bethe, "Zur Theorie der Metalle," *Zeitschrift fur Physik*, vol. 71, no. 3-4, pp. 205–226, 1931.

[7] L. Faddeev, E. Sklyanin, and L. Takhtajan, "The Quantum Inverse Problem Method. I," *Theoretical and Mathematical Physics*, vol. 40, pp. 688–706, 1980.

[8] L. A. Takhtadzhan and L. D. Faddeev, "The quantum method of the inverse problem and the Heisenberg XYZ model," *Russian Mathematical Surveys*, vol. 34, no. 5, pp. 11–68, 1979.

[9] E. Sklyanin, "Quantum version of the method of inverse scattering problem," *Journal of Soviet Mathematics.*, vol. 19, pp. 1546–1596, 1982.

[10] S. R. White, "Density matrix formulation for quantum renormalization groups," *Physical Review Letters*, vol. 69, pp. 2863–2866, 1992.

[11] S. R. White, "Density-matrix algorithms for quantum renormalization groups," *Physical Review B*, vol. 48, pp. 10345–10356, 1993.

[12] I. Peschel, M. Kaulke, and Legeza, "Density-matrix spectra for integrable models," *Annalen der Physik*, vol. 8, no. 2, p. 153–164, 1999.

[13] C. Karrasch, J. H. Bardarson, and J. E. Moore, "Reducing the numerical effort of finite-temperature density matrix renormalization group calculations," *New Journal of Physics*, vol. 15, no. 8, p. 083031, 2013.

[14] A. J. Daley, C. Kollath, U. Schollwöck, and G. Vidal, "Time-dependent density-matrix renormalization-group using adaptive effective Hilbert spaces," *Journal of Statistical Mechanics: Theory and Experiment*, vol. 2004, no. 04, p. P04005, 2004.

[15] G. Vidal, "Efficient Simulation of One-Dimensional Quantum Many-Body Systems," *Physical Review Letters*, vol. 93, p. 040502, 2004.

[16] S. R. White and A. E. Feiguin, "Real-time evolution using the density matrix renormalization group," *Physical Review Letters*, vol. 93, p. 076401, 2004.

[17] T. Barthel, U. Schollwöck, and S. R. White, "Spectral functions in one-dimensional quantum systems at finite temperature using the density matrix renormalization group," *Physical Review B*, vol. 79, p. 245101, 2009.

[18] O. A. Castro-Alvaredo, B. Doyon, and T. Yoshimura, "Emergent hydrodynamics in integrable quantum systems out of equilibrium," *Physical Review X*, vol. 6, p. 041065, 2016.

[19] B. Bertini, M. Collura, J. De Nardis, and M. Fagotti, "Transport in Out-of-Equilibrium XXZ Chains: Exact Profiles of Charges and Currents," *Physical Review Letters*, vol. 117, no. 20, 2016.

[20] L. N. Lipatov, "High-energy scattering in QCD and in quantum gravity and two-dimensional field theories," *Nuclear Physics B*, vol. 365, pp. 614–632, 1991.

[21] H. L. Verlinde and E. P. Verlinde, "QCD at high-energies and two-dimensional field theory," *arXiv:hep-th/9302104*, 1993.

[22] I. Aref'eva, "Large N QCD at high energies as two-dimensional field theory," *Physics Letters B*, vol. 328, no. 3-4, p. 411–419, 1994.

[23] B. Durhuus and J. Frohlich, "A connection between ν-dimensional Yang-Mills theory and $(\nu-1)$-dimensional, nonlinear σ-models," *Communications in Mathematical Physics*, vol. 75, pp. 103–151, 1980.

[24] T. Kinoshita, T. Wenger, and D. S. Weiss, "A quantum Newton's cradle," *Nature*, vol. 440, pp. 900–903, 2006.

[25] A. Foerster and E. Ragoucy, "Exactly solvable models in atomic and molecular physics," *Nuclear Physics B*, vol. 777, pp. 373–403, 2007.

[26] X.-W. Guan, M. T. Batchelor, and C. Lee, "Fermi gases in one dimension: From Bethe Ansatz to experiments," *Reviews of Modern Physics*, vol. 85, no. 4, p. 1633–1691, 2013.

[27] M. Batchelor and A. Foerster, "Yang-Baxter integrable models in experiments: From condensed matter to ultracold atoms," *Journal of Physics A: Mathematical and Theoretical*, vol. 49, 2015.

[28] F. Vind, A. Foerster, I. Oliveira, R. Sarthour, D. Soares-Pinto, A. Souza, and I. Roditi, "Experimental realization of the Yang-Baxter Equation via NMR interferometry," *Scientific Reports*, vol. 6, p. 20789, 2016.

[29] T. Giamarchi, "One-dimensional physics in the 21st century," *Comptes Rendus Physique*, vol. 17, no. 3, pp. 322–331, 2016.

[30] J. Gibbon, P. Caudrey, R. K. Bullough, and J. Eilbeck, "An n-soliton solution of a nonlinear optics equation derived by a general inverse method," *Lettere al Nuovo Cimento*, vol. 8, pp. 775–779, 1973.

[31] T. Giamarchi, *Quantum physics in one dimension*. International series of monographs on physics, Oxford: Clarendon Press, 2004.

[32] Y. Tserkovnyak, B. I. Halperin, O. M. Auslaender, and A. Yacoby, "Finite-Size Effects in Tunneling between Parallel Quantum Wires," *Physical Review Letters*, vol. 89, p. 136805, 2002.

[33] A. Kleine, C. Kollath, I. P. McCulloch, T. Giamarchi, and U. Schollwöck, "Spin-charge separation in two-component Bose gases," *Physical Review A*, vol. 77, p. 013607, 2008.

[34] N. Malvania, Y. Zhang, Y. Le, J. Dubail, M. Rigol, and D. S. Weiss, "Generalized hydrodynamics in strongly interacting 1d bose gases," *Science*, vol. 373, no. 6559, p. 1129–1133, 2021.

[35] Z. Wang, J. Wu, W. Yang, A. K. Bera, D. Kamenskyi, A. T. M. N. Islam, S. Xu, J. M. Law, B. Lake, C. Wu, and A. Loidl, "Experimental observation of Bethe strings," *Nature*, vol. 554, no. 7691, p. 219–223, 2018.

[36] I. Brouzos and A. Foerster, "Broken Integrability Trace on Stationary Correlation Properties," *Physical Review A*, vol. 89, 2014.

[37] J. Durnin, M. J. Bhaseen, and B. Doyon, "Non-equilibrium dynamics and weakly broken integrability," *arXiv:2004.11030*, 2020.

[38] A. J. Friedman, S. Gopalakrishnan, and R. Vasseur, "Diffusive hydrodynamics from integrability breaking," *Physical Review B*, vol. 101, no. 18, 2020.

[39] M. Znidaric, "Weak integrability breaking: Chaos with integrability signature in coherent diffusion," *Physical Review Letters*, vol. 125, p. 180605, 2020.

[40] B. Sutherland, *Beautiful Models*. World Scientific, 2004.

[41] M. Jimbo, *Yang-Baxter Equation in Integrable Systems*. Advanced series in mathematical physics, World Scientific, 1990.

[42] C. Kassel, *Quantum Groups*, vol. 155 of *Graduate Texts in Mathematics*. Springer-Verlag New York, 1995.

[43] C. Gomez, G. Sierra, and M. Ruiz-Altaba, *Quantum groups in two-dimensional physics*. Cambridge Monographs on Mathematical Physics, Cambridge University Press, 2011.

[44] J.-S. Caux and J. Mossel, "Remarks on the notion of quantum integrability," *Journal of Statistical Mechanics: Theory and Experiment*, vol. 2011, no. 02, p. P02023, 2011.

[45] G. Mussardo, *Statistical field theory, an introduction to exactly solved models in statistical physics*. Oxford Graduate Texts, Oxford University Press, 2010.

[46] A. B. Zamolodchikov and A. B. Zamolodchikov, "Factorized S-matrices in two dimensions as the exact solutions of certain relativistic quantum field theory models," *Annals of Physics*, vol. 120, no. 2, pp. 253–291, 1979.

[47] D. Bombardelli, "S-matrices and integrability," *Journal of Physics A: Mathematical and Theoretical*, vol. 49, no. 32, p. 323003, 2016.

[48] J. Cao, S. Cui, W.-L. Yang, K. Shi, and Y. Wang, "Spin-1/2 XYZ model revisit: General solutions via off-diagonal Bethe ansatz," *Nuclear Physics B*, vol. 886, p. 185–201, 2014.

[49] R. Shankar and E. Witten, "The S-Matrix of the Supersymmetric Nonlinear Sigma Model," *Physical Review D*, vol. 17, p. 2134, 1978.

[50] D. Iagolnitzer, "Factorization of the multiparticle s-matrix in two-dimensional space-time models," *Physical Review D*, vol. 18, pp. 1275–1285, 1978.

[51] S. J. Parke, "Absence of Particle Production and Factorization of the S-Matrix in $(1+1)$-dimensional Models," *Nuclear Physics B*, vol. 174, pp. 166–182, 1980.

[52] S. Coleman and J. Mandula, "All Possible Symmetries of the S-Matrix," *Physical Review*, vol. 159, pp. 1251–1256, 1967.

[53] A. B. Zamolodchikov, "Tetrahedra equations and integrable systems in three-dimensional space," *Soviet Journal of Experimental and Theoretical Physics*, vol. 52, p. 325, 1980.

[54] A. B. Zamolodchikov, "Tetrahedron Equations and the Relativistic S-Matrix of Straight Strings in (2+1)-dimensions," *Communications in Mathematical Physics*, vol. 79, pp. 489–505, 1981.

[55] R. J. Baxter, "On Zamolodchikov's solution of the tetrahedron equations," *Communications in Mathematical Physics*, vol. 88, no. 2, pp. 185 – 205, 1983.

[56] V. V. Bazhanov and R. J. Baxter, "New solvable lattice models in three-dimensions," *Journal of Statistical Physics*, vol. 69, pp. 453–585, 1992.

[57] A. M. Polyakov, "Hidden symmetry of the two-dimensional chiral fields," *Physics Letters B*, vol. 72, no. 2, pp. 224–226, 1977.

[58] C. N. Yang, "Some Exact Results for the Many-Body Problem in one Dimension with Repulsive Delta-Function Interaction," *Physical Review Letters*, vol. 19, pp. 1312–1315, 1967.

[59] R. J. Baxter, "Partition function of the Eight-Vertex lattice model," *Annals of Physics*, vol. 70, no. 1, pp. 193–228, 1972.

[60] L. Onsager, "Crystal Statistics. I. A Two-Dimensional Model with an Order-Disorder Transition," *Physical Review*, vol. 65, pp. 117–149, 1944.

[61] V. G. Turaev, "The Yang-Baxter equation and invariants of links," *Inventiones mathematicae*, vol. 92, pp. 527–553, 1988.

[62] S. Mandelstam, "Determination of the Pion-Nucleon Scattering Amplitude from Dispersion Relations and Unitarity. General Theory," *Physical Review*, vol. 112, pp. 1344–1360, 1958.

[63] J. Miramontes, "Hermitian analyticity versus Real analyticity in two-dimensional factorised S-matrix theories," *Physics Letters B*, vol. 455, no. 1-4, p. 231–238, 1999.

[64] B. Schroer, T. Truong, and P. Weisz, "Towards an explicit construction of the sine-Gordon field theory," *Physics Letters B*, vol. 63, no. 4, pp. 422–424, 1976.

[65] C. N. Yang and C. P. Yang, "Thermodynamics of a One-Dimensional System of Bosons with Repulsive Delta-Function Interaction," *Journal of Mathematical Physics*, vol. 10, no. 7, pp. 1115–1122, 1969.

[66] P. Weisz, "Exact quantum Sine-Gordon soliton form factors," *Physics Letters B*, vol. 67, no. 2, pp. 179–182, 1977.

[67] M. Karowski and P. Weisz, "Exact form factors in $(1 + 1)$-dimensional field theoretic models with soliton behaviour," *Nuclear Physics B*, vol. 139, no. 4, pp. 455–476, 1978.

[68] G. Arutyunov and S. Frolov, "Foundations of the $AdS_5 \times S^5$ superstring: I," *Journal of Physics A: Mathematical and Theoretical*, vol. 42, no. 25, p. 254003, 2009.

[69] G. Breit and E. Wigner, "Capture of slow neutrons," *Physical Review*, vol. 49, pp. 519–531, 1936.

[70] A. G. I. V. E. Korepin and N. M. Bogoliubov, *Quantum Inverse Scattering Method, Correlation Functions and Algebraic Bethe Ansatz*. Cambridge University Press, 1993.

[71] E. Ilievski, M. Medenjak, T. Prosen, and L. Zadnik, "Quasilocal charges in integrable lattice systems," *Journal of Statistical Mechanics*, vol. 2016, no. 6, p. 064008, 2016.

[72] R. J. Baxter, "One-dimensional anisotropic Heisenberg chain," *Annals of Physics*, vol. 70, pp. 323–337, 1972.

[73] J. Hubbard and B. H. Flowers, "Electron correlations in narrow energy bands," *Proceedings of the Royal Society of London. Series A. Mathematical and Physical Sciences*, vol. 276, no. 1365, pp. 238–257, 1963.

[74] F. H. L. Essler, H. Frahm, F. Göhmann, A. Klümper, and V. E. Korepin, *The One-Dimensional Hubbard Model*. Cambridge University Press, 2005.

[75] C. Kim, A. Y. Matsuura, Z.-X. Shen, N. Motoyama, H. Eisaki, S. Uchida, T. Tohyama, and S. Maekawa, "Observation of Spin-Charge Separation in One-Dimensional $SrCuO_2$," *Physical Review Letters*, vol. 77, pp. 4054–4057, 1996.

[76] H. Fujisawa, T. Yokoya, T. Takahashi, S. Miyasaka, M. Kibune, and H. Takagi, "Angle-resolved photoemission study of sr_2cuo_3," *Physical Review B*, vol. 59, pp. 7358–7361, Mar 1999.

[77] A. Damascelli, Z. Hussain, and Z.-X. Shen, "Angle-resolved photoemission studies of the cuprate superconductors," *Reviews of Modern Physics*, vol. 75, no. 2, p. 473–541, 2003.

[78] E. H. Lieb and F. Y. Wu, "Absence of Mott Transition in an Exact Solution of the Short-Range, One-Band Model in One Dimension," *Physical Review Letters*, vol. 20, pp. 1445–1448, 1968.

[79] F. Woynarovich, "Excitations with complex wavenumbers in a Hubbard chain. I. States with one pair of complex wavenumbers," *Journal of Physics C: Solid State Physics*, vol. 15, no. 1, pp. 85–96, 1982.

[80] T. Deguchi, "Thermodynamics and excitations of the one-dimensional Hubbard model," *Physics Reports*, vol. 331, no. 5, p. 197–281, 2000.

[81] M. Takahashi, "One-Dimensional Heisenberg Model at Finite Temperature," *Progress of Theoretical Physics*, vol. 46, no. 2, pp. 401–415, 1971.

[82] M. Takahashi, "One-Dimensional Hubbard Model at Finite Temperature," *Progress of Theoretical Physics*, vol. 47, no. 1, pp. 69–82, 1972.

[83] A. Zamolodchikov, "Thermodynamic Bethe ansatz in relativistic models: Scaling 3-state Potts and Lee-Yang models," *Nuclear Physics B*, vol. 342, no. 3, pp. 695–720, 1990.

[84] D. Fioretto and G. Mussardo, "Quantum quenches in integrable field theories," *New Journal of Physics*, vol. 12, no. 5, p. 055015, 2010.

[85] J. Mossel and J.-S. Caux, "Generalized TBA and generalized Gibbs," *Journal of Physics A: Mathematical and Theoretical*, vol. 45, no. 25, p. 255001, 2012.

[86] F. H. L. Essler and M. Fagotti, "Quench dynamics and relaxation in isolated integrable quantum spin chains," *Journal of Statistical Mechanics: Theory and Experiment*, vol. 6, p. 064002, 2016.

[87] J. M. Deutsch, "Quantum statistical mechanics in a closed system," *Physical Review A*, vol. 43, pp. 2046–2049, 1991.

[88] M. Srednicki, "Chaos and quantum thermalization," *Physical Review E*, vol. 50, no. 2, p. 888–901, 1994.

[89] M. Rigol, V. Dunjko, and M. Olshanii, "Thermalization and its mechanism for generic isolated quantum systems," *Nature*, vol. 452, no. 7189, p. 854–858, 2008.

[90] P. W. Anderson, "Absence of diffusion in certain random lattices," *Physical Review*, vol. 109, pp. 1492–1505, 1958.

[91] I. V. Gornyi, A. D. Mirlin, and D. G. Polyakov, "Interacting electrons in disordered wires: Anderson localization and low-t transport," *Physical Review Letters*, vol. 95, p. 206603, 2005.

[92] D. Basko, I. Aleiner, and B. Altshuler, "Metal–insulator transition in a weakly interacting many-electron system with localized single-particle states," *Annals of Physics*, vol. 321, no. 5, pp. 1126–1205, 2006.

[93] R. Nandkishore and D. A. Huse, "Many-body localization and thermalization in quantum statistical mechanics," *Annual Review of Condensed Matter Physics*, vol. 6, no. 1, pp. 15–38, 2015.

[94] *Created with BioRender.com.*

[95] P. Calabrese and J. L. Cardy, "Evolution of entanglement entropy in one-dimensional systems," *Journal of Statistical Mechanics*, vol. 0504, p. P04010, 2005.

[96] P. Calabrese and J. L. Cardy, "Time-dependence of correlation functions following a quantum quench," *Physical Review Letters*, vol. 96, p. 136801, 2006.

[97] P. Calabrese and J. Cardy, "Quantum quenches in (1+1)-dimensional conformal field theories," *Journal of Statistical Mechanics*, vol. 1606, no. 6, p. 064003, 2016.

[98] V. Alba and P. Calabrese, "Entanglement and thermodynamics after a quantum quench in integrable systems," *Proceedings of the National Academy of Sciences*, vol. 114, no. 30, pp. 7947–7951, 2017.

[99] S. Bose, "Quantum communication through spin chain dynamics: an introductory overview," *Contemporary Physics*, vol. 48, no. 1, pp. 13–30, 2007.

[100] M. Rigol, V. Dunjko, V. Yurovsky, and M. Olshanii, "Relaxation in a completely integrable many-body quantum system: An ab initio study of the dynamics of the highly excited states of 1d lattice hard-core bosons," *Physical Review Letters*, vol. 98, p. 050405, 2007.

[101] M. Brockmann, B. Wouters, D. Fioretto, J. D. Nardis, R. Vlijm, and J.-S. Caux, "Quench action approach for releasing the Néel state into the spin-1/2 XXZ chain," *Journal of Statistical Mechanics: Theory and Experiment*, vol. 2014, no. 12, p. P12009, 2014.

[102] T. Prosen and E. Ilievski, "Families of Quasilocal Conservation Laws and Quantum Spin Transport," *Physical Review Letters*, vol. 111, p. 057203, 2013.

[103] T. Prosen, "Open XXZ Spin Chain: Nonequilibrium Steady State and a Strict Bound on Ballistic Transport," *Physical Review Letters*, vol. 106, p. 217206, 2011.

[104] T. Prosen, "Quasilocal conservation laws in XXZ spin-1/2 chains: Open, periodic and twisted boundary conditions," *Nuclear Physics B*, vol. 886, pp. 1177–1198, 2014.

[105] E. Ilievski, J. De Nardis, B. Wouters, J.-S. Caux, F. H. L. Essler, and T. Prosen, "Complete Generalized Gibbs Ensembles in an Interacting Theory," *Physical Review Letters*, vol. 115, p. 157201, 2015.

[106] M. Kollar and M. Eckstein, "Relaxation of a one-dimensional Mott insulator after an interaction quench," *Physical Review A*, vol. 78, p. 013626, 2008.

[107] J.-S. Caux and R. M. Konik, "Constructing the Generalized Gibbs Ensemble after a Quantum Quench," *Physical Review Letters*, vol. 109, p. 175301, 2012.

[108] M. Collura, S. Sotiriadis, and P. Calabrese, "Equilibration of a Tonks-Girardeau Gas Following a Trap Release," *Physical Review Letters*, vol. 110, p. 245301, 2013.

[109] B. Pozsgay, "Quantum quenches and generalized Gibbs ensemble in a Bethe Ansatz solvable lattice model of interacting bosons," *Journal of Statistical Mechanics: Theory and Experiment*, vol. 2014, no. 10, p. P10045, 2014.

[110] P. Calabrese and J. Cardy, "Quantum quenches in extended systems," *Journal of Statistical Mechanics: Theory and Experiment*, vol. 2007, no. 06, pp. P06008–P06008, 2007.

[111] B. Pozsgay, "The generalized Gibbs ensemble for Heisenberg spin chains," *Journal of Statistical Mechanics: Theory and Experiment*, vol. 2013, no. 07, p. P07003, 2013.

[112] B. Wouters, J. De Nardis, M. Brockmann, D. Fioretto, M. Rigol, and J.-S. Caux, "Quenching the Anisotropic Heisenberg Chain: Exact Solution and Generalized Gibbs Ensemble Predictions," *Physical Review Letters*, vol. 113, p. 117202, 2014.

[113] M. Gring, M. Kuhnert, T. Langen, T. Kitagawa, B. Rauer, M. Schreitl, I. Mazets, D. A. Smith, E. Demler, and J. Schmiedmayer, "Relaxation and Prethermalization in an Isolated Quantum System," *Science*, vol. 337, no. 6100, pp. 1318–1322, 2012.

[114] T. Langen, S. Erne, R. Geiger, B. Rauer, T. Schweigler, M. Kuhnert, W. Rohringer, I. E. Mazets, T. Gasenzer, and J. Schmiedmayer, "Experimental observation of a generalized Gibbs ensemble," *Science*, vol. 348, no. 6231, pp. 207–211, 2015.

[115] L. Vidmar and M. Rigol, "Generalized Gibbs ensemble in integrable lattice models," *Journal of Statistical Mechanics: Theory and Experiment*, vol. 2016, no. 6, p. 064007, 2016.

[116] C. Boldrighini, R. L. Dobrushin, and Y. M. Suhov, "One-dimensional hard rod caricature of hydrodynamics: Navier-Stokes correction," *Communications in Mathematical Physics*, vol. 189, pp. 577–590, 1997.

[117] B. Doyon, T. Yoshimura, and J.-S. Caux, "Soliton Gases and Generalized Hydrodynamics," *Physical Review Letters*, vol. 120, no. 4, 2018.

[118] M. Fagotti, "Higher-order generalized hydrodynamics in one dimension: The noninteracting test," *Physical Review B*, vol. 96, p. 220302, 2017.

[119] J. De Nardis, D. Bernard, and B. Doyon, "Hydrodynamic Diffusion in Integrable Systems," *Physical Review Letters*, vol. 121, p. 160603, 2018.

[120] J. D. Nardis, D. Bernard, and B. Doyon, "Diffusion in generalized hydrodynamics and quasiparticle scattering," *SciPost Physics*, vol. 6, p. 49, 2019.

[121] S. Gopalakrishnan, D. A. Huse, V. Khemani, and R. Vasseur, "Hydrodynamics of operator spreading and quasiparticle diffusion in interacting integrable systems," *Physical Review B*, vol. 98, p. 220303, 2018.

[122] V. Khemani, A. Vishwanath, and D. A. Huse, "Operator spreading and the emergence of dissipative hydrodynamics under unitary evolution with conservation laws," *Physical Review X*, vol. 8, p. 031057, 2018.

[123] B. Doyon and T. Yoshimura, "A note on generalized hydrodynamics: inhomogeneous fields and other concepts," *SciPost Physics*, vol. 2, p. 014, 2017.

[124] A. Bastianello, V. Alba, and J.-S. Caux, "Generalized Hydrodynamics with Space-Time Inhomogeneous Interactions," *Physical Review Letters*, vol. 123, p. 130602, 2019.

[125] J.-S. Caux, B. Doyon, J. Dubail, R. Konik, and T. Yoshimura, "Hydrodynamics of the interacting Bose gas in the Quantum Newton Cradle setup," *SciPost Physics*, vol. 6, no. 6, 2019.

[126] M. Schemmer, I. Bouchoule, B. Doyon, and J. Dubail, "Generalized Hydrodynamics on an Atom Chip," *Physical Review Letters*, vol. 122, p. 090601, 2019.

[127] J. Eisert, M. Friesdorf, and C. Gogolin, "Quantum many-body systems out of equilibrium," *Nature Physics*, vol. 11, no. 2, pp. 124–130, 2015.

[128] R. Vasseur and J. E. Moore, "Nonequilibrium quantum dynamics and transport: from integrability to many-body localization," *Journal of Statistical Mechanics*, vol. 2016, no. 6, p. 064010, 2016.

[129] D. Bernard and B. Doyon, "Conformal field theory out of equilibrium: a review," *Journal of Statistical Mechanics*, vol. 2016, no. 6, p. 064005, 2016.

[130] L. D'Alessio, Y. Kafri, A. Polkovnikov, and M. Rigol, "From quantum chaos and eigenstate thermalization to statistical mechanics and thermodynamics," *Advances in Physics*, vol. 65, no. 3, pp. 239–362, 2016.

[131] C. Gogolin and J. Eisert, "Equilibration, thermalisation, and the emergence of statistical mechanics in closed quantum systems," *Reports on Progress in Physics*, vol. 79, no. 5, p. 056001, 2016.

[132] B. Doyon, "Lecture notes on generalised hydrodynamics," *SciPost Physics Lecture Notes*, 2020.

[133] M. Peskin and D. Schröder, "An introduction to quantum field theory," *Frontiers in Physics*, 1995.

[134] S. Weinberg, "The quantum theory of fields," *Cambridge University Press, Cambridge*, 1995.

[135] R. Eden, P. Landshoff, D. Olive, and J. Polkinghorne, "The analytic s-matrix," *Cambridge University Press*, 1998.

[136] M. Kormos, M. Collura, G. Takács, and P. Calabrese, "Real time confinement following a quantum quench to a non-integrable model," *Nature Physics.*, vol. 13, pp. 246–249, 2017.

[137] N. J. Robinson, A. J. A. James, and R. M. Konik, "Signatures of rare states and thermalization in a theory with confinement," *Physical Review B*, vol. 99, no. 19, 2019.

[138] Z.-C. Yang, F. Liu, A. V. Gorshkov, and T. Iadecola, "Hilbert-space fragmentation from strict confinement," *Physical Review Letters*, vol. 124, p. 207602, 2020.

[139] O. A. Castro-Alvaredo, M. Lencsés, I. M. Szécsényi, and J. Viti, "Entanglement oscillations near a quantum critical point," *Physical Review Letters*, vol. 124, no. 23, 2020.

[140] N. Kitanine, J. Maillet, and V. Terras, "Form factors of the XXZ Heisenberg finite chain," *Nuclear Physics B*, vol. 554, no. 3, p. 647–678, 1999.

[141] J.-S. Caux and J. M. Maillet, "Computation of Dynamical Correlation Functions of Heisenberg Chains in a Magnetic Field," *Physical Review Letters*, vol. 95, p. 077201, 2005.

[142] C. R. Fernández-Pousa, M. V. Gallas, T. J. Hollowood, and J. Miramontes, "Solitonic integrable perturbations of parafermionic theories," *Nuclear Physics B*, vol. 499, no. 3, p. 673–689, 1997.

[143] C. R. Fernandez-Pousa, M. V. Gallas, J. Hollowood, and J. Luis Miramontes, "The symmetric space and homogeneous sine-Gordon theories," *Nuclear Physics B*, vol. 484, no. 3, p. 609–630, 1997.

[144] J. Miramontes and C. Fernández-Pousa, "Integrable quantum field theories with unstable particles," *Physics Letters B*, vol. 472, no. 3-4, p. 392–401, 2000.

[145] C. R. Fernández-Pousa and J. L. Miramontes, "Semi-classical spectrum of the homogeneous sine-Gordon theories," *Nuclear Physics B*, vol. 518, no. 3, p. 745–769, 1998.

[146] O. A. Castro-Alvaredo and A. Fring, "Renormalization group flow with unstable particles," *Physical Review D*, vol. 63, no. 2, 2000.

[147] O. A. Castro-Alvaredo and A. Fring, "Decoupling the $\mathrm{SU}(N)_2$-homogeneous sine-Gordon model," *Physical Review D*, vol. 64, p. 085007, 2001.

[148] O. Castro-Alvaredo, A. Fring, and C. Korff, "Form factors of the homogeneous sine-Gordon models," *Physics Letters B*, vol. 484, no. 1-2, p. 167–176, 2000.

[149] O. Castro-Alvaredo and A. Fring, "Identifying the operator content, the homogeneous sine-Gordon models," *Nuclear Physics B*, vol. 604, no. 1-2, p. 367–390, 2001.

[150] O. Castro-Alvaredo, A. Fring, C. Korff, and J. Miramontes, "Thermodynamic Bethe ansatz of the homogeneous sine-Gordon models," *Nuclear Physics B*, vol. 575, no. 3, p. 535–560, 2000.

[151] O. A. Castro-Alvaredo, J. Dreißig, and A. Fring, "Integrable scattering theories with unstable particles," *The European Physical Journal C*, vol. 35, no. 3, p. 393–411, 2004.

[152] O. A. Castro-Alvaredo, "Bootstrap methods in 1+1 dimensional quantum field theories: The Homogeneous Sine-Gordon models," other thesis, 2001.

[153] A. V. Mikhailov, M. A. Olshanetsky, and A. M. Perelomov, "Two-dimensional generalized Toda lattice," *Communications in Mathematical Physics*, vol. 79, no. 4, pp. 473 – 488, 1981.

[154] G. Wilson, "The modified Lax and two-dimensional Toda lattice equations associated with simple Lie algebras," *Ergodic Theory and Dynamical Systems*, vol. 1, no. 3, p. 361–380, 1981.

[155] M. Toda, *Theory of Nonlinear Lattices*. Springer-Verlag Berlin Heidelberg, 1989.

[156] A. N. Leznov and M. V. Saveliev, "Two-dimensional exactly and completely integrable dynamical systems. Monopoles, instantons, dual models, relativistic strings, Lund-Regge model, generalized Toda lattice, etc," *Communications in Mathematical Physics*, vol. 89, no. 1, pp. 59 – 75, 1983.

[157] L. A. Ferreira, J.-L. Gervais, J. Sanchez Guillen, and M. V. Savelev, "Affine Toda systems coupled to matter fields," *Nuclear Physics B*, vol. 470, pp. 236–290, 1996.

[158] J. Luis Miramontes, "Tau-functions generating the conservation laws for generalized integrable hierarchies of KdV and affine toda type," *Nuclear Physics B*, vol. 547, no. 3, pp. 623–663, 1999.

[159] P. Di Francesco, P. Mathieu, and D. Sénéchal, *Conformal field theory*. Graduate texts in contemporary physics, New York: Springer, 1997.

[160] A. B. Zamolodchikov, "Integrable field theory from conformal field theory," *Advanced Studies in Pure Mathematics*, vol. 19, pp. 641–674, 1989.

[161] A. B. Zomolodchikov, ""Irreversibility" of the flux of the renormalization group in a 2D field theory," *Soviet Journal of Experimental and Theoretical Physics Letters*, vol. 43, p. 730, 1986.

[162] M. A. Virasoro, "Subsidiary Conditions and Ghosts in Dual-Resonance Models," *Physical Review D*, vol. 1, pp. 2933–2936, 1970.

[163] E. Witten, "Nonabelian Bosonization in Two-Dimensions," *Communications in Mathematical Physics*, vol. 92, pp. 455–472, 1984.

[164] V. Knizhnik and A. Zamolodchikov, "Current algebra and Wess-Zumino model in two dimensions," *Nuclear Physics B*, vol. 247, no. 1, pp. 83–103, 1984.

[165] E. Witten, "Global aspects of current algebra," *Nuclear Physics B*, vol. 223, no. 2, pp. 422–432, 1983.

[166] Q.-H. Park, "Deformed coset models from gauged wzw actions," *Physics Letters B*, vol. 328, no. 3, pp. 329–336, 1994.

[167] Q.-H. Park and H. Shin, "Deformed minimal models and generalized Toda theory," *Physics Letters B*, vol. 347, no. 1, pp. 73–79, 1995.

[168] A. B. Zamolodchikov, "Resonance factorized scattering and roaming trajectories," *Journal of Physics A: Mathematical and General*, vol. 39, no. 41, pp. 12847–12861, 2006.

[169] M. J. Martins, "Renormalization-group trajectories from resonance factorized S-matrices," *Physical Review Letters*, vol. 69, pp. 2461–2464, 1992.

[170] P. Dorey and F. Ravanini, "Staircase models from affine Toda field theory," *International Journal of Modern Physics A*, vol. 08, no. 05, p. 873–893, 1993.

[171] A. B. Zamolodchikov, "$Z(4)$ symmetric factorized S-matrix in two space-time dimensions," *Communications in Mathematical Physics*, vol. 69, pp. 165–178, 1979.

[172] G. Mussardo and S. Penati, "A quantum field theory with infinite resonance states," *Nuclear Physics*, vol. 567, pp. 454–492, 2000.

[173] O. A. Castro-Alvaredo and A. Fring, "Constructing infinite particle spectra," *Physical Review D*, vol. 64, p. 085005, 2001.

[174] D. Gepner, "New conformal field theories associated with Lie algebras and their partition functions," *Nuclear Physics B*, vol. 290, pp. 10–24, 1987.

[175] E. Fradkin, C. Nayak, and K. Schoutens, "Landau-Ginzburg theories for non-abelian quantum Hall states," *Nuclear Physics B*, vol. 546, no. 3, pp. 711–730, 1999.

[176] E. Ardonne and K. Schoutens, "New Class of Non-Abelian Spin-Singlet Quantum Hall States," *Physical Review Letters*, vol. 82, pp. 5096–5099, 1999.

[177] O. A. Castro-Alvaredo, C. D. Fazio, B. Doyon, and F. Ravanini, "On the Hydrodynamics of Unstable Excitations," *arXiv:2005.11266*, 2020.

[178] O. A. Castro-Alvaredo, C. De Fazio, B. Doyon, and A. A. Ziolkowska, "Tails of instability and decay: a hydrodynamic perspective," *arXiv:2103.03735*, 2021.

[179] O. A. Castro-Alvaredo, C. D. Fazio, B. Doyon, and A. A. Ziolkowska, "Generalised hydrodynamics of particle creation and decay," *arXiv:2112.05462*, 2021.

[180] B. Doyon, J. Dubail, R. Konik, and T. Yoshimura, "Large-Scale Description of Interacting One-Dimensional Bose Gases: Generalized Hydrodynamics Supersedes Conventional Hydrodynamics," *Physical Review Letters*, vol. 119, no. 19, 2017.

[181] F. S. Møller and J. Schmiedmayer, "Introducing iFluid: a numerical framework for solving hydrodynamical equations in integrable models," *SciPost Physics*, vol. 8, no. 3, 2020.

[182] F. S. Møller, G. Perfetto, B. Doyon, and J. Schmiedmayer, "Euler-scale dynamical correlations in integrable systems with fluid motion," *SciPost Physics Core*, vol. 3, no. 2, 2020.

[183] V. B. Bulchandani, R. Vasseur, C. Karrasch, and J. E. Moore, "Solvable hydrodynamics of quantum integrable systems," *Physical Review Letters*, vol. 119, Nov 2017.

[184] B. Doyon, H. Spohn, and T. Yoshimura, "A geometric viewpoint on generalized hydrodynamics," *Nuclear Physics B*, vol. 926, pp. 570–583, 2018.

[185] G. Perfetto and B. Doyon, "Euler-scale dynamical fluctuations in non-equilibrium interacting integrable systems," *SciPost Physics*, vol. 10, no. 5, 2021.

[186] M. Abramowitz and I. A. Stegun, *Handbook of Mathematical Functions with Formulas, Graphs, and Mathematical Tables*. New York: Dover, 1964.

[187] "Video: Time evolution of spectral density and the effective velocity," *https://youtu.be/mvNnzBL7vYs*.

[188] "Video: Time evolution of the spectral density with and without a bath," *https://youtu.be/yyLcuTn4lBY*.

[189] C. Boldrighini, R. L. Dobrushin, and Y. M. Sukhov, "One-dimensional hard rod caricature of hydrodynamics," *Journal of Statistical Physics*, vol. 31, no. 3, pp. 577–616, 1983.

[190] H. Weimer, M. Müller, I. Lesanovsky, P. Zoller, and H. P. Büchler, "A Rydberg quantum simulator," *Nature Physics*, vol. 6, no. 5, p. 382–388, 2010.

[191] M. Schemmer and I. Bouchoule, "Cooling a Bose Gas by Three-Body Losses," *Physical Review Letters*, vol. 121, p. 200401, 2018.

[192] W. H. Zurek, "Decoherence, einselection, and the quantum origins of the classical," *Reviews of Modern Physics*, vol. 75, pp. 715–775, 2003.

[193] M. A. Nielsen and I. L. Chuang, *Quantum Computation and Quantum Information*. Cambridge University Press, 2000.

[194] T. Botzung, S. Diehl, and M. Müller, "Engineered dissipation induced entanglement transition in quantum spin chains: from logarithmic growth to area law," *arXiv:2106.10092*, 2021.

[195] B. Horstmann, J. I. Cirac, and G. Giedke, "Noise-driven dynamics and phase transitions in fermionic systems," *Physical Review A*, vol. 87, p. 012108, 2013.

[196] M. J. Kastoryano, D. Reeb, and M. M. Wolf, "A cutoff phenomenon for quantum Markov chains," *Journal of Physics A: Mathematical and Theoretical*, vol. 45, no. 7, p. 075307, 2012.

[197] E. Vernier, "Mixing times and cutoffs in open quadratic fermionic systems," *SciPost Physics*, vol. 9, no. 4, 2020.

[198] S. Diehl, A. Micheli, A. Kantian, B. Kraus, H. P. Büchler, and P. Zoller, "Quantum states and phases in driven open quantum systems with cold atoms," *Nature Physics*, vol. 4, no. 11, p. 878–883, 2008.

[199] F. Verstraete, M. M. Wolf, and J. I. Cirac, "Quantum computation, quantum state engineering, and quantum phase transitions driven by dissipation," *Nature Physics*, vol. 5, pp. 633–636, 2009.

[200] J. C. Budich, P. Zoller, and S. Diehl, "Dissipative preparation of Chern insulators," *Physical Review A*, vol. 91, p. 042117, 2015.

[201] F. Iemini, D. Rossini, R. Fazio, S. Diehl, and L. Mazza, "Dissipative topological superconductors in number-conserving systems," *Physical Review B*, vol. 93, p. 115113, 2016.

[202] S. Bandyopadhyay, S. Laha, U. Bhattacharya, and A. Dutta, "Exploring the possibilities of dynamical quantum phase transitions in the presence of a Markovian bath," *Scientific Reports*, vol. 8, 08 2018.

[203] G. Lindblad, "On the Generators of Quantum Dynamical Semigroups," *Communications in Mathematical Physics*, vol. 48, p. 119, 1976.

[204] V. Gorini, A. Kossakowski, and E. Sudarshan, "Completely Positive Dynamical Semigroups of N Level Systems," *Journal of Mathematical Physics*, vol. 17, p. 821, 1976.

[205] MIT OpenCourseWare, "Quantum theory of radiation interactions," Fall 2002.

[206] H.-P. Breuer, "Non-Markovian generalization of the Lindblad theory of open quantum systems," *Physical Review A*, vol. 75, no. 2, p. 022103, 2007.

[207] S. Nakajima, "On quantum theory of transport phenomena," *Progress of Theoretical Physics*, vol. 20, no. 6, pp. 948–959, 1958.

[208] R. Zwanzig, "Ensemble method in the theory of irreversibility," *The Journal of Chemical Physics*, vol. 33, no. 5, pp. 1338–1341, 1960.

[209] F. Shibata, Y. Takahashi, and N. Hashitsume, "A generalized stochastic Liouville equation. Non-Markovian versus memoryless master equations," *Journal of Statistical Physics*, vol. 17, no. 4, pp. 171–187, 1977.

[210] H.-P. Breuer and F. Petruccione, *The theory of open quantum systems*. Oxford University Press Inc., New York, 2010.

[211] J. P. Garrahan, "Aspects of non-equilibrium in classical and quantum systems: Slow relaxation and glasses, dynamical large deviations, quantum nonergodicity, and open quantum dynamics," *Physica A: Statistical Mechanics and its Applications*, vol. 504, pp. 130–154, 2018.

[212] A. Li, F. Petruccione, and J. Koch, "Perturbative approach to Markovian open quantum systems," *Scientific Reports*, vol. 4, 2014.

[213] L. M. Sieberer, M. Buchhold, and S. Diehl, "Keldysh field theory for driven open quantum systems," *Reports on Progress in Physics*, vol. 79, no. 9, p. 096001, 2016.

[214] F. Verstraete, J. J. García-Ripoll, and J. I. Cirac, "Matrix product density operators: Simulation of finite-temperature and dissipative systems," *Physical Review Letters*, vol. 93, p. 207204, 2004.

[215] D. Jaschke, S. Montangero, and L. D. Carr, "One-dimensional many-body entangled open quantum systems with tensor network methods," *Quantum Science and Technology*, vol. 4, no. 1, p. 013001, 2018.

[216] J. Cui, J. I. Cirac, and M. C. Banuls, "Variational matrix product operators for the steady state of dissipative quantum systems," *Physical Review Letters*, vol. 114, p. 220601, 2015.

[217] J.-S. Bernier, R. Tan, L. Bonnes, C. Guo, D. Poletti, and C. Kollath, "Light-cone and diffusive propagation of correlations in a many-body dissipative system," *Physical Review Letters*, vol. 120, p. 020401, 2018.

[218] D. Yuan, H. Wang, Z. Wang, and D.-L. Deng, "Solving the Liouvillian Gap with Artificial Neural Networks," *arXiv:2009.00019*, 2020.

[219] L.-H. Gwa and H. Spohn, "Six-vertex model, roughened surfaces, and an asymmetric spin Hamiltonian," *Physical Review Letters*, vol. 68, p. 725, 1992.

[220] D. Kim, "Bethe ansatz solution for crossover scaling functions of the asymmetric XXZ chain and the Kardar-Parisi-Zhang-type growth model," *Physical Review E*, vol. 52, p. 3512, 1995.

[221] O. Golinelli and K. Mallick, "Hidden symmetries in the asymmetric exclusion process," *Journal of Physics A*, vol. 37, p. 3321, 2004.

[222] J. de Gier and F. H. L. Essler, "Bethe Ansatz solution of the asymmetric exclusion process with open boundaries," *Physical Review Letters*, vol. 95, p. 240601, 2005.

[223] J. de Gier and F. H. L. Essler, "Slowest relaxation mode of the partially asymmetric exclusion process with open boundaries," *Journal of Physics A*, vol. 41, p. 485002, 2008.

[224] J. Eisert and T. Prosen, "Noise-driven quantum criticality," *arXiv:1012.5013*, 2010.

[225] C. Guo and D. Poletti, "Solutions for bosonic and fermionic dissipative quadratic open systems," *Physical Review A*, vol. 95, p. 052107, 2017.

[226] T. Prosen, "Third quantization: A general method to solve master equations for quadratic open fermi systems," *New Journal of Physics*, vol. 10, 2008.

[227] M. V. Medvedyeva, F. H. L. Essler, and T. Prosen, "Exact Bethe Ansatz Spectrum of a Tight-Binding Chain with Dephasing Noise," *Physical Review Letters*, vol. 117, p. 137202, 2016.

[228] D. A. Rowlands and A. Lamacraft, "Noisy coupled qubits: Operator spreading and the Fredrickson-Andersen model," *Physical Review B*, vol. 98, p. 195125, 2018.

[229] N. Shibata and H. Katsura, "Dissipative quantum Ising chain as a non-Hermitian Ashkin-Teller model," *Physical Review B*, vol. 99, p. 224432, 2019.

[230] N. Shibata and H. Katsura, "Dissipative spin chain as a non-Hermitian Kitaev ladder," *Physical Review B*, vol. 99, p. 174303, 2019.

[231] P. Ribeiro and T. Prosen, "Integrable quantum dynamics of open collective spin models," *Physical Review Letters*, vol. 122, p. 010401, 2019.

[232] M. Nakagawa, N. Kawakami, and M. Ueda, "Exact Liouvillian Spectrum of a One-Dimensional Dissipative Hubbard Model," *arXiv:2003.14202*, 2020.

[233] S. Lerma-Hernández, A. Rubio-García, and J. Dukelsky, "Trigonometric $SU(N)$ Richardson–Gaudin models and dissipative multi-level atomic systems," *Journal of Physics A: Mathematical and Theoretical*, vol. 53, no. 39, p. 395302, 2020.

[234] B. Buca, C. Booker, M. Medenjak, and D. Jaksch, "Dissipative Bethe Ansatz: Exact Solutions of Quantum Many-Body Dynamics Under Loss," *arXiv:2004.05955*, 2020.

[235] F. H. L. Essler and L. Piroli, "Integrability of 1D Lindbladians from operator-space fragmentation," *arXiv:2009.11745*, 2020.

[236] J. Robertson and F. Essler, "Exact solution of a quantum asymmetric exclusion process with particle creation and annihilation," *arXiv:2105.08828*, 2021.

[237] A. A. Ziolkowska and F. H. Essler, "Yang-Baxter integrable Lindblad equations," *SciPost Physics*, vol. 8, p. 44, 2020.

[238] M. de Leeuw, C. Paletta, and B. Pozsgay, "Constructing Integrable Lindblad Superoperators," *arXiv:2101.08279*, 2021.

[239] M. V. Medvedyeva, F. H. L. Essler, and T. Prosen, "Exact Bethe Ansatz Spectrum of a Tight-Binding Chain with Dephasing Noise," *Physical Review Letters*, vol. 117, no. 13, p. 137202, 2016.

[240] M. Schmutz, "Real-time green's functions in many body problems," *Zeitschrift für Physik B: Condensed Matter*, vol. 30, pp. 97–106, 1978.

[241] A. A. Dzhioev and D. S. Kosov, "Nonequilibrium perturbation theory in liouville–fock space for inelastic electron transport," *Journal of Physics: Condensed Matter*, vol. 24, no. 22, p. 225304, 2012.

[242] J. de Gier and F. H. L. Essler, "Exact spectral gaps of the asymmetric exclusion process with open boundaries," *Journal of Statistical Mechanics: Theory and Experiment*, vol. 12, p. 12011, 2006.

[243] T. Prosen and B. Buča, "Exact matrix product decay modes of a boundary driven cellular automaton," *Journal of Physics A: Mathematical General*, vol. 50, p. 395002, 2017.

[244] T. Prosen, "Matrix product solutions of boundary driven quantum chains," *Journal of Physics A: Mathematical General*, vol. 48, p. 373001, 2015.

[245] B. S. Shastry, "Infinite conservation laws in the one-dimensional Hubbard model," *Physical Review Letters*, vol. 56, p. 1529, 1986.

[246] B. S. Shastry, "Decorated star-triangle relations and exact integrability of the one-dimensional Hubbard model," *Journal of Statistical Physics*, vol. 50, p. 57, 1988.

[247] Z. Maassarani, "Exact integrability of the $SU(n)$ Hubbard model," *Modern Physics Letters*, vol. B12, pp. 51–56, 1998.

[248] M. J. Martins, "On the integrability of the $SU(N)$ Hubbard model," *Physics Letters A*, vol. 247, p. 218, 1998.

[249] J. M. Drummond, G. Feverati, L. Frappat, and E. Ragoucy, "Super-Hubbard models and applications," *Journal of High Energy Physics*, vol. 2007, no. 05, p. 008, 2007.

[250] G. Feverati, L. Frappat, and E. Ragoucy, "Universal Hubbard models with arbitrary symmetry," *Journal of Statistical Mechanics: Theory and Experiment*, vol. 2009, no. 04, p. P04014, 2009.

[251] M. J. Martins and P. B. Ramos, "The quantum inverse scattering method for Hubbard-like models," *Nuclear Physics*, p. 413, 1998.

[252] M. Shiroishi and M. Wadati, "Decorated star-triangle relations for the free-fermion model and a new solvable bilayer vertex model," *Journal of the Physical Society of Japan*, vol. 64, p. 57, 1995.

[253] M. S. Y. Umeno and M. Wadati, "Fermionic R-operator and integrability of the one-dimensional Hubbard model," *Journal of the Physical Society of Japan*, vol. 67, p. 7, 1998.

[254] F. Carollo and V. Alba, "Emergent dissipative quasi-particle picture in noninteracting markovian open quantum systems," *arXiv:2106.11997*, 2021.

[255] G. C. Wick, "The Evaluation of the Collision Matrix," *Physical Review*, vol. 80, pp. 268–272.

[256] B. Bertini, F. H. Essler, S. Groha, and N. J. Robinson, "Prethermalization and Thermalization in Models with Weak Integrability Breaking," *Physical Review Letters*, vol. 115, no. 18, 2015.

[257] Z. Maassarani, "The $su(n)$ Hubbard model," *Physical Review A*, vol. 239, p. 187, 1998.

[258] Z. Maassarani, "Hubbard Models as Fusion Products of Free Fermions," *International Journal of Modern Physics B*, vol. 12, pp. 1893–1906, 1998.

[259] P. Jordan and E. Wigner, "Über das Paulische Äquivalenzverbot," *Zeitschrift fur Physik*, 1928.

[260] F. Göhmann and S. Murakami, "Fermionic representations of integrable lattice systems," *Journal of Physics A: Mathematical and General*, vol. 30, p. 5269, 1998.

[261] A. G. Izergin, A. G. Pronko and N. I. Abarenkova, "Temperature correlators in the one-dimensional Hubbard model in the strong coupling limit," *Physics Letters A*, vol. 245, p. 537, 1998.

[262] B. Kumar, "Exact solution of the infinite-U Hubbard problem and other models in one dimension," *Physical Review B*, vol. 79, p. 155121, 2009.

[263] A. Nocera, F. H. L. Essler and A. E. Feiguin, "Finite-temperature dynamics of the Mott insulating Hubbard chain," *Physical Review B*, vol. 97, p. 045146, 2018.

[264] V. Fomin, L. Frappat, and E. Ragoucy, "Including a phase in the bethe equations of the hubbard model," *Journal of High Energy Physics*, vol. 04, p. 062, 2010.

[265] C. K. Lai, "Lattice gas with nearest-neighbor interaction in one dimension with arbitrary statistics," *Journal of Mathematical Physics*, vol. 15, p. 1675, 1974.

[266] B. Sutherland, "Model for a multicomponent quantum system," *Physical Review B*, vol. 12, pp. 3795–3805, 1975.

[267] B. S. Shastry and B. Sutherland, "Twisted boundary conditions and effective mass in Heisenberg-Ising and Hubbard rings," *Physical Review Letters*, vol. 65, p. 243, 1990.

[268] G. A. P. Ribeiro, M. J. Martins and W. Galleas, "Integrable $SU(N)$ vertex models with general toroidal boundary conditions," *Nuclear Physics B*, vol. 675, p. 567, 2003.

[269] A. P. Tonel, A. Foerster, J. Links, and A. L. Malvezzi, "Integrable anisotropic spin-ladder model," *Physical Review B*, vol. 64, p. 054420, 2001.

[270] A. P. Tonel, A. Foerster, K. Hibberd, and J. Links, "Integrable generalized spin ladder models based on the $SU(1,3)$ and $SU(3,1)$ algebras," *Journal of Mathematical Physics*, vol. 44, no. 12, pp. 6032–6039, 2003.

[271] P. Kulish and E. Sklyanin, "Solutions of the Yang-Baxter equation," *Journal of Soviet Mathematics*, no. 19, p. 1596–1620, 1982.

[272] P. P. Kulish, "Integrable graded magnets," *Journal of Soviet Mathematics*, vol. 35, p. 2648, 1986.

[273] F. H. L. Essler, V. E. Korepin, and K. Schoutens, "New exactly solvable model of strongly correlated electrons motivated by high-T_c superconductivity," *Physical Review Letters*, vol. 68, pp. 2960–2963, 1992.

[274] F. H. L. Essler, V. E. Korepin and K. Schoutens, "Exact solution of an electronic model of superconductivity," *International Journal of Modern Physics B*, vol. 8, p. 3205, 1994.

[275] F. H. L. Essler, V. E. Korepin and K. Schoutens, "Spectrum of low-lying excitations in a supersymmetric extended Hubbard model," *International Journal of Modern Physics B*, vol. 8, p. 3243, 1994.

[276] S. Belliard and E. Ragoucy, "The nested Bethe ansatz for "all" closed spin chains," *Journal of Physics A*, vol. 41, p. 295202, 2008.

[277] V. Gritsev and D. Baeriswyl, "Exactly soluble isotropic spin-1/2 ladder models," *Journal of Physics A: Mathematical General*, vol. 36, pp. 12129–12142, 2003.

[278] F. C. Alcaraz, D. Arnaudon, V. Rittenberg and M. Scheunert, "Finite chains with quantum affine symmetries," *International Journal of Modern Physics A*, vol. 9, p. 3473, 1994.

[279] S. Albeverio, S. M. Fei and Y. P. Wang, "An exactly solvable model of generalized spin ladder," *Europhysics Letters*, vol. 47, p. 364, 1999.

[280] N. Crampe, E. Ragoucy, and M. Vanicat, "Integrable approach to simple exclusion processes with boundaries. Review and progress," *Journal of Statistical Mechanics: Theory and Experiment*, vol. 2014, no. 11, p. P11032, 2014.

[281] E. K. Sklyanin, "Boundary conditions for integrable quantum systems," *Journal of Physics A: Mathematical and General*, vol. 21, no. 10, pp. 2375–2389, 1988.

[282] C. Arita, A. Ayyer, K. Mallick, and S. Prolhac, "Recursive structures in the multispecies TASEP," *Journal of Physics A: Mathematical and Theoretical*, vol. 44, no. 33, p. 335004, 2011.

[283] C. Arita, A. Ayyer, K. Mallick, and S. Prolhac, "Generalized matrix Ansatz in the multispecies exclusion process—the partially asymmetric case," *Journal of Physics A: Mathematical and Theoretical*, vol. 45, no. 19, p. 195001, 2012.

[284] C. Finn, E. Ragoucy, and M. Vanicat, "Matrix product solution to multi-species ASEP with open boundaries," *Journal of Statistical Mechanics: Theory and Experiment*, vol. 2018, no. 4, p. 043201, 2018.

[285] V. Eisler, "Crossover between ballistic and diffusive transport: the quantum exclusion process," *Journal of Statistical Mechanics: Theory and Experiment*, vol. 2011, no. 06, p. P06007, 2011.

[286] Avinash, C. Jana, R. Loganayagam, and A. Rudra, "Renormalization in Open Quantum Field theory I: Scalar field theory," *arXiv:1704.08335*, 2017.

[287] G. H. Golub and J. H. Welsch, "Calculation of Gauss quadrature rules," *Mathematics of Computation*, vol. 23, 1969.

[288] I. Bogaert, "Iteration-free computation of Gauss–Legendre quadrature nodes and weights," *SIAM Journal on Scientific Computing*, vol. 36, 2014.

[289] J. H. H. Perk and C. L. Schultz, "New families of commuting transfer matrices in q-state vertex models," *Physics Letters A*, vol. 84, p. 407, 1981.

[290] C. L. Schultz, "Eigenvectors of the multi-component generalization of the six-vertex model," *Physica A*, vol. 122, p. 71, 1983.

[291] N. Muramoto and M. Takahashi, "Integrable magnetic model of two chains coupled by four-body interactions," *Journal of the Physical Society of Japan*, vol. 68, p. 2098, 1999.

[292] A. A. Zvyagin and A. Klümper, "Quantum phase transitions and thermodynamics of quantum antiferromagnets with next-nearest-neighbor couplings," *Physical Review B*, vol. 68, p. 144426, 2003.

[293] C. Trippe and A. Klümper, "Quantum phase transitions and thermodynamics of quantum antiferromagnets with competing interactions," *Low Temperature Physics*, vol. 33, p. 920, 2007.

[294] F. C. Alcaraz and R. Z. Bariev, "Interpolation between Hubbard and supersymmetric t-J models: two-parameter integrable models of correlated electrons," *Journal of Physics A: Mathematical General*, vol. 32, pp. L483–L488, 1999.

[295] Y. Qiao, Z. Xin, J. Cao, W.-L. Yang, K. Shi, and Y. Wang, "Exact solution of an integrable $J_1 - J_2$ spin chain model," *arXiv:1812.09316*, 2018.